SPRINGER TRACTS
220 IN MODERN PHYSICS

Stefan Roth

Precision Electroweak Physics at Electron-Positron Colliders

Springer

Springer Tracts in Modern Physics
Volume 220

Springer Tracts in Modern Physics

Springer Tracts in Modern Physics provides comprehensive and critical reviews of topics of current interest in physics. The following fields are emphasized: elementary particle physics, solid-state physics, complex systems, and fundamental astrophysics.
Suitable reviews of other fields can also be accepted. The editors encourage prospective authors to correspond with them in advance of submitting an article. For reviews of topics belonging to the above mentioned fields, they should address the responsible editor, otherwise the managing editor.
See also springer.com

Stefan Roth

Precision Electroweak Physics at Electron-Positron Colliders

With 107 Figures

Springer

Stefan Roth
RWTH Aachen University
3rd Institute for Physics
Sommerfeldstrasse
D-52056 Aachen
E-mail: roth@physik.rwth-aachen.de

Library of Congress Control Number: 2006931936

Physics and Astronomy Classification Scheme (PACS):
13.66.Jn, 12.15.Ji, 12.15.Lk, 14.70.Fm

ISSN print edition: 0081-3869
ISSN electronic edition: 1615-0430
ISBN-10 3-540-35164-7 Springer Berlin Heidelberg New York
ISBN-13 978-3-540-35164-1 Springer Berlin Heidelberg New York

Typesetting: by the author and techbooks using a Springer LaTeX macro package
Cover production: WMXDesign GmbH, Heidelberg

Printed on acid-free paper SPIN: 11394471 56/techbooks 5 4 3 2 1 0

Preface

Electron-Positron Colliders have played a key role in the development of modern particle physics. The first particle accelerators designed for the study of e^+e^- collisions were the machines ADONE (Frascati), SPEAR (SLAC) and DORIS (DESY). They provided clean events originating from a well-defined initial state, a great advantage typical to all following e^+e^- colliders. Moreover, in contrary to hadron colliders, here the scattering of point-like particles is studied, which can be calculated with very high precision in theory. Therefore the e^+e^- colliders are ideal places for accurate measurements, especially for precision tests of the electroweak Standard Model. On the other hand, the discovery of charmonium and the tau lepton at SPEAR (SLAC) and of the gluon at PETRA (DESY) showed that in certain circumstances e^+e^- collisions are not limited to precision physics, but can also lead to discoveries. In addition, the PETRA accelerator was the first electron-positron collider that contributed to the test of electroweak interactions. For example, measuring the forward-backward asymmetry in muon-pair production, $e^+e^- \to \mu^+\mu^-$, showed contributions from the exchange of the, at that time still undiscovered, Z boson, the gauge boson of the weak neutral current.

At the Large Electron-Positron Collider, LEP, and the Stanford Linear Collider, SLC, the first e^+e^- colliders reaching centre-of-mass energies of 91 GeV, the resonance production of Z bosons was explored. Analysing in total 16 million Z decays allowed to measure the properties of the Z boson with high precision. In consequence the neutral weak current of electroweak interactions is now tested at the quantum-loop level. In the year 1996 the centre-of-mass energy of LEP was increased above the threshold for the production of W pairs. More than 40,000 W-pair events in all W decay modes have been recorded by the LEP experiments allowing the determination of the gauge couplings of the W boson and a precision measurement of the W mass.

In recent years, the masses of elementary particles have attracted more and more attention in particle physics. Especially the discovery of non-vanishing neutrino masses recalls the open question of mass generation. Understanding

the origin of mass could also shed light on the question why there are three fermion families and on the nature of dark matter and dark energy in the universe.

Within the Standard Model the masses of the particles are generated via the Higgs mechanism. The heaviest elementary particles known to date, the electroweak gauge bosons W and Z and the top quark, play an exceptional role in this context. The top quark exhibits a huge mass nearly as large as the gold atom. In the Standard Model it couples to the mass-generating Higgs field with a strength proportional to its mass via the Yukawa interaction. Therefore, studying the properties of the top quark with high precision should reveal a deeper insight into the process of mass generation. In the Standard Model the ratio of the gauge bosons masses is related to the ratio of the electroweak couplings and can therefore be predicted by the measurement of the electroweak mixing angle. Precision measurements of the Z and the W mass together with an accurate determination of the electroweak mixing angle are testing this relation at the level of quantum corrections. Assuming the validity of the Higgs mechanism as the mass-generating process, allows an estimation of the mass of the Higgs boson from the measurement of these quantum corrections.

The Higgs boson, the key to the generation of particle masses, still awaits discovery. If it exists it will be detected at the Large Hadron Collider (LHC) going into operation in 2007. Once discovered at the LHC, the mass and decay properties of the Higgs boson have to be studied with the best possible accuracy to pin down the Standard-Model parameter set or to find hints for physics beyond the Standard Model. An ideal place to perform these studies would be an e^+e^- linear collider, a Higgs factory per se.

This review is organised as follows: In Chap. 1 it starts with a short introduction to the theory of electroweak interactions. After giving an overview of accelerators and detectors used for e^+e^- physics in Chap. 2 the electroweak measurements at the Z resonance are shortly summarised in Chap. 3. The electroweak processes observed at centre-of-mass energies well above the Z resonance are presented in Chap. 4. Chapter 5 is dedicated to the production of W-boson pairs, whereas in Chap. 6 the measurement of the W mass is discussed in detail. In Chap. 7 the electroweak data are then used to test the electroweak theory in a global Standard Model fit . In Chap. 8 the contributions to the electroweak physics, which could be made by a future e^+e^- Linear Collider, are reviewed.

The results in this review represent the status at the time of the summer conferences 2006.

Aachen *Stefan Roth*
July 2006

Contents

1

Electroweak Interactions

All elementary particles, known at present, and their interactions are successfully described by the Standard Model of particle physics. The fundamental constituents of matter, point-like fermions with spin 1/2, interact by the exchange of the force carriers, bosons with spin 1. The fermions are classified in two types of quarks and two types of leptons, which themselves are grouped into one of three particle families. Fermions of the same type but from different families are completely identical, except of their mass and consequently their lifetime. It is a complete mystery of nature why there are three copies of identical particles, but it is assumed to be closely related to the question of mass generation.

The interactions between the fundamental fermions are mediated by different types of gauge bosons: Eight gluons for the strong interaction, which binds the quarks inside proton and neutron, the photon, responsible for all electromagnetic interactions and the weak bosons Z and $\mathrm{W}^{\pm}$, where the latter allows transformations between the two types of quarks or leptons, respectively. Gravity is not included in the Standard Model.

The Standard Model is a quantum field theory, where interactions are explained by demanding invariance of the theory with respect to local gauge group transformations. The part of the Standard Model describing electroweak interactions [1] is formulated as a non-Abelian gauge theory governed by the symmetry groups $SU(2) \times U(1)$, where the ideas of a Yang-Mills theory [2] based on isospin invariance and of the Higgs mechanism [3] explaining spontaneous symmetry breaking are merged. After symmetry breaking it decomposes into the pure QED part, $U(1)_{\mathrm{em}}$, staying unbroken and mediated by the massless photon, and the interactions of the heavy gauge bosons, W and Z, which are governed by the $SU(2)_{\mathrm{L}}$ group. One distinguishes the charged-current (CC) interactions, mediated by the electrically charged W^{+} or W^{-} boson, and the neutral-current (NC) interactions, which are mediated by the Z boson.

Stefan Roth: *Precision Electroweak Physics at Electron-Positron Colliders*
STMP **220**, 1–11 (2006)
DOI 10.1007/3-540-35165-5_1

1.1 Gauge Invariance and Formulation of the Theory

The experimental investigation of the nuclear β decay lead to the conclusion that the charged-current interactions are only active between the left-handed fermions. Because of the electrical charge of the W bosons, the charged current is causing particle transformations, for example within the electron-neutrino doublet. Accordingly, the left-handed fermions are arranged into doublets of the weak isospin with values of $\pm 1/2$ for its third component, I_3, whereas the right-handed fermions form isospin singlets. To further characterise the isospin singlets, the weak hypercharge, Y, is introduced such that the Gell-Mann-Nishijima relation for the electric charge, Q, is valid:

$$Q = I_3 + \frac{Y}{2} \ . \tag{1.1}$$

To assure local gauge invariance for the $SU(2)$ group a triplet of gauge fields, W_1^μ, W_2^μ, W_3^μ, is introduced. Similarly, a gauge field, B^μ, is necessary for the $U(1)$ part of the theory. Invariance of the Dirac equation with respect to $SU(2)$ and $U(1)$ transformations is accomplished by replacing the gradient ∂^μ by the covariant derivative:

$$\partial^\mu \rightarrow D^\mu = \partial^\mu + ig \sum_{k=1}^{3} \frac{\tau_k}{2} W_k^\mu + ig' \frac{Y}{2} B^\mu \ , \tag{1.2}$$

where g and g' denote the coupling strengths of the $SU(2)$ and $U(1)$ gauge bosons, respectively. These two coupling strengths are free parameters of the theory and have to be determined by experiments.

Hence, the carrier of the charged-current interaction, the charged W^+ and W^- boson, are described by the following fields:

$$W^{\pm\mu} = \frac{1}{\sqrt{2}} (W_1^\mu \mp i W_2^\mu) \tag{1.3}$$

The electromagnetic field A^μ is identified as a linear combination of W_3^μ and B^μ in such a way that the coupling to the electrically neutral neutrinos vanishes while the coupling to the charged leptons is $-e$:

$$A^\mu = B^\mu \cos\theta_\mathrm{w} + W_3^\mu \sin\theta_\mathrm{w} \ , \tag{1.4}$$

with

$$e = g' \cos\theta_\mathrm{w} = g \sin\theta_\mathrm{w} \ , \tag{1.5}$$

where θ_w is the weak mixing angle. The field describing the neutral current interactions is chosen orthogonal to A^μ:

$$Z^\mu = -B^\mu \sin\theta_\mathrm{w} + W_3^\mu \cos\theta_\mathrm{w}, \tag{1.6}$$

These four gauge fields give rise to four different electroweak gauge bosons, which are the massless photon mediating electromagnetic interactions, the W

boson responsible for the weak charged current interactions and the Z boson which leads to weak neutral current processes. The Z and W bosons carry weak isospin, in addition the W bosons are electrically charged. This leads to self interactions between the electroweak gauge bosons caused by the underlying non-Abelian $SU(2)$ symmetry of the weak gauge transformations.

Evidence for the existence of weak neutral currents was first found in experiments analysing neutrino-electron scattering [4]. Neutrino-scattering experiments also obtained the first precise measurements of the weak mixing angle. This measurement together with the muon lifetime provided a first estimation of the masses of the heavy gauge bosons. The W and Z bosons were first produced in proton anti-proton collisions [5] and found to be rather massive, with masses of about 80 GeV and 91 GeV, respectively. This fact also explains the weakness of the weak interactions, because interactions mediated by massive bosons are restricted to short ranges and the corresponding cross sections and decay rates are suppressed accordingly.

The concept of gauge invariance requires long-range gauge fields, corresponding to massless gauge bosons, which assure the freedom of local gauge transformations. Gauge invariance would be destroyed, if explicit mass terms for the gauge bosons were introduced into the theory. On the other hand it is an experimental fact that three of the four electroweak gauge bosons are massive. In the Standard Model this is explained by the Higgs mechanism, where the gauge bosons stay massless in the formulation of the theory, but receive effective masses dynamically via interaction with a spin-zero Higgs field. The Higgs field consists of two complex components, which form a doublet of the weak isospin:

$$\Phi = (\phi^+, \phi^0) \tag{1.7}$$

The introduction of the scalar potential

$$V(\Phi) = \mu^2|\Phi|^2 + \lambda^2|\Phi|^4 \tag{1.8}$$

with $\mu^2 < 0$ yields an energy minimum at $\Phi \neq 0$. In the ground state, which is our vacuum, the neutral component, ϕ^0, therefore acquires a non-vanishing expectation value, $v/\sqrt{2} = \sqrt{-\mu^2/\lambda}$. This breaks the $SU(2) \times U(1)$ gauge symmetry spontaneously and leaves only the electromagnetic gauge group $U(1)_{\mathrm{em}}$ intact. The dynamical origin of this effect is still unclear. The non-vanishing ground state of the Higgs field should also experience quantum excitations around the potential minimum, which would materialise as the yet undiscovered Higgs boson.

The weak gauge bosons obtain masses via their gauge couplings to the Higgs field. The different couplings g and $\sqrt{g^2 + g'^2}$ of the W and the Z bosons result in the following relation between the masses of the two massive gauge bosons:

$$\cos\theta_{\mathrm{w}} = \frac{m_{\mathrm{W}}}{m_{\mathrm{Z}}} \tag{1.9}$$

This is a remarkable result, because it links the gauge sector of the theory describing the electroweak couplings with the Higgs sector responsible for the

mass generation. Because the photon does not couple to the neutral component of the Higgs field, ϕ^0, it stays massless.

To this point the theory is based on massless fermions. A massless fermion can be decomposed into the left- and the right-handed state, which are invariant under Lorentz transformations. On the contrary, for massive fermions one can go into their rest frame and by means of a rotation change the direction of polarisation. Introducing an explicit mass term for each fermion into the theory would therefore add two identical terms of opposite parity. As the $SU(2)_{\mathrm{L}}$ group of the electroweak theory acts only on the left-handed component of the fermion wavefunctions the gauge transformations of the right-handed and the left-handed components would be different, spoiling local gauge invariance.

Thus local gauge invariance under $SU(2)_{\mathrm{L}}$ can only be accomplished by the dynamical generation of the fermion masses, for example via their coupling to the Higgs field. In this way a new type of interaction is introduced, the Yukawa coupling between the fermions and the Higgs field. The coupling strength for each fermion to the Higgs field is a free parameter of the theory and determined by the measured fermion mass. One prediction of the Yukawa sector is that the decay rates of the Higgs boson into a fermion-antifermion pair is proportional to the mass of the given fermion species. This can be tested experimentally once the Higgs boson has been discovered and is produced in sufficient quantity.

The mass of the Higgs boson, m_{H}, is not predicted by the theory. It enters the electroweak processes measured so far only via radiative corrections. A precise determination of the electroweak parameters aims to test the internal consistency of the theory. If the precision is sufficiently high to be sensitive to the radiative corrections involving the Higgs boson it offers in addition the chance to reveal information about the Higgs-boson mass.

1.2 Parameters of the Theory

The electroweak gauge interactions of the Standard Model are determined completely by three parameters: the gauge coupling constants g and g' of the $SU(2)$ and $U(1)$ gauge fields and the vacuum expectation value of the Higgs field v. Therefore, at tree level, only three measurements are required to define the gauge couplings and to calculate the other observables. Independent measurements of these observables then constitute a test of the internal consistency of the theory. One obvious set of physical parameters which are experimentally accessible and can be measured with high precision would be the fine-structure constant α and the masses of the heavy gauge bosons, m_{Z} and m_{W}. After measuring these parameters the gauge coupling in the electroweak sector are fixed and the cross sections of electroweak processes can be calculated.

Many of the experimental results can be expressed in terms of the weak mixing angle, θ_{w}, which enters in three different ways into the electroweak theory:

1. The ratio between the electromagnetic and the weak coupling constant: $\sin\theta_{\mathrm{w}} = e/g$

2. The ratio between the $SU(2)$ and the $U(1)$ components of the weak neutral current which determines the vector coupling constant to the fermions: $g_{\mathrm{V}} = I_3^f - 2Q^f \sin^2\theta_{\mathrm{w}}$

3. The ratio of the masses of the electroweak gauge bosons W and Z: $\cos\theta_{\mathrm{w}} = m_{\mathrm{W}}/m_{\mathrm{Z}}$

Therefore, comparing the weak mixing angle determined in different measurements constitutes a consistency check of the theory.

Additional parameters of the Standard Model are the mass of the Higgs boson, m_{H}, generated by the Higgs self-coupling, and the strong coupling constant α_{s}. In the Yukawa sector the coupling of each fermion to the Higgs field generates a fermion mass, m_f, and the mixing between the mass eigenstates and the weak eigenstates of the fermions are described by mixing angles. These additional parameters modify the electroweak observables by second order effects, for example via radiative corrections (e.g. m_{t} and m_{H}), due to phase space corrections (e.g. m_{b}) or due to flavour oscillations in the final state (e.g. $\mathrm{b\bar{b}}$ mixing).

For precision tests of the theory the input parameters to the calculations should be known as accurately as possible. The parameters with the best experimental precision [6] are the fine-structure constant α, measured precisely in $g-2$ experiments or using the quantum Hall effect, the Fermi constant G_{F}, derived from the muon lifetime, and the Z-boson mass m_{Z}, determined with the Z resonance scan of LEP. They are listed in Table 1.1 together with their current experimental precision.

Table 1.1. Input parameters to the electroweak calculations; also given are the measured values and their relative accuracy

$\alpha = \dfrac{e^2}{4\pi}$	$1/137.03599911(46)$	$3.3 \cdot 10^{-9}$
$G_{\mathrm{F}} = \dfrac{1}{\sqrt{2}\,v^2}$	$1.16637(1) \cdot 10^{-5}$ GeV^{-2}	$1 \cdot 10^{-5}$
$m_{\mathrm{Z}} = \dfrac{ev}{2\sin\theta_{\mathrm{w}}\,\cos\theta_{\mathrm{w}}}$	91.1875(21) GeV	$2.3 \cdot 10^{-5}$

1.3 Radiative Corrections

An experimental precision test of the Standard Model needs theoretical calculations of adequate accuracy. This can only by achieved including higher order radiative corrections. The higher order terms show up as real corrections involving the radiation of photons and gluons and as virtual corrections which consist of Feynman diagrams with closed loops. Precision measurements sensitive to these radiative corrections can be considered as tests of the electroweak theory at the quantum-loop level.

Moreover, a meaningful quantum field theory must stay predictive when higher order corrections are included. That this is the case for the electroweak Standard Model was first shown by 't Hooft and Veltman [7]. They proved the renormalisability of the electroweak theory which provides the basis to perform perturbative calculations for observables in terms of a few input parameters order by order in perturbation theory. The input parameters themselves are not predicted by the theory but can be inferred from precision measurements of the electroweak observables.

One prominent example for the impressive success of quantum field theories is the quantum theory of the photon, Quantum Electrodynamics (QED). Originally developed by Stückelberg, Schwinger, Dyson and Feynman [8] it allows for example the prediction of the anomalous magnetic moment of the electron and the muon. The theoretical calculation matches the experimental precision which is of the order of $4 \cdot 10^{-12}$ for the electron case. The agreement between measurement and calculation at this level of precision is unique in the area of probing fundamental laws of physics.

Another example for quantum corrections is the running of the fine-structure constant α. The energy dependence of $\alpha(q^2)$ is caused by the effect of vacuum polarisation. This effect can be calculated by adding up the loop diagrams contributing to the photon self-energy as shown in Fig. 1.1. The precise determination of α has been performed at a very low energy scale. This value of α has to be transfered to the typical energy scale of the interactions at LEP:

$$\alpha(m_{\mathrm{Z}}) = \frac{\alpha}{1 - \Delta\alpha} \,. \tag{1.10}$$

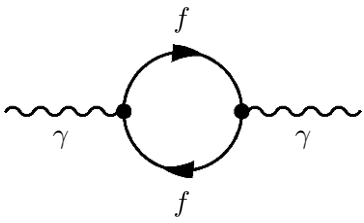

Fig. 1.1. Loop diagrams contributing to the vacuum polarisation which generate a running coupling constant $\alpha(q^2)$

The contributions of the charged leptons, $\Delta\alpha_{\mathrm{lept}}$, and of the top quark, $\Delta\alpha_{\mathrm{top}}$, can be calculated in perturbation theory. On the other hand the contribution of the lighter quarks, $\Delta\alpha^{(5)}_{\mathrm{had}}$, are difficult to calculate since their masses are not well defined and non-perturbative QCD effects dominate their contribution to the vacuum polarisation. Therefore the total contribution of the light quarks is evaluated through dispersion relations from the cross-section measurement of $\mathrm{e^+e^-} \to$ hadrons at low centre-of-mass energies [9]. The result for the QED coupling constant at the Z mass is

$$\alpha(m_{\mathrm{Z}})^{-1} = 127.918 \pm 0.018 \; . \tag{1.11}$$

The strength of the coupling of the charged weak current to the fermions is governed by the weak mixing angle and proportional to $\alpha/\sin^2\theta_{\mathrm{w}}$. At the beginning of the LEP program the weak mixing angle was not known with sufficient precision. Therefore one decided to use the Fermi constant, G_{F}, instead. It can be measured precisely in the muon decay [10]:

$$G_{\mathrm{F}} = 1.16637 \pm 0.00001 \cdot 10^{-5}\,\mathrm{GeV}^{-2} \; . \tag{1.12}$$

The Fermi constant combines the W-boson mass and the weak mixing angle into one variable

$$\frac{G_{\mathrm{F}}}{\sqrt{2}} = \frac{\pi\alpha}{2}\,\frac{1}{m_{\mathrm{W}}^2 \sin^2\theta_{\mathrm{w}}} \; . \tag{1.13}$$

Again this constant is determined at low momentum transfers and higher order corrections modify this relation. The calculation of radiative corrections to the masses of the weak vector bosons when derived from G_{F} and $\sin^2\theta_{\mathrm{w}}$ was first performed by Veltman, Marciano and Sirlin [11].

The relations between the input parameters and the observables vary with the renormalisation scheme used for these calculations. In the on-shell scheme [12] the relation $\sin^2\theta_{\mathrm{w}} = 1 - m_{\mathrm{W}}^2/m_{\mathrm{Z}}^2$ holds in all orders of perturbation theory. As a drawback the relation between G_{F} and the gauge boson masses gets large contributions from higher order corrections:

$$\frac{G_{\mathrm{F}}}{\sqrt{2}} = \frac{\pi\alpha}{2}\,\frac{1}{m_{\mathrm{W}}^2 \sin^2\theta_{\mathrm{w}}^2}\,\frac{1}{1-\Delta r} \; . \tag{1.14}$$

The correction term Δr combines the effect of the running of the fine-structure constant, $\Delta\alpha$, corrections to the ρ parameter, $\Delta\rho$, plus remainder terms:

$$\Delta r = \Delta\alpha - \cot^2\theta_{\mathrm{w}}\Delta\rho + \ldots \tag{1.15}$$

In analogy to the corrections of G_{F} a similar relation exists between $\sin^2\theta_{\mathrm{w}} = 1 - m_{\mathrm{W}}^2/m_{\mathrm{Z}}^2$, defined from the W and Z masses, and the effective mixing angle $\sin^2\theta_{\mathrm{eff}}$, measured in the $\mathrm{Z}f\bar{f}$ couplings of the Z boson to the fermions:

$$\sin^2\theta_{\mathrm{eff}} = \sin^2\theta_{\mathrm{w}} + \cos^2\theta_{\mathrm{w}}\Delta\rho + \ldots \tag{1.16}$$

The remainders consist of $\mathrm{Z}\gamma$ self-energy terms and vertex corrections specific to the given fermion species (see Sect. 3.1).

The leading contribution to $\Delta\rho$ comes from the top-bottom loop in the self-energy of the W propagator which is depicted in Fig. 1.2. The correction is quadratic in m_t, namely

$$\Delta\rho_\mathrm{t} = \frac{3G_\mathrm{F}}{8\pi^2\sqrt{2}} \left(m_\mathrm{t}^2 + m_\mathrm{b}^2 - 2\,\frac{m_\mathrm{t}^2 m_\mathrm{b}^2}{m_\mathrm{t}^2 - m_\mathrm{b}^2} \ln \frac{m_\mathrm{t}^2}{m_\mathrm{b}^2} \right) \tag{1.17}$$

$$\approx \frac{3G_\mathrm{F}}{8\pi^2\sqrt{2}}\, m_\mathrm{t}^2 \qquad \text{for} \quad m_\mathrm{b} \ll m_\mathrm{t}\ . \tag{1.18}$$

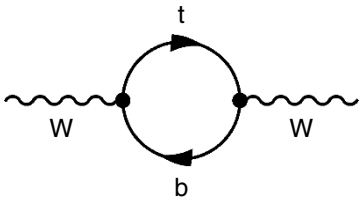

Fig. 1.2. Contribution of the top-bottom loop to the self-energy of the W boson

The weak isospin symmetry breaking due to the large mass splitting in the top-bottom quark doublet modifies the ρ parameter which is unity at lowest order. In spontaneously broken gauge theories loops involving heavy particles do not always decouple while in QED the running of α is not affected by heavy particles with mass $m \gg Q$ according to the decoupling theorem [13]. This theorem does not hold for the electroweak interactions, because a theory without the top quark is no more renormalisable and the gauge symmetry is broken if the b quark is left with no partner. Therefore electroweak precision measurements are sensitive to particles with masses higher than the centre-of-mass energy and hints for new physics could show up even if the new particles are too heavy for their direct production.

Additional electroweak radiative corrections to the self-energy of the W boson include the Higgs boson. The relevant Feynman diagram is shown in Fig. 1.3. The dependence of the radiative corrections on the mass of the Higgs boson is logarithmic:

$$\Delta\rho_\mathrm{H} = -\frac{3G_\mathrm{F}}{8\pi^2\sqrt{2}}\,(m_\mathrm{Z}^2 - m_\mathrm{W}^2) \left(\ln \frac{m_\mathrm{H}^2}{m_\mathrm{W}^2} - \frac{5}{6} \right)\ . \tag{1.19}$$

Quadratic terms proportional to $G_\mathrm{F}^2 m_\mathrm{H}^2$ only appear at the two loop level and are small. The difference to the corrections from the top quark is that $m_\mathrm{t}^2 - m_\mathrm{b}^2$ is a direct breaking of the gauge symmetry that already affects the one-loop diagrams, while the Higgs couplings to the gauge bosons are $SU(2)$ symmetric in first order.

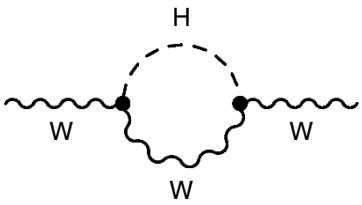

Fig. 1.3. Contribution of the Higgs boson to the self-energy of the W boson

While radiative corrections are quite sensitive to the top mass, they are much less dependent on the Higgs mass. If they were sufficiently sensitive to the mass of this last undiscovered particle of the Standard Model, we could precisely predict the Higgs mass assuming the validity of the Standard Model. On the other hand the test of the quantum structure of the theory would be much less stringent, because any deviation in the radiative corrections coming from new physics could eventually be re-absorbed by a shift of the Higgs mass.

1.4 Beyond the Standard Model

The Standard Model of particle physics describes all fundamental particles and their interactions. The electroweak sector of the Standard Model has been tested to very high precision, and no significant deviations of the experimental results have been observed up to now. The tests are performed at the level of quantum loop corrections as for many observables the tree level calculations are not sufficient to match the experimental accuracy.

In spite of this tremendous success the Standard Model is not believed to be the final theory of particle physics. First of all the Standard Model does not include gravitation, the longest known fundamental interaction in physics. Moreover, only two of the three fundamental interactions of the Standard Model are unified, the electromagnetic and the weak interactions.

Within a Grand Unified Theory (GUT) all three interactions of the Standard Model are unified and described by one symmetry. Two energy scales are present in a GUT: the energy of electroweak unification at about $M_{\mathrm{EW}} = 10^2$ GeV and an energy of $M_{\mathrm{GUT}} = 10^{16}$ GeV where the strong interaction is incorporated as well. The mass of the Higgs boson is expected to lie in the range of the electroweak energy scale. On the other hand, radiative corrections to the Higgs mass are found to be of the order of $M_{\mathrm{EW}} \cdot \mathcal{O}(M^2_{\mathrm{GUT}}/M^2_{\mathrm{EW}})$. To keep the Higgs mass at the energy scale of electroweak unification a fine-tuning of the parameters of the overlying GUT with a precision at the level of 10^{26} would be necessary. This sounds unphysical and is known as the hierarchy problem.

The hierarchy problem is naturally solved within supersymmetric models which accompany each Standard Model particle with a supersymmetric

partner carrying the same quantum numbers but different spin. In unbroken supersymmetry each quantum loop in the Higgs propagator with a Standard Model particle is exactly compensated by a quantum loop with its supersymmetric partner. Obviously exact supersymmetry is not realized in nature, because supersymmetric partners of the Standard Model particles are not observed. If supersymmetry is existing, but broken at an energy scale of $\mathcal{O}(10^3$ GeV), most of the loop cancellations in the Higgs propagator are still present and at the same time the supersymmetric particles receive masses larger than the Standard Model particles. The minimal supersymmetric extension of the Standard Model, the MSSM, predicts a spectrum of supersymmetric particles with masses in the range between 10^2 GeV and 10^3 GeV.

If the effective coupling constants of the weak, the electromagnetic and the strong interaction are scaled via the renormalisation group equation to higher energies, they do not merge at one energy scale as expected for a GUT. The new particle spectrum, predicted by the MSSM, modifies the running of the three couplings in such way that they merge at the GUT unification scale of 10^{16} GeV. At this energy scale, where all three interactions are unified, the weak mixing angle can be predicted in GUT theories to be $\sin^2\theta_\mathrm{w} = 3/8$. This value is modified by radiative corrections when going back to the electroweak energy scale and especially in the MSSM the theory prediction of $\sin^2\theta_\mathrm{w}$ is found to be in agreement with the measurement.

The spontaneous breaking of the $SU(2) \times U(1)$ gauge symmetry using the Higgs mechanism requires a Higgs potential with the parameter μ^2 being negative. While in the Standard Model μ^2 is postulated to be negative, in the MSSM the negative sign of μ^2 is dynamically generated. Here, the parameter μ^2 becomes negative when transferring the model from the GUT energy scale to the electroweak scale. This is caused by the strong coupling of the parameter μ^2 to the heavy top quark [14].

In contrary to the Standard Model, where the mass of the Higgs boson is a free parameter, the Higgs self-interaction in the MSSM is determined by its gauge structure. On tree level this leads to a strong bound on the mass of the lightest Higgs boson, $m_\mathrm{h} < m_\mathrm{Z}$, which is already ruled out experimentally. Radiative corrections shift the upper bound of the Higgs mass to about 150 GeV [15]. Hence a light Higgs mass is preferred by the MSSM.

In the MSSM additional radiative corrections to the electroweak precision observables are present. Due to the high masses of the supersymmetric particles their influence on $\Delta\alpha$ is negligible. The largest corrections to $\Delta\rho$ are caused by the stop-sbottom dublett. This additional contribution to Δr [16] changes the prediction of the W mass when derived from the value of the Fermi constant, G_F. A very precise determination of the W mass could therefore help to decide between the Standard Model and the MSSM.

References

1. S.L. Glashow, Nucl. Phys. **22**, 579 (1961);
   A. Salam, J.C. Ward, Phys. Lett. **13**, 168 (1964);
   S. Weinberg, Phys. Rev. Lett. **19**, 1264 (1967)
2. C.N. Yang and R. Mills, Phys. Rev. **96**, 191 (1954)
3. P.W. Higgs, Phys. Lett. **12**, 132 (1964);
   P.W. Higgs, Phys. Rev. Lett. **13**, 508 (1964);
   P.W. Higgs, Phys. Rev. **145**, 1156 (1966);
   T.W.B. Kibble, Phys. Rev. **155**, 1554 (1967)
4. F.J. Hasert et al, Phys. Lett. **B 46**, 121 (1973);
   J. Blietschau et al, Nucl. Phys. **B 114**, 189 (1976);
   H. Faissner et al, Phys. Rev. Lett. **41**, 213 (1978)
5. UA1 Collaboration, G. Arnison et al, Phys. Lett. **B 122**, 103 (1983);
   UA2 Collaboration, M. Banner et al, Phys. Lett. **B 122**, 476 (1983);
   UA1 Collaboration, G. Arnison et al, Phys. Lett. **B 126**, 398 (1983);
   UA2 Collaboration, P. Bagnaia et al, Phys. Lett. **B 129**, 130 (1983);
   UA1 Collaboration, G. Arnison et al, Phys. Lett. **B 129**, 273 (1983)
6. P.J. Mohr and B.N. Taylor, Rev. Mod. Phys. **72**, 351 (2000)
7. M. Veltman, Nucl. Phys. **B 7**, 637 (1968);
   G. 't Hooft, Nucl. Phys. **B 35**, 167 (1971);
   G. 't Hooft and M. Veltman, Nucl. Phys. **B 44**, 189 (1972);
   G. 't Hooft and M. Veltman, Nucl. Phys. **B 50**, 318 (1972)
8. E.C.G. Stückelberg, Helv. Phys. Acta **14.32L**, 588 (1941);
   J. Schwinger, Phys. Rev. **74**, 1439 (1948);
   F.J. Dyson, Phys. Rev. **75**, 486 (1949);
   R.P. Feynman, Phys. Rev. **76**, 749 (1949)
9. H. Burkhardt and B. Pietrzyk, Phys. Rev. **D 72**, 057501 (2005);
   H. Burkhardt and B. Pietrzyk, Phys. Lett. **B 513**, 46 (2001)
10. S. Eidelman et al, Phys. Lett. **B 592**, 1 (2004)
11. M. Veltman, Nucl. Phys. **B 123**, 89 (1977);
    W.J. Marciano, Phys. Rev. **D 20**, 274 (1979);
    M. Veltman, Phys. Lett. **B 91**, 95 (1980);
    A. Sirlin, Phys. Rev. **D 22**, 971 (1980);
    W.J. Marciano and A. Sirlin, Phys. Rev. **D 22**, 2695 (1980)
12. A. Sirlin, Phys. Rev. **D 29**, 89 (1984);
    D.C. Kennedy and B.W Lynn, Nucl. Phys. **B 322**, 1 (1989);
    D.Y. Bardin, Z. Phys. **C 44**, 493 (1989);
    W. Hollik, Fortsch. Phys. **38**, 165 (1990)
13. Th. Appelquist and J. Carazzone, Phys. Rev. **D 11**, 2856 (1975)
14. G.G. Ross and R.G. Roberts, Nucl. Phys. **B 377**, 571 (1992)
15. H.R. Haber and R. Hempfling, Phys. Rev. Lett. **66**, 1815 (1991);
    Y. Okada, M. Yamaguchi and T. Yanagida, Prog. Theor. Phys. **85**, 1 (1991);
    J. Ellis, G. Ridolfi and F. Zwirner, Phys. Lett. **B 257**, 83 (1991)
16. S. Heinemeyer et al., Eprint hep-ph/0604147;
    S. Heinemeyer, W. Hollik and G. Weiglein, Phys. Rept. **425**, 265 (2006);
    A. Djouadi et al., Phys. Rev. Lett. **78**, 3626 (1997)

2

The Accelerators SLC and LEP

A great success of the e^+e^- colliders PETRA and TRISTAN were the precision measurements at centre-of-mass energies where the observed processes are no longer exclusively described by QED, but interference effects with the weak interaction have to be considered in addition. Using these measurements allowed to predict the mass of the Z boson and to constrain the values of the coupling constants, g_{V}^f and g_{A}^f, of the neutral current to the fermions. After the discovery of the W and Z bosons at the SPS collider at CERN it became desirable to record e^+e^- collisions also on the Z resonance leading to the projects SLC and LEP. Whereas the SLC was the first e^+e^- linear collider and reached centre-of-mass energies around the Z resonance, the LEP e^+e^- collider was constructed according to the traditional storage-ring concept. In contrary to the SLC, the LEP collider additionally aimed at sufficiently high centre-of-mass energies to allow the pair-production of W bosons.

2.1 The Stanford Linear Collider SLC

The Stanford Linear Collider SLC at SLAC was constructed by modifying the famous Stanford Linear Accelerator. This machine had been originally used for fixed target experiments studying electron-nucleon scattering revealing the quarks as the point-like constituents of the proton. In the 1980's is was modified to allow the acceleration of both electrons and positrons. An overview of the SLC accelerator complex is shown in Fig. 2.1.

A new type of electron source was installed, which provided polarised electrons produced by shining circularly polarised laser light on to a cathode consisting of a 0.1 μm thick layer of strained Gallium-Arsenide on basis of GaAsP. The strain in the GaAs lattice breaks the degeneracy of the energy levels in the valence band. Therefore, using photons with an energy exactly in between 1.43 eV and 1.48 eV selects one specific spin transformation. In that way photons with given helicity produce electrons with the same helicity.

Stefan Roth: *Precision Electroweak Physics at Electron-Positron Colliders*
STMP **220**, 13–26 (2006)
DOI 10.1007/3-540-35165-5_2

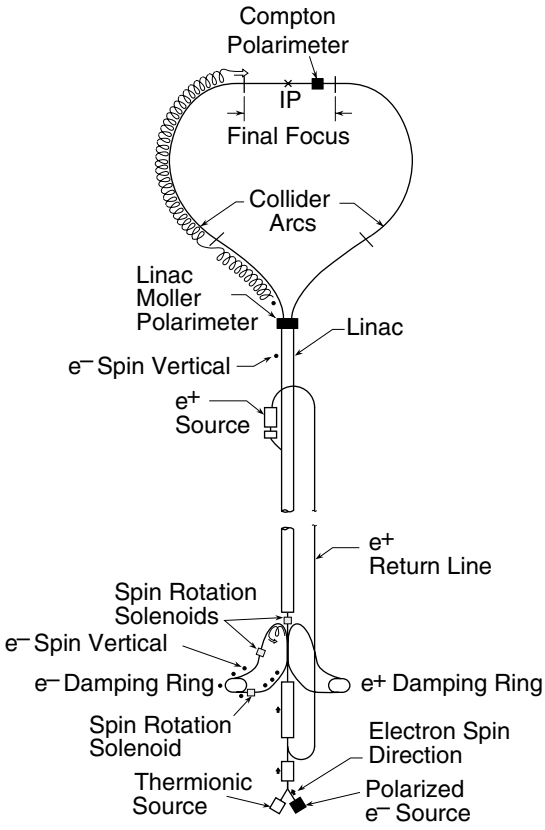

Fig. 2.1. Acceleration scheme of the SLC with electron and positron sources, damping rings, main linac and the two arcs bringing both beams into collision

Using spin rotating solenoid magnets the longitudinal polarisation of the electrons was converted into transverse polarisation before injection into the damping rings. Here the transverse emittance of the beam was reduced to the intended value before the electrons were accelerated in the main linac to the nominal energy of the colliding beams. Some of the accelerated electron bunches were steered onto a target in order to produce positrons. The positrons were collected, transfered into a damping ring and then accelerated by passing the main linac. No polarisation of the positron beam was intended in the SLC design.

The 3 km long linear accelerator was equipped with copper cavities which accelerated alternately electron and positron bunches to an energy of 50 GeV. At the end of the linac the electrons and positrons were separated and brought into collision using two arcs of bending magnets. Passing the arcs the spin orientation of the particles was manipulated by suitably chosen betatron oscillations to obtain longitudinal polarisation at the interaction point. With a beam current of 0.8 μA a specific luminosity of $2.5 \cdot 10^{30}$ $\mathrm{cm}^{-2}\mathrm{s}^{-1}$ was achieved.

The degree of polarisation of the electron beam was measured by a Compton polarimeter installed after the interaction region. Here, circularly polarised laser photons were scattered from the electron beam leaving the interaction point. The Compton-scattering cross section was measured for parallel and anti-parallel orientation of photon and electron helicities. The asymmetry between both cross sections measures the product of laser light and electron beam polarisations. With this method the polarisation of the electron beam was continuously monitored. Polarisations of the electron beam of up to 80% were obtained (see Fig. 2.2). The measurement of the average polarisation has a precision of 0.7% and is limited by systematic uncertainties.

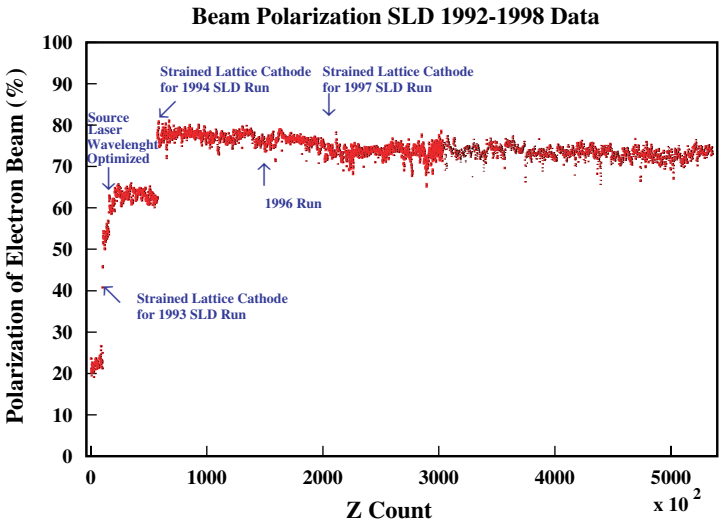

Fig. 2.2. Evolution of the polarisation at SLC with the time of operation in terms of the number of Z bosons registered

The energy calibration of the beams at the SLC was accomplished using a precision spectrometer directly after the interaction point [1], where the angular deflection of the beams was determined measuring the direction of synchrotron radiation emitted before and after the bending magnet of the spectrometer. This allowed to detemine the beam with a precision of $5 \cdot 10^{-4}$.

2.2 The Large Electron Positron Collider LEP

The Large Electron Positron Collider LEP was situated in a ring tunnel of 27 km circumference at CERN near Geneva. It was operated from the year 1989 until 2000, when it made way for the installation of the Large Hadron Collider LHC. The electrons were delivered by the linear accelerator LIL. Here,

also positrons were produced and collected using an accumulation ring. Using the older accelerators PS and SPS the electrons and positrons were accelerated to an energy of 20 GeV and then injected into the LEP storage ring. This storage ring consisted of eight bending sections with an effective radius of 3.0 km, where dipole magnets with a maximum field strength of up to 0.1 T kept the particles on their path. Two of the eight straight sections housed the acceleration system. Normal conducting copper cavities and superconducting cavities made from niobium-sputtered copper were operated, yielding a total accelerating gradient of 3.6 GV per turn. Such a high gradient was necessary to replace the energy loss of the beams due to synchrotron radiation, limiting the maximum achievable centre-of-mass energy to 208 GeV. An overview of the LEP accelerator complex is given in Fig. 2.3.

2.3 Calibration of the LEP Beam Energy

At beam energies of 41 GeV $< E_{\mathrm{beam}} <$ 61 GeV the calibration of the LEP beam energy is based on the resonant spin depolarisation technique. It uses the characteristic feature of electron storage rings that transverse polarisation of the circulating particles builds up during their passage through the magnetic field of bending dipoles. This is called the Sokolov-Ternov effect [2].

Once polarised, the electron spin precesses around the B-field direction. A relation between the particle energy and the number of spin precessions per revolution around the storage ring, the spin tune ν_s, can be derived:

$$\nu_s = \frac{g-2}{2\,m_{\mathrm{e}}}\,E_{\mathrm{beam}} = \frac{E_{\mathrm{beam}}}{440.6486\ \mathrm{MeV}}\ . \tag{2.1}$$

An external high frequency magnetic field is used to destroy the beam polarisation. The frequency where depolarisation occurs is identical to the non-integer part of the spin tune and hence the beam energy can be determined. The degree of polarisation of the electron beam is measured using a Compton polarimeter. The method of resonant spin depolarisation has an intrinsic precision of 0.2 MeV [3].

However, effects such as small imperfections of the magnetic field disturb the spin direction and lead to depolarisation of the beam. These depolarising effects can act on the beam effectively, if the trajectory of the particle is a multiple of the ring circumference. As a consequence the spin tune ν_s must not be close to an integer value. Suitable points for energy calibration are separated by $\Delta\nu_s = \pm 1$, i.e. by ± 0.88 GeV in centre-of-mass energy and special beam energy values in between have to be avoided to prevent accidental depolarisation of the beam. With increasing beam energy the synchrotron radiation grows proportional to E^4_{beam} leading to an increased amplitude of synchrotron oscillations. This also leads to a larger beam energy spread as the particles now see larger differences in the accelerating fields of the RF cavities. If this energy spread becomes too large some of the beam particles cross the

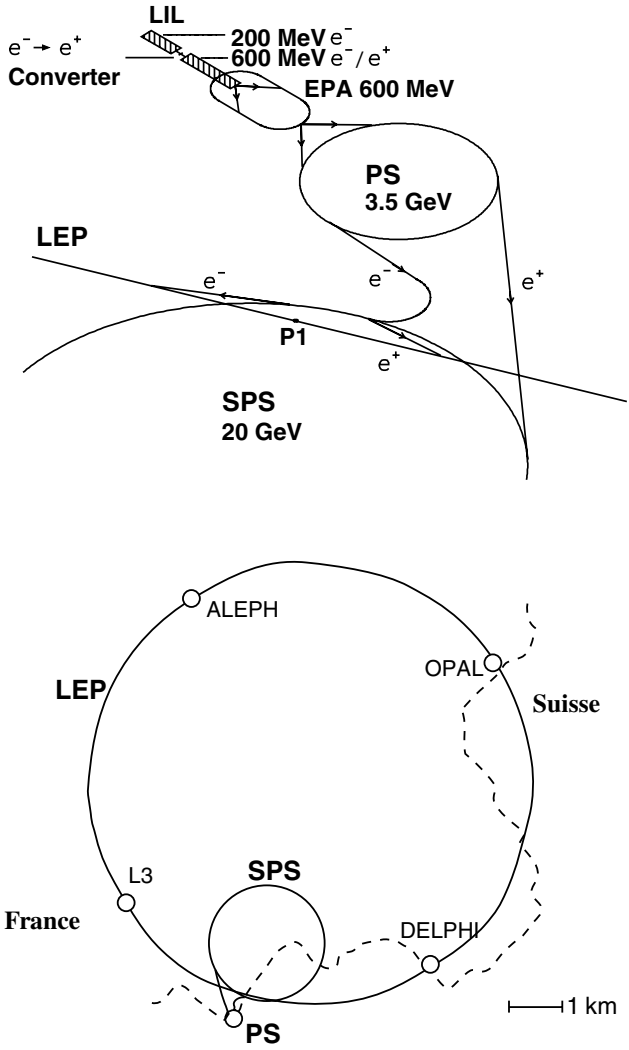

Fig. 2.3. Overview of the LEP accelerator complex. The upper sketch shows the layout of the pre-accelerator system with the linear accelerator LIL, the e^+e^- accumulator ring EPA, and the synchrotrons PS and SPS accelerating in several stages up to 20 GeV before injection into LEP. On the lower plot the location of LEP relative to the pre-accelerators and the positions of the four experiments are shown

depolarising energy points and the beam polarisation is destroyed. Therefore the method of resonant spin depolarisation (RDP) can not be used directly for the beam energies of the physics runs at LEP 2, well above 60 GeV.

To cope with this problem, B-field measurements were accomplished using 16 NMR probes situated in selected bending dipoles [4] which were read out during physics runs as well as during the procedure of resonant depolarisation. The beam energies for the physics running in the regime 80 GeV $< E_{\mathrm{beam}} <$ 104 GeV were derived from the NMR model extrapolating the results of the RDP technique to the higher energies. Corrections caused by the additional bending fields due to non-central orbits through the focusing quadrupoles had to be taken into account. Also the local beam energy present at the interaction points of each experiment had to be derived by correcting for the energy loss in the bending arcs and the energy gains in the accelerating sections.

The systematic uncertainty of the NMR model was derived by comparison with three independent measures of the LEP beam energy: The synchrotron tune, Q_s, of a storage ring depends on the beam energy and on the energy loss per turn, which is known from the total accelerating RF voltage, V_{RF}. The beam energy can be derived from the variation of Q_s with V_{RF}. The flux-loop was a sequence of cable loops installed into each of the bending magnets and sensing the change of the magnetic flux during the ramp of the B field. A beam-energy spectrometer was installed in 1999 and used during the run of the year 2000. This setup, shown in Fig. 2.4, allowed to measure the deflection angle of the electron beam caused by the magnetic field and hence the beam energy. It was composed of a steel dipole with an accurately surveyed field map and a triplet of beam-position monitors (BPM) on either side of the dipole.

The relative differences between the result obtained from the NMR model and the alternative measurements are shown in Fig. 2.5. The comparison of the alternative methods with the default NMR measurement allows to estimate the systematic uncertainty of the LEP beam energy. This uncertainty increases linearly with the distance in energy to the calibration points where the precise energy calibration using the depolarisation method is performed.

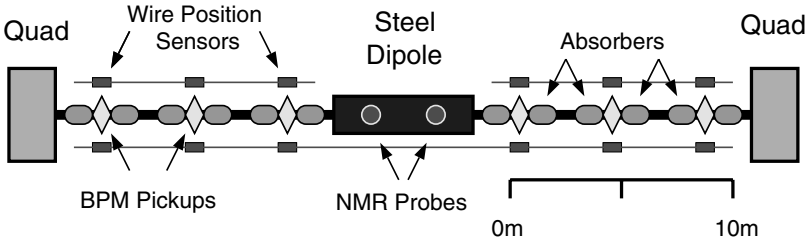

Fig. 2.4. Sketch of the beam-energy spectrometer including beam position monitors (BPM) and the magnetic dipole

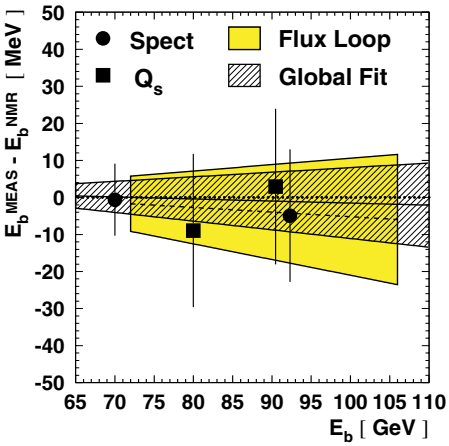

Fig. 2.5. Differences between the results from the NMR model and the alternative methods, using the magnetic spectrometer, the flux loop coils and the synchrotron tunes. The systematic uncertainty assigned to the LEP energy measurement due to this comparison is depicted as hatched area

The centre-of-mass energies at each interaction point and for each period of data taking are obtained by correcting for effects due to the RF system which depend on the location around the LEP ring, and by applying the LEP energy model which takes into account time-variable effects like, for example, ground motions caused by the tides of the moon. For the majority of LEP 2 running the calibration of the centre-of-mass energy was performed with an accuracy of $1.2 \cdot 10^{-4}$. This is sufficiently precise in order to do not dominate the experimental uncertainty of the W-mass measurement.

2.4 Detectors at Electron-Positron Colliders

The principle layout of the SLD detector [5] and of the four LEP detectors ALEPH [6], DELPHI [7], L3 [8] and OPAL [9] is similar. They are all-purpose detectors, which are designed to measure all possible final states of e^+e^- interactions. As examples the layout of the SLD and the OPAL detectors are shown in Fig. 2.6.

Starting from the interaction point the first sub-detectors are the vertex detectors which are constructed using silicon-strip sensors. They allow the reconstruction of the decay vertices of long lived particles like, for example, B mesons. Then tracks of charged particles are registered by various types of drift chambers. In addition the momentum of the particles is determined with high precision by measuring the curvature of the tracks in the magnetic field of the detectors. The energy of electrons and photons is measured in the electromagnetic calorimeters and the hadronic component of jets is reconstructed

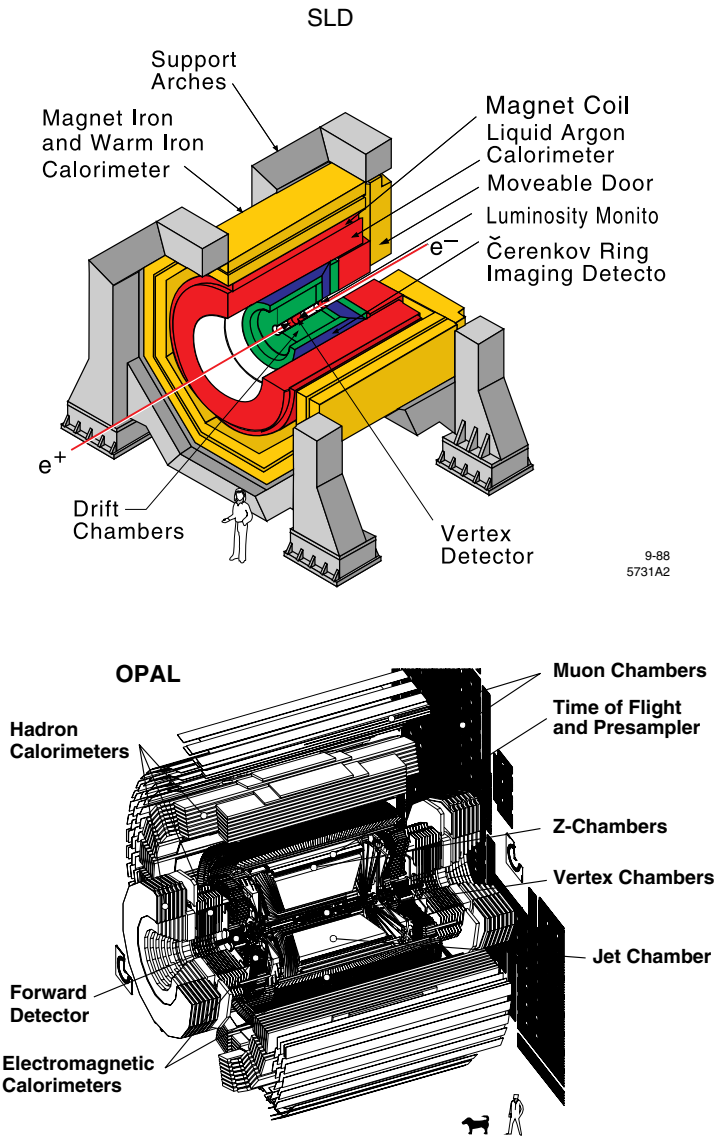

Fig. 2.6. The SLD detector at the SLC and the OPAL detector at LEP as examples for typical detectors at e^+e^- colliders

using the hadronic calorimeters. Muons penetrate the calorimeter system and are identified using drift chambers surrounding the detector. All five detectors are provided with a solenoidal magnetic field.

In all experiments a special sub-detector, the so-called luminosity monitor [10], registers the events of small-angle Bhabha scattering and allows to determine the luminosity of the colliding beams. It consists of an electromagnetic calorimeter which detects the scattered beam particles and a silicon-strip detector which measures the scattering angle of the particles with high precision. Because of the steep rise of the differential cross section of Bhabha scattering when going to small scattering angles the spatial accuracy of the monitors is of crucial importance. A detailed description of the luminosity measurement is found in Sect. 2.5.

In the following examples, the detection capabilities of the five experiments are presented. The SLD experiment exploited the special feature of a linear collider where beams with very tiny diameters are brought into collision. This allowed to place the first layer of the silicon vertex detector at a distance of only 2.8 cm from the beam line. The inner part of the SLD vertex detector was a pixel detector based on the CCD technology. More than 307 million pixels provided a very accurate spatial resolution allowing to identify secondary vertices with high efficiency. For the identification of b-quark final states, this vertex information is used together with other observables to construct a vertex mass for the given jet [11]. The resulting vertex mass distribution is shown in Fig. 2.7.

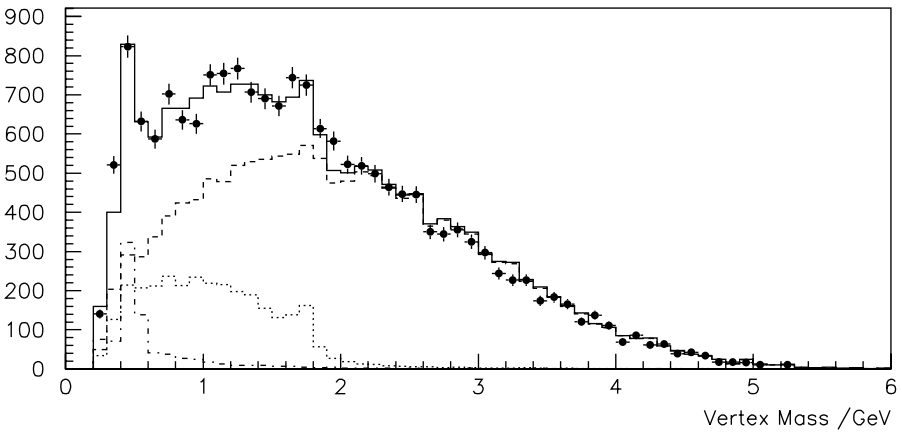

Fig. 2.7. Reconstructed secondary-vertex mass for SLD data (*points*) and Monte Carlo (*solid line*). The Monte Carlo simulation is composed of the $b\bar{b}$ final state (*dashed line*), the $c\bar{c}$ final state (*dotted line*) and the contribution from light quarks (*dashed-dotted line*)

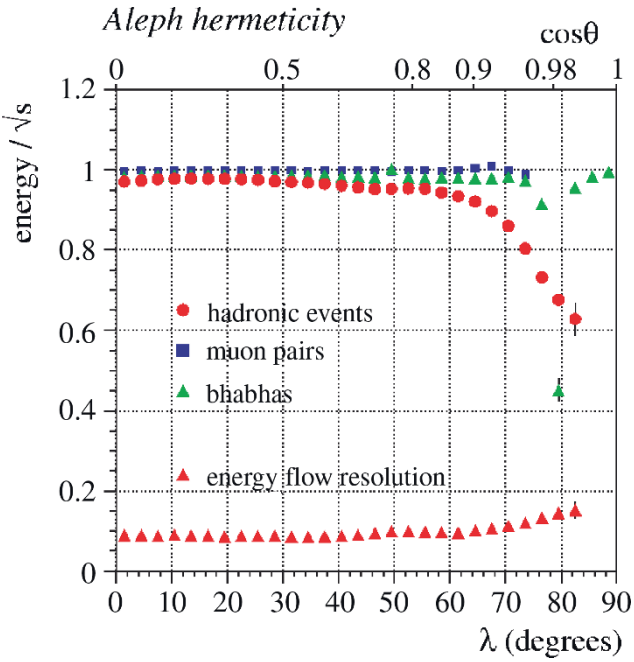

Fig. 2.8. Hermeticity of the ALEPH detector for hadronic final states, muon pairs and Bhabha event. Also shown is the energy resolution of hadronic jets using the energy-flow algorithm

The ALEPH collaboration built an all-purpose particle detector with special emphasis on homogeneity and hermeticity. In Fig. 2.8 the fraction of the centre-of-mass energy which was registered in the detector is shown for the hadronic final states, the muon-pair production and Bhabha scattering. For events comprised within the angular region of $|\cos\theta| < 0.9$ nearly the completely available event energy is measured. In the forward detector region more and more particles are lost in the inactive region around the beam line, leading to a total loss of the muon pairs and a degrading hermeticity for hadronic final states. ALEPH has developed the energy-flow algorithm [12] which tries to associate to each charged particle track the corresponding calorimetric cluster. This algorithm provides excellent energy resolution for the reconstructed jets over the full acceptance of the detector. The energy resolution obtained is also shown in Fig. 2.8 versus the angular region of the detector.

A speciality of the DELPHI detector was its capability of particle identification. The large volume Time Projection Chamber (TPC) of the DELPHI detector allowed a precise measurement of the specific ionisation, $\mathrm{d}E/\mathrm{d}x$, of the charged particles. An additional detector system, the Ring Imaging Cherenkov detector (RICH) [13], was introduced to further improve the particle identifi-

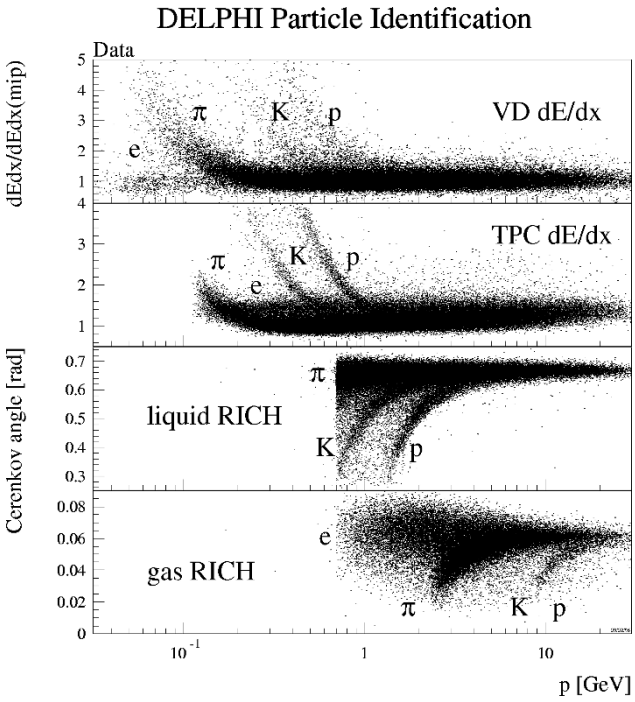

Fig. 2.9. Particle ID measurements using various sub-detectors of the DELPHI experiment

cation. Figure 2.9 shows the separation of the different particle species using the various sub-detectors of DELPHI.

The L3 detector was designed for optimal energy resolution for muons, electrons and photons. This goal was reached using a high resolution electromagnetic calorimeter made from BGO crystals. A large system of drift chambers outside the calorimetric system but still within the solenoid magnet, constituted a high precision muon spectrometer. A momentum resolution of 2.5% was obtained for muons from Z decays as it is shown in Fig. 2.10. Also shown is the measured mass distribution of π^0 mesons reconstructed from its decay into two photons. The achieved mass resolution of 7 MeV demonstrates the excellent resolution of the BGO calorimeter for electromagnetic energy.

The OPAL detector was designed to be a well balanced answer to accommodate all demands given by the various physics cases in e^+e^- interactions. Vertexing was performed using silicon detectors, a drift chamber was used for tracking and particle identification and the calorimetric system allowed the measurement of neutral particles. The very important measurement of the luminosity collected by the experiment was achieved using specialised detectors placed at the very forward region of each of the LEP detectors. In the exam-

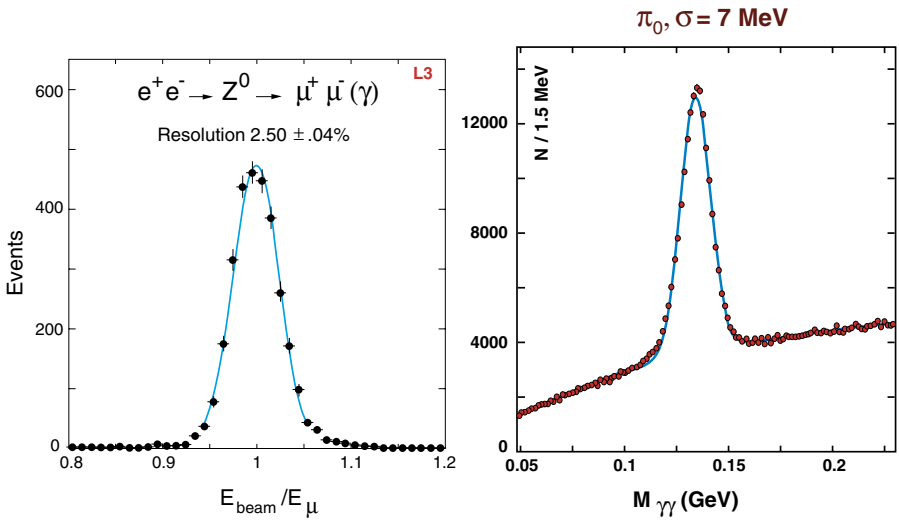

Fig. 2.10. Resolution of muon momentum using Z decays (*left*) and π^0 mass resolution from the electromagnetic calorimeter energy (*right*) in the L3 detector

ple of OPAL this so called luminometer [14] consisted of an electromagnetic calorimeter made from a silicon-tungsten sandwich structure.

2.5 Luminosity Measurement

In parallel to Z-decay events registered in the main part of the detector the data acquisition also records small-angle Bhabha events within the luminosity monitor. In this way the measured integrated luminosity represents exactly the data-taking period under study and readout dead times are automatically taken into account. The positions and energies of the scattered electrons and positrons are measured with a detector consisting of a calorimeter and a precision silicon tracker placed close to the beam line. It records a back-to-back electron-positron pair at small polar angles, typically between 25 mrad and 60 mrad. As the cross section depends strongly on the scattering angle ($\mathrm{d}\sigma/\mathrm{d}\theta \propto \theta^3$), the exact knowledge of the angular acceptance is very important for the accuracy of the luminosity measurement. Figure 2.11 shows the distribution of the impact position of the scattered electrons on the luminosity monitor, which has been determined with very high precision.

While the angular measurement of the silicon detector is crucial for the exact definition of the acceptance region, the calorimetric system discriminates against lower-energetic background events which are mainly beam induced. The amount of background events can be estimated by extrapolating the tails of the energy distributions into the signal region. The final experimental systematic uncertainty on the measured luminosity stays well below 1 permill.

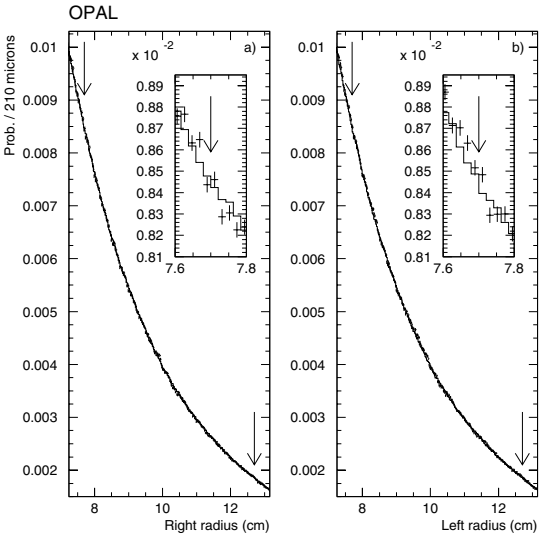

Fig. 2.11. Impact position of Bhabha events in the OPAL luminosity monitor

Even directly at the Z resonance the process of small angle Bhabha scattering within the acceptance of the luminosity monitors occurs more frequently than all Z-decay processes together. Therefore the statistical uncertainty of the measurement is small. The luminosity events are mainly caused by the t-channel photon exchange, a pure QED process. However, to match the experimental accuracies also weak diagrams and radiative corrections have to be added in the calculation of the accepted cross section. To perform this calculation and for the precise modelling of these events the Monte-Carlo program BHLUMI [15] has been developed. It has been estimated that these calculations contain a theoretical uncertainty of about 0.5 permill.

References

1. J. Kent et al., IEEE Part. Accel. 1989, 1550
2. A.A. Sokolov and I.M. Ternov, Sov. Phys. Dokl. **8**, 1203 (1964)
3. LEP Energy Working Group, L. Arnaudon et al., Z. Phys. **C 66**, 45 (1995);
   LEP Energy Working Group, R. Assmann et al., Eur. Phys. J. **C 6**, 187 (1999)
4. LEP Energy Working Group, R. Assmann et al., Eur. Phys. J. **C 39**, 253 (2005)
5. SLD Collaboration, SLD Design Report, Preprint SLAC-0273
6. ALEPH Collaboration, D. Decamp et al., Nucl. Inst. Meth. **A 294**, 121 (1990)
7. DELPHI Collaboration, P. Aarnio et al., Nucl. Inst. Meth. **A 303**, 233 (1991)
8. L3 Collaboration, B. Adeva et al., Nucl. Inst. Meth. **A 289**, 35 (1990)
9. OPAL Collaboration, K. Ahmet et al., Nucl. Inst. Meth. **A 305**, 275 (1991)
10. D. Bederede et al., Nucl. Inst. Meth. **A 365**, 117 (1995);
    I. C. Brock et al., Nucl. Inst. Meth. **A 381**, 236 (2000);
    G. Abbiendi et al., Eur. Phys. J. **C 14**, 373 (2000)

11. SLD Collaboration, K. Abe et al., Phys. Rev. Lett. **80**, 660 (1998); D. J. Jackson, Preprint SLAC-PUB-7215 (1996)
12. D. Buskulic et al., Nucl. Inst. Meth. **A 360**, 481 (1995)
13. E. Albrecht et al., Nucl. Inst. Meth. **A 433**, 47 (1999)
14. G. Abbiendi et al., Eprint hep-ex/0206074 (2002)
15. S. Jadach et al., Comp. Phys. Comm. **102**, 229 (1997)

3

Electroweak Measurements on the Z Resonance

The Standard Model is confirmed at the permill level using electroweak precision measurements gathered at the Large Electron Positron Collider LEP and at the Stanford Linear Collider SLC. The analysis of electron-positron collisions at centre-of-mass energies around the Z resonance has delivered a wealth of precisely measured electroweak observables. The measurement of the total cross sections of the processes $\mathrm{e^+e^-} \to f\bar{f}$ are used to determine the mass, m_Z, and the width, Γ_Z, of the Z boson. The forward-backward asymmetries of the lepton and heavy-quark production and the final-state polarisation of the τ leptons measure the couplings of the Z boson to the fermions. Additionally, at the SLC, where a polarised electron beam was available, the asymmetry between cross sections for left and right polarised electron beam is used for a precise determination of the weak mixing angle, $\sin^2\theta_\mathrm{w}$.

3.1 Fermion-Pair Production in $\mathrm{e^+e^-}$ Collisions

In $\mathrm{e^+e^-}$ collisions the production of a fermion-antifermion pair proceeds via the s-channel exchange of a neutral electroweak boson, the photon or the Z boson, as depicted in Fig. 3.1. Due to the Z-boson resonance the cross section shows a sharp enhancement at a centre-of-mass energy of $\sqrt{s} = m_\mathrm{Z}$. For example, the hadronic final state, obtained from the production of a quark-antiquark pair, reaches a cross section of more than 30 nb at the Z pole.

Near the Z resonance the reaction $\mathrm{e^+e^-} \to f\bar{f}$ is dominated by the Z exchange diagram. For non-electron final states ($f \neq \mathrm{e}$) the differential cross section on Born level is given by

$$\frac{\mathrm{d}\sigma}{\mathrm{d}\Omega} = \frac{9}{4}\,\frac{\Gamma_\mathrm{ee}\Gamma_{ff}}{m_\mathrm{Z}^2\Gamma_\mathrm{Z}^2}\,\frac{s\Gamma_\mathrm{Z}^2}{(s-m_\mathrm{Z}^2)^2+m_\mathrm{Z}^2\Gamma_\mathrm{Z}^2} \cdot \left[(1-P_\mathrm{e}A_\mathrm{e})(1+\cos^2\theta)+2(A_\mathrm{e}-P_\mathrm{e})A_f\cos\theta\right] , \tag{3.1}$$

where θ is the scattering angle of the outgoing fermion (f) with respect to the direction of the incoming electron beam ($\mathrm{e^-}$). P_e is the degree of polarisation

Stefan Roth: *Precision Electroweak Physics at Electron-Positron Colliders*
STMP **220**, 27–38 (2006)
DOI 10.1007/3-540-35165-5_3

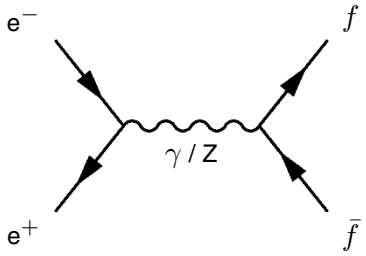

Fig. 3.1. The lowest order Feynman diagram of the process $e^+e^- \to f\bar{f}$ with $f \neq e$. Fermion pairs are produced via a γ or Z propagator in the s-channel

of the beam electrons, relevant at the SLC, and the parameter A_f is defined as

$$A_f = 2\,\frac{g_{\mathrm{V}}^f/g_{\mathrm{A}}^f}{1+(g_{\mathrm{V}}^f/g_{\mathrm{A}}^f)^2}\;, \tag{3.2}$$

where g_{V}^f and g_{A}^f are the vector and axial-vector coupling constants of the Z boson to the fermion f, respectively. The partial width, Γ_{ff}, of the Z decay channel $\mathrm{Z} \to f\bar{f}$ is given by

$$\Gamma_{ff} = \frac{\sqrt{2}G_{\mathrm{F}}m_{\mathrm{Z}}^3}{12\pi}N_{\mathrm{c}}^f\,\left((g_{\mathrm{V}}^f)^2+(g_{\mathrm{A}}^f)^2\right)\;, \tag{3.3}$$

with the colour factor N_{c}^f which is 3 for quarks and 1 for leptons.

Radiative corrections due to photon radiation in the initial state change the shape of the measured Z resonance, $\sigma(s)$. These photons lead to a reduced the effective centre-of-mass energy, s', of the hard scattering process. If one could determine the radiated photon energy for each individual event, the unfolded cross section $\sigma(s')$ would be accessible and thereby the pure line-shape. Instead, most of the initial-state photons escape along the beam-line and stay undetected. Therefore initial-state radiation (ISR) is considered by convoluting the Born cross section with a radiator function. Due to the high beam energies photon radiation appears frequently and consequently these corrections are large. They lower for example the maximum of the total cross section by 36% and shift its position by about +100 MeV.

Most of the electroweak virtual corrections are considered by the replacement $m_{\mathrm{Z}}^2\Gamma_{\mathrm{Z}}^2 \to s^2\Gamma_{\mathrm{Z}}^2/m_{\mathrm{Z}}^2$ in the denominator of the Breit-Wigner function, effectively introducing a s-dependent width of the Z boson, and by the introduction of effective coupling constants $\bar{g}_{\mathrm{V}}^f$ and $\bar{g}_{\mathrm{A}}^f$:

$$\bar{g}_{\mathrm{A}}^f = \sqrt{\rho_{\mathrm{eff}}^f}\;I_3^f \qquad \text{and} \qquad \bar{g}_{\mathrm{V}}^f = \sqrt{\rho_{\mathrm{eff}}^f}\;(I_3^f - 2Q_f\sin^2\theta_{\mathrm{eff}}^f)\;. \tag{3.4}$$

Here, an overall factor $\rho_{\mathrm{eff}} = (1+\Delta\rho)$ is coming from the renormalisation of the weak coupling and dominated by the top-bottom loop in the W boson propagator. Moreover the $\mathrm{Z}f\bar{f}$ vertex is modified for instance by the loop

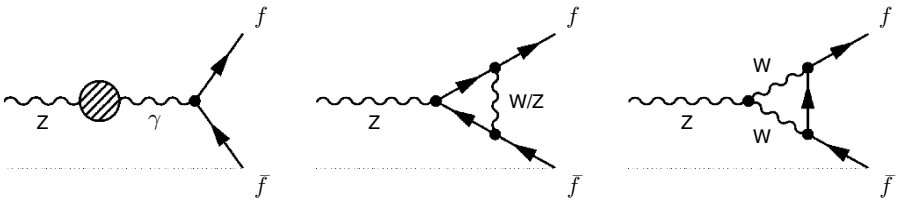

Fig. 3.2. Corrections to the coupling of the Z boson to a fermion-antifermion pair. The tree level diagram with a pure $Zf\bar{f}$ vertex is accompanied by loop diagrams (*left*) which contain a small contribution from the $\gamma f\bar{f}$ vertex. Additional vertex corrections (*middle* and *right*) depend on the fermion type in the final state

diagrams, shown in Fig. 3.2, which yield small contributions from the $\gamma f\bar{f}$ vertex. In principle, each of the effective couplings is different for the various fermion species because of flavour dependent vertex corrections. However, with exception of the $Zb\bar{b}$ vertex these corrections are small and effective mixing angles obtained from the measurement of different decays $Z \to f\bar{f}$ are compared by translating the results to $\sin^2\theta_{\mathrm{eff}}^{\mathrm{lept}}$, the mixing angle from leptonic Z decays.

Photonic vertex corrections are part of the calculation of QED radiative corrections which are dominated by the emission of real bremsstrahlung photons. The effect of initial-state radiation has been explained above. Photon radiation from one of the final-state fermions, called final-state radiation (FSR), must also be considered. For inclusive observables, where cuts on the final state photon energy are avoided, one integrates over the available photon phase space. In this case the Kinoshita-Lee-Nauenberg theorem [1] is effective and the corrections are small. For instance, the total cross section of leptonic final states is multiplied by $1 + 3\alpha/4\pi$ which is an increase of 0.17%. The factor is different for hadronic final states and depends on the quark charge. Here, an additional correction factor of about $1 + \alpha_{\mathrm{s}}/\pi$ has to be applied to account for gluon radiation from the quarks.

The narrow Z peak is equivalent to a long lifetime of of the Z boson ($\tau_{\mathrm{Z}} = 1/\Gamma_{\mathrm{Z}}$), which decouples the initial and the final state. Therefore, the interference between ISR and FSR is suppressed for measurements on the Z resonance. The correction to the total cross section is of the order of $\frac{\alpha}{\pi}(\Gamma_{\mathrm{Z}}/m_{\mathrm{Z}})^2 \approx 2 \cdot 10^{-6}$ and can be neglected. For the forward-backward asymmetries the same holds true as long as no explicit or implicit cut on the photon energy in the final state is applied. Nevertheless, to match the precision in data these interference effect have to be treated properly by the Monte-Carlo generator programs [2].

3.2 Measurement of the Z Lineshape

During the LEP1 phase data were taken at seven different centre-of-mass energies around the Z peak. The total hadronic cross sections obtained at these energies by averaging the individual measurements of the four LEP experiments [3] is shown in Fig. 3.3. They are compared to the theory prediction calculated with the program ZFITTER [4]. Also shown is the Z lineshape after unfolding the effects due to photon radiation. From this lineshape curve the resonance parameters of the Z boson, namely the mass, m_{Z}, the total decay width, Γ_{Z}, and the peak cross section σ^0_{had} are extracted using the following parametrisation

$$\sigma_{\mathrm{had}}(s) = \sigma^0_{\mathrm{had}} \frac{s}{(s - m_{\mathrm{Z}}^2)^2 + s^2\Gamma_{\mathrm{Z}}^2/m_{\mathrm{Z}}^2} \tag{3.5}$$

for the term from the Z exchange in the s-channel. The contribution from photon exchange and the γZ interference are taken from the Standard Model prediction assuming the same Z mass.

The position of the cross section maximum yields m_{Z}, the width of the lineshape curve measures Γ_{Z} and the height of the curve determines σ^0_{had}. For the determination of m_{Z}, systematic errors in the cross section determination cancel out to a large extent as they are correlated between the different centre-of-mass energies. An important part of the mass measurement is the precise

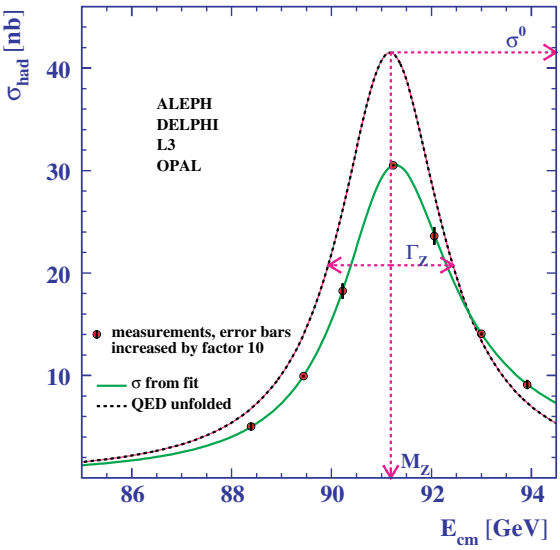

Fig. 3.3. The lineshape scan of the Z resonance. Shown are the total hadronic cross sections at various centre-of-mass energies, as measured by the four LEP collaborations. They are compared to the theory prediction (*solid line*). Also shown is the resulting Z lineshape after unfolding effects due to initial-state photon radiation

energy calibration of the LEP collider which has been obtained by exploiting the technique of resonant spin depolarisation [5]. Including effects coming from ground motions caused by the tides of the moon, the level of Lake Geneva and the parasitic currents from nearby passing TGV trains pinned down the relative error in the determination of the beam energy to $1.5 \cdot 10^{-5}$. Today the Z mass is known with a precision of 23 ppm [6]

$$m_{\mathrm{Z}} = 91.1875 \pm 0.0021 \text{ GeV} \tag{3.6}$$

and the Z decay width is measured to be

$$\Gamma_{\mathrm{Z}} = 2.4952 \pm 0.0023 \text{ GeV} . \tag{3.7}$$

From the height of the measured Z lineshape the peak cross sections, σ_f^0 can be derived. They are parametrised as

$$\sigma_f^0 = 12\pi \, \frac{\Gamma_{\mathrm{ee}} \Gamma_{ff}}{m_{\mathrm{Z}}^2 \Gamma_{\mathrm{Z}}^2} , \tag{3.8}$$

which allows to extract the partial widths Γ_{ff} from the measurements of the total cross sections for individual final states $\mathrm{Z} \to f\bar{f}$.

The systematic uncertainties on the mass and width of the Z boson are dominated by the LEP energy calibration. For Γ_{Z} additional contributions are due to the estimation of the background contamination. The measurement of the peak cross sections strongly depends on the accuracy of the determination of the integrated luminosity.

From the measurement of the total width from the lineshape scan and all visible partial widths one can determine the invisible partial width for $\mathrm{Z} \to \nu\bar{\nu}$:

$$\Gamma_{\mathrm{inv}} = \Gamma_{\mathrm{Z}} - \Gamma_{\mathrm{had}} - \Gamma_{\mathrm{ee}} - \Gamma_{\mu\mu} - \Gamma_{\tau\tau} . \tag{3.9}$$

Assuming that $\Gamma_{\mathrm{inv}} = N_\nu \Gamma_\nu$, where Γ_ν is the partial width into pairs of a single neutrino species, one obtains

$$N_\nu = \frac{\Gamma_{\mathrm{inv}}/\Gamma_{\ell\ell}}{(\Gamma_\nu/\Gamma_{\ell\ell})_{\mathrm{SM}}} = 2.9840 \pm 0.0082 , \tag{3.10}$$

where $\Gamma_{\ell\ell}$ is the partial width into one species of charged leptons, assuming vanishing lepton masses. This has the advantage that uncertainties due to electroweak corrections are common to both partial widths and cancel out in their ratio. The Z lineshape is shown in Fig. 3.4 along with the theory prediction for two, three or four neutrino species. Assuming Standard Model couplings to the Z boson the measurement confirms the number of light neutrino flavours to be three. On the other hand the measurement of Γ_{inv} is two standard deviations below the expectation for three neutrino families. This could be a hint to potential anomalously low $\mathrm{Z}\nu\nu$ couplings compared to the Standard Model expectation. The implication for the recent result of the neutrino experiment NuTeV, pointing into the same direction, will be discussed in Sect. 7.1.

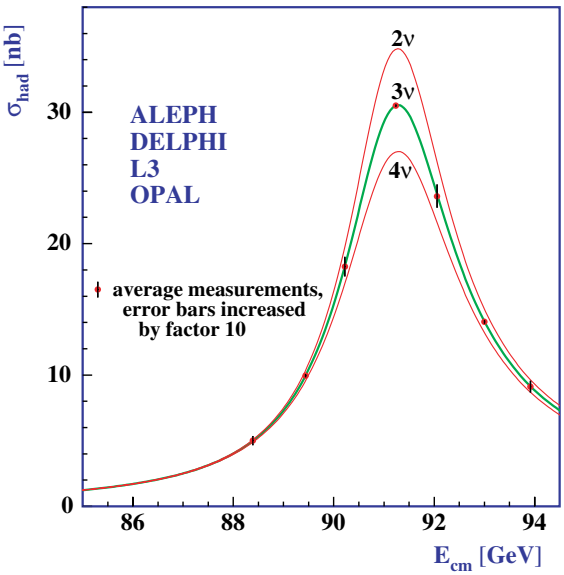

Fig. 3.4. The lineshape scan of the Z resonance along with the theory prediction for two, three and four neutrino species

The result can also be turned into a quantitative limit on extra, non-standard contributions to the invisible width. The difference between the measured value of the invisible width and its Standard Model expectation is found to be $\Delta\Gamma_{\mathrm{inv}} = -2.7^{+1.8}_{-1.5}$MeV. This results in a limit on non-standard contributions to the invisible width of $\Delta\Gamma_{\mathrm{inv}} < 2.0$ MeV at the 95% confidence level.

3.3 Forward-Backward Asymmetries

The forward-backward asymmetry, A^f_{FB}, is defined by the relative difference between forward (F) and backward (B) scattering of the fermion, f, with respect to the incident electron, e^-:

$$A^f_{\mathrm{FB}} = \frac{\sigma^f_{\mathrm{F}} - \sigma^f_{\mathrm{B}}}{\sigma^f_{\mathrm{F}} + \sigma^f_{\mathrm{B}}} = \frac{3}{4} A_{\mathrm{e}} A_f \ . \tag{3.11}$$

At a centre-of-mass energy directly on the Z resonance the contribution from the γZ interference vanishes and inspection of Equation 3.1 shows that the determination of A^f_{FB} measures the coefficient $A_{\mathrm{e}}A_f$ in the term depending linearly on $\cos\theta$.

The measurement of forward-backward asymmetries requires the determination of $\cos\theta$ and the discrimination between fermions and anti-fermions,

based on their electric charges. For the $\mu^+\mu^-$ final state the direction and the charge of the muons can be measured directly. The same holds for e^+e^- final states, but here the large contribution from the t-channel Bhabha scattering has to be corrected for. In the case of $\tau^+\tau^-$ events the direction and charge of the τ lepton is derived from its decay products. For b-quark final states the direction of the b-quark is determined from the jet direction and its flavour is derived, for example, from the charge of the leading particles in B-meson decays [7]. In Fig. 3.5 the combined forward-backward asymmetries for leptonic final states measured at centre-of-mass energies around the Z resonance are shown [3].

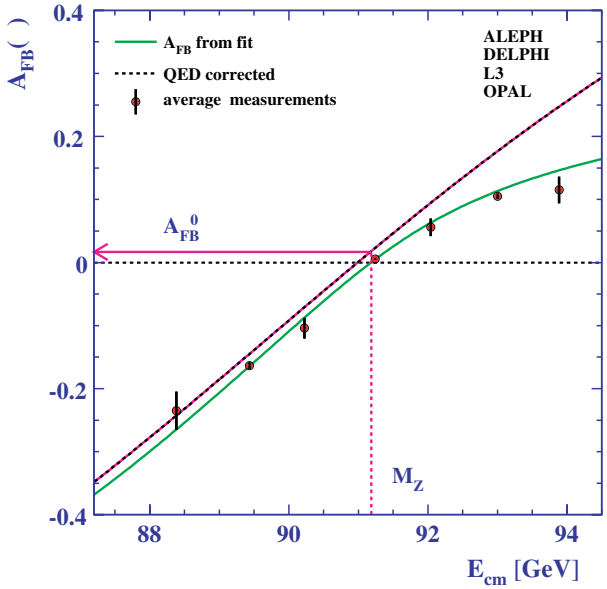

Fig. 3.5. Forward-backward asymmetries measured around the Z resonance. Shown are the average forward-backward asymmetries at various centre-of-mass energies, as measured by the four LEP collaborations. They are compared to the theory prediction (*solid line*). Also shown is the asymmetry curve after unfolding the effects due to initial-state photon radiation

The measurement of the forward-backward asymmetry is insensitive to detection in-efficiencies, as long as these are not asymmetric in charge and in $\cos\theta$ at the same time. Another source of systematic uncertainty arises from the charge confusion, for which the A_{FB}^f measurement has to be corrected for.

All A_{FB} measurements are used to extract an on-peak asymmetry A_{FB}^0, where the radiative corrections and the contributions of the γ exchange are taken into account. Assuming lepton universality A_{FB}^0 the leptonic asymmetries can be combined into one measurement of the effective weak mixing

angle:

$$\sin^2\theta_{\mathrm{eff}} = 0.23099 \pm 0.00053 \; . \tag{3.12}$$

Equivalently, the result on the b-quark forward-backward asymmetry can be translated into

$$\sin^2\theta_{\mathrm{eff}} = 0.23221 \pm 0.00029 \; , \tag{3.13}$$

differing from the value for the leptonic result by two standard deviations.

3.4 Tau Polarisation

The helicity of the final-state fermions can be detected in $\mathrm{e^+e^-} \rightarrow \tau^+\tau^-$ events, where the parity violating decay of the tau lepton serves as an helicity analyser. The average tau helicity can be obtained from the energy spectra of its decay products. In the simplest case, the tau decay into a charged pion, the pion preferentially goes along the direction of the tau helicity vector within the centre-of-mass system of the tau. After being boosted into the laboratory frame, a pion from the decay of a right-handed tau is on average more energetic than a pion from a left-handed tau.

The tau polarisation measured on the Z peak is calculated from the relative asymmetry between the cross sections for the production of right-handed (R) and left-handed (L) tau leptons:

$$P_\tau = \frac{\sigma_{\mathrm{R}} - \sigma_{\mathrm{L}}}{\sigma_{\mathrm{R}} + \sigma_{\mathrm{L}}} = -A_\tau \; . \tag{3.14}$$

The results from the LEP collaborations [8] are averaged and transformed into a determination of

$$A_\tau = 0.1439 \pm 0.0043 \; . \tag{3.15}$$

Measuring also the $\cos\theta$ dependence of the tau polarisation gives additional information on A_{e}. The tau polarisation measurements using the full LEP data sample result in a determination of the effective weak mixing angle of

$$\sin^2\theta_{\mathrm{eff}} = 0.23159 \pm 0.00041 \; . \tag{3.16}$$

3.5 Left-Right Asymmetry

The left-right asymmetry, accessible with the polarised electron beam at the SLC, is defined as the relative difference between the interaction rates with left (L) and right (R) longitudinally polarised electron bunches. Neglecting the contribution from the photon exchange, A_{LR}^f on the Z resonance is given by

$$A_{\mathrm{LR}}^{f} = \frac{1}{P_{\mathrm{e}}} \frac{\sigma_{\mathrm{L}}^{f} - \sigma_{\mathrm{R}}^{f}}{\sigma_{\mathrm{L}}^{f} + \sigma_{\mathrm{R}}^{f}} = A_{\mathrm{e}} \; . \tag{3.17}$$

For measurements on the Z resonance Equation 3.1 shows that A_{LR}^{f} measures directly the asymmetry parameter A_{e} of the electron. Because the measurement of A_{LR}^{f} does not need the detection of the flavour of the outgoing fermions, all visible Z decays can be used. Especially due to its high cross section, the left-right asymmetry of the hadronic final state allows a competitive determination of the couplings of the Z boson to the electrons.

Defined as a cross-section asymmetry the measurement of A_{LR}^{f} is an observable nearly unaffected by detector-dependent systematic effects or by deficiencies of the Monte-Carlo modelling. On the other hand the measurement depends strongly on the accuracy of the determination of the polarisation of the electron beam. Another source of systematic uncertainties comes from the knowledge of beam energy, which is used to correct the asymmetry measurement to the value directly on the Z resonance.

In the years 1992–1998 the SLD experiment at SLC collected about half a million Z decays with beam polarisations up to 77%. Taking into account radiative corrections, the contribution from the γ exchange and the extrapolation to the exact position of the Z peak the average peak asymmetry for the complete SLD data set is obtained as [9]:

$$A_{\mathrm{LR}}^{0} = 0.1513 \pm 0.0021 \; . \tag{3.18}$$

With

$$A_{\mathrm{LR}}^{0} = A_{\mathrm{e}} = \frac{2\,(1 - 4\,\sin^2\theta_{\mathrm{eff}})}{1 + (1 - 4\,\sin^2\theta_{\mathrm{eff}})^2} \tag{3.19}$$

this can be translated into a measurement of the effective weak mixing angle of

$$\sin^2\theta_{\mathrm{eff}} = 0.23098 \pm 0.00026 \; . \tag{3.20}$$

3.6 Determination of the Effective Weak Mixing Angle

The various asymmetries measured on the Z resonance are related to the coupling of the weak neutral current to the fermions, and can therefore be expressed in terms of the effective weak mixing angle, $\sin^2\theta_{\mathrm{eff}}$. The measurements of the lepton forward-backward asymmetry, $A_{\mathrm{fb}}^{0,\mathrm{l}}$, the left-right asymmetry at SLD, $A_{\mathrm{l}}(\mathrm{SLD})$, the τ polarisation at LEP, $A_{\mathrm{l}}(P_\tau)$, and the forward-backward asymmetry of the b-quark and c-quark final state, $A_{\mathrm{fb}}^{0,\mathrm{b}}$ and $A_{\mathrm{fb}}^{0,\mathrm{c}}$ are translated to the effective mixing angle for the leptonic final state, $\sin^2\theta_{\mathrm{eff}}^{\mathrm{lept}}$, and compared in Fig. 3.6.

A difference of 2.9 standard deviations is observed between the two most precise measurements, the left-right asymmetry and the b-quark forward-backward asymmetry. However, combining all measurements results in an accuracy at the sub-permill level [10]:

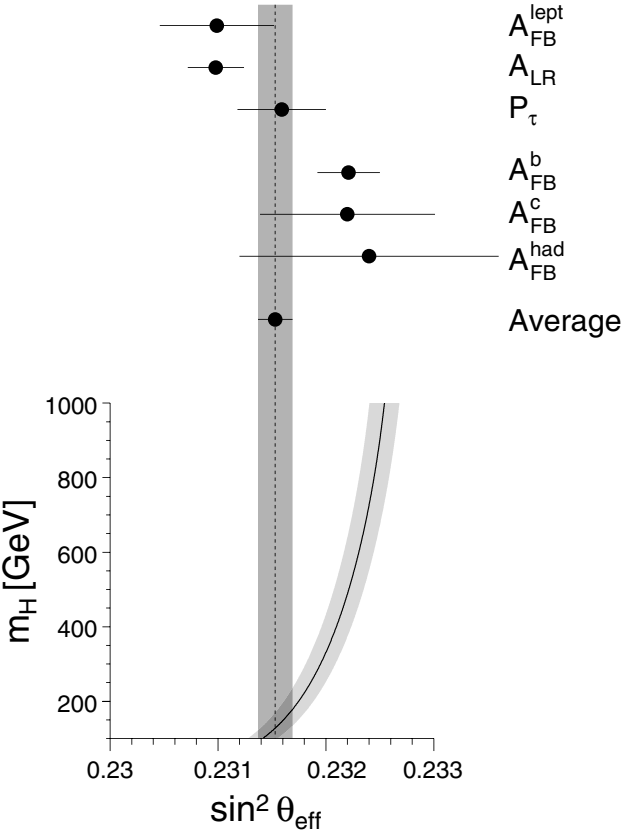

Fig. 3.6. Measurements of the effective weak mixing angle from Z decays and comparison with the Standard Model prediction as function of the Higgs mass. The theory uncertainty is dominated by the uncertainties in m_t and $\Delta\alpha$ and shown as a band whose width represents the quadratic sum of both effects

$$\sin^2\theta_{\rm eff}^{\rm lept} = 0.23153 \pm 0.00016\ . \tag{3.21}$$

Also shown is the Standard Model prediction for $\sin^2\theta_{\rm eff}^{\rm lept}$ as a function of the Higgs mass, $m_{\rm H}$. Comparing the prediction with the measurement result shows a preference for a light Higgs boson.

3.7 Effective Couplings and Weak Radiative Corrections

The cross-section and asymmetry measurements presented above can be translated into the measurements of the effective couplings $\bar{g}_{\rm V}^f$ and $\bar{g}_{\rm A}^f$ of the Z boson to the fermions of type f. For the leptonic final states these coupling constants

can be compared directly and were found to agree within the experimental precision, thus indicating lepton universality.

Alternatively they can be transformed into measurements of ρ_{eff} and $\sin^2\theta_{\mathrm{eff}}$ by means of Equations 3.4. This has to be done separately for each fermion type f. From Equations 3.2 and 3.3 it is evident that ρ_{eff} is mainly measured by the partial decay widths of the Z boson while $\sin^2\theta_{\mathrm{eff}}$ is determined by the various asymmetries.

It is remarkable that the specific values of the charge and the weak isospin of the quarks imply that the sensitivity of A_{q} to $\sin^2\theta_{\mathrm{eff}}$ is much smaller than it is the case for A_{e}. Therefore, the quark asymmetries $A_{\mathrm{fb}}^{0,\mathrm{q}} = \frac{3}{4}A_{\mathrm{e}}A_{\mathrm{q}}$ can be translated into a determination of $\sin^2\theta_{\mathrm{eff}}^{\mathrm{lept}}$ through the factor A_{e}. Likewise, as all measured cross sections depend on Γ_{ee}, the observable $\rho_{\mathrm{eff}}^{\mathrm{lept}}$ is the one with the highest precision. The measured values are [10]:

$$\rho_{\mathrm{eff}}^{\mathrm{lept}} = 1.0050 \pm 0.0010 \tag{3.22}$$

$$\sin^2\theta_{\mathrm{eff}}^{\mathrm{lept}} = 0.23153 \pm 0.00016 \tag{3.23}$$

It is worthwhile to investigate the question whether the electroweak data gathered on the Z resonance proof the existence of genuine electroweak radiative corrections beyond those of QED. The Born-term values of the ρ parameter and the weak mixing angle θ_{w} can be derived by setting $\Delta\rho$ and the remainder weak corrections to zero:

$$\rho = 1 \tag{3.24}$$

$$\sin^2\theta_{\mathrm{w}} = \frac{1}{2}\left(1 - \sqrt{1 - 4\frac{\pi\alpha(m_{\mathrm{Z}}^2)}{\sqrt{2}G_{\mathrm{F}}m_{\mathrm{Z}}^2}}\right) = 0.23098 \pm 0.00012\,. \tag{3.25}$$

The measurements presented above show significant deviations from these Born-term predictions thus indicating the need for pure weak radiative corrections to describe the Z-peak data. The prediction of $\sin^2\theta_{\mathrm{w}}$ from G_{F} suffers from the large uncertainty in $\Delta\alpha_{\mathrm{had}}$, which enters the calculations as one has to transfer from the low-energy scale of G_{F} to the Z peak.

References

1. T. Kinoshita, J. Math. Phys. **3**, 650 (1962);
   T.D. Lee and M. Nauenberg, Phys. Rev. **133**, 1549 (1964)
2. S. Jadach, B.F.L. Ward and Z. Wąs, Phys. Rev. **D 63**, 113009 (2001)
3. ALEPH Collaboration, R. Barate et al., Eur. Phys. J. **C 14**, 1 (2000);
   DELPHI Collaboration, P. Abreu et al., Eur. Phys. J. **C 16**, 371 (2000);
   L3 Collaboration, M. Acciarri et al., Eur. Phys. J. **C 16**, 1 (2000);
   OPAL Collaboration, G. Abbiendi et al., Eur. Phys. J. **C 19**, 587 (2001)
4. D. Bardin at al., Comp. Phys. Comm. **133**, 229 (2001);
   A.B. Arbuzov et al., Preprint DESY-05-034 and hep-ph/0507146 (2005)

5. LEP Energy Working Group, L. Arnaudon et al., Z. Phys. **C 66**, 45 (1995);
LEP Energy Working Group, R. Assmann et al., Eur. Phys. J. **C 6**, 187 (1999)
6. ALEPH, DELPHI, L3, OPAL and SLD Collaborations, Phys. Rept. **427**, 257 (2006)
7. ALEPH Collaboration, A. Heister et al., Eur. Phys. J. **C 24**, 177 (2002);
ALEPH Collaboration, A. Heister et al., Eur. Phys. J. **C 22**, 201 (2001);
DELPHI Collaboration, J. Abdallah et al., Eur. Phys. J. **C 40**, 1 (2005);
DELPHI Collaboration, J. Abdallah et al., Eur. Phys. J. **C 34**, 109 (2004);
L3 Collaboration, M. Acciarri et al., Phys. Lett. **B 448**, 152 (1999);
L3 Collaboration, M. Acciarri et al., Phys. Lett. **B 439**, 225 (1998);
OPAL Collaboration, G. Abbiendi et al., Phys. Lett. **B 577**, 18 (2003);
OPAL Collaboration, G. Abbiendi et al., Phys. Lett. **B 546**, 29 (2002)
8. ALEPH Collaboration, A. Heister et al., Eur. Phys. J. **C 20**, 401 (2001);
DELPHI Collaboration, P. Abreu et al., Eur. Phys. J. **C 14**, 585 (2000);
L3 Collaboration, M. Acciarri et al., Phys. Lett. **B 429**, 387 (1998);
OPAL Collaboration, G. Abbiendi et al., Eur. Phys. J. **C 21**, 1 (2001)
9. SLD Collaboration, K. Abe et al., Phys. Rev. Lett. **86**, 1162 (2001);
SLD Collaboration, K. Abe et al., Phys. Rev. Lett. **84**, 5945 (2000)
10. LEP Electroweak Working Group, Eprint hep-ex/0511027 and
`http://lepewwg.web.cern.ch/LEPEWWG/`

4

Electroweak Physics Above the Z Resonance

As the electron and the positron are fundamental and point-like particles, e^+e^- collisions allow clean studies of the fundamental interactions of the electroweak Standard Model. Due to the absence of coloured particles in the initial state they are mediated solely via the electroweak gauge bosons. Typical reactions are depicted in Fig. 4.1.

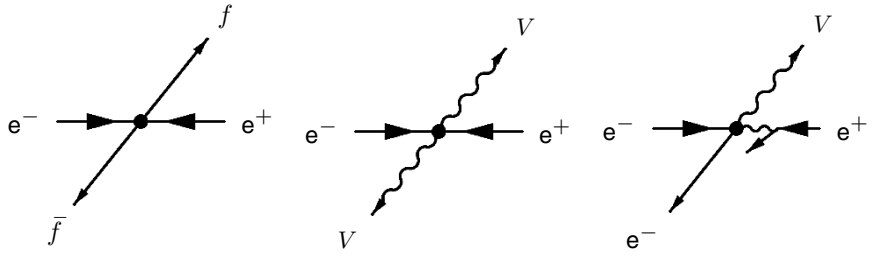

Fig. 4.1. The main electroweak reactions which are studied in e^+e^- collisions: The production of fermion-antifermion pairs, the production of vector-boson pairs and single-boson production

The most prominent example is the direct annihilation of the e^+e^- pair into a photon or a Z boson and the production of a fermion-antifermion pair via s-channel scattering. In Sect. 3 the fermion-pair production was presented as the basis of the electroweak precision measurements performed at the Z resonance. Fermion-pair events are also analysed at centre-of-mass energies well above the Z peak, as described in Sect. 4.1.

The second class of reactions contains all the diagrams with a fermion exchange in the t-channel, which lead to the production of vector-boson pairs. The processes $e^+e^- \to \gamma\gamma$, $e^+e^- \to \gamma Z$, $e^+e^- \to ZZ$ and $e^+e^- \to W^+W^-$ are possible. In the latter case also an s-channel diagram can contribute due to the existence of the triple gauge couplings (see Fig. 5.1). The Z boson and

Stefan Roth: *Precision Electroweak Physics at Electron-Positron Colliders*
STMP **220**, 39–65 (2006)
DOI 10.1007/3-540-35165-5_4

the W boson are unstable particles and immediately decay into a fermion-antifermion pair, which leads to four-fermion final states in the case of ZZ and W^+W^- production.

In e^+e^- collisions the incoming electrons and positrons are surrounded by virtual photons, which themselves can interact in a hard scattering process. This is the case in the third type of reactions, where a quasi-real photon (a photon with very small virtuality) is radiated from one of the beams and then scattered with an electron (or positron) from the other beam leading to different kinds of Compton scattering. These processes yield single photons, Z bosons or W bosons in the final state. In the case of single-W production an additional diagram with a t-channel W exchange and a γWW vertex exists (see Fig. 4.12).

The scattering of two virtual photons, each from one of the beams, is also possible. It is known as photon-photon collision or the two-photon process. Because the photon has identical quantum numbers as the neutral vector mesons, the virtual photons can fluctuate into these, yielding an hadronic component of the photon. The scattering of two such mesons dominate the total cross section of photon-photon collisions (vector meson dominance). Additionally, the deep inelastic scattering of a beam electron (or positron) can be used to reveal the interior hadronic structure of the photon (resolved processes). Throughout this review two-photon collisions are only considered as a source of background to the selection of electroweak processes.

To produce the charged weak gauge bosons W^+ and W^- in pairs, it was necessary to increase the centre-of-mass energy of LEP from the 90 GeV range, where the studies of the Z resonance took place, to energies of more than 160 GeV, the threshold of W-pair production. After the installation of superconducting accelerating cavities the LEP storage ring was able to cope with increased energy loss of the electrons due to the enhanced synchrotron radiation. In the years from 1996 to 2000 the LEP energy was continuously increased from 161 GeV, just above the kinematic threshold of W-pair production, up to 209 GeV. At energies above the W-pair threshold a total luminosity of about 0.7 pb^{-1} was recorded by each of the four experiments.

As an example, Fig. 4.2 shows the cross section results from the L3 experiment for the various electroweak processes at LEP. The highest production rate is observed for the production of fermion-antifermion pairs, where the processes of quark-pair production, $e^+e^- \to q\bar{q}$, and muon-pair production, $e^+e^- \to \mu^+\mu^-$, are shown as examples. Also shown are the cross sections of the pair production of vector bosons. The cross section of photon-pair production, $e^+e^- \to \gamma\gamma$, shows the $1/s$ dependence of this QED process. W-pair production, $e^+e^- \to W^+W^-$, and Z-pair production, $e^+e^- \to ZZ$, exhibits the typical threshold behaviour due to the boson masses. Also an example for the production of single gauge bosons, the single-W production $e^+e^- \to We\nu$, is depicted in Fig. 4.2. This cross section is relatively small at LEP energies, but rising with $\sqrt{s}$.

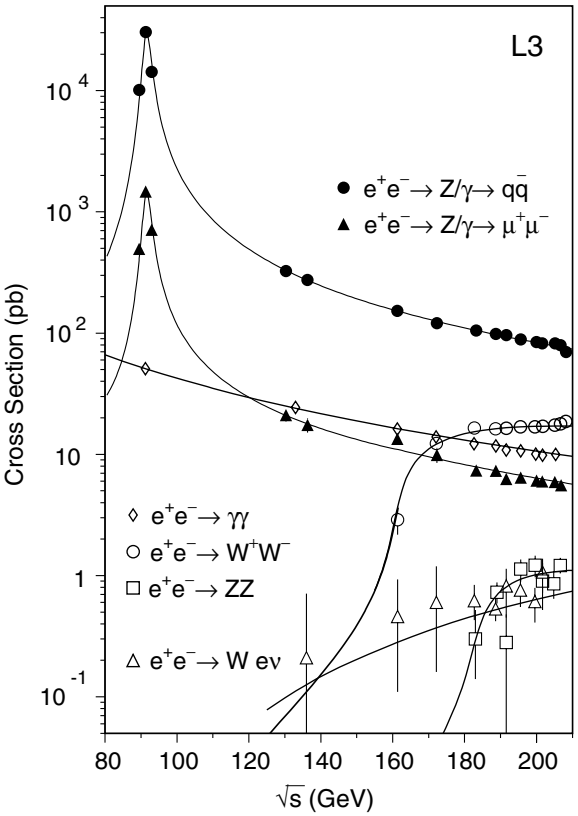

Fig. 4.2. Cross section results for various electroweak processes measured with the L3 detector. Shown are the total cross sections of fermion-pair and boson-pair production as well as of single-W production

In the next section the studies of fermion-pair production at centre-of-mass energies above the Z resonance are discussed. Then an overview is given on the various processes that produce electroweak gauge bosons. The production of Zγ events is described in more detail, because it can be used to measure the mass of the Z boson in analogy to the W-mass measurement. Alternatively it can serve as a cross check of the calibration of the LEP beam energy. The production of W pairs is postponed to Chap. 5.

4.1 Fermion-Pair Production Above the Z Resonance

On the Z resonance the fermion-pair processes, $e^+e^- \to f\bar{f}$, are dominated by the production and decay of an on-shell Z boson. At higher centre-of-mass energies, $\sqrt{s}$, the total cross sections decrease rapidly as one is leaving the resonance. The relative contribution of the photon exchange increases, which

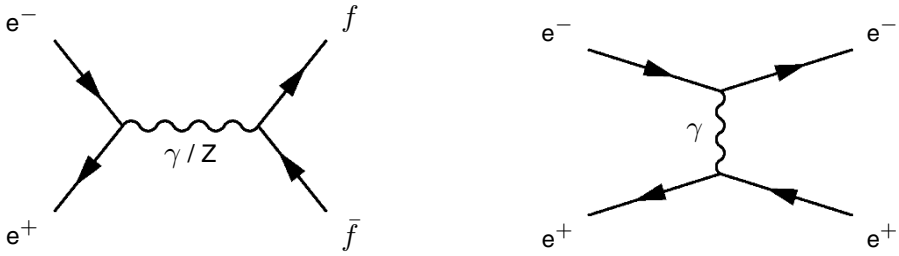

Fig. 4.3. The lowest order Feynman diagrams of the process $e^+e^- \to f\bar{f}$. Fermion pairs are produced via a γ or Z propagator in the s-channel (*left*). For the e^+e^- final state (Bhabha scattering) an additional t-channel diagram exists (*right*)

leads to stronger interference effects such as the forward-backward asymmetry of the produced charged leptons.

While photon radiation is largely suppressed in resonance production, especially the initial-state radiation (ISR) becomes a very important effect at these higher energies. One consequence is the advent of reactions where the ISR photon radiates so much energy that the remaining centre-of-mass energy, $\sqrt{s'}$, is approximately equal to the Z mass and resonant fermion-pair production takes place again. This effect, which is called the "Return to the Z", will be explained in more detail in Sect. 4.3.

An overview of all measurements of forward-backward asymmetries of muon-pair production has been compiled by the L3 collaboration and is presented in Fig. 4.4. All measurements are corrected for effects of photon

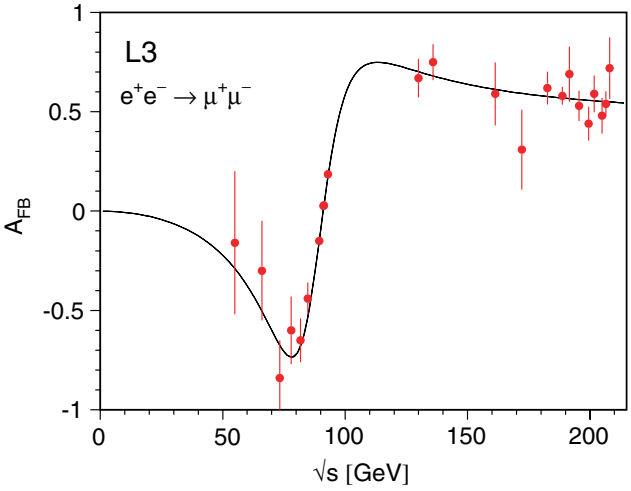

Fig. 4.4. Summary of all measurements of forward-backward asymmetries of muon-pair production performed with the L3 detector at various centre-of-mass energies in the range between 50 and 210 GeV

radiation and compared to the theory prediction at the improved-Born level. For the measurements above the Z resonance the Z-return events have been excluded by the selection whereas the data points at centre-of-mass energies below the Z mass are based on a dedicated selection of events with hard initial-state radiation. Applying such selection to data recorded on the Z resonance yields events with an effective centre-of-mass energy well below the Z mass which provide information on the asymmetries in this energy regime.

The cross sections in the energy range of 160 GeV $< \sqrt{s} <$ 209 GeV are more than three orders of magnitude smaller than the ones on the Z resonance as illustrated in Fig. 4.2. Here, one distinguishes between the total cross section and a measurement, which is restricted to events without hard ISR radiation. The latter cross section represents the processes where the fermion pair is produced at the nominal centre-of-mass energy. To select such events the effective centre-of-mass energy after ISR radiation, $\sqrt{s'}$, is required to be larger than 85% of $\sqrt{s}$. Details of the $\sqrt{s'}$ analysis and the measured $\sqrt{s'}$ spectra are presented in Sect. 4.3. Since the electric charge of the quarks is only a fraction of 1/3 or 2/3 of that of the charged leptons their coupling to the photon is also smaller. On the other hand the coupling of the quarks to the Z boson is stronger than that of the charged leptons. Therefore the radiative return to the Z is more pronounced for hadronic final states than for muon or tau pairs. Only about 20% of the hadronic events, but about 40% of the muon and tau pair events are produced with $\sqrt{s'}/\sqrt{s} > 0.85$. Because Bhabha scattering has a large contribution from the t-channel exchange, the relative fraction of the radiative return is small.

For the cross section measurement a detailed simulation of the detector resolutions and efficiencies for the considered processes is mandatory. The program KK2F [1] is used to simulate fermion-pair production with muon, tau and quark final states, whereas the Bhabha scattering is modelled using the program BHWIDE [2]. Both programs are generator programs which are based on $\mathcal{O}(\alpha)$ calculations, but the effect of initial-state radiation is included in higher orders using the Yennie-Frautschi-Suura exponentiation scheme.

The selections of the final states of fermion-pair production follow the strategy to clearly identify jets or leptons in the events and to reject background from other processes using cuts on the event kinematics [3]. The experimental precision of the cross-section measurement is about 1% for quark-pairs and Bhabha scattering and about 2% for muon- and tau-pair production. The combined cross-section measurements of the four LEP experiments are summarised in Fig. 4.5. Good agreement with the Standard Model expectation is observed. In the case of muon- and tau-pair production also the forward-backward asymmetry of the production cross section is measured. The results are also shown in Fig. 4.5 after combining the measurements of the four LEP experiments.

The measurement of fermion-pair production above the Z resonance can be used to search for indirect signals of physics beyond the Standard Model. New and heavy particles, like for example leptoquarks or an additional vector

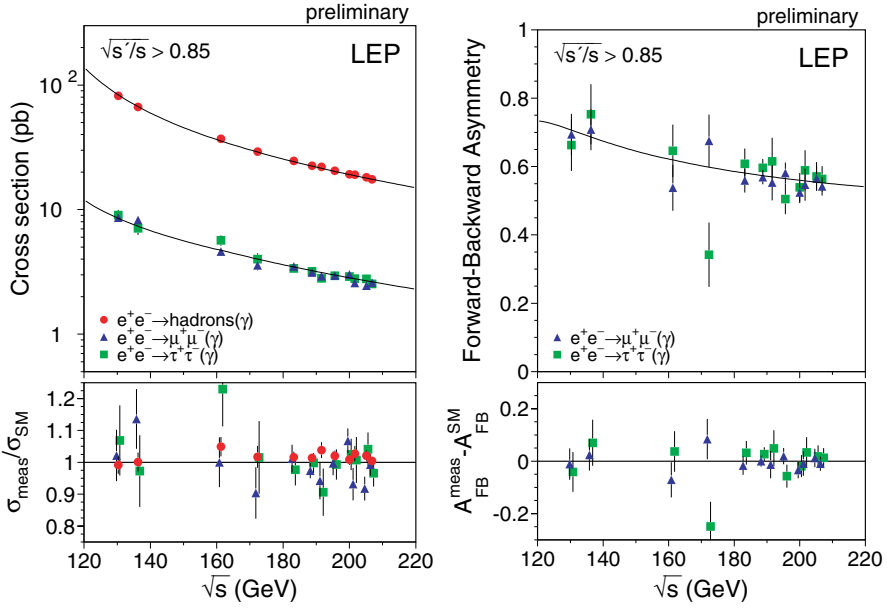

Fig. 4.5. Measurements of cross section and forward-backward asymmetry of fermion-pair production above the Z resonance [5].

boson Z′, would cause small variations in the propagators of the fermion-pair processes and would lead to deviations of the cross-section and asymmetry measurements from the Standard-Model prediction. No such deviations have been observed and from the precision of the measurements exclusion limits on the existence of these heavy particles can be derived.

The existence of a Z′ boson would lead to interference with the ordinary Z boson and change the cross section even at energies much lower than its mass. The data indicate that the mass of the Z′ has to be greater than 340 GeV and for specific models even higher mass exclusion limits can be set [5]. Because it has identical quantum numbers a heavy Z′ could also mix with the ordinary Z, which would then change the couplings of the neutral current to the fermions. But these couplings are strongly constrained by the measurements performed at the Z resonance.

A more general approach is the search for potential four-fermion contact interactions in the process $e^+e^- \rightarrow f\bar{f}$. These would be the remnants of a new interaction, which acts at much higher energies. The Feynman diagram of such contact interaction is depicted in Fig. 4.6. Combining all LEP data exclusion limits on the energy scale Λ, where the new interaction takes places, can be set. They range between 2 and 20 TeV depending on the model [5].

Using one of the contact interaction models and assuming a coupling strength equal to the electromagnetic coupling, the results obtained for

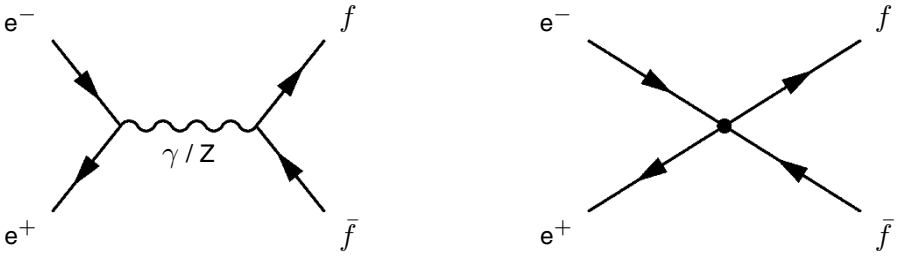

Fig. 4.6. The Feynman diagram of the process $e^+e^- \to f\bar{f}$ (*left*) and a potential additional four-fermion contact interaction caused by new physics (*right*)

Bhabha scattering, $e^+e^- \to e^+e^-$, can be interpreted as an upper limit on the electron size, $r_e < 1.4 \times 10^{-19}$ m [5].

4.2 Production of Electroweak Gauge Bosons

In e^+e^- collisions electroweak gauge bosons are produced singly or in pairs. Single-boson production can be interpreted as radiative events of Bhabha scattering, where the scattered electron or positron radiates a photon or Z boson or even emits a W boson transforming itself into a neutrino. In the preferred phase space region of these processes one of the beam particles (electron or positron) continues along the beam direction at a very small scattering angle. Hence, a t-channel photon with a very small virtuality is exchanged and this quasi-real photon collides head-on with an electron (or positron) of the other beam. As the quasi-real photon does not exhibit the full beam energy, the hard scattering process takes place at a reduced centre-of-mass energy. The processes of Compton scattering, single-Z and single-W production are possible.

On the contrary, in events with e^+e^- annihilation the complete centre-of-mass energy is available for the production of a pair of gauge bosons. Such reactions lead to the production of two photons, two Z bosons, a $Z\gamma$ pair or a W^+W^- pair.

4.2.1 Compton Scattering

Quasi-real photons, i.e. photons with a virtuality much smaller than any other mass scales in the process, can be radiated from one of the incoming beams and lead to Compton scattering. The Feynman diagrams of this process are shown in Fig. 4.7.

The phase space of the radiative $e^+e^- \to e^+e^-\gamma$ process, where either the electron or positron has a very small scattering angle, is not covered by the BHWIDE generator. This type of reactions is simulated by the program TEEGG [4]. Assuming a three-particle final state, with one electron (or

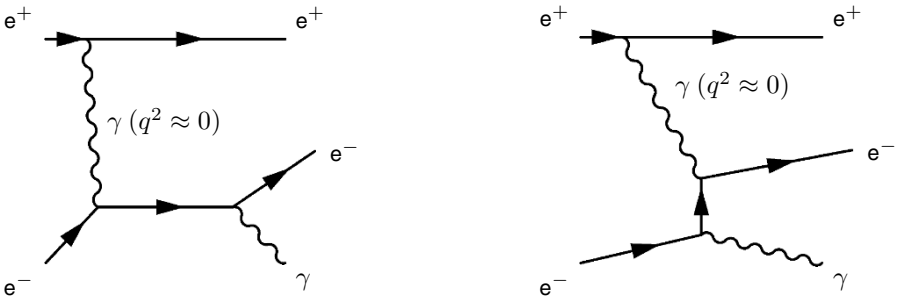

Fig. 4.7. The Feynman diagrams of quasi-real Compton scattering

positron) escaping along the beam direction, allows the calculation of $\sqrt{s'}$ purely from the angular measurements of the detected positron (or electron) and the photon:

$$\sqrt{s'} = \sqrt{s}\,\frac{\sin\theta_{\mathrm{e}} + \sin\theta_{\gamma} - |\sin(\theta_{\mathrm{e}} + \theta_{\gamma})|}{\sin\theta_{\mathrm{e}} + \sin\theta_{\gamma} + |\sin(\theta_{\mathrm{e}} + \theta_{\gamma})|}\,. \tag{4.1}$$

The L3 collaboration analysed about 600 pb^{-1} of data in the energy range of 189 GeV $< \sqrt{s} <$ 209 GeV, which corresponds to effective centre-of-mass energies, $\sqrt{s'}$, of the Compton scattering process of up to 175 GeV [6]. Events from Compton scattering must contain an identified electron or positron and a high-energy photon. Two clusters in the electromagnetic calorimeter are required where one of the clusters must be associated to a track in the tracking chamber. An example of an event of Compton scattering as recorded by the L3 detector is shown in Fig. 4.8 From the Monte Carlo simulation the average

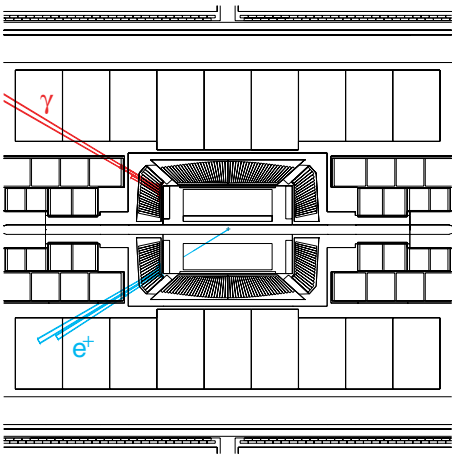

Fig. 4.8. Example of an event of Compton scattering as recorded by the L3 experiment. The final state consists of one photon and one positron

virtuality, Q^2, for the selected events is derived to be 0.48 GeV^2, which validates the assumption of quasi-real photons. Systematic uncertainties of the measurements are caused by the calorimeter energy scale, the simulation of the photon conversion probability, the track efficiency and the prediction of background contamination.

If one assumes that the virtual photon flux around the electrons is correctly described by the Monte Carlo simulation the comparison between the selected number of events in data with the Monte Carlo prediction directly measures the cross section of Compton scattering. The result of the measurement is presented in Fig. 4.9.

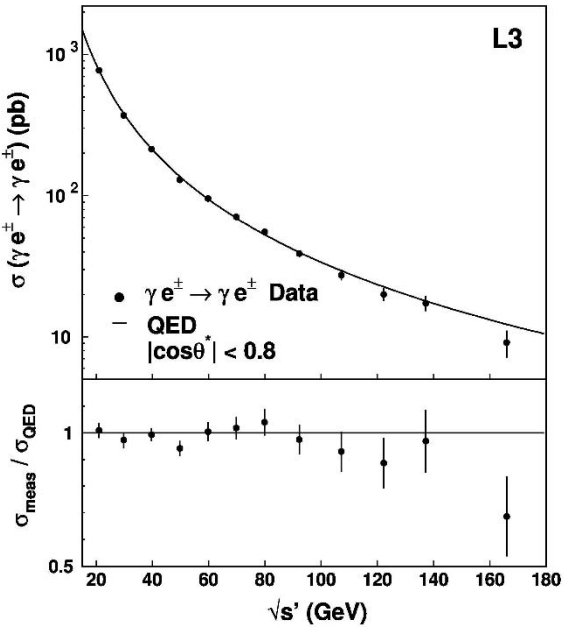

Fig. 4.9. Cross section of quasi-real Compton scattering as measured by the L3 collaboration

4.2.2 Single-Z Production

The Feynman diagrams of single-Z production are depicted in Fig. 4.10. These diagrams are very similar to the ones of quasi-real Compton scattering (Fig. 4.7) and hence this process is often denoted as electroweak Compton scattering. These diagrams are only two examples of in total 48 diagrams contributing to the $e^+e^- \to f\bar{f}ee$ process ($f \neq e$). Special phase space cuts have to be applied to enhance the contribution of the single-Z diagrams.

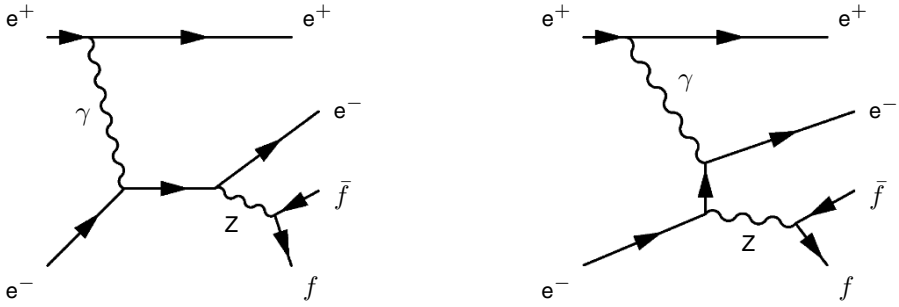

Fig. 4.10. The Feynman diagrams of single-Z production

Single-Z production was analysed by three of the four LEP collaborations [7]. The L3 collaboration performed a selection of the qq̄ee and the $\mu\mu$ee final states with predicted cross sections of 0.6 pb and 0.04 pb, respectively. As either the incoming electron or positron escapes along the beam direction, these events are selected by requiring one isolated electron in the detector with energy above 3 GeV and two jets or two muons, respectively. Important background sources are quark-pair and muon-pair production. The analyses from ALEPH and OPAL yield comparable results. As an example Fig. 4.11 shows the invariant-mass spectrum of the selected, singly produced, Z bosons for the ALEPH selection.

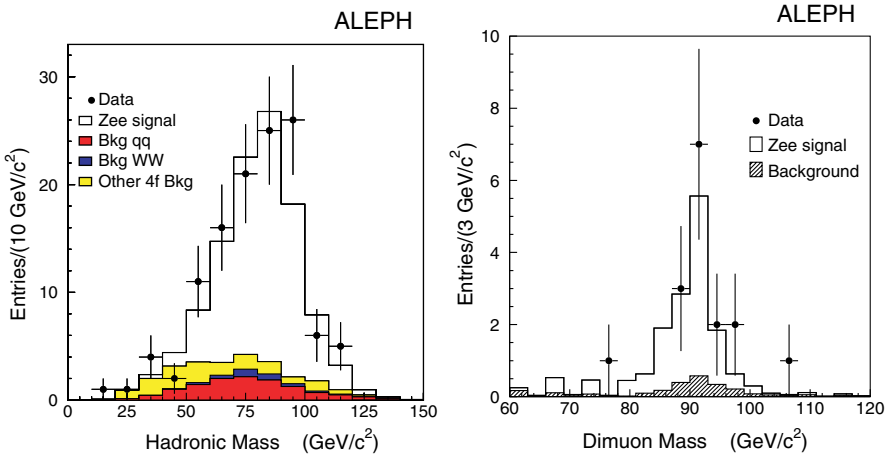

Fig. 4.11. Invariant mass spectrum of the decay products of singly produced Z bosons: $q\bar{q}$ee (*left*) and $\mu\mu$ee (*right*) final states as measured by ALEPH

4.2.3 Single-W Production

Single-W production proceeds via the Feynman diagrams shown in Fig. 4.12. The dominant phase space of this reaction features a t-channel photon with very small virtuality. This photon is produced by nearly collinear radiation from one of the beams, where the radiating electron (or positron) escapes along the beam direction. In analogy to the Compton scattering process also single-W production can be understood as the interaction of quasi-real photons radiated off one of the beams. In contrast to Compton scattering an additional type of Feynman diagrams appears where photon and W boson interact directly via the gauge-boson vertex γWW. The study of single-W production provides a direct measurement of the γWW vertex. Therefore it gives complementary information to the determination of the trilinear gauge boson couplings in W-pair production.

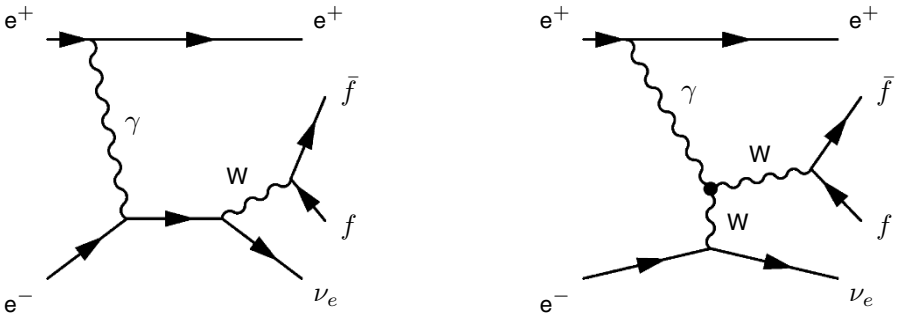

Fig. 4.12. The Feynman diagrams of single-W production

Because the γWW vertex is involved, the single-W cross section depends on the two parameters describing this vertex, κ_γ and λ_γ (see Sect. 5.8). These form factors are related to the magnetic dipole and the electric quadrupole moment of the W boson and the Standard Model predicts them to be $\kappa_\gamma = 1$ and $\lambda_\gamma = 0$ at tree level. Higher order contributions are small and potential deviations from these predictions would point to non-standard radiative corrections or an internal structure of the W boson. Further information on the trilinear gauge couplings and their measurement is given is Sect. 5.8.

The electron (positron) emitting the quasi-real photon escapes detection due to its small scattering angle. The second lepton in the final state, the neutrino, is not detectable and therefore the event signature solely consists of the decay products of the produced W boson. We expect either two hadronic jets with large missing momentum, especially in the transverse direction, or a single, high-energy, charged lepton originating from a leptonic W decay. Two examples of these events are shown in Fig. 4.13. The energy spectrum of the charged leptons, as measured by the L3 collaboration, is shown in Fig. 4.14.

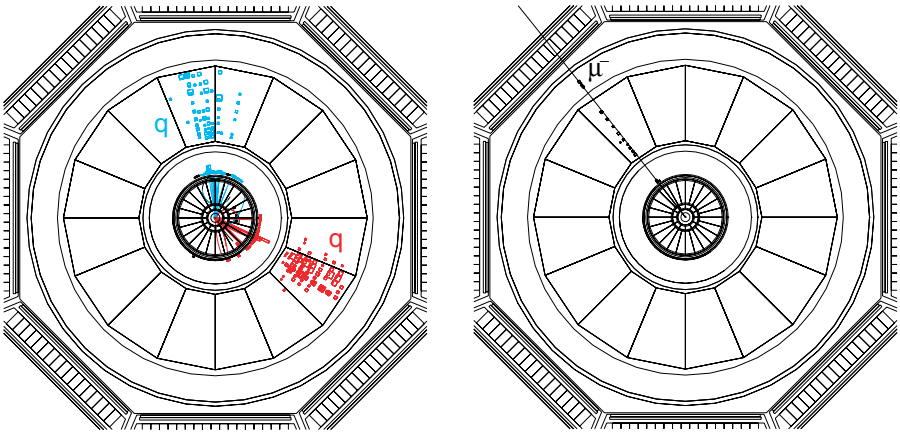

Fig. 4.13. Events of single-W production as recorded in the L3 experiment. The W bosons decay hadronically (*left*) or leptonically (*right*)

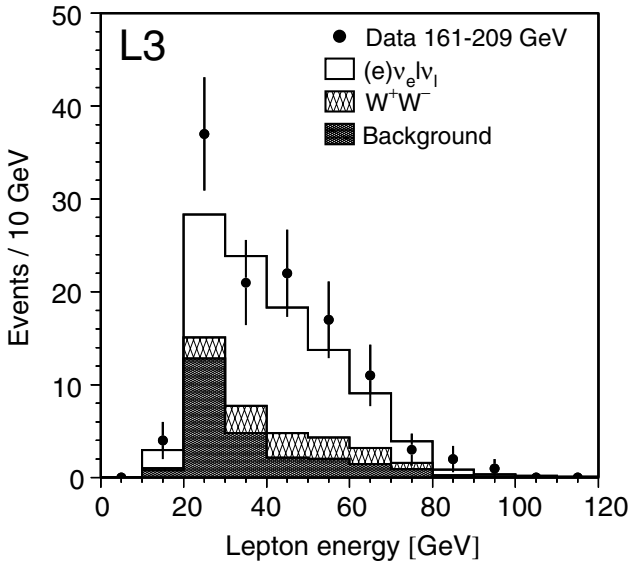

Fig. 4.14. Energy spectrum of the leptons coming from leptonic decays of singly produced W bosons

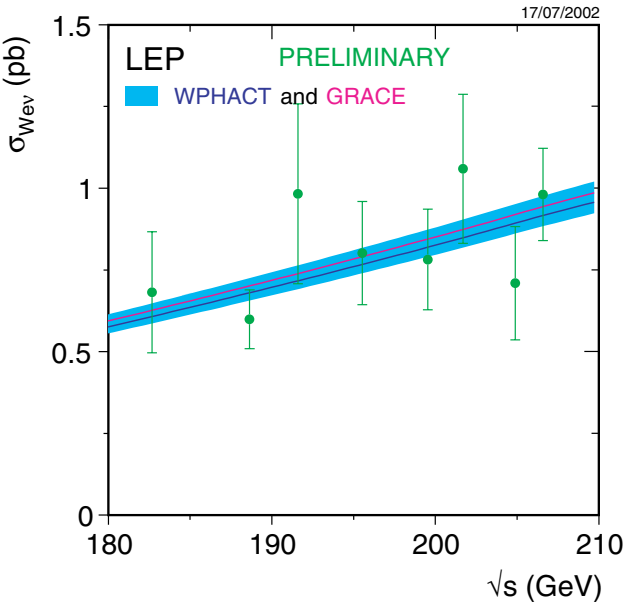

Fig. 4.15. Combination of cross-section measurements of single-W production at LEP and comparison with theoretical expectation.

All LEP experiments have selected and analysed the events of single-W production [8]. The selection of the hadronic final states is mainly based on a complex neural network analysis, where the discriminating variables should be sensitive to the 2-jet topology of the events. In the leptonic selection one searches for events with a high-energy lepton and no other activity in the detector.

The combined result of the measurements of the total cross section of single-W production is presented in Fig. 4.15. Here the measurements are compared to the expected cross sections calculated with the programs WPHACT [9] and GRC4F [10].

4.2.4 Photon Production

The Feynman diagrams of the e^+e^- annihilation into two photons are shown in Fig. 4.16. These diagrams are completely described by Quantum Electrodynamics (QED). Weak interactions contribute only via loop diagrams. Therefore the measurement of the $e^+e^- \rightarrow \gamma\gamma$ reaction at LEP is an ideal possibility to test the validity of QED at the highest centre-of-mass energies.

Because the final state photons are not distinguishable, the t-channel process is accompanied by a u-channel diagram. The lowest order differential cross section is given by

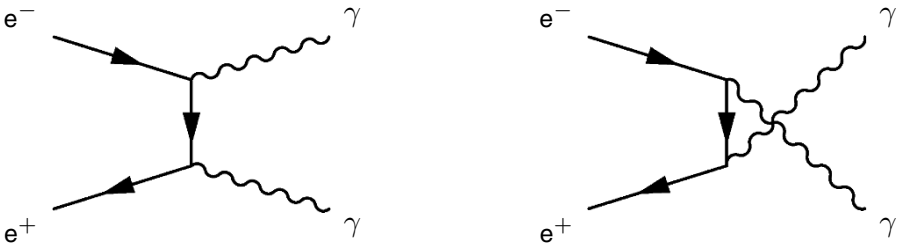

Fig. 4.16. The Feynman diagrams of photon-pair production

$$\frac{\mathrm{d}\sigma}{\mathrm{d}\Omega} = \frac{\alpha^2}{s} \frac{1+\cos^2\theta}{1-\cos^2\theta} \,. \tag{4.2}$$

Higher order effects can yield additional photons in the final state and also modify the angular distributions.

Deviations from the QED prediction are predicted by various models. One very general assumption is an additional short-range exponential deviation from the Coulomb potential, which is described by a cut-off parameter $\Lambda_{\pm}$. This changes the Born cross section by an additional term:

$$\frac{\mathrm{d}\sigma}{\mathrm{d}\Omega} = \frac{\alpha^2}{s} \frac{1+\cos^2\theta}{1-\cos^2\theta} \pm \frac{\alpha^2 \pi s}{\Lambda_{\pm}^4}(1+\cos^2\theta) \,. \tag{4.3}$$

Other potential deviations from the QED prediction are described in terms of contact interactions, which introduce an additional constant term to the differential cross section. The exchange of an excited electron, e^*, even with a mass, m_{e^*}, higher than the centre-of-mass energy, would change the differential cross section of the process $\mathrm{e}^+\mathrm{e}^- \to \gamma\gamma(\gamma)$. A precise measurement of the differential cross section therefore allows to set limits on m_{e^*}.

The analyses [11] of the process $\mathrm{e}^+\mathrm{e}^- \to \gamma\gamma(\gamma)$ require at least two high-energy depositions in the electromagnetic calorimeter with no track associated to them. Due to the identical signature in the calorimeters and the much higher cross section Bhabha scattering is a severe background source for multi-photon production. Only the tracking chamber information is able to discriminate between an electron and a photon. Therefore, the tracking system must be highly efficient during the data taking period to assure the rejection of Bhabha events. A lot of effort has been invested in the study of tracking efficiencies, e.g. by using hadronic final states with high charged multiplicity. Another signature of Bhabha events is the curvature of the electrons in the magnetic field of the detector. In non-radiative events this curvature is detectable as a small angular deviation from the back-to-back configuration and in turn allows the determination of the Bhabha background independent of the Monte Carlo simulation.

Another source of systematic deviations between data and Monte Carlo simulation could be the prediction of the conversion rates in the detector

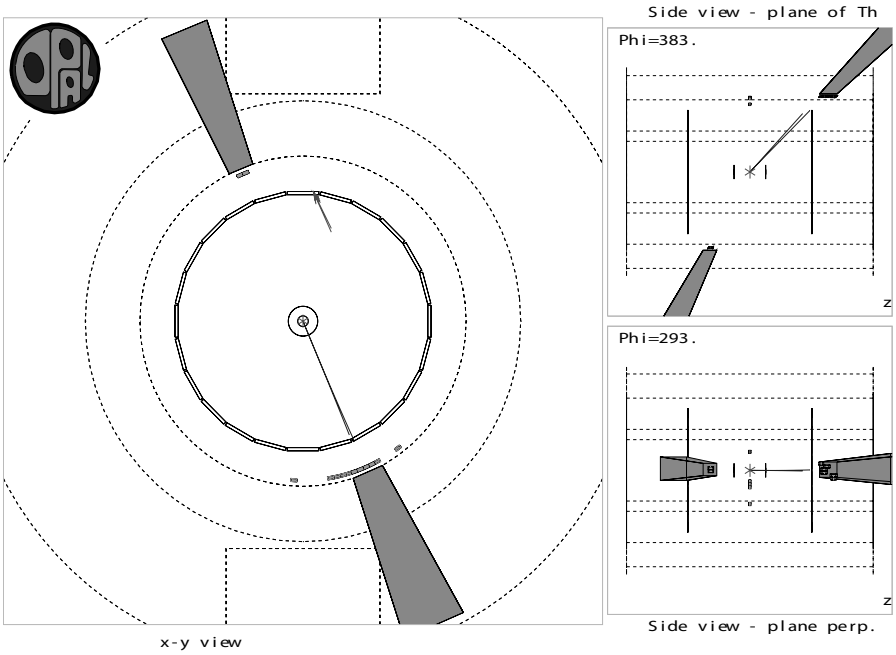

Fig. 4.17. OPAL event of the process $e^+e^- \to \gamma\gamma(\gamma)$. The two photons produce a high-energy cluster in the electromagnetic calorimeter. One of the photons has converted into a e^+e^- pair within the silicon vertex detector

parts in front of the electromagnetic calorimeter. The conversion probability predicted by the simulation strongly depends on the correct implementation of the amount of material in the tracker and especially in the vertex detector. On the other hand the conversion rate can be measured in data, either by reconstruction of two nearby tracks pointing to a secondary vertex or, in the case that the two tracks could not be resolved, by the measurement of $\mathrm{d}E/\mathrm{d}x$ in the tracker. In the latter case the e^+e^- pair, wrongly reconstructed as a single particle track, yields a $\mathrm{d}E/\mathrm{d}x$ measurement twice as large as expected from a single electron track.

The differential cross section of $e^+e^- \to \gamma\gamma(\gamma)$ as measured by the L3 collaboration is shown in Fig. 4.18. Excellent agreement with the prediction from QED is found. All LEP collaborations used this measurement to set exclusion limits on the previously discussed models. The fits on the measured differential cross section typically excludes $\Lambda_\pm$ values below 300 GeV and the energy scale of contact interactions is constrained above 800 GeV. Under the assumption that the excited electron exhibits an identical electromagnetic coupling strength as the normal electron, a lower limit of about 250 GeV can be set on its mass.

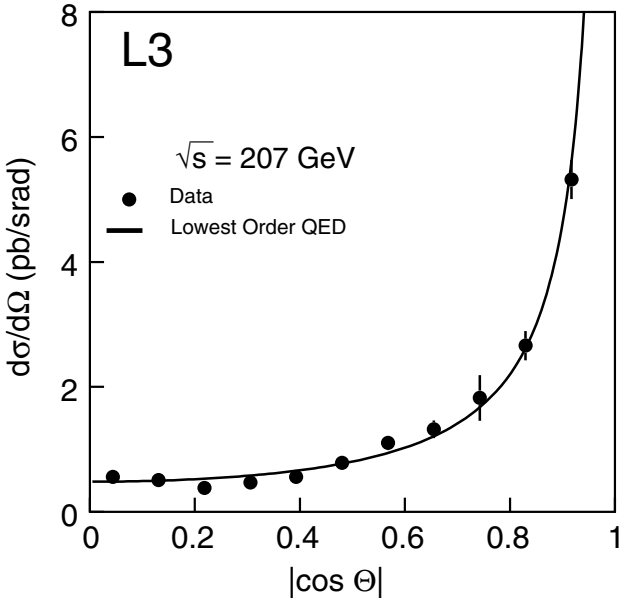

Fig. 4.18. Differential cross section of photon-pair production as measured by the L3 experiment

4.2.5 Z-pair Production

When the centre-of-mass energy of LEP was raised above the production threshold of twice the Z mass, the production of Z-boson pair events was made possible. In lowest order the process $e^+e^- \rightarrow ZZ$ is described by two Feynman diagrams which are depicted in Fig. 4.19. The Z bosons immediately decay into fermion-antifermion pairs, which leads to a large number of possible four-fermion final states. Many of these final states are also produced by other processes, for example the W-pair production. Kinematic cuts in the final state such as the requirement that each of the pairs of final-state fermions exhibits an invariant mass consistent with the Z mass enhance the contribution from the ZZ diagrams.

The study of Z-pair production offers a further test of the neutral current sector of the Standard Model. In Fig. 4.2 the total cross sections of W-pair and Z-pair production can be compared. The much smaller total cross section of Z-pair production with respect to W-pair production is mainly due to the smaller coupling of the electrons to the neutral current as compared to the charged current. Whereas in W-pair production triple gauge boson couplings are present, tree level vertices such as γZZ or ZZZ do not exist in the Standard Model. However, physics beyond the Standard Model could introduce such triple gauge couplings in the neutral boson sector and hence lead to deviations in the total and differential cross sections of Z-pair production.

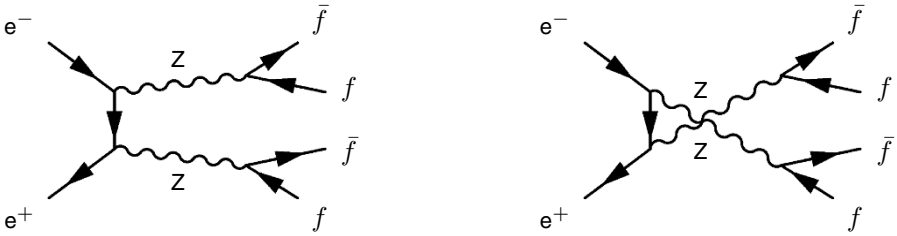

Fig. 4.19. The Feynman diagrams of Z-pair production

To select events of the process $e^+e^- \rightarrow ZZ$ individual selection procedures for the various final states were established. The methods vary between cut-based selections and the use of neural networks. Figure 4.20 shows a four-muon event recorded by the DELPHI detector as an example for a Z-pair final state. From the number of selected events the total cross section of the process $e^+e^- \rightarrow ZZ$ can be derived. The LEP result, based on a combination of the experiments [12], is presented in Fig. 4.21. The measurement shows good agreement with the Standard Model expectation.

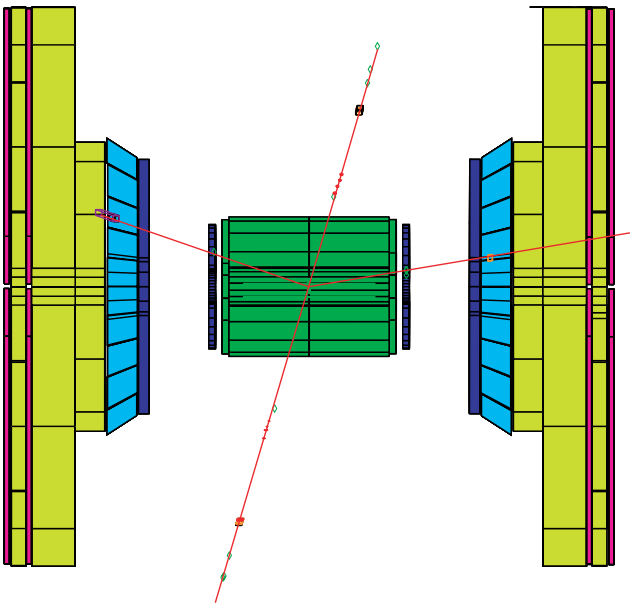

Fig. 4.20. Event of the reaction $e^+e^- \rightarrow ZZ \rightarrow \mu^+\mu^-\,\mu^+\mu^-$ recorded with the DELPHI detector

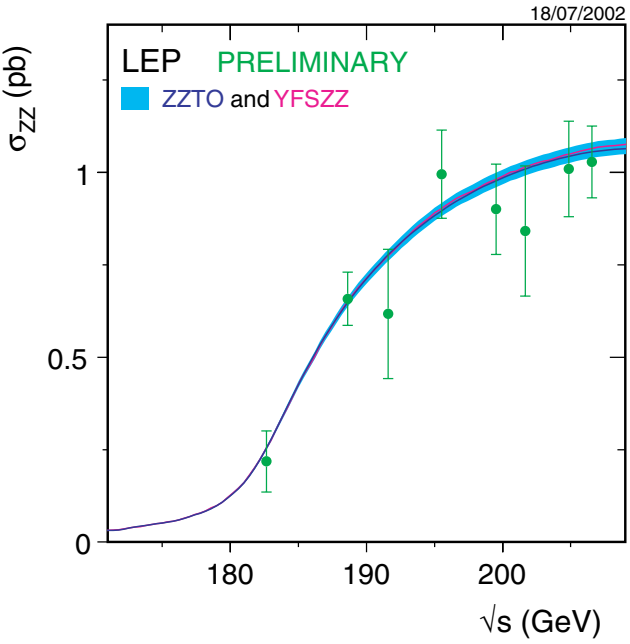

Fig. 4.21. Combination of cross section measurements of Z-pair production at LEP [5].

4.3 Measurement of Zγ Production

At centre-of-mass energies well above the Z peak, the process $e^+e^- \to f\bar{f}(\gamma)$ frequently occurs with hard initial-state radiation (ISR). The Feynman diagrams leading to these processes are depicted in Fig. 4.22. Due to the strong resonance in the reaction $e^+e^- \to Z \to f\bar{f}$, such an energy of the ISR photon is preferred that the invariant mass of the fermion pair recoiling against the photon is close to the mass of the Z boson, m_Z. The strong forward peaking of the ISR process yields photons which usually remain undetected in the beam pipe but in a small fraction of events they are detected. These final states containing a fermion-antifermion pair and a photon can also be interpreted to result from the $e^+e^- \to Z\gamma$ process, where the Z boson decays into $f\bar{f}$.

These processes occur in different phase spaces. If the t-channel electron in Fig. 4.22 is highly virtual this reaction is denominated as "Zγ production", if this electron is quasi-real the reaction is called "return to the Z". The cross section for the latter is much larger due to the virtual electron propagator.

4.3.1 Neutrino-Pair Production in Zγ Events

Neutrinos escape detection due to their extremely small interaction probability with the detector material. Nevertheless, neutrino-pair events can be

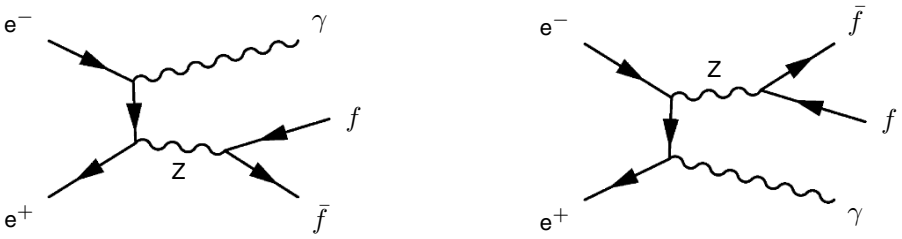

Fig. 4.22. Feynman diagrams of the process $e^+e^- \to Z\gamma$, which can also be seen as fermion-pair production with initial-state radiation

detected, if they make themselves visible by photon radiation inside the detector acceptance. Clearly, these photons can only be radiated from the initial state and at centre-of-mass energies above the Z resonance the photon spectrum is again dominated by the effect of the radiative Z return.

The selection of events with only one photon and nothing else in the detector [13] requires a perfect understanding of the electromagnetic calorimeter, a precise determination of the trigger efficiency and a reliable estimation of the photon conversion probability in the inner detector. The main backgrounds are radiative Bhabha scattering, $e^+e^- \to e^+e^-(\gamma)$, and multi-photon production, $e^+e^- \to \gamma\gamma(\gamma)$. The events are used to study the process of radiative return to the Z for the neutrino final state. In addition to the process of $Z\gamma$ production also W-boson exchange in the t-channel is possible for the process, $e^+e^- \to \nu\bar{\nu}(\gamma)$. The additional Feynman diagrams are depicted in Fig. 4.23.

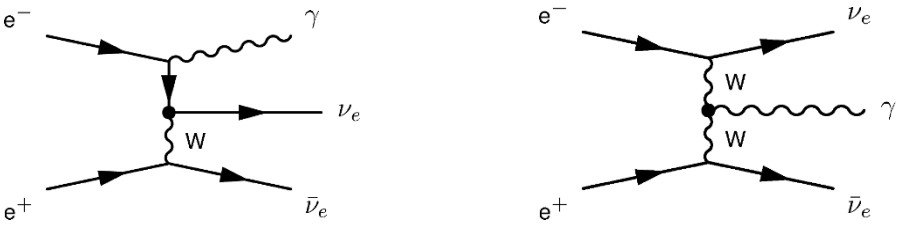

Fig. 4.23. Additional Feynman diagrams that contribute to the process of radiative neutrino-pair production, $e^+e^- \to \nu\bar{\nu}\gamma$

The L3 collaboration selected 1898 single-photon events within 619 pb^{-1} of data at $\sqrt{s} = 189 - 209$ GeV. Detection efficiencies of more than 80 % for the available phase space with a purity of better than 99% were reached. All LEP experiments have analysed the recoil-mass spectra of the single-photon events [13]. Figure 4.24 shows the ALEPH measurement. The peak at recoil masses of about m_Z is due to events, where the photon energy matches the production of an on-shell Z boson, which then decays into a $\nu\bar{\nu}$ pair. The number of light neutrino species, N_ν, can be determined with this experiment. In

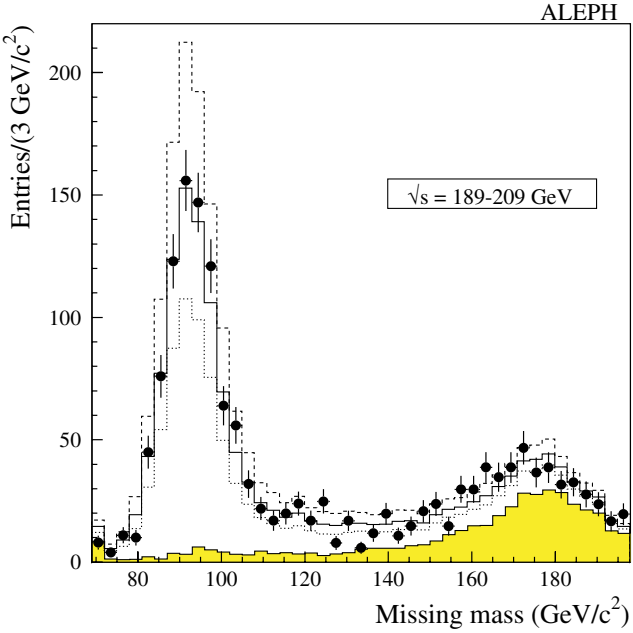

Fig. 4.24. Recoil-mass spectrum from events with one single, highly energetic, photon in the final state as measured by the ALEPH collaboration. Shown are the data, the predictions from the Z-return diagram (*white histogram*) and from the t-channel W exchange (*shaded histogram*). The expectations for $N_\nu = 2$ (*dotted line*) and $N_\nu = 4$ (*dashed line*) are also given

Fig. 4.24 the measured spectrum is compared to the Standard Model prediction including the Z return and the t-channel exchange of a W boson. Additionally, expectations for $N_\nu = 3$ and 4 are shown. Releasing N_ν as a free parameter and fitting the expected spectrum to the data yields

$$N_\nu = 2.86 \pm 0.09 \,, \tag{4.4}$$

which is consistent with 3 and also with the more precise result from the determination of $\Gamma_{\rm inv}$ in the lineshape measurement, presented in Chap. 3.

4.3.2 Reconstruction of the Z Resonance with Zγ Events

Data recorded with the four LEP detectors at $\sqrt{s} > m_{\rm Z}$ are used to extract the mass of the Z boson, using Z decays into quarks or pairs of charged leptons [14]. In all analyses a three particle final state produced by the reaction $\mathrm{e^+e^-} \to f\bar{f}\gamma$ is assumed. The typical kinematic configuration of such events with the photon escaping along the beam-line is shown in Fig. 4.25. Figure 4.26 shows an event of the radiative return to the Z with a hadronic final state as recorded by the L3 experiment.

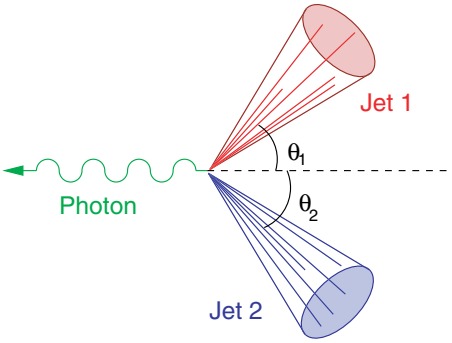

Fig. 4.25. Typical kinematic configuration of the radiative return to the Z. The initial-state photon is radiated in direction of the beam-line, the jets from the Z decay are boosted in the opposite direction

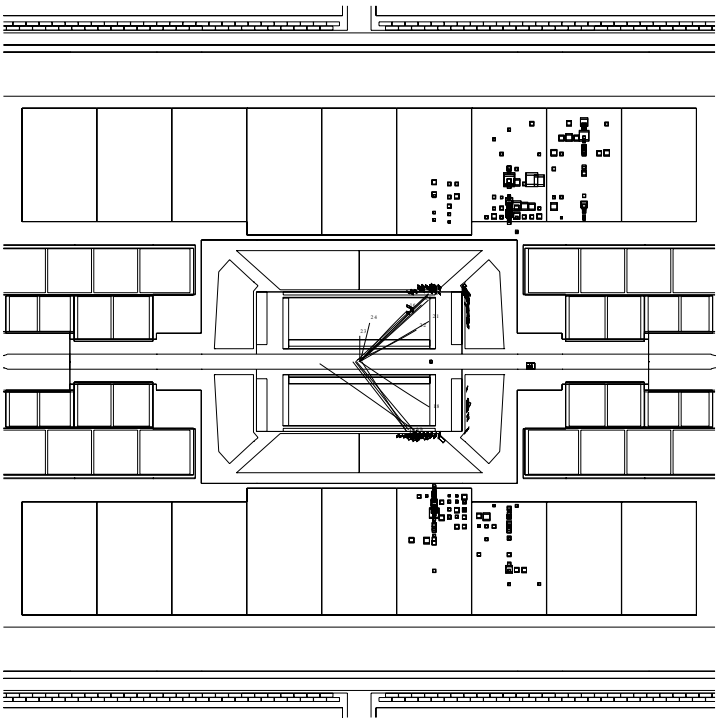

Fig. 4.26. Z-return event with hadronic final state as recorded by the L3 detector

In the case of lepton pairs the event kinematics and therefore the photon energy, E_γ, is fully determined by the measurement of the angles between the lepton directions and the photon, θ_1 and θ_2. If no photon is found in the detector the angles between the fermions and the beam direction are used

assuming a single, undetected, collinear ISR photon. From the reconstructed photon energy, E_γ, and therefore from θ_1 and θ_2 the effective centre-of-mass energy of the fermion pair, $\sqrt{s'}$, can be calculated as

$$\sqrt{s'} = \sqrt{s}\,\frac{\sin\theta_1 + \sin\theta_2 - |\sin(\theta_1+\theta_2)|}{\sin\theta_1 + \sin\theta_2 + |\sin(\theta_1+\theta_2)|}\,. \tag{4.5}$$

In the case of hadronic final states the mass of the hadronic system after applying a kinematic fit, m_{inv}, is directly related to m_{Z}. The distributions of m_{inv} or $\sqrt{s'}$ are used to extract the Z mass. The result is then compared with the precision measurement, derived from the Z-lineshape scan at centre-of-mass energies around the Z pole. This comparison serves as a cross check of the W-mass measurement which uses similar techniques or alternatively provides a measurement of the LEP centre-of-mass energy to be compared with the value determined by the LEP energy working group [15].

The LEP experiments concentrate in their Z-return analysis on the $\mathrm{e^+e^-} \to q\bar{q}\gamma$ and $\mathrm{e^+e^-} \to \mu^+\mu^-\gamma$ processes. The first process offers an event sample with high statistics and the latter one contains the events with the best $\sqrt{s'}$ resolution. The OPAL experiment additionally exploits the $\mathrm{e^+e^-}\gamma$ and the $\tau^+\tau^-\gamma$ final states.

Whereas the other LEP experiments use slightly modified versions of their standard fermion-pair selection, only L3 has developed an independent event selection, which is tuned to select the Z return with high efficiency and low background. In the selection of hadronic events longitudinal energy imbalance (along the beam axis) of less then 80% of $\sqrt{s}$ and total transverse energy (perpendicular to the beam) of more then 15% of $\sqrt{s}$ is required. Hadronic final states from two-photon collisions are typically boosted along the beam and effectively removed by these cuts. Four-jet events from W-pair and Z-pair production exhibit a more spherical event shape than two-jet events from the $\mathrm{e^+e^-} \to \mathrm{Z}\gamma$ process. Therefore the events with large hadronic energy are boosted to the rest frame of the hadronic system and a cut on the thrust, T, of the boosted event of $T > 0.85$ is applied. Z-return events of the $\mathrm{e^+e^-} \to \mu^+\mu^-\gamma$ final state are selected by the criterion that the two muons are back-to-back in the plane perpendicular to the emitted photon. In addition the measured momentum, p_μ, of the muon which has the largest polar angle, θ_1, has to exceed 60% of the the momentum as expected from the reconstructed muon angles:

$$p_\mu^{\mathrm{exp}} = \sqrt{s}\,\frac{\sin\theta_2}{\sin\theta_1 + \sin\theta_2 + |\sin(\theta_1+\theta_2)|}\,. \tag{4.6}$$

The cut on the thrust for the hadronic selection and on the momentum measurement in the muon-pair selection are shown in Fig. 4.27.

4.3.3 Extraction of the Z Mass from the Mass Spectrum

The analyses of the Z return of the LEP experiments follow a similar procedure: First, in each selected event an isolated high-energy photon is searched

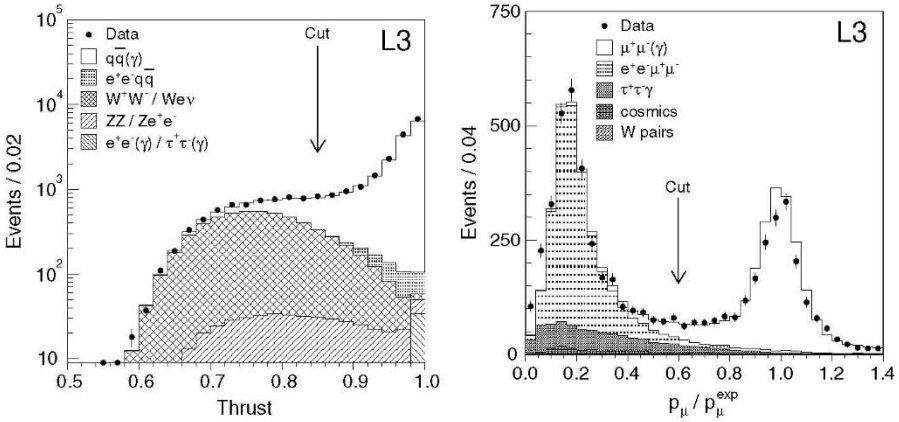

Fig. 4.27. Selection of the Z-return process in the L3 analysis. Thrust in the centre-of-mass frame of the jets (*left*) and measured muon momentum normalised to the expected one (*right*)

for. If none is found, a photon escaping along the beam direction is assumed. Hadronic events are then forced into two jets using for example the Durham algorithm, but excluding the photon candidate. Then either a kinematic fit is applied to the three particle final state by imposing four-momentum conservation to the event or the angles of the reconstructed jets are used in order to determine $\sqrt{s'}$ according to Equation 4.5. In the case of lepton final states always the angular method is used. The distributions of the mass spectra as reconstructed from the OPAL data are shown in Fig. 4.28.

The reconstructed Z-boson resonance in these distributions is described in different ways. OPAL and DELPHI are using an empirical analytic function constituting modifications of a Breit-Wigner function. A theoretical calculation of the differential cross section $\mathrm{d}\sigma/\mathrm{d}\sqrt{s'}$ is used in the cases of ALEPH and L3.

In the OPAL analysis the empirical function is directly fitted to the observed $\sqrt{s'}$ spectrum in data. Corrections due to photon radiation, hadronisation and detector resolution are determined by applying the same fit to a fully-simulated Monte-Carlo sample and comparing the result with the input value of m_{Z}. ALEPH, DELPHI and L3 re-weight fully simulated Monte-Carlo events in order to describe the measured mass spectra. The re-weighting method is explained in more detail within the W mass analysis (see Sect. 6.4). Whereas ALEPH and DELPHI directly fit the mass distribution of the Monte-Carlo to the data spectrum using a binned likelihood fit, the L3 analysis performs an unbinned likelihood fit, where the probability of each data event is calculated by averaging Monte-Carlo events inside a bin centred around the $\sqrt{s'}$ value of the given event. This method takes both detector resolution and selection efficiency automatically into account. Details of this "box method" are also presented in Sect. 6.4.

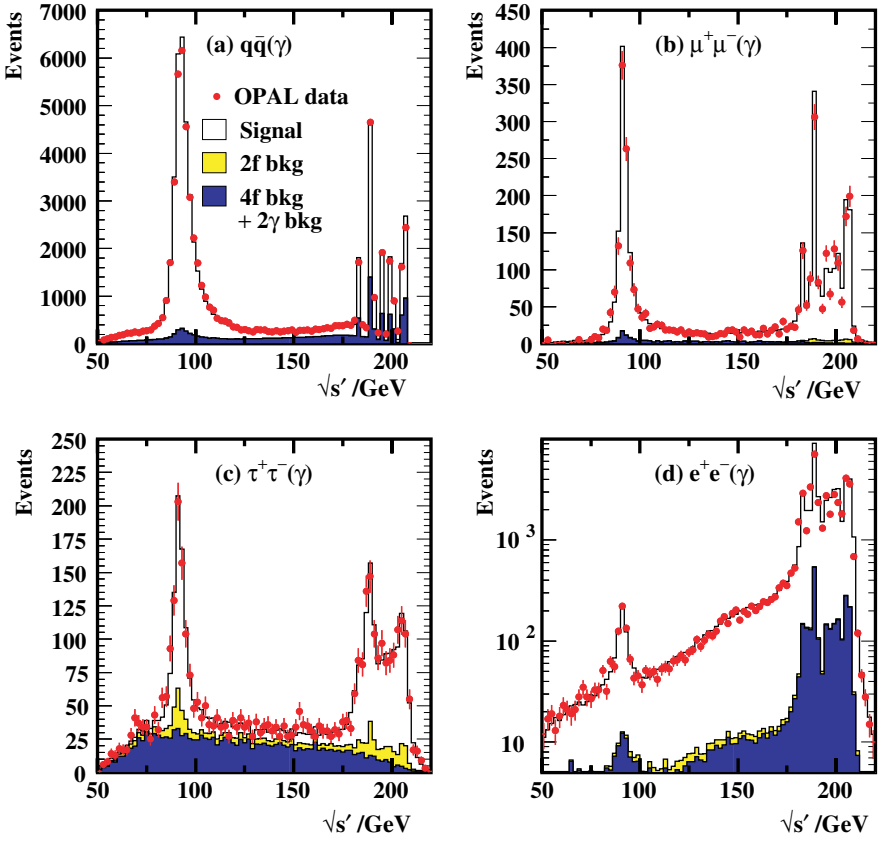

Fig. 4.28. Distribution of the reconstructed masses as measured by OPAL for the four different final states of fermion-pair production

Systematic uncertainties arise from modelling of photon radiation, hadronisation and detector effects. Extracting m_Z from the measured $\sqrt{s'}$ spectrum involves the centre-of-mass energy, $\sqrt{s}$, and therefore the accuracy of the LEP beam energy measurement.

The L3 collaboration used the Z-return events from the data recorded at $\sqrt{s} = 183 - 209$ GeV to measure the mass of the Z boson. They obtained

$$m_Z^{qq} = 91.271 \pm 0.031 \text{ (stat.)} \pm 0.039 \text{ (syst.) GeV} \tag{4.7}$$

for hadronic events and

$$m_Z^{\mu\mu} = 91.276 \pm 0.105 \text{ (stat.)} \pm 0.021 \text{ (syst.) GeV} \tag{4.8}$$

for muon-pair events. Averaging the results obtained from the hadronic and muon pair samples, including all correlations, yields

$$m_{\mathrm{Z}}^{f\bar{f}} = 91.272 \pm 0.046 \text{ GeV} . \tag{4.9}$$

This value is in agreement with the precision mass measurement of L3 obtained at the Z resonance, $m_{\mathrm{Z}} = 91.1898 \pm 0.0031\text{GeV}$.

4.3.4 Cross Check of the LEP Energy Calibration

The measurement can also be interpreted as a determination of the LEP centre-of-mass energy, $\sqrt{s}$. A difference between the measured mass, $m_{\mathrm{Z}}^{f\bar{f}}$, and the precision mass from the Z lineshape, m_{Z}, can be attributed to a deviation from the nominal centre-of-mass energy, $\sqrt{s}_{\mathrm{LEP}}$, given by the LEP energy group:

$$\Delta\sqrt{s} = \sqrt{s} - \sqrt{s}_{\mathrm{LEP}} = \sqrt{s}\,\frac{m_{\mathrm{Z}} - m_{\mathrm{Z}}^{f\bar{f}}}{m_{\mathrm{Z}}}. \tag{4.10}$$

When the measurements are interpreted as a determination of the mean centre-of-mass energy the systematic uncertainty on m_{Z} coming from the LEP energy error is separated off. Table 4.1 lists the average shifts of $\sqrt{s}$ with respect to the LEP energy calibration as determined by the four LEP experiments using Z-return events of the hadronic and the leptonic final states, respectively. These results are also summarised in Fig. 4.29 and show good agreement between the four experiments.

Table 4.1. Difference between the $\sqrt{s}$ value measured by the Z-return analyses of the four experiments and the value coming from the LEP beam energy calibration

	$\Delta\sqrt{s}$ [MeV]	
Experiment	$q\bar{q}$	$\ell^+\ell^-$
ALEPH	-86 ± 133	-334 ± 205
DELPHI	-116 ± 166	$+242 \pm 157$
L3	-173 ± 105	-185 ± 229
OPAL	$+2 \pm 110$	-4 ± 133

All LEP measurements are combined including the correlations between the systematic uncertainties. This yields as difference between the $\sqrt{s}$ measurement using the Z-return process and the nominal energy calibration using beam parameters:

$$\Delta\sqrt{s} = -54 \pm 40 \text{ (stat.)} \pm 36 \text{ (syst.) MeV} . \tag{4.11}$$

In conclusion, the Z mass measured in Z-return events is consistent with the determination on the Z resonance, validating the method used for the measurement of the mass of the W boson. Interpreted as a determination of the centre-of-mass energy it agrees with the energy calibration performed by the LEP energy working group [15].

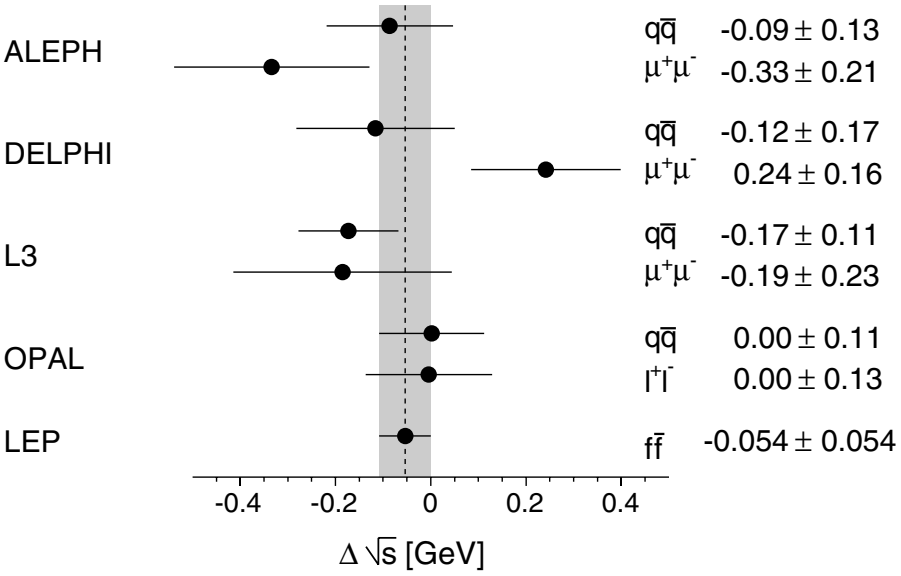

Fig. 4.29. Difference between the $\sqrt{s}$ value measured by the Z-return analyses of the four experiments and the value coming from the LEP beam energy calibration

References

1. S. Jadach et al., Comp. Phys. Comm. **153**, 462 (2003)
2. S. Jadach, W. Placzek and B.F.L. Ward, Phys. Lett. **B 390**, 298 (1997)
3. ALEPH Collaboration, Conference note ALEPH 2002-032;
   DELPHI Collaboration, J. Abdallah et al., Eur. Phys. J. **C 45**, 589 (2006);
   L3 Collaboration, P. Achard et al., Eur. Phys. J. **C 47**, 1 (2006);
   OPAL Collaboration, G. Abbiendi et al., Eur. Phys. J. **C 33**, 173 (2004)
4. D. Karlen, Nucl. Phys. **B 289**, 23 (1987)
5. LEP Electroweak Working Group, Eprint hep-ex/0511027 and
   `http://lepewwg.web.cern.ch/LEPEWWG/`
6. L3 Collaboration, P. Achard et al., Phys. Lett. **B 616**, 145 (2005)
7. ALEPH Collaboration, S. Schael et al., Phys. Lett. **B 605**, 49 (2005);
   DELPHI Collaboration, P. Abreu et al., Phys. Lett. **B 515**, 238 (2001);
   L3 Collaboration, P. Achard et al., Phys. Lett. **B 561**, 73 (2003);
   OPAL Collaboration, G. Abbiendi et al., Eur. Phys. J. **C 24**, 1 (2002)
8. ALEPH Collaboration, S. Schael et al., Phys. Lett. **B 605**, 49 (2005);
   DELPHI Collaboration, J. Abdallah et al., Eur. Phys. J. **C 45**, 273 (2006);
   L3 Collaboration, P. Achard et al., Phys. Lett. **B 547**, 151 (2002)
9. E. Accomando, A. Ballestrero and E. Maina, Comp. Phys. Comm. **150**, 166 (2003)
10. J. Fujimoto at al., Comp. Phys. Comm. **100**, 128 (1997)
11. ALEPH Collaboration, A. Heister et al., Eur. Phys. J. **C 28**, 1 (2003);
    DELPHI Collaboration, J. Abdallah et al., Eur. Phys. J. **C 37**, 405 (2004);

L3 Collaboration, P. Achard et al., Phys. Lett. **B 531**, 28 (2002);
OPAL Collaboration, G. Abbiendi et al., Eur. Phys. J. **C 26**, 331 (2003)
12. DELPHI Collaboration, J. Abdallah et al., Eur. Phys. J. **C 30**, 447 (2003);
L3 Collaboration, P. Achard et al., Phys. Lett. **B 572**, 133 (2003);
OPAL Collaboration, G. Abbiendi et al., Eur. Phys. J. **C 32**, 303 (2003)
13. DELPHI Collaboration, J. Abdallah et al., Eur. Phys. J. **C 38**, 395 (2005);
L3 Collaboration, P. Achard et al., Phys. Lett. **B 587**, 16 (2004);
OPAL Collaboration, G. Abbiendi et al., Phys. Lett. **B 602**, 167 (2004)
14. ALEPH Collaboration, R. Barate et al., Phys. Lett. **B 464**, 339 (1999) and Preprint CERN-PH-EP/2006-004;
DELPHI Collaboration, J. Abdallah et al., Eur. Phys. J. **C 46**, 295 (2006);
L3 Collaboration, P. Achard et al., Phys. Lett. **B 585**, 42 (2004);
OPAL Collaboration, G. Abbiendi et al., Phys. Lett. **B 604**, 31 (2004)
15. LEP Energy Working Group, R. Assmann et al., Eur. Phys. J. **C 39**, 253 (2005)

5

W-Boson Pair Production

In e^+e^- collisions, W bosons can be produced singly or in pairs. At LEP 2 energies above the kinematic threshold of W-pair production the $e^+e^- \to W^+W^-$ cross section is higher than that of single-W production, $e^+e^- \to W^+\nu_e$ or $e^+e^- \to W^-\bar{\nu}_e$. Figure 5.1 shows the lowest order Feynman diagrams of W-pair production. These diagrams are known as CC03 diagrams, as the three diagrams describe charged-current interactions. W-boson pairs are produced via the t-channel neutrino exchange and the γ and Z exchange in the s-channel. The non-Abelian gauge structure of the Standard Model appears here at lowest order in the γWW and the ZWW vertices. Subsequently, the W bosons decay either into a quark-antiquark pair, $W^- \to \bar{u}d$ or $\bar{c}s$, or a lepton-antilepton pair, $W^- \to e^-\bar{\nu}_e$, $\mu^-\bar{\nu}_\mu$ or $\tau^-\bar{\nu}_\tau$. The final state consists of four fermions and the events can be classified into three groups, the fully-hadronic events with four quarks, $qqqq$, the semi-leptonic events with one hadronically and one leptonically decaying W, $qq\ell\nu$, and the purely-leptonic events, $\ell\nu\ell\nu$. One example for each of these three event categories is shown in Fig. 5.2.

The results presented in this chapter are obtained from e^+e^- collisions recorded at centre-of-mass energies, 161 GeV $< \sqrt{s} <$ 206 GeV, during the operation of LEP in the years 1996–2000. Each of the four experiments collected

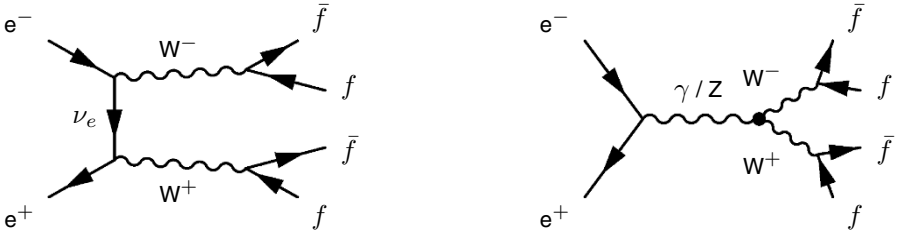

Fig. 5.1. Feynman diagrams of W-pair production on tree level: The t-channel exchange of a neutrino and the two s-channel processes via photon or Z-boson exchange. This set of diagrams is denoted as CC03

Stefan Roth: *Precision Electroweak Physics at Electron-Positron Colliders*
STMP **220**, 67–98 (2006)
DOI 10.1007/3-540-35165-5_5

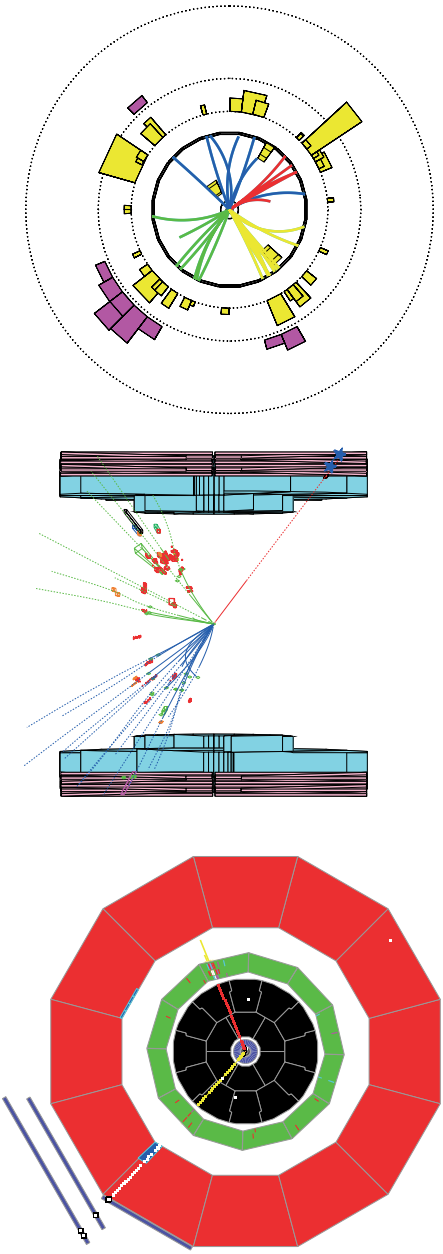

Fig. 5.2. W-pair events as recorded by the LEP detectors. The first one is an example of a fully-hadronic event with four jets in the final state, the second one an example of a semi-leptonic event with two jets and a charged lepton, and the third one is purely-leptonic with two charged leptons reconstructed

a total luminosity of about 0.7 fb^{-1}, where more than 40,000 W-pair events have been recorded by the four LEP experiments.

5.1 Simulation of Four-Fermion Production

The production of W pairs, the so-called double-resonant process, represents only one part of the Feynman diagrams leading to a given four-fermion final state. Also contributions from other charged-current (CC) and in addition from neutral-current (NC) diagrams exist. On Born-level, for example, ten different graphs contribute to the $qq\mu\nu$ final state. These diagrams, belonging to the CC10 set, are shown in Fig. 5.3. The effect of the singly-resonant or non-resonant diagrams are usually small, except where an electron appears in the final state. As pointed out previously for the single-W process, poles in the cross section appear for small scattering angles for one of the incoming electrons. Therefore, already 20 diagrams contribute to the $qqe\nu$ final state, where six of the additional diagrams are singly-resonant causing single-W production. The most complicated final state, $e\nu e\nu$, consists of 56 diagrams at tree level.

Including radiative corrections increases the number of diagrams which have to be considered even further. Including one additional photon to the four-fermion final states increases the number of diagrams to more than one thousand. For the $\mathcal{O}(\alpha)$ corrections more than about 10^4 loop diagrams have to be taken into account. To keep the calculation of this large amount of diagrams within a reasonable extent one in general has to resort to approximations.

As the W bosons are unstable particles a gauge-invariant treatment of finite-width effects becomes necessary. This is accomplished by a decomposition of the matrix element according to its mass poles [2]. The extracted terms are the basis for the calculation of gauge-invariant higher-order corrections. If corrections are calculated, only the leading terms in this expansion are considered and terms proportional to $\Gamma_\mathrm{W}/m_\mathrm{W}$ are neglected. Hence, in the case of W-pair production only terms containing double-pole residues are included. This scheme, called leading-pole approximation (LPA) or, more specifically, double-pole approximation (DPA) in the case of boson-pair production, is only applicable near the resonance of the unstable particle. Sufficiently far above the production threshold, the W bosons in W-pair production are produced resonantly, and the double-pole approximation is valid.

The W-pair production can be decomposed into several sub-processes, the production of the W-boson pair, the propagation of both W bosons and the subsequent decay of each W boson. In the framework of double-pole approximation one distinguishes between factorisable and non-factorisable corrections (see Fig. 5.4). The former are reducible to the two W-boson lines and the corrections are applied independently for production, propagation and decay of the W bosons. The latter ones include corrections where the production and decay processes are not independent. This is only possible via the exchange

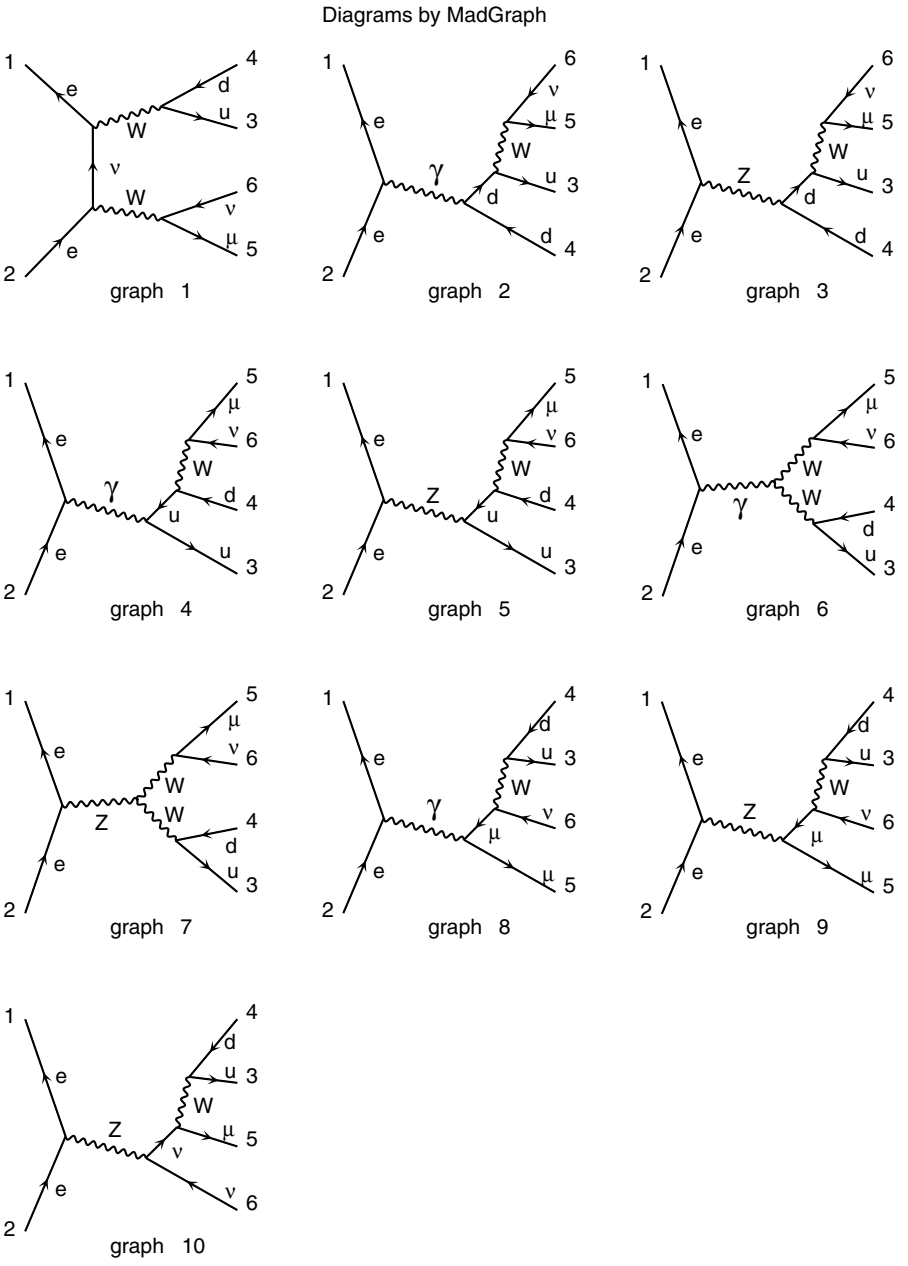

Fig. 5.3. Feynman diagrams for the $qq\mu\nu$ final state at lowest order as given by the program MadGraph [1]. Only the graphs 1, 6 and 7 proceed via W-pair production

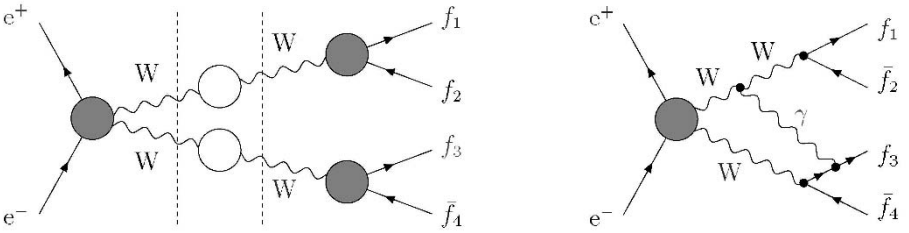

Fig. 5.4. Structure of the factorisable corrections to W-pair production (*left*) and example for non-factorisable corrections (*right*)

of soft photons with energies below $\mathcal{O}(\Gamma_{\mathrm{W}})$ for which the W-bosons are not brought off-resonance.

The corrections on inclusive variables, e.g. the total cross section, are small compared to the effect on distributions of variables, e.g. the invariant mass. In the case of the invariant-mass distribution the corrections additionally depend on the way this variable is calculated. In contrary to the case of the line-shape scan of the Z resonance this time also final-state radiation can cause distortions of the measured W resonance [3]. Photon radiation from the final state fermions of W decays, $\mathrm{W} \to f\bar{f}$, introduces a dependence of the invariant mass of the $f\bar{f}$ pair on the photon energy. Alternatively, if the invariant mass of the $f\bar{f}\gamma$ is reconstructed, the W line-shape is not changed. However, in data it is in general unknown whether the photon is radiated in the initial state, from the W bosons or from the final-state fermions. Therefore, in practice one relies on Monte Carlo simulations. Several Monte-Carlo programs have been used by the LEP community for modelling the events of W-pair production.

The KoralW [4] generator simulates four-fermion production implementing the complete set of Feynman diagrams in lowest order, calculated with the Grace [5] package. KoralW simulates photon radiation up to $\mathcal{O}(\alpha^3)$ in the initial state and uses the Photos [6] package to model radiation off the final-state fermions. Interference between ISR and FSR diagrams is not implemented. Full $\mathcal{O}(\alpha)$ corrections have been calculated using the method of pole expansion described above. The programs KandY and RacoonWW are based on such calculations.

The KandY [7] program combines the YFSWW [8] generator, which simulates the W-pair production with $\mathcal{O}(\alpha)$ corrections using the leading-pole approximation [9], and the KoralW generator, which contributes the other non-resonant four-fermion diagrams in lowest order. KandY models the ISR using the Yennie-Frautschi-Suura (YFS) exponentiation scheme [10], while FSR is simulated by the program Photos in the case of charged leptons and by Pythia in the case of quarks. Interference between ISR and FSR is neglected.

The RacoonWW [11] program implements the $\mathcal{O}(\alpha)$ corrections in the double-pole approximation [12] with a precision similar to that of YFSWW. It contains the full $\mathcal{O}(\alpha)$ matrix element of the radiative four-fermion production,

$e^+e^- \to ffff\gamma$. Higher order ISR corrections coming from the radiation of multiple photons in the initial state are implemented using a structure function ansatz, with a cut-off on the minimum photon energy of about 100 MeV. In contrast to KandY, the calculations implemented in RacoonWW are based on massless fermions. The fermion masses are added after the generation of the four-fermion final state keeping the total four-momentum and the W masses. Using massless fermions prevents the simulation of photons radiated collinear to the fermion and a cut-off on the minimum photon-fermion angle is implemented in RacoonWW.

5.2 Hadronisation Models

The generator programs just presented give parton level final states. The programs Pythia [13], Ariadne [14] and Herwig [15] are then used to simulate the hadronisation process, the transition from quarks to hadronic jets. Special hadronisation parameters have to be given as external input for all three of them. These parameters are determined in a detailed event-shape studies of large Z-decay samples recorded on the Z resonance and enriched by light-flavour (u,d,s,c) final states. Results for mass and width of the W boson presented in the following are usually based on the Pythia model.

The hadronisation in the Pythia Monte Carlo generator is based on the program Jetset, which has been widely used for QCD studies at LEP 1. The philosophy of Pythia is to use exact matrix elements for the lowest-order cross sections only and to generate higher-order corrections in the parton shower approach. The parton shower ansatz is based on the radiation of gluons from quarks and the consequent splitting of these gluons into quark-antiquark or gluon pairs. Each parton in the shower is characterised by its virtuality Q^2. The virtuality provides a time ordering in the shower and is gradually decreasing. Shower evolution is cut off at a scale Q_0, typically around 1 GeV. The first gluon branching of the parton shower is modified using the first order matrix element to improve the predicted rates of hard and non-collinear gluon radiation. The non-perturbative part of the QCD shower evolution follows the string fragmentation model [16], which was introduced by Artru and Menessier [17]. Considering the production of a back-to-back moving $q\bar{q}$ pair, a colour flux tube will evolve stretched between the q and the $\bar{q}$, the so called string. This is a result of linear confinement at large distances as predicted by QCD. The transverse dimension of the strings is of the typical hadron size, roughly 1 fm, and contains an energy density of about 1 GeV/fm. As the q and the $\bar{q}$ move apart, the potential energy stored in the string increases and the string breaks, producing a new quark-antiquark pair. Several break-ups of the string will follow until only on-mass-shell hadrons remain, each hadron corresponding to a small piece of the string.

The Ariadne program implements the Dipole Cascade Model (DCM) for the simulation of the parton shower [18]. In this model quark-antiquark pairs

form coloured dipoles which serve as sources of gluon emission. After the creation of a gluon the colour flow from quark to antiquark is intermitted and two new dipoles are formed at the gluon-quark and the gluon-antiquark interconnection. The first gluon is emitted using the correct first order matrix element. Further gluon emission incorporates angular ordering as in conventional parton showers. As a result, a chain of dipoles is created where one dipole connects two partons and a gluon connects two dipoles. As the basic DCM model only describes gluon emission, the gluon splitting into a quark-antiquark pair is added according to Reference [19]. Ariadne itself only handles the perturbative part of the hadronisation process. Therefore it is interfaced to the Pythia program to simulate the non-perturbative part of the hadron shower and the particle decays.

The generator Herwig (Hadron Emission Reactions With Interfering Gluons) is a multipurpose Monte Carlo generator, which can be used completely independently of the Pythia package. It uses sophisticated parton shower algorithms to provide a description of the perturbative QCD jet evolution. Coherence effects, correct angular ordering and the azimuthal distribution for soft gluons are taken into account. Due to the choice of evolution parameters, events with hard gluon emission are not generated in the parton shower process. This problem is solved by integrating the correct three parton matrix element and adding the missing events later on. The non-perturbative part is simulated by the cluster hadronisation model described in Reference [20]. At the end of the shower evolution remaining gluons are split into $q\bar{q}$ pairs. The quark from one splitting and the antiquark from an adjacent one are combined into a colourless cluster. The available phase space is then the main criterion for the choice of flavour and spin of the primarily produced hadron. The primary hadrons subsequently decay into the final hadrons visible in the detector.

5.3 Colour Reconnection in the *qqqq* Channel

In the fully-hadronic final state of W-pair production both W bosons decay into a quark-antiquark pair, each of the pairs forming a colour singlet. If cross-talk between the partons from different W decays is neglected both singlets hadronise independently. The partons first undergo the perturbative phase, where additional partons are radiated, and then the non-perturbative phase, where the partons fragment into hadrons. The spatial extension of the hadronisation process is given by the range of the strong interaction of about 1 fm. This is about one order of magnitude larger than the mean decay length of the W boson. Therefore, the hadronisation of both colour singlets exhibits a significant space-time overlap. Due to this overlap the W bosons may not hadronise independently, i.e. a re-arrangement of the colour flow is possible. This effect is called colour reconnection.

The consequences of re-arranged colour dipoles was first studied by Gustafson, Petterson and Zerwas (GPZ) [21]. In their model the dipole mass sets the scale for the amount of gluon radiation during the hadronisation process. An immediate colour re-arrangement after the W decay would change the invariant mass of the quark dipoles from the W mass to a smaller mass. This would cause large changes in the event properties. However, it can be shown that the separation between the two W-decay vertices is large enough for the energetic gluon radiation to occur independently within each original dipole [22].

As a consequence of the SU(3) group structure of QCD, at least two gluons have to be exchanged to generate a colour re-arrangement. Moreover, only the interference term between both gluon emissions contributes to colour reconnection. The magnitude of the interference term is constrained by the relatively small width of the W boson. This can easily be understood by the following consideration: If the lifetime of the W boson was much shorter, $\Gamma_{\mathrm{W}} \to \infty$, both quark-antiquark pairs would be produced instantaneously and they would radiate coherently, because they show up at the same vertex. If the lifetime of the W was very long, $\Gamma_{\mathrm{W}} \to 0$, the two quark-antiquark pairs appear at very different space-time coordinates and the two colour dipoles would radiate gluons independently and produce hadrons according to the non-reconnection scenario. Therefore, gluon radiation at energy scales where the W width can be neglected will appear incoherently between the two colour dipoles. This is the reason why sizeable colour reconnection effects are only expected due to soft gluon emission in the non-perturbative phase of the QCD jet evolution.

The effect of colour reconnection in the non-perturbative phase can only be modelled within the available hadronisation models Pythia, Herwig and Ariadne. The SK models developed by Sjöstrand and Khoze [23] are based on the string fragmentation model implemented in Pythia. In the SK-I model strings are assumed to have a finite width of about 1 fm, the typical range of the strong interaction. Therefore the two strings originating from the two hadronically decaying W bosons can exhibit a non-vanishing space-time volume over which the two strings overlap. If this is large enough, the strings are reconnected at the point of largest space time overlap. After reconnection the colour flow starting from the quark of the W^+ boson is ending at the antiquark of the W^- boson and vice versa. In the SK-II model reconnections take place when the cores of two strings cross. The reconnection probability P_{reco} is a predicted quantity in the SK-II model, whereas in the SK-I model the reconnection probability is proportional to the space-time overlap multiplied by a free parameter k_I. For a k_I value of 0.6, the two models yield a similar reconnection rate at $\sqrt{s} = 170$ GeV, allowing a comparison between both models.

As stated before colour reconnection is only relevant for gluon energies smaller than Γ_{W}. Although the Ariadne program is limited to the non-perturbative part of the QCD jet evolution, also soft gluons are emitted

here. Therefore, colour reconnection has been studied for gluon energies below 2 GeV [24]. The Ariadne I branch simulates colour reconnection within one W boson, whereas Ariadne II additionally implements the inter-W colour reconnection. The effect of colour reconnection is then estimated from the comparison of Ariadne I and Ariadne II.

The Herwig program implements colour reconnection within the cluster fragmentation scheme. If colour reconnection is enabled, a colour reconnection code is called immediately after the parton showering has terminated and just before cluster formation. The parton shower produces quark-antiquark pairs connected by a continuous colour line. The reconnection code then tries, with a given probability, to re-arrange these quark-antiquark pairs such that they still form colour singlets, but their space-time separation is reduced. This reconnection is enabled not only within each shower, but also between the different showers, thus allowing partons from different W bosons to form a cluster.

Because the Pythia model serves as the baseline simulation for the W-mass analysis, colour reconnection effects have been studied extensively within this model. Especially the SK-I model by Sjöstrand and Khoze is very popular, because it allows a variation of the colour reconnection effect by means of the free parameter k_{I}. It is therefore desirable to get information on this free parameter by comparing the Monte-Carlo model with data.

Many observables have been studied to find an experimental signature of colour reconnection. Inclusive event variable, for example particle multiplicities, have not shown sufficient sensitivity to colour-reconnection effects. In analogy to the observation of the string effect [25] in 3-jet events, $\mathrm{e^+e^-} \to q\bar{q}g$, the particle flow between the four jets of fully-hadronic events is therefore studied to derive the colour flow between the individual jets. Detailed searches for colour reconnection in hadronic decays of W pairs were performed using the event particle flow method [26]. In the analysis, the four jets are grouped into the two pairs originating from the decay of a W boson and the particle flow in four different jet-jet regions are studied: two regions between jets with the same parent W boson (intra-W) and two in which the parents differ (inter-W). To analyse the particle flow in a one-dimensional distribution the particles are projected onto the jet-pair planes and the particle density is calculated as a function of the projected angle, ϕ, of the particle relative to one jet in the plane. To account for the variation in the jet-jet opening angles, ϕ_0, rescaled angles, $\phi_{\mathrm{resc}} = \phi/\phi_0$, are constructed for each event.

The particle flow of the fully-hadronic W-pair events, as measured with the L3 experiment, is shown in Fig. 5.5 versus the azimuthal angle, ϕ, with respect to the jet with highest energy. This angle is defined in the plane spanned by the most energetic jet and the jet with the largest opening angle to this jet. This maximises the probability that both jets belong to the same W boson. It exhibits the typical four-jet structure of these events. If colour reconnection between the jets of different W decays is present, the particle flow between

the jets would be changed. More particles are expected to be emitted between jets from different W bosons.

To quantify this effect, the particle flow in between jets coming from the same W (intra-W region) is divided by the particle flow in the regions between the W bosons (inter-W region). The result is given in Fig. 5.5. Here, the measured ratio as function of the rescaled angle, ϕ_{resc}, is compared to the predictions from Pythia without colour reconnection and prediction from the SK-I model. L3 and DELPHI are using a "topological selection" which selects events that are more planar than the events of the normal *qqqq* selection. ALEPH and OPAL use event selections which are based on their W-mass analyses. Whereas the first kind of analysis has an overall selection efficiency of only 15%, the latter selections have much higher efficiencies of up to 90%.

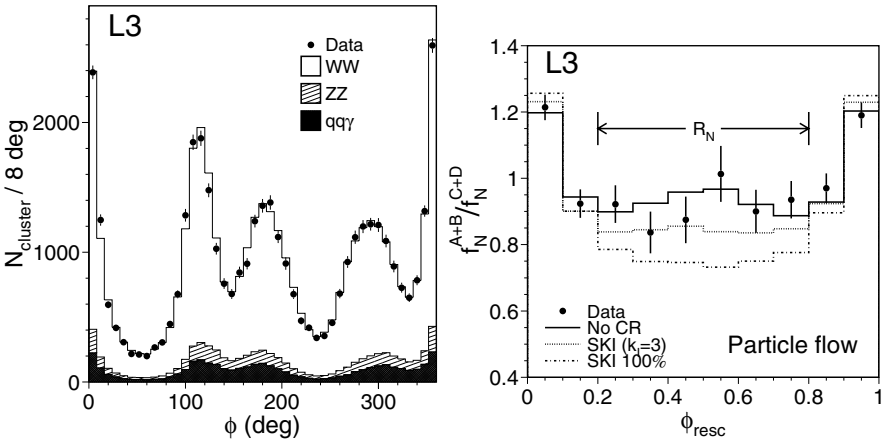

Fig. 5.5. Event particle flow for data and Monte-Carlo predictions (*left*) and ratio of particle distributions in the intra-W region to that in the inter-W region (*right*) measured by the L3 experiment

The differences between the models with and without colour reconnection are larger in the centre of the inter-jet regions. Therefore, in order to quantify the colour reconnection effects with a single number, the particle flows are integrated in the interval $0.2 < \phi_{\mathrm{resc}} < 0.8$ and the ratio R_{N} between the inter-W and the intra-W regions is computed. From the complete L3 data sample one obtains

$$R_{\mathrm{N}}(L3) = 0.915 \pm 0.023\ (\mathrm{stat.}) \pm 0.021\ (\mathrm{syst.})\ . \tag{5.1}$$

Figure 5.6 shows the measured R_{N} as a function of $\sqrt{s}$ together with the Pythia predictions with and without colour reconnection. The data indicate little or no colour reconnection.

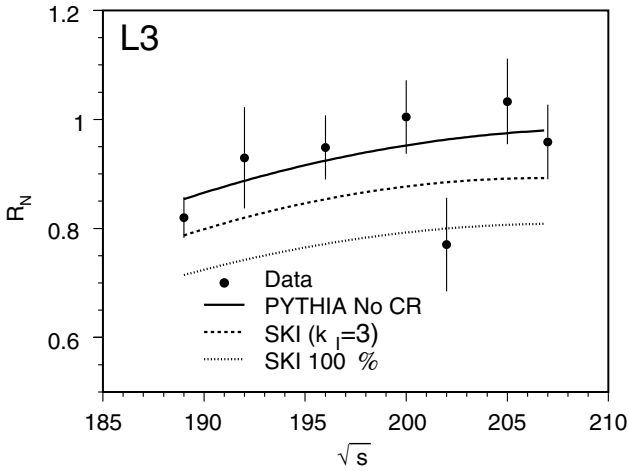

Fig. 5.6. The integrated ratio of the particle-flow distributions, R_{N}, between the intra-W and the inter-W regions as measured by the L3 experiment

To determine the dependence of R_{N} on the reconnection probability Monte-Carlo samples with different values of k_{I} are used. The dependence is parametrised as $R_{\mathrm{N}}(k_{\mathrm{I}}) = p_1(1-\exp(-p_2 k_{\mathrm{I}})) + p_3$ where the p_i are free parameters. A χ^2 fit to the L3 data yields a value of $k_{\mathrm{I}} = 0.08$ and is consistent with no colour reconnection effect within the statistical accuracy of the data. A constraint of $k_{\mathrm{I}} < 1.1$ is derived at the 68 % confidence level. The extreme SK-I scenario, in which colour reconnection occurs in essentially all events, is disfavoured by 4.9 σ. However, the colour reconnection models of Ariadne and Herwig show no significant effect on the particle flow.

To combine the results on R_{N} from the LEP experiments, they are translated to the reference centre-of-mass energy of 189 GeV and normalised to the Monte-Carlo prediction without colour reconnection. The variable r is defined as the ratio between the measurement of R_{N} in data and in the simulation without inter-W colour reconnection:

$$r = \frac{R_{\mathrm{N}}(\mathrm{data})}{R_{\mathrm{N}}(\mathrm{MC-noCR})} \,. \tag{5.2}$$

In absence of colour reconnection each experiment should find r equal to unity.

In Fig. 5.7 the results of the four analyses of the LEP experiments are compared to each other and to the prediction of the SK-I model with full colour reconnection. The average value r from a combination of the preliminary results of ALEPH, DELPHI and OPAL and the final L3 measurement yields [27]

$$r = 0.969 \pm 0.011\ (\mathrm{stat.}) \pm 0.009\ (\mathrm{syst.\ cor.}) \pm 0.006\ (\mathrm{syst.\ unc.})\,, \tag{5.3}$$

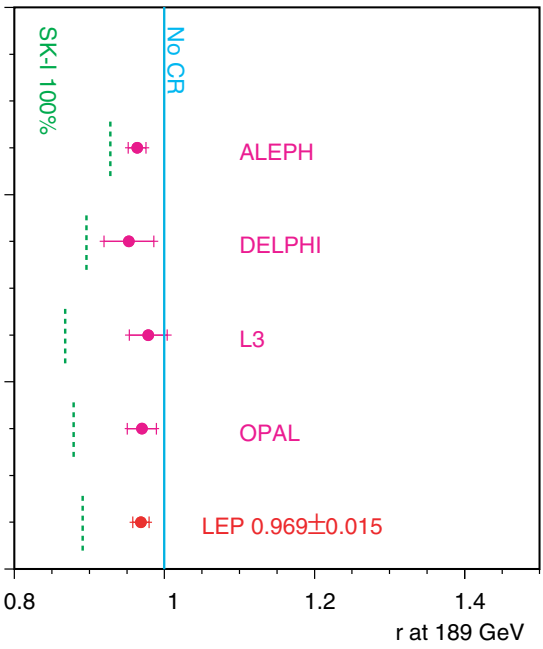

Fig. 5.7. Preliminary result on the combination of the particle flow results of the four LEP experiments. The error bars show the total error and the inner part indicates the statistical uncertainty. The predicted value of r for the SK-I model with full colour reconnection is shown for each experiment by the *dashed lines*

where one would expect $r = 0.891$ in the case of the SK-I model with 100% colour reconnection. The combined average slightly prefers a non-vanishing contribution from colour reconnection. This is mainly caused by the ALEPH result. An upper limit at 68% confidence level is set at $k_{\mathrm{I}} = 2.1$. The data disfavour the extreme version of the SK-I model with full colour reconnection by 5.2 standard deviations.

5.4 Bose-Einstein Correlations in the *qqqq* Channel

Bose-Einstein correlations are caused by interference effects between identical bosons which are close to each other in phase space. They are well known in particle physics and have been observed in hadronic interactions [28] as well as in $\mathrm{e^+e^-}$ annihilations [29]. Bose-Einstein correlations manifest themselves as an enhanced production of identical bosons (mostly pions) at small four-momentum difference, which has been measured in hadronic Z decays at LEP 1 [30]. Assuming a spherical and Gaussian shaped source emitting the bosons, the two-particle correlation function can be written as

$$C(Q) = 1 - \lambda \exp(-Q^2 R^2) \tag{5.4}$$

where Q is the distance between the two bosons in momentum space, R is the radius of the source and λ parametrises the correlation strength. The studies of Bose-Einstein effects in hadronic Z decays suggest $\lambda \approx 1$ and $R \approx 0.5$ fm.

According to the concept of factorisation in QCD and due to causality, the parton shower will not be influenced by the non-perturbative phase of hadronisation. Therefore, Bose-Einstein effects will only be active after the formation of final colourless hadrons and only minor influence on the event kinematics is expected. Bose-Einstein correlations within the two jets from a hadronically decaying W (intra-W BEC) are expected to take place in analogy to the observed correlations in Z decays. In fully-hadronic W-pair events the W-decay products overlap in space-time. Therefore, it is natural to expect also Bose-Einstein correlations between hadrons originating from different W bosons (inter-W BEC). These correlations could lead to momentum exchange between the two W decay systems and serve as a source of systematic bias in the mass analysis. The influence of Bose-Einstein correlations on the measured W mass at LEP was first investigated by Lönnblad and Sjöstrand [31].

The Bose-Einstein correlations are a genuine quantum mechanical effect originating from the symmetrisation of the overall wave function of identical final state bosons. This can not be accomplished by the fragmentation models using a probabilistic ansatz where the generation of the different hadrons occurs incoherently. However, there exist two different approaches in Monte-Carlo simulations to accommodate Bose-Einstein correlations.

The first approach is to calculate weights that are applied to the events generated without Bose-Einstein correlations. One example for such an event weighting procedure was introduced by Kartvelishvili and Kvatadze [32]. By weighting Monte-Carlo events according to their prescriptions, the experimentally observed Bose-Einstein enhancement at small Q values is reproduced. One weakness of the global weighting ansatz is that factorisation between the perturbative parton shower and the non-perturbative fragmentation part might be violated. Especially event properties determined by the perturbative part of the process like mass, width and jet-multiplicity of the Z boson should not be changed by the event weights of the Bose-Einstein model. To circumvent this problem another type of weighting procedure has been implemented into the Pythia program by Todorova-Nová and Rameš [33]. Every prompt boson generated by the Pythia string fragmentation undergoes a local re-weighting procedure. All direct hadrons from the same string are re-weighted together in such way that the fragmentation of each string is repeated until the correlation function satisfies a weighting criterion. By the authors this ansatz is called "local weighting procedure". Here, in principle no correlations between different strings and therefore no correlations between hadrons from different W bosons are present. These inter-W correlations would only cause systematic effects on the W-mass reconstruction if strings are reconnected, that means as a second-order effect of colour reconnection.

The second ansatz is based on a characteristic feature of Bose-Einstein correlations which tend to bring pairs of equal bosons closer together in momentum space. Lönnblad and Sjöstrand introduced an algorithm implemented in the Pythia Monte-Carlo program which mimics the effect of Bose-Einstein correlations as a mean field potential attraction between identical bosons. Locally, the four-momenta of pairs of identical bosons are changed in such way that the mean momentum difference Q between the particles decreases. In this model factorisation is preserved by construction, because the local change of particle momenta does not change the underlying parton structure of the event. The main problem of this algorithm is the fact that energy conservation can only be restored by a global rescaling of particle momenta.

A lot of effort has been invested in the question of how to conserve total four momentum. The naive global rescaling of all momenta by a common factor, denoted as BE model, introduces a large negative shift in m_{W}. Ensuring four-momentum conservation locally leads to a model where nearby particles are shifted closer together and those somewhat further away are shifted apart. This scheme is implemented in the BE3 and the BE32 models. For quantitative studies of Bose-Einstein effects in W-pair events and for the estimation of possible mass biases the Monte-Carlo model BE32 [34] from Lönnblad and Sjöstrand is widely used. The values of the BE32 parameters are found by tuning the Monte Carlo to Z-decay data, depleted in b-quark events.

Genuine intra-W Bose-Einstein correlations are expected due to the symmetrisation of the final wave function of identical mesons in the final state. This effect was measured by L3 [35] and the Bose-Einstein correlations in W bosons were found to agree well with those measured in Z decays, which were depleted of b quarks. However, these intra-W correlations do not bias the mass reconstruction. The LEP collaborations also searched for inter-W Bose-Einstein correlations [36].

To study these correlations one defines the two-particle densities, $\rho_2(Q)$, measured as

$$\rho_2(Q) = \frac{1}{N_{\mathrm{events}}} \frac{\mathrm{d}N_{\mathrm{pairs}}}{\mathrm{d}Q} \tag{5.5}$$

for the number of pairs of identical bosons, N_{pairs}, with four-momenta difference $Q = \sqrt{-(p_1 - p_2)^2}$.

All LEP collaborations follow a method proposed by Chekanov, de Wolf and Kittel in [37]. They propose a direct search for inter-W Bose-Einstein correlations using only the data, with no need of Monte-Carlo models. Here, a comparison of Bose-Einstein correlations in fully-hadronic W-pair events ($qqqq$) with those in semi-hadronic events ($qq\ell\nu$) serves as a probe to study inter-W Bose-Einstein correlations.

In the following, the assumption is made that the two-particle densities for the W^+ and the W^- are the same. If we assume that in full-hadronic events the two W decays occur independently, the two-particle density can be written as the sum of two terms

$$\rho_2^{\mathrm{WW}}(p_1, p_2) = 2\,\rho_2^{\mathrm{W}}(p_1, p_2) + 2\,\rho_1^{\mathrm{W}}(p_1)\rho_1^{\mathrm{W}}(p_2)\ . \tag{5.6}$$

Here, $\rho_2^{\mathrm{W}}(p_1, p_2)$ is the two-particle correlation function for pions coming from the same W boson and can be measured using semi-hadronic events. The product of single-particle densities $\rho_1^{\mathrm{W}}(p_1)\rho_1^{\mathrm{W}}(p_2)$ describes the case if one pion comes from one W boson and the second from the other W boson. This part is determined using artificially constructed $\mathrm{WW} \to q\bar{q}q\bar{q}$ events from the hadronic decay products of two semi-hadronic final states, $\mathrm{WW} \to q\bar{q}l\nu$. The particle pairs from different W bosons in the mixed events are uncorrelated by construction, because the two W bosons originate from different events. Summing over all pairs with equal Q one expects in absence of inter-W effects

$$\rho_2^{\mathrm{WW}}(Q) = 2\,\rho_2^{\mathrm{W}}(Q) + 2\,\rho_{\mathrm{mix}}^{\mathrm{W}}(Q)\ . \tag{5.7}$$

If this equation can be validated by a measurement one proves the absence of inter-W Bose-Einstein correlations in the data. In particular, the difference and the ratio of the left- and right-hand side of this equation can be used as a test variable:

$$\Delta\rho(Q) = \rho_2^{\mathrm{WW}}(Q) - 2\rho_2^{\mathrm{W}}(Q) - 2\rho_{\mathrm{mix}}^{\mathrm{WW}}(Q)\ . \tag{5.8}$$

Alternatively, the ratio of both terms can be constructed:

$$D(Q) = \frac{\rho_2^{\mathrm{WW}}(Q)}{2\rho_2^{\mathrm{W}}(Q) + 2\rho_{\mathrm{mix}}^{\mathrm{WW}}(Q)}\ . \tag{5.9}$$

If there are no correlations between particles originating from different W bosons, these variables will by construction have the values: $\Delta\rho(Q) = 0$ and $D(Q) = 1$. In case inter-W Bose-Einstein correlations exist one expects deviations at small values of Q for like-sign pions.

The studies of Bose-Einstein correlations in W-pair events are concentrated on charged pion production. Charged pions are identified using information from the tracking and the calorimetric system. Typically one million of like-sign particles are selected in the fully-hadronic and about 200,000 in the semi-hadronic channel, using all data of one LEP experiment. Care has to be taken on the QCD background from $\mathrm{Z}/\gamma \to 4$ jets events, because these events could mimic inter-WW Bose-Einstein correlations.

Figure 5.8 shows the distribution of $\Delta\rho$ for like-sign, $(\pm,\pm)$, and for unlike-sign, $(+,-)$, particle pairs. Also shown are the predictions of the Monte-Carlo program KoralW after full detector simulation, both with and without inter-W Bose-Einstein correlations implemented. In the inter-W scenario the variable $\Delta\rho$ of the like-sign pairs shows an enhancement for small values of the momentum difference Q. In the spectrum of the unlike-sign pairs a much smaller enhancement is observed which is due to an artefact from the shifting of particle momenta in the Monte-Carlo implementation of the Bose-Einstein effects which is needed to enforce energy-momentum conservation locally. The

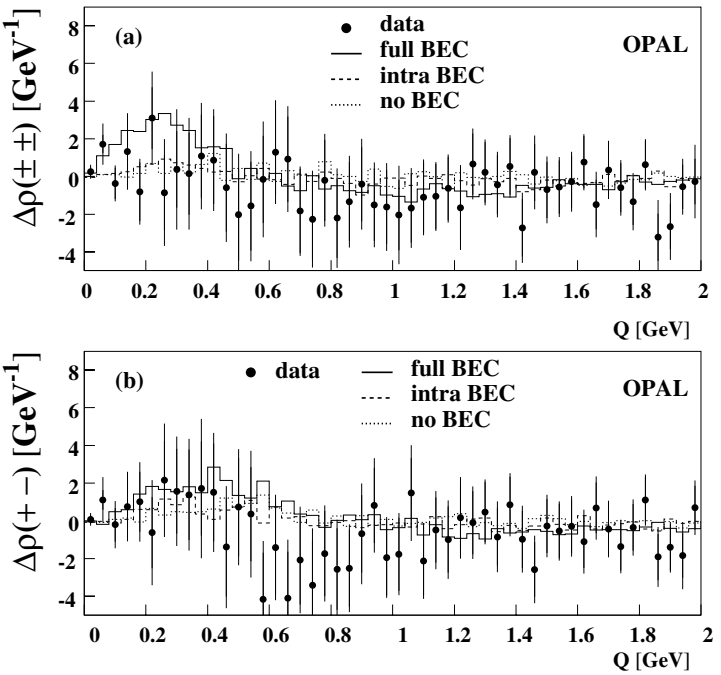

Fig. 5.8. Measurement of the test variables (a) $\Delta\rho(\pm,\pm)$ for like-sign pion pairs and (b) $\Delta\rho(+,-)$ for unlike-sign pion pairs as measured by OPAL. Also shown are the Monte-Carlo predictions using Pythia with and without inter-W Bose-Einstein correlations

$\Delta\rho(\pm,\pm)$ distribution is described by the Monte Carlo without inter-W effects, whereas the inter-W scenario is strongly disfavoured.

To allow a quantitative statement the integral

$$J(\pm,\pm) = \int_0^{Q_{\max}} \Delta\rho(Q)\,\mathrm{d}Q \tag{5.10}$$

is computed. The results on J for the individual centre-of-mass energies are consistent between each other and their dependence on $Q_{\max}$ is shown in Fig. 5.9.

L3 has derived J from the complete set of W-pair events:

$$J(\pm,\pm) = 0.03 \pm 0.33\ (\text{stat.}) \pm 0.15\ (\text{syst.})\ . \tag{5.11}$$

From the Monte-Carlo simulation with inter-W Bose-Einstein correlations a value of $J(\pm,\pm) = 1.38 \pm 0.10$ is expected, where the given uncertainty is due to limited Monte-Carlo statistics. It disagrees with the measured data value by 3.6 standard deviations. As a cross check, for unlike-sign pairs one obtains $J(+,-) = 0.01 \pm 0.36 \pm 0.16$, which is consistent with zero.

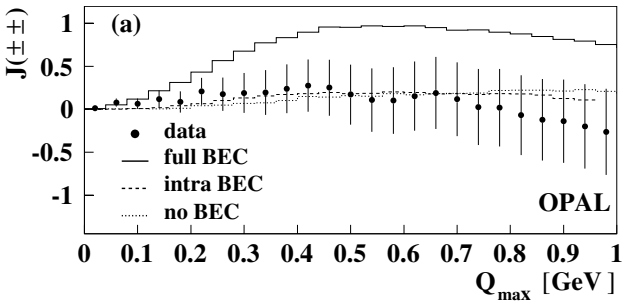

Fig. 5.9. The integral J as measured by OPAL for like-sign particle pairs compared with different Bose-Einstein scenarios

A combination of the results of the four LEP experiments has been performed [27] by averaging the results of various analyses using different estimators for the size of Bose-Einstein correlations. Figure 5.10 shows the measured size of correlations as a relative fraction of the BE32 model including full inter-W correlations. Combining the individual results gives an average fraction of 0.17 ± 0.13. This means that the data prefer only little inter-W correlations, at most at the level of one third of the BE32 model.

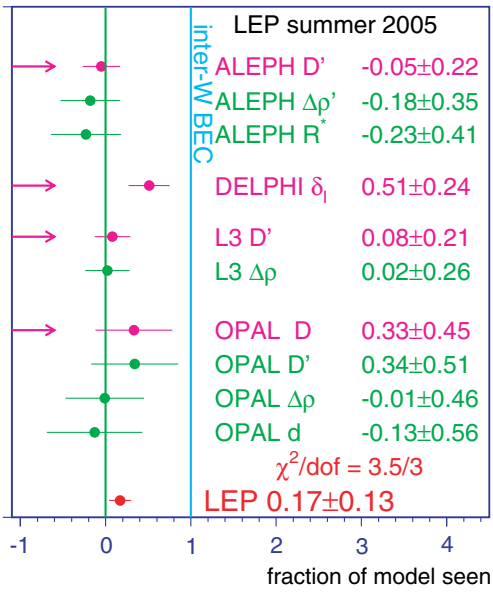

Fig. 5.10. Measured Bose-Einstein correlations given in terms of a relative fraction to the size expected from the BE32 model including full inter-W correlations. The arrows indicate the measurements used in the LEP combination

5.5 Selection of W-Boson Pairs

The event selection of W-pair production is based on the analyses [38] that have been performed for the precision measurement of the W-pair cross section. These selections are designed to minimise the expected cross-section uncertainty for every final state and complementary cuts are chosen to avoid double counting of events.

The selections of the four LEP experiments follow similar strategies. First the final-state fermions are identified in the event. Electrons are selected as energy depositions in the electromagnetic calorimeter having an electromagnetic shower shape and matching a track in the central tracking chamber. Muons are either identified as tracks in the muon chambers or as a signature from a minimum-ionising particle (MIP) in the calorimeters. The search for a hadronic τ jet is usually based on a neural network algorithm which is trained using the characteristics of a τ decay: low multiplicity, small jet opening angle and low jet mass. The hadronic jets are clustered from the tracks or the calorimetric energy depositions, where the Durham algorithm is widely used.

5.5.1 Selection of Fully-Leptonic Events

Fully-leptonic events, $\ell\nu\ell\nu$, are characterised by two high energy acoplanar leptons and substantial missing energy. On the contrary, the background processes $e^+e^- \to \ell^+\ell^-$ and $\gamma\gamma \to \ell^+\ell^-$ yield events which are balanced transversely to the beam and contain two leptons which are back-to-back in the $r - \phi$ plane. This can be exploited either by applying corresponding cuts in the event selection or by training a neural network on these variables. Both methods have been used and selection efficiencies of more than 60% and purities of 70% and better are obtained . These values are the averages over all possible $\ell\nu\ell\nu$ channels, where the $\tau\nu\tau\nu$ channel is the one with the lowest efficiency and purity. The distribution of the transverse missing momentum is shown in Fig. 5.11.

An additional background originates from $\ell^+\ell^-\nu\bar{\nu}$ final states, where the neutrinos are from a different species (e, μ, τ) than the charged lepton pair. These events can not be produced by W-pair production, but only via neutral current diagrams. Since the neutrinos escape undetected, the only difference between these events and the signal events is the appearance of the peak in the invariant mass distribution of the charged lepton pair due to its resonant production via the Z boson. They can not be separated experimentally from the signal and their predicted cross section is subtracted as background. Another correction is applied to account for the contribution from singly- or non-resonant diagrams to the fully-leptonic final states of W-pair production.

5.5.2 Selection of Semi-Leptonic Events

The typical characteristics of the semi-leptonic events can be exploited via a cut based selection (L3), an analysis constructing one likelihood or discrimi-

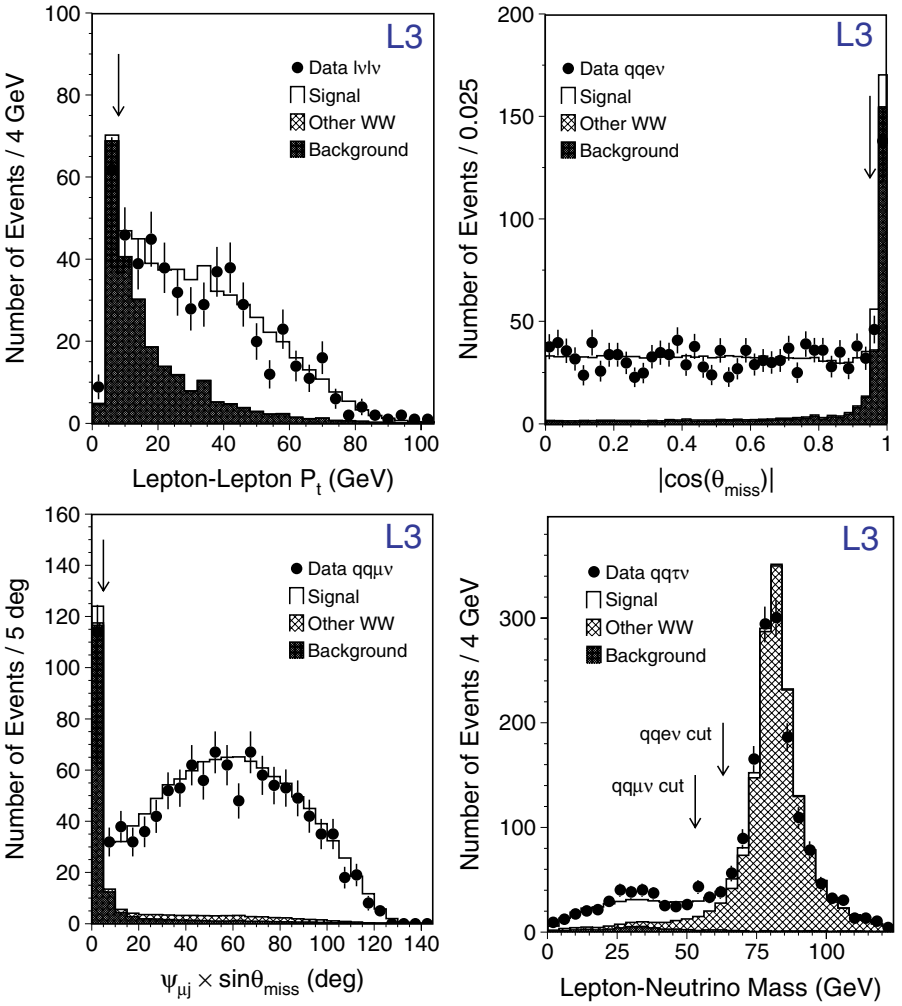

Fig. 5.11. The transverse missing energy of the event (*upper left*) in $\ell\nu\ell\nu$ events, the polar angle of the missing momentum (*upper right*) in $qqe\nu$ events, the discriminant variable $\psi_{\mu j} \sin\theta_{\mathrm{miss}}$ (*lower left*) in $qq\mu\nu$ events and the cuts on the invariant mass of the leptonic system (*lower right*) in the $qq\tau\nu$ selection of L3

nant per event (DELPHI and OPAL) or by using the output of an artificial neural network, which has been trained to these variables on Monte-Carlo samples (ALEPH).

The selection of the $qqe\nu$ final state requires the identification of a high-energy electron and two or more hadronic jets. Additionally, the event has to exhibit missing momentum due to the neutrino, where the direction of the missing momentum, presented in Fig. 5.11, should point into an active

region of the detector. All particles other than the identified electron are then clustered into two jets using the Durham algorithm. The invariant masses of the two jets, m_{jj}, and of the lepton pair, $m_{e\nu}$, are then required to be consistent with the W mass.

A purity of the selection of more than 90% has been obtained, where the accepted background is dominated by the reaction $e^+e^- \to q\bar{q}$ and four-fermion events from neutral current production, namely $e^+e^- \to ZZ \to \ell\ell qq$ and $e^+e^- \to Zee \to \ell\ell ee$.

The selection of the $qq\mu\nu$ final state requires an identified high-energy muon and missing momentum due to the neutrino. All particles other than the muons are then clustered into two jets. The neutrino momentum is calculated using momentum conservation in the event. The invariant mass of the jet pair and of the lepton system have to be compatible with the W mass. In addition the muon has to be separated from the jets to reject events from the process $e^+e^- \to q\bar{q}$ with an inclusive muon coming from a hadron decay. L3, for example, requires the product of $\psi_{\mu j}$, the angle between the muon and the closest jet, and $\sin\theta_{\mathrm{miss}}$, the angle of the missing momentum vector, to be greater than 5.5°. This exploits additionally the fact that many $e^+e^- \to q\bar{q}$ events exhibit missing momentum only along the beam direction due to ISR radiation. A plot of this variable is presented in Fig. 5.11. The selection purity is found to be better than 90%. The remaining background is dominated by Z-pair production with the $qq\mu\nu$ final state and by the $e^+e^- \to q\bar{q}$ process.

For the selection of the $qq\tau\nu$ final state, a low momentum, isolated electron or muon or a narrow jet are searched for in events with high multiplicity and missing momentum. Then again the measured invariant masses of the hadronic and leptonic W decays are tested to be compatible with the assumption of W-pair production. Here, the recoiling mass against the jet-pair is used as a measure for the invariant mass of the $\tau\nu$ pair, which can not be determined directly. In the case of leptonic tau decays the invariant mass built up of the reconstructed charged lepton and the missing momentum of the event is required to be much smaller than the W mass in order to remove events from the $qqe\nu$ and the $qq\mu\nu$ channel as shown in Fig. 5.11.

The Monte-Carlo simulation predicts a purity of more than 80% for this selection. The dominating background consists of events from the process $e^+e^- \to q\bar{q}$ and from single-W production.

5.5.3 Selection of Fully-Hadronic Events

In the case of the $qqqq$ final state a preselection algorithm is used, which requires events with high multiplicity, little missing energy and a four-jet topology. After the preselection the events are clustered into four jets and a cut on the jet-resolution parameter, y_{34}, where the event topology changes from three to four jets, is applied. Additionally, the longitudinal missing momentum, the energy of reconstructed hard photons in the detector and the event invariant mass can be used to reject Z-return events, $e^+e^- \to q\bar{q}\gamma$.

To further purify the W-pair event sample, either a neural network algorithm is trained using this sample of preselected events (ALEPH, DELPHI and L3) or several event variables are combined into an event likelihood (OPAL). The main background sources are quark-pair production with double gluon radiation, $e^+e^- \to q\bar{q}gg$, and four-fermion background from the process $e^+e^- \to ZZ \to qqqq$.

Background discriminating variables are fed into the neural network. They describe the event shape, the kinematics of the events and jet characteristics. Typical event shape observables are thrust, sphericity or the jet-resolution parameter y_{34}, which discriminate between the spherical 4-jet events of W-pair production and the 2-jet like QCD background. Other characteristic variables are the energy differences between the various jets and the inter-jet angles. Jet properties such as jet broadenings, b-tags and jet-multiplicity discriminate against jets coming from gluon radiation or b-quarks. For the given four-jet configuration OPAL compares the matrix-element values calculated for the QCD process $e^+e^- \to q\bar{q}gg$ with the one for the CC03 diagrams of $e^+e^- \to W^+W^- \to qqqq$.

The energy of the most energetic jet as measured by L3 is shown in Fig. 5.12. Here, also the final neural network output is presented, which yields a clear distinction between signal and background. The purity of the $qqqq$ selection is found to be 79% with the largest background contribution coming from the process $e^+e^- \to q\bar{q}$.

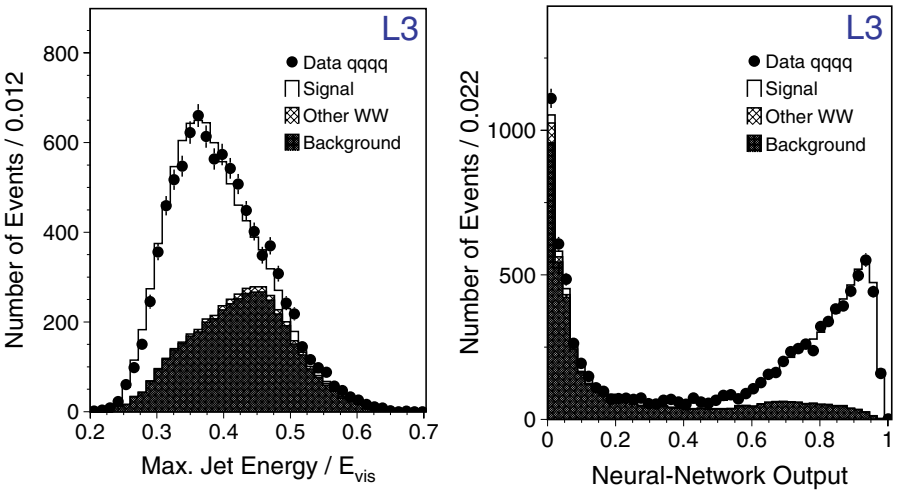

Fig. 5.12. The maximum jet energy (*left*) and the neural network output (*right*) in the $qqqq$ selection of L3

5.6 Measurement of the W-Pair Cross Section

All LEP experiments present their cross-section measurements of W-pair production as corrected to the CC03 cross section, which represents a natural definition of resonant W-pair production. The three CC03 Feynman diagrams are depicted in Fig. 5.1. Although the CC03 cross section is not an experimentally accessible observable, it nevertheless can be seen as a pseudo-observable, containing for example the sensitivity of the total cross section on m_{W} near threshold. To extract this CC03 cross section from the data the observed cross section of a given four-fermion final state is corrected for the calculated difference between the complete four-fermion production rate and the rate predicted using only the CC03 diagrams.

Events from other processes than four-fermion production and four-fermion final states, which can not be produced by W pairs, are counted as background events. On the contrary, mis-identified W-pair final states are not included in the background, but are rather taken into account by off-diagonal entries in the efficiency matrix.

A simultaneous fit of the individual final state cross sections to the selected event samples is performed, which automatically takes cross-feed between the final states into account. Here, the corresponding matrix of efficiencies and backgrounds from Monte Carlo simulation is used. In this fit, either the Poissonian probability of the number of selected events is used or a likelihood function is constructed, which shows how well a given normalisation of the Monte Carlo simulation represents the measured distribution of the neural network output or of a likelihood variable.

L3 and OPAL simultaneously fit cross sections of the ten possible final states of W-pair production, namely six different mixtures from two fully-leptonic W decays, three different semi-leptonic and the fully-hadronic final state. ALEPH and DELPHI perform the cross section extraction separately in each of the three event classes $\ell\nu\ell\nu$, $qq\ell\nu$ and $qqqq$.

Assuming lepton universality the total cross section for each of the three event classes can be extracted. Alternatively, one can fix the W-decay branching fractions to the values predicted by the Standard Model, which yields the total cross section of W-pair production.

A combination of the results on the W-pair cross section from the four individual LEP experiments is performed in Reference [27]. Correlations between the systematic uncertainties of different experiments are taken into account. In Fig. 5.13 the combined measurement of the W-pair cross section at the different centre-of-mass energies is compared to the theory prediction. The theory calculations are based on the two programs YFSWW and RacoonWW. Both codes have been compared in great detail and their results agree within 0.5% at LEP 2 energies.

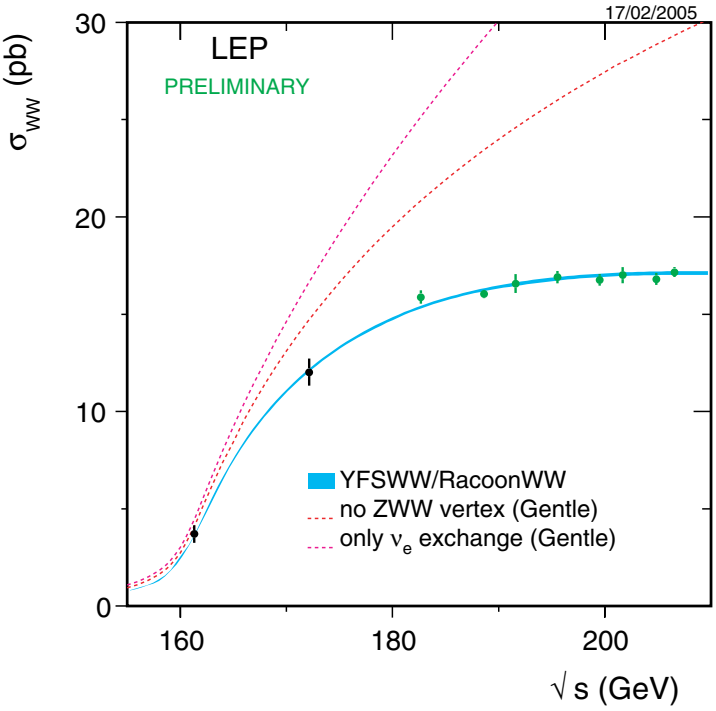

Fig. 5.13. Cross section of W-pair production corrected to the CC03 contribution. The average cross-section results from the four LEP experiments at various centre-of-mass energies are compared to the theory prediction calculated using the programs YFSWW and RacoonWW

5.7 Measurement of W-Boson Polarisation

The existence of longitudinally polarised W bosons is a consequence of their non-vanishing mass that is generated by the Higgs mechanism of electroweak symmetry breaking. The fractions of longitudinally and transversely polarised W bosons in W-pair production are determined by the triple-gauge-boson couplings.

W-pair events of the final states $qqe\nu$ and $qq\mu\nu$ are used by the L3 collaboration to measure the fractions of the three helicity states of the W boson [39]. These final states allow simultaneously the determination of the direction and the charge of the W bosons. To measure the polarisations of the W bosons the parity violating W decays are used as a polarisation analyser. The differential cross section of W^- decays as a function of the decay angle θ^* in the W rest frame is given by:

$$\frac{1}{N}\frac{\mathrm{d}N}{\mathrm{d}\cos\theta^*} = f_-\frac{3}{8}(1+\cos\theta^*)^2 + f_+\frac{3}{8}(1-\cos\theta^*)^2 + f_0\frac{3}{4}\sin^2\theta^* \ , \qquad (5.12)$$

where f_0, f_-, and f_+ are the fractions of W bosons with longitudinal polarisation, with negative and with positive helicity, respectively. For W^+ bosons a similar equation with exchanged angular dependencies exists. The fraction of the different W-boson helicity states in the recorded W-pair events is obtained from a fit of this function to the measured decay-angle distributions. In Fig. 5.14 the decay-angle distribution of the leptonically decaying W boson is shown. Only if longitudinally polarised W bosons are included the fit agrees with the measured data.

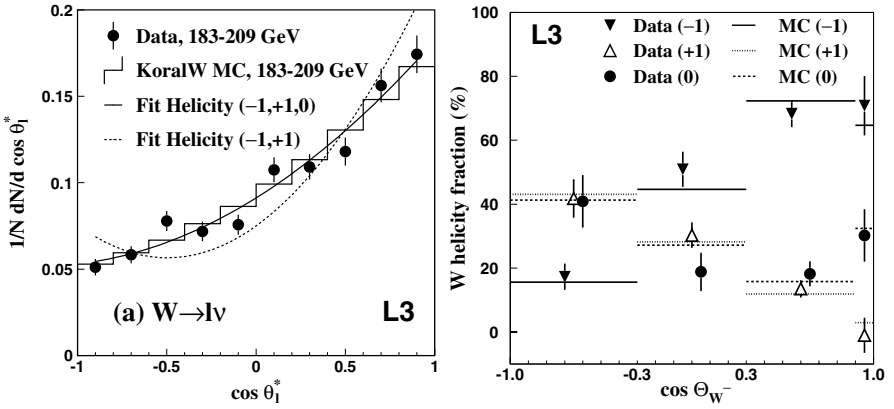

Fig. 5.14. Decay angle distributions from leptonic decaying W bosons (*left*) and measured helicity fractions of the W bosons in four different bins of the W-boson polar angle (*right*)

Using the data recorded at 183 GeV $< \sqrt{s} <$ 209 GeV the L3 collaboration determines the fraction of longitudinally polarised W bosons to be 0.218 ± 0.027 (stat.) ± 0.016 (syst.). The fractions of the three W-boson helicity states are also measured as function of the W-boson polar angle. The result is shown in Fig. 5.14.

An analysis [40] performed by OPAL uses the semi-leptonic final states of the data recorded at 183 GeV $< \sqrt{s} <$ 207 GeV. It measures the differential cross section of longitudinally and transversely polarised W boson as function of the W production angle, $\cos\theta_{\mathrm{W}}$. The result is shown in Fig. 5.15.

5.8 Triple Gauge Boson Couplings

The Standard Model describes the charged-current weak interactions as a result of the SU(2) gauge invariance. The non-Abelian structure of the SU(2)

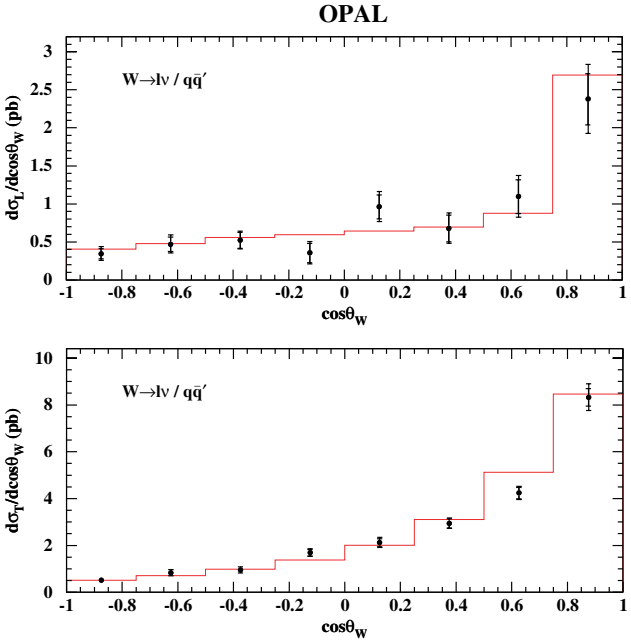

Fig. 5.15. Polarised differential cross section of W production, averaged over the centre-of-mass energies, 183 GeV $< \sqrt{s} <$ 207 GeV

gauge group immediately implies the existence of self couplings between the corresponding gauge bosons. The direct observation and measurement of these gauge-boson self interactions constitutes an important test of the theory of electroweak interactions. At LEP the expected uncertainty on the gauge couplings is much larger than their radiative corrections. Thus the LEP analyses of W-boson self interactions are a test of the Standard Model at tree level.

Already before the start of LEP 2 stringent constraints were put on the triple gauge couplings using the precision LEP 1 data [41]. At LEP 2 the triple gauge boson vertices γWW and ZWW show up in the s-channel diagrams of the process $e^+e^- \rightarrow W^+W^-$ as depicted in Fig. 5.16. The existence of these triple gauge couplings (TGC) is already proven by the measurement of the total cross section. The cross section of W-pair production in absence of the TGC vertices, mediated only by ν_e exchange, is predicted to increase more rapidly with $\sqrt{s}$ than the Standard Model cross section. This can be seen in Fig. 5.13 where the cross-section prediction without TGC is compared to the measurements and definitely ruled out. Also the measured fraction of longitudinally polarised W bosons indicates that the contributions of the triple gauge boson vertices to the process of W pair production are in agreement with the Standard Model expectation.

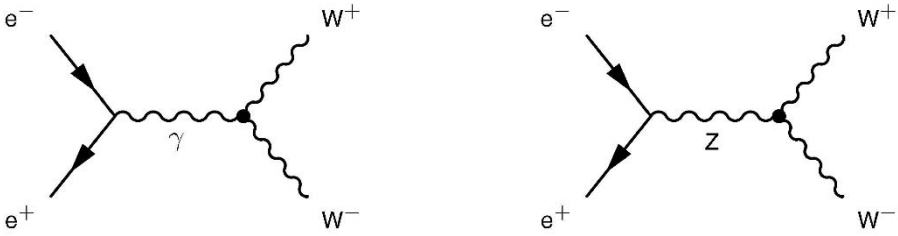

Fig. 5.16. The two Feynman diagrams of W-pair production which contain a triple gauge boson vertex

The most general Lorentz invariant ansatz of vector boson self couplings has seven complex couplings for each of the γWW and the ZWW vertex [42]. Requiring CP conservation as well as electromagnetic gauge invariance five parameters are left: the relative coupling strength of the W boson to the neutral current, g_1^{Z}, and four form factors, two for the ZWW vertex, κ_{Z} and λ_{Z}, and two equivalent form factors for the γWW vertex, κ_γ and λ_γ. The assumption of custodial SU(2) symmetry, which is established by the precision measurements of LEP 1, imposes two more constraints, which leaves three free parameters: g_1^{Z}, κ_γ, λ_γ. At tree level the Standard Model predicts them to be:

$$g_1^{\mathrm{Z}} = 1\,, \qquad \kappa_\gamma = 1 \quad \text{and} \quad \lambda_\gamma = 0\,. \tag{5.13}$$

The couplings κ_γ and λ_γ can be related to the magnetic dipole moment, μ_{W}, and the electric quadrupole moment, Q_{W}, of the W boson:

$$\mu_{\mathrm{W}} = \frac{e}{2m_{\mathrm{W}}}(1 + \kappa_\gamma + \lambda_\gamma) \tag{5.14}$$

$$Q_{\mathrm{W}} = -\frac{e}{2m_{\mathrm{W}}}(\kappa_\gamma - \lambda_\gamma) \tag{5.15}$$

Deviations of the triple gauge couplings (TGC) from the Standard Model prediction would mainly affect the production angle and the polarisation of the produced W bosons. The latter can be accessed experimentally via the angular distributions in the decay of the W bosons. On tree level and in the approximation of vanishing W width the kinematics of the four-fermion final state is unequivocally given by a set of five angles, i.e. the polar angle, Θ_{W}, between the incident e^- and the W^- boson and the decay angles (θ_f^*, ϕ_f^*) and $(\theta_{\bar{f}}^*, \phi_{\bar{f}}^*)$ in the respective rest frames of W^- and W^+. These angles are sketched in Fig. 5.17.

The semi-leptonic final states $qqe\nu$ and $qq\mu\nu$ are most useful for this analysis, because here the charge of the leptonically decaying W boson is tagged by the measurement of the charged lepton [43]. Simultaneously, the direction of this W boson is inferred as being opposite to the fully reconstructed momen-

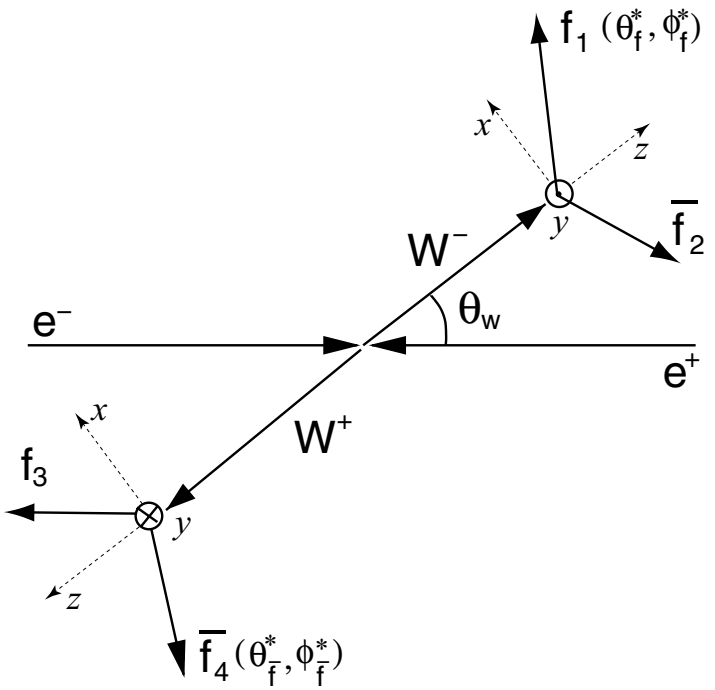

Fig. 5.17. The set of five angles determining the kinematics of the four-fermion final state

tum of the hadronically decaying W boson and therefore the decay angles of the lepton in the W rest frame can be measured. In the hadronic decaying W system the charge of the quarks is generally not measured and the differential distributions of the decay angles of the quark are folded with the distributions of the antiquark. The distributions of each of these five angles as measured by the OPAL experiment are shown in Fig. 5.18.

The triple gauge couplings are measured via a fit of the multi-differential cross section with respect to these angles to the observed data distribution. To take effects such as W width, gluon and photon radiation and detector resolution into account, a re-weighting of Monte Carlo events as a function of the considered parameter is performed until the data and Monte Carlo distributions show the best agreement. Alternatively the method of optimal observables has been exploited. Here, the dependence of the multi-dimensional cross section on the anomalous couplings is linearised. By construction, the sensitivity for each of the anomalous couplings is contained in one optimal observable. To extract the TGC couplings from the data only the mean value of the optimal observables has to be determined. Potential influence of effects

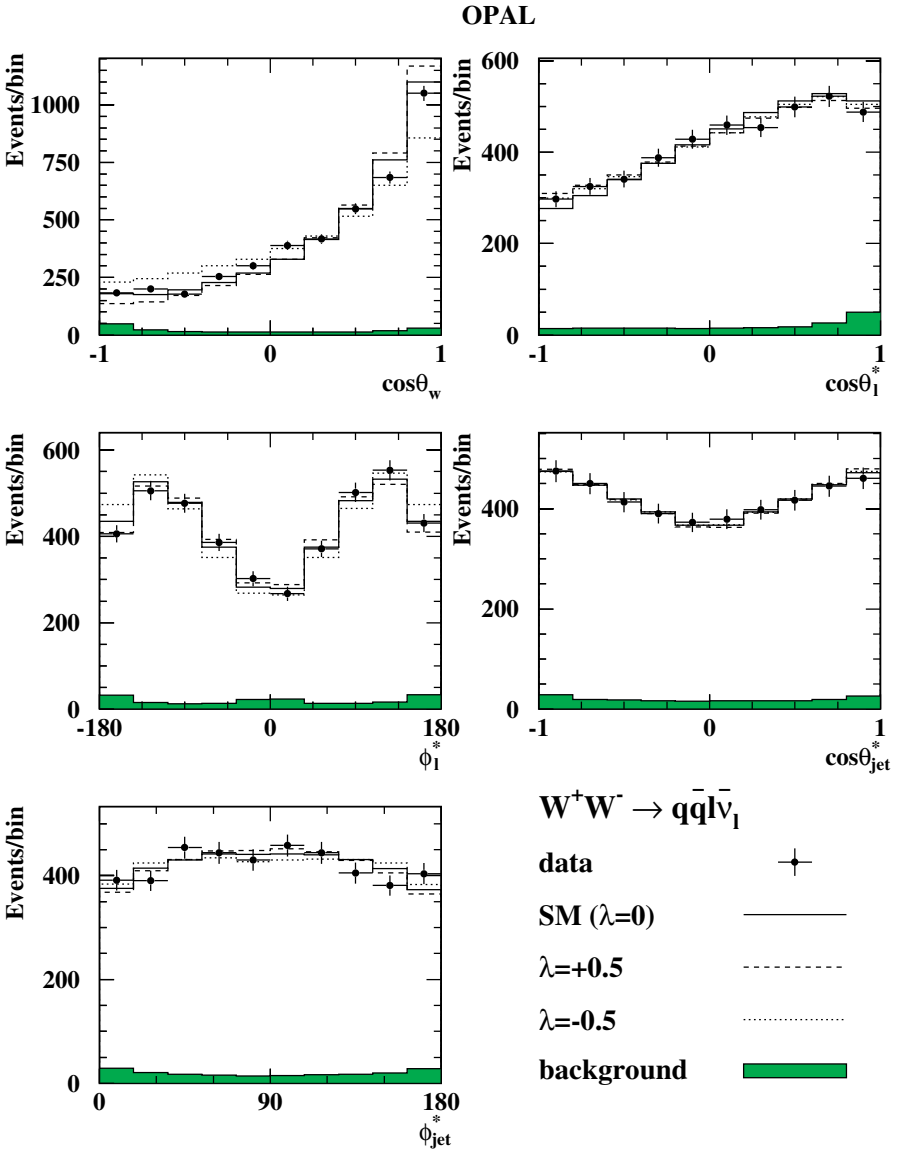

Fig. 5.18. Measured distributions for the five angles specifying the event kinematics as measured by OPAL. The histograms show the Standard Model expectations as well as the expectations of $\lambda = \pm 0.5$

such as hadronisation, detector resolution and event selection are simulated with a reference Monte Carlo and corrected for.

Additional information on the γWW vertex can be gained from the processes of single-W and single-photon production. Figure 5.19 shows the relevant Feynman diagrams, which contain the γWW vertex. The cross-section measurements of both processes were presented in Sect. 4.2.3 and Sect. 4.3.1, respectively. From the results the form factors κ_γ and λ_γ can further be constrained.

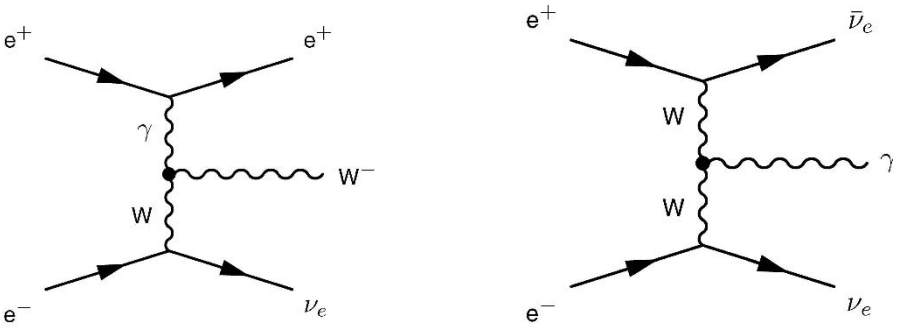

Fig. 5.19. The two Feynman diagrams of single-W and single-photon production which contain the γWW vertex

The combined result of all LEP data for the triple gauge coupling parameters g_1^Z, κ_γ and λ_γ is given in Fig. 5.20. Shown are the regions preferred by the data at 68% confidence level. The Standard Model predictions of these parameters are contained within these regions. Alternatively, single-parameter fits are performed where the parameter under study is varied while the remaining two are fixed to their Standard Model values. For the individual parameters the results are [27]:

$$\begin{aligned} g_1^Z &= \quad 0.991^{+0.022}_{-0.021} \\ \kappa_\gamma &= \quad 0.984^{+0.042}_{-0.047} \\ \lambda_\gamma &= -0.016^{+0.021}_{-0.029} \end{aligned}$$

Potential anomalous couplings with absolute values of these parameters exceeding the order of 0.1 are excluded.

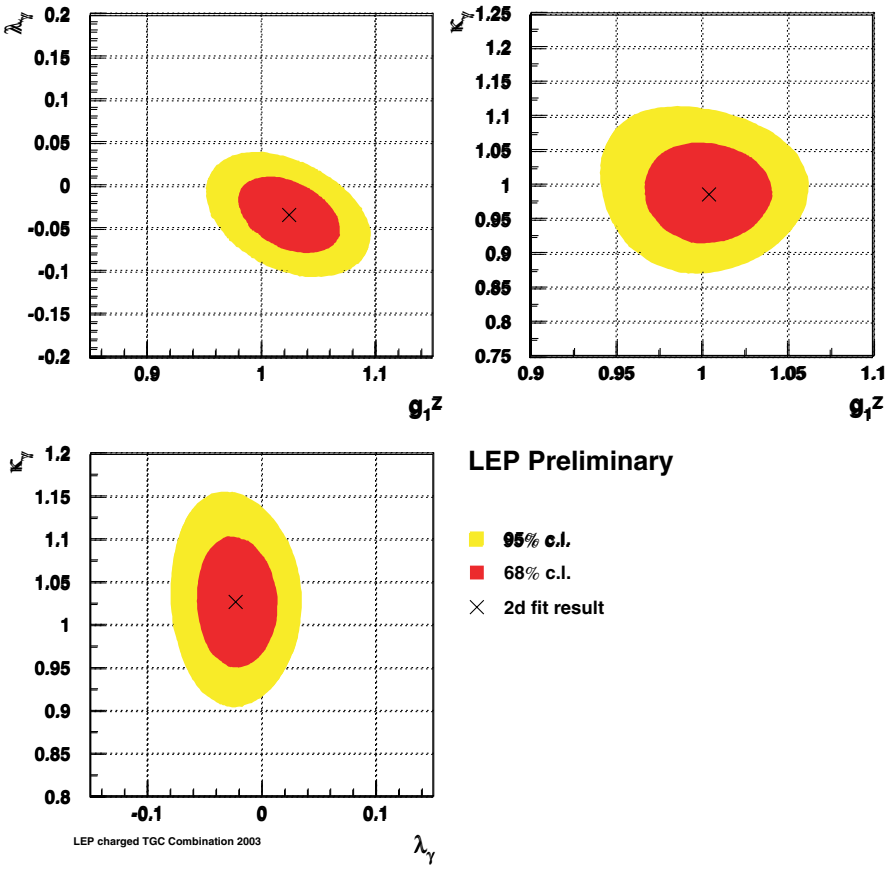

Fig. 5.20. Simultaneous determination of the anomalous couplings g_1^Z, κ_γ, λ_γ from the combination of all LEP results

References

1. F. Maltoni and T. Stelzer, JHEP **0302**, 027 (2003)
2. R.G. Stuart, Phys. Lett. **B 262**, 113 (1991);
   A. Aeppli, F. Cuypers and G.J. van Oldenborgh, Phys. Lett. **B 314**, 413 (1993);
   H. Veltman, Z. Phys. **C 62**, 35 (1994);
   W. Beenakker and A. Denner, Int. J. Mod. Phys. **A 9**, 4837 (1994)
3. W. Beenakker, F.A. Berends and A.P. Chapovsky, Phys. Lett. **B 435**, 233 (1998)
4. S. Jadach et al., Comp. Phys. Comm. **119**, 272 (1999)
5. J. Fujimoto at al., Comp. Phys. Comm. **100**, 128 (1997)
6. E. Barberio and Z. Wąs, Comp. Phys. Comm. **79**, 291 (1994)
7. S. Jadach et al., Comp. Phys. Comm. **140**, 475 (2001)
8. S. Jadach et al., Phys. Rev. **D 65**, 093010 (2002)
9. S. Jadach et al., Phys. Lett. **B 417**, 326 (1998)
10. D.R. Yennie, S.C. Frautschi and H. Suura, Ann. Phys. **13** (1961) 379

11. A. Denner et al., Comp. Phys. Comm. **153**, 462 (2003)
12. A. Denner, S. Dittmaier and M. Roth, Nucl. Phys. **B 519**, 39 (1998)
13. T. Sjöstrand, Comp. Phys. Comm. **135**, 238 (2001)
14. L. Lönnblad, Comp. Phys. Comm. **71**, 15 (1992)
15. G. Marchesini et al., Comp. Phys. Comm. **67**, 465 (1992)
16. B. Andersson et al., Phys. Rep. **97**, 31 (1983)
17. X. Artru and G. Mennessier, Nucl. Phys. **B 70**, 93 (1974)
18. G. Gustafson and U. Pettersson, Nucl. Phys. **B 306**, 746 (1988)
19. B. Andersson, G. Gustafson and L. Lönnblad, Nucl. Phys. **B 339**, 393 (1990)
20. B.R. Webber, Nucl. Phys. **B 238**, 492 (1984)
21. G. Gustafson, U. Petterson and P. Zerwas, Phys. Lett. **B 209**, 90 (1988)
22. T. Sjöstrand and V. Khoze, Preprint CERN-TH 7011/93 (1993)
23. T. Sjöstrand and V. Khoze, Z. Phys. **C 62**, 281 (1994);
    T. Sjöstrand and V. Khoze, Phys. Rev. Lett. **72**, 28 (1994)
24. L. Lönnblad, Z. Phys. **C 70**, 107 (1996)
25. B. Andersson, G. Gustafson and T. Sjöstrand, Phys. Lett. **B 94** (1980) 211;
    JADE Collaboration, W. Bartel et al., Phys. Lett. **B 101** (1981) 129;
    DELPHI Collaboration, P. Abreu et al., Z. Phys. **C 70** (1996) 179;
    L3 Collaboration, M. Acciarri et al., Phys. Lett. **B 345** (1995) 74;
    OPAL Collaboration, R. Akers et al., Z. Phys. **C 68** (1995) 531
26. ALEPH Collaboration, Conference note ALEPH 2002-020;
    DELPHI Collaboration, Conference note DELPHI 2003-021;
    L3 Collaboration, P. Achard et al., Phys. Lett. **B 561**, 202 (2003);
    OPAL Collaboration, G. Abbiendi et al., Eur. Phys. J. **C 45**, 291 (2006)
27. LEP Electroweak Working Group, Eprint hep-ex/0511027 and
    `http://lepewwg.web.cern.ch/LEPEWWG/`
28. G. Goldhaber et al., Phys. Rev. Lett. **3**, 181 (1959);
    M. Deutschmann et al., Nucl. Phys. **B 103**, 198 (1976)
29. TPC Collaboration, H. Aihara et al., Phys. Rev. **D 31**, 996 (1985);
    CLEO Collaboration, P. Avery et al., Phys. Rev. **D 32**, 2294 (1985);
    TASSO Collaboration, M. Althoff et al., Z. Phys. **C 30**, 355 (1986)
30. ALEPH Collaboration, A. Heister et al., Eur. Phys. J. **C 36**, 147 (2004);
    DELPHI Collaboration, P. Abreu et al., Phys. Lett. **B 471**, 460 (2000);
    L3 Collaboration, P. Acciarri et al., Phys. Lett. **B 458**, 517 (1999);
    OPAL Collaboration, G. Abbiendi et al., Phys. Lett. **B 559**, 131 (2003)
31. L. Lönnblad and T. Sjöstrand, Phys. Lett. **B 351**, 293 (1995)
32. V. Kartvelishvili and R. Kvatadze, Phys. Lett. **B 514**, 7 (2001);
    B. Andersson and M. Ringner, Nucl. Phys. **B 513**, 627 (1998)
33. S. Todorova-Nová, J. Rameš, Eprint hep-ph/9710280 (1997)
34. L. Lönnblad and T. Sjöstrand, Eur. Phys. J. **C 2**, 165 (1998)
35. L3 Collaboration, P. Achard et al., Phys. Lett. **B 547**, 139 (2002)
36. ALEPH Collaboration, St. Schael et al., Phys. Lett. **B 606**, 265 (2005);
    DELPHI Collaboration, J. Abdallah et al., Eur. Phys. J. **C 44**, 161 (2005);
    L3 Collaboration, P. Achard et al., Phys. Lett. **B 547**, 139 (2002);
    OPAL Collaboration, G. Abbiendi et al., Eur. Phys. J. **C 36**, 297 (2004)
37. S.V. Chekanov, E.A. Wolf, W. Kittel, Eur. Phys. J. **C 2**, 403 (1999)
38. ALEPH Collaboration, A. Heister et al., Eur. Phys. J. **C 38**, 147 (2004);
    DELPHI Collaboration, J. Abdallah et al., Eur. Phys. J. **C 34**, 127 (2004);
    L3 Collaboration, P. Achard et al., Phys. Lett. **B 600**, 22 (2004);
    OPAL Collaboration, G. Abbiendi et al., Phys. Lett. **B 493**, 249 (2000) and
    OPAL physics note 469

39. L3 Collaboration, P. Achard et al., Phys. Lett. **B 557**, 147 (2003)
40. OPAL Collaboration, G. Abbiendi et al., Phys. Lett. **B 585**, 223 (2004)
41. A. De Rujula et al., Nucl. Phys. **B 384**, 3 (1992)
42. G. Gounaris et al., CERN 96-01, Vol. 1, p. 525.
43. ALEPH Collaboration, S. Schael et al., Phys. Lett. **B 614**, 7 (2005);
DELPHI Collaboration, Conference note DELPHI-2004-018;
L3 Collaboration, P. Achard et al., Phys. Lett. **B 586**, 151 (2004);
OPAL Collaboration, G. Abbiendi et al., Eur. Phys. J. **C 33**, 463 (2004)

6

Measurement of the W Mass at LEP

The mass, m_{W}, and the total decay width, Γ_{W}, are fundamental properties of the W boson. Together with other electroweak parameters such as the Z-boson mass and the weak mixing angle the precise determination of m_{W} provides a stringent test of the Standard Model at the level of quantum corrections. In addition to the measurement of the Z mass and the weak mixing angle performed at LEP 1 and SLC a precise measurement of the W mass is mandatory for this test. The precision of the direct measurement of the W mass has to compete with the 23 MeV accuracy on m_{W} when it is derived indirectly from the electroweak precision data acquired on the Z resonance.

The results on m_{W} and Γ_{W} presented in this chapter are obtained by the LEP experiments at centre-of-mass energies, 161 GeV $< \sqrt{s} <$ 209 GeV. The cross section of W-pair production near threshold is sensitive to m_{W}. Therefore, at the centre-of-mass energies of 161 GeV and 172 GeV, m_{W} is derived from the measurement of the total cross section of W-pair production. At higher centre-of-mass energies, well above the kinematic threshold, the W-pair events are directly reconstructed and the invariant mass of the decay products are used for the determination of the W mass.

W bosons decay into hadrons, mostly through $\mathrm{W}^- \to \bar{\mathrm{u}}\mathrm{d}$ or $\mathrm{W}^- \to \bar{\mathrm{c}}\mathrm{s}$, or leptons, $\mathrm{W}^- \to \ell\bar{\nu}_\ell$. The measured objects in W-pair events are the charged leptons from the leptonically decaying W bosons and the jets originating from hadronic W decays. For the determination of the W mass via direct reconstruction the invariant mass of the decay products of each W boson is calculated. In the case of hadronic decays the mass of the decaying W boson can be measured directly from the quark and gluon jets, whereas in the case of leptonic decays the neutrino momentum first has to be inferred using the assumption of momentum conservation in the event. The additional knowledge of the centre-of-mass energy coming from the LEP energy calibration leads to an over-constrained system in the case of $qqqq$ and $qq\ell\nu$ events. A kinematic fit finds the most probable solution for the kinematic configuration of each event. Due to the two undetected neutrinos in the $\ell\nu\ell\nu$ final state a complete reconstruction of the final-state kinematics is not possible.

Stefan Roth: *Precision Electroweak Physics at Electron-Positron Colliders*
STMP **220**, 99–132 (2006)
DOI 10.1007/3-540-35165-5_6

The LEP experiments evaluate the reconstructed invariant-mass spectrum with two different methods:

- The measured spectrum is compared to the mass spectra obtained from Monte-Carlo simulations, which were re-weighted in order to represent different W-mass hypotheses.
- For each data event a likelihood to observe the reconstructed kinematics of the event is calculated as a function of m_{W}. The likelihood curves of all selected events are combined to form one global likelihood, which is then minimised with respect to m_{W}.

The first method has the advantage that all corrections like photon radiation, hadronisation and detector resolutions are incorporated in the mass extraction fit and are calculated individually for each event. On the other hand the fit to an invariant-mass spectrum uses only one of several mass-sensitive observables. In the second method the complete information which is included in the kinematics is used for each event. However, a global bias correction has to be obtained from a large Monte-Carlo sample subject to the same likelihood analysis.

In the next section the extraction of the W mass from the measurement of the threshold cross section of W-pair production is explained. A short description of the W-mass determination using the lepton energy spectrum in $\ell\nu\ell\nu$ events follows. Then the direct reconstruction of the W mass and the extraction of m_{W} and Γ_{W} from the measured mass spectra in the $qq\ell\nu$ and $qqqq$ channels is presented. Finally, the estimation of the systematic uncertainties is discussed. Unless otherwise stated, the L3 experiment is used as an example.

6.1 The W Mass from the Threshold Cross Section

In the year 1996 each of the four LEP experiments collected about 10 pb^{-1} at a centre-of-mass energy, $\sqrt{s} = 161.33 \pm 0.05$ GeV, just above the kinematic threshold of W-pair production [1]. Each experiment selected about 30 W-pair events and after averaging the four results the total cross section was measured to be

$$\sigma_{\mathrm{WW}} = 3.69 \pm 0.45 \text{ pb} . \tag{6.1}$$

This measurement is used to extract the mass of the W boson since the threshold cross section depends strongly on m_{W}. This is illustrated in Fig. 6.1, where the Standard Model cross section for W-pair production for various values of the W mass is compared to the measured cross section. The cross-section measurement is translated into a determination of m_{W}, shown on the right hand side of Fig. 6.1. The cross section measurement quoted above corresponds to a mass of the W boson of

$$m_{\mathrm{W}} = 80.40 \pm 0.22 \pm 0.03 \text{ GeV} , \tag{6.2}$$

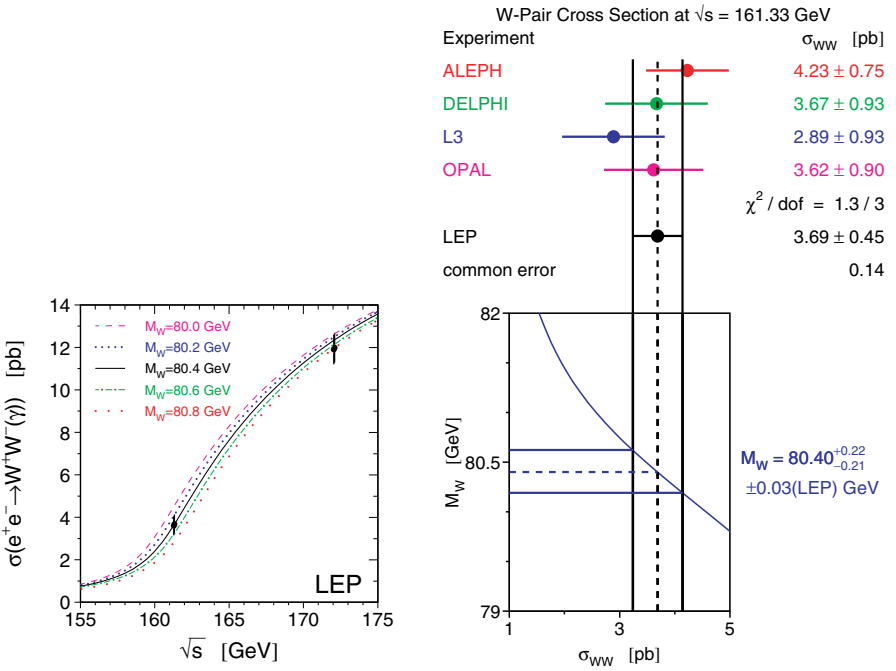

Fig. 6.1. Measurement of m_{W} at threshold (from [2]): On the left the predicted cross section of W-pair production as function of $\sqrt{s}$ is compared to the LEP measurement for various values of m_{W}; on the right the measured cross section of W-pair production is compared to the predicted cross section as function of m_{W}

where the first uncertainty is experimental and the second is due to uncertainties in the calibration of the LEP beam energy at this centre-of-mass energy.

This measurement of the W mass relies on the theoretical calculation of the W-pair cross section. At the time of the presented analysis the $\mathcal{O}(\alpha)$ corrections were not yet available and a scale uncertainty of 2% is assumed for the predicted cross section. The background subtraction is known with a precision of 0.1 pb and accounts to 50 MeV on the uncertainty of m_{W}. After combining the results of the four experiments the statistical uncertainty of the measurement contributes with 210 MeV to the total experimental uncertainty and therefore constitutes the dominant error source.

For future experiments at a high-luminosity $\mathrm{e^+e^-}$ linear collider the extraction of m_{W} from a threshold scan promises to be the method with the smallest systematic uncertainties. From the above arguments it is clear that it will rely on a precise calculation of the W-pair cross section and on the accurate determination of the beam energy. This measurement is discussed in more detail in Sect. 8.2.

6.2 Measurement of the W Mass Using the Lepton Energy

In fully-leptonic W-pair events, $e^+e^- \to \ell\nu\ell\nu$, two undetected neutrinos inhibit the complete determination of the final state kinematics and the invariant mass of the W decay products can not be reconstructed. Alternatively, one can try to use other variables than the invariant mass, which are also sensitive to the mass of the W boson. The most prominent example here is the energy of the charged lepton.

Neglecting the width of the W and the mass of the leptons, the energy of the charged lepton in a W decay is given by:

$$E_\ell = \frac{\sqrt{s}}{4} + \cos\theta^\star_\ell \sqrt{\frac{s}{16} - \frac{m_W^2}{4}}\,, \tag{6.3}$$

where $\theta^\star_\ell$ is the decay angle of the charged lepton in the rest frame of the W boson. This angle can not be measured, but the endpoints of the resulting energy distribution ($\cos\theta^\star_\ell = \pm 1$) are sensitive to m_W. Because of the limited detector resolution, the natural width of the W and initial-state radiation the endpoints of the energy distribution are smeared out. The energy spectrum of the charged leptons measured by the OPAL experiment is shown in Fig. 6.2

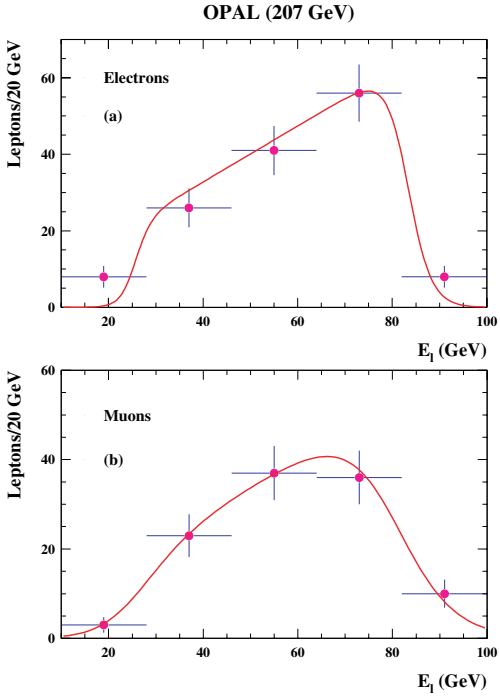

Fig. 6.2. Measured energy spectrum of the charged lepton for the data recorded by OPAL at $\sqrt{s} = 207$ GeV for electrons and muons

The ALEPH analysis [4] additionally uses the missing energy, E_{miss}, of the event as an observable sensitive to m_{W}. At the end it contributes only 5% to the mass determination in the $\ell\nu\ell\nu$ channel. In the OPAL analysis [3] a pseudo-mass is constructed under the assumption that both neutrinos are in the same plane as the charged leptons. Then the kinematics can be solved and two solutions for the pseudo-mass, $M_{\pm}$, are found. One observes that only the larger solution, M_{+}, is sensitive to m_{W}.

In the case of ALEPH, the measurement of the lepton energy contributes to the standard fit of the W mass, whereas OPAL has published a separate result for the $\ell\nu\ell\nu$ analysis. The measured W mass is:

$$m_{\mathrm{W}} = 80.41 \pm 0.41 \text{ (stat.)} \pm 0.13 \text{ (syst.) GeV} , \tag{6.4}$$

where the systematic error is dominated by the uncertainty on the lepton energy scale.

6.3 Direct Reconstruction of the Invariant-Mass Spectrum

In the direct measurement of the W mass the event kinematics of the $qq\ell\nu$ and the $qqqq$ events is reconstructed as completely as possible. The masses of the decaying W bosons are then calculated from the invariant mass of their decay products. In leptonic W decays, the undetected neutrino is identified with the missing momentum of the event and it is combined with the measured charged lepton to reconstruct the W boson. For W decays into quarks, $\mathrm{W} \to \mathrm{q\bar{q}}$, the invariant mass can not be calculated from the four-momenta of the quarks since they hadronise. It has to be derived from the reconstructed jets. The usual expression is used to calculate the hadronic mass from the jets:

$$m_{\mathrm{inv}}^2 = m_1^2 + m_2^2 + 2E_1E_2 - 2|\boldsymbol{p}_1||\boldsymbol{p}_2| \cos\theta_{12} , \tag{6.5}$$

where E_1 and E_2 are the jet energies, $\boldsymbol{p}_1$ and $\boldsymbol{p}_2$ are the jet momenta, m_1 and m_2 the jet masses and θ_{12} is the opening angle between the two jet directions. The jet energies, E_i, are the sum of the energies of all particles assigned to the given jet. The jet momentum, $\boldsymbol{p}$, is the vectorial sum of the particle momenta, where the particles are often taken as massless and their momentum is just given by the particle energy and its direction. From the measured jet energy and momentum, the jet mass can be calculated. The determination of m_{W} from direct reconstruction therefore depends on a precise reconstruction and measurement of high energy jets.

The mass and width of the W boson are measured using a clean sample of W-pair events. In the mass analyses of the four LEP experiments the event selection is based on the measurement of W-pair cross section, which is discussed in detail in Sect. 5.6. In some cases the selection criteria are slightly changed with respect to the cross section measurement to further reduce the

background or to reject events, where the reconstruction algorithm of the event kinematics failed.

6.3.1 Identification of the Final State Fermions

The selected events are analysed in order to reconstruct the four-vectors of the four final-state fermions of W-pair production.

In the semi-leptonic final states the charged leptons directly coming from a W decay have to be well separated from the hadronic part of the event. The high energy electrons and muons are measured in the electromagnetic calorimeter and in the muon system, respectively. Angular information is usually taken from the inner tracking detectors. Hadronic τ jets are identified by the visible τ decay products, being either electron or muon of moderate energy or a narrow hadronic jet. Calorimetric energy close to the identified charged lepton is assumed to originate from final-state radiation and is added to the lepton momentum. Finally, the momentum of the neutrino is calculated assuming momentum conservation in the event.

The jets originating from quarks are reconstructed using the Durham algorithm [8]. For semi-leptonic final states the non-leptonic part of the event is clustered into two jets. In the case of fully-hadronic events the mass resolution can be improved by taking into account possible gluon radiation from one of the quarks. L3, for example, uses the Durham jet-resolution parameter y_{45} to separate events with and without gluon radiation. In the OPAL analysis the probabilities of the various kinematic fits to the 4-jet and 5-jet configuration are compared to decide if the event is treated as a 4-jet or a 5-jet event.

Hard photons originating from initial-state radiation are taken into account in the analysis by excluding their energy from the calculation of the invariant masses. For both W decays of the event, the invariant mass is calculated using the reconstructed four-momentum vectors of the decay products. The known masses of the charged leptons are used as well as the individually measured masses of the hadronic jets in the given event.

In the ideal case of a detector with perfect energy resolution the mass of the hadronically decaying W would be identical to the invariant mass of the decay products. The clustering algorithm combines the individual hadrons, normally assumed to be massless, by adding their four-momenta. This results in a non-vanishing mass of the reconstructed jet. Calculating the invariant mass of the two massive jets also gives the mass of the W boson. The reconstruction of individual jets becomes relevant when a kinematic fit is applied to the event to improve the limited energy resolution of the detector.

6.3.2 Kinematic Fit

The degraded mass resolution of a real detector is mainly caused by the limited energy resolution of the calorimeters. However, the angular measurement

of the jets is very precise and its contribution to the uncertainty of the reconstructed W mass is small. In a first approach the mass resolution can be improved by the assumption that the total energy of the W decay products is equal to half the centre-of-mass energy. This is equivalent to a scaling of energy and momentum of the jets by the same factor such that the energy of the W boson is identical to the beam energy. But one should keep in mind that due to the natural width of the W boson the energies of the two W bosons of one event are not the same. Moreover, this method can not be applied to leptonically decaying W bosons and therefore, in the case of semi-leptonic events, the information from the momentum measurement of the charged lepton would not be used.

Alternatively, a kinematic fit is applied to each of the events to further improve the resolution of the energies, E_f, momenta, p_f, polar, θ_f, and azimuthal, ϕ_f, angles of the visible fermions. During the fit one imposes four kinematic constraints, namely the conservation of the total energy and of the three components of the momentum vector. All measured quantities, the energies and directions of the jets and charged leptons are varied within their resolution by the kinematic fit such that the constraints due to energy and momentum conservation are fulfilled:

$$\sum_f E_f = \sqrt{s} \qquad \text{and} \qquad \sum_f \boldsymbol{p}_f = 0 \tag{6.6}$$

In the semi-leptonic final states three of these constraints are needed to determine the momentum and direction of the undetected neutrino. Additionally, in $qq\tau\nu$ events the energy of the τ lepton has to be inferred from the fourth constraint. This results in a four-constraint (4C) kinematic fit for the $qqqq$ events and a one-constraint (1C) fit for the $qqe\nu$ and $qq\mu\nu$ events. The $qq\tau\nu$ events can be reconstructed unequivocally, but no additional constrained is left. The measured observables do not suffice to completely reconstruct the fully-leptonic final states, $\ell\nu\ell\nu$.

The fact that two identical bosons are produced in the event can be used to further constrain the event kinematics. One requires the invariant masses of the two reconstructed W bosons to be equal within their natural width:

$$|m_{\mathrm{inv}_1} - m_{\mathrm{inv}_2}| < \Gamma_{\mathrm{W}} \tag{6.7}$$

Eventually, this results in a fit with two constraints (2C) for the $qq\mu\nu$ and $qqe\nu$ final states and a fit with five constraints (5C) for the fully-hadronic final state.

In general, a kinematic fit is realised by performing a χ^2 minimisation of the difference between the measured four-momenta and their fitted values including the covariance matrix containing the uncertainties and correlations between them. However, one can simplify the calculation by using the measured energies, E_f, the azimuthal, ϕ_f, and the polar, θ_f, angles of the reconstructed jets and leptons. In this case the uncertainties are just the detector resolutions and one can safely neglect correlations between these quantities.

The constraints of energy and momentum conservation can either be realised by introducing Lagrange multipliers or through penalty terms that are added to the χ^2 term. For example, the energy conservation can be taken into account by the term $(E_{\mathrm{tot}} - \sqrt{s})/\sigma_s$, where E_{tot} represents the energy sum of the four fermions and $\sqrt{s}$ is the centre-of-mass energy. The parameter σ_s gives the uncertainty in the determination of the centre-of-mass energy coming from the LEP energy calibration (see Sect. 2.3).

As an example, in the case of the semi-leptonic final state, three fermion momenta are reconstructed which leads to a set of nine quantities measured in the detector: E_i^{meas}, θ_i^{meas}, ϕ_i^{meas} $(i = 1..3)$. These quantities are used as start values for a fit of nine free parameters: E_i, θ_i, ϕ_i $(i = 1..3)$. The χ^2 function which has to be minimised is the following:

$$\chi^2 = \sum_{i=1}^{3} \left\{ \left(\frac{E_i - E_i^{\mathrm{meas}}}{\sigma(E_i)} \right)^2 + \left(\frac{\theta_i - \theta_i^{\mathrm{meas}}}{\sigma(\theta_i)} \right)^2 + \left(\frac{\phi_i - \phi_i^{\mathrm{meas}}}{\sigma(\phi_i)} \right)^2 \right\} + \left(\frac{\sum_{i=1}^{4} E_i - \sqrt{s}}{\sigma_s} \right)^2 + \left(\frac{m_{\mathrm{jj}} - m_{\mathrm{l}\nu}}{\Gamma_{\mathrm{W}}} \right)^2 , \tag{6.8}$$

where $\sigma(E_i)$, $\sigma(\theta_i)$ and $\sigma(\phi_i)$ are the uncertainties of the measurements E_i^{meas}, θ_i^{meas} and ϕ_i^{meas} as derived from detector resolution studies and partially from simulation. During the minimisation the jet velocities, $\beta_i = |\boldsymbol{p_i}|/E_i$, are kept fixed, because the energy scale, which is the main parameter adjusted by the kinematic fit, cancels in this ratio. As the masses of the charged leptons are known, the total momentum of the three measured fermions and therefore the missing momentum carried away by the undetected neutrino can be calculated at each minimisation step. This is technically more efficient than introducing three additional parameters for the neutrino and adding three penalty terms for momentum conservation to the χ^2.

Also the invariant masses, m_{jj} and $m_{\mathrm{l}\nu}$, are recalculated in each minimisation step from the four-momenta of the final-state fermions using the actual parameter set of energies and angles. The resolution chosen for the invariant-mass difference in the equal-mass constraint is the natural width of the W boson, Γ_{W}. In general, the fermion angles are a priori better measured than the energies and momenta. Therefore, the kinematic fit improves more the energy measurement than the determination of the angles.

The effect on the invariant-mass spectrum due to the implementation of kinematic constraints is shown in Fig. 6.3 using Monte Carlo events of the $qq\mu\nu$ final state simulated with the L3 detector simulation. The distribution of the resulting χ^2 probability of the kinematic fit is also given. As expected, the probabilitiy values are equally distributed with the exception of very small values representing events where the kinematic fit has failed. The resolution of the invariant mass of the hadronic system is already improved by a factor of two due to the scaling of the measured jet energies such that their sum equals to the beam energy. The introduction of the 2C kinematic fit improves

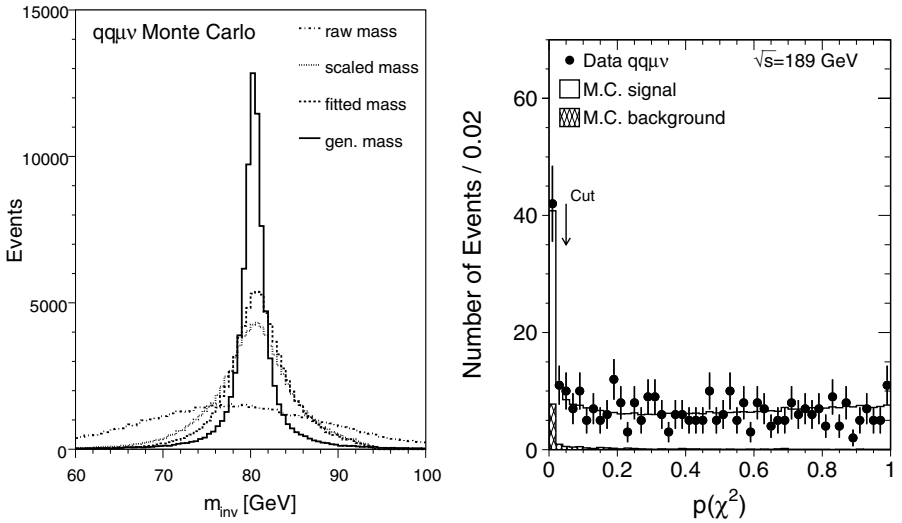

Fig. 6.3. The invariant-mass spectrum of the hadronic system of $qq\mu\nu$ events using the raw jet energies, after energy scaling, after applying a kinematic fit and on generator level (*left*) and the χ^2 probability distribution (*right*) of the kinematic fit for $qq\mu\nu$ events recorded at 189 GeV

the resolution by an additional factor of about 2.3 yielding a final resolution of 2.8 GeV which is still significantly larger than the mass uncertainty caused by the natural width of the W boson.

In the case of the $qq\tau\nu$ final state additional energy is carried away by neutrinos produced in the τ decay. In W decays the τ lepton gains a rather high energy compared to its mass and the decay products of the τ are concentrated in a narrow cone. Therefore the angular direction of the τ can be derived from the direction of the decay products, but the energy of the τ lepton has to be treated as an additional free parameter. Only one constraint is left in the kinematic fit of the $qq\tau\nu$ events and in this case the result of the kinematic fit equals exactly to the rescaling of the jet energies by a common factor such that the sum of their energies equals half the centre-of-mass energy, effectively imposing an equal-mass constraint between the two W bosons.

A comparison of the invariant mass spectra before and after applying kinematic constraints is shown in Fig. 6.4. The resolution of the invariant mass of the hadronic system in $qq\tau\nu$ events is already improved by a factor of 2.5 due to the scaling of the measured jet energies such that their sum equals to the beam energy. In the case of $qqe\nu$ and $qq\mu\nu$ events, the introduction of the 2C kinematic fit improves the resolution by a factor of three, whereas the mass resolution of the $qqqq$ events is improved by a factor of eight after applying the 5C fit.

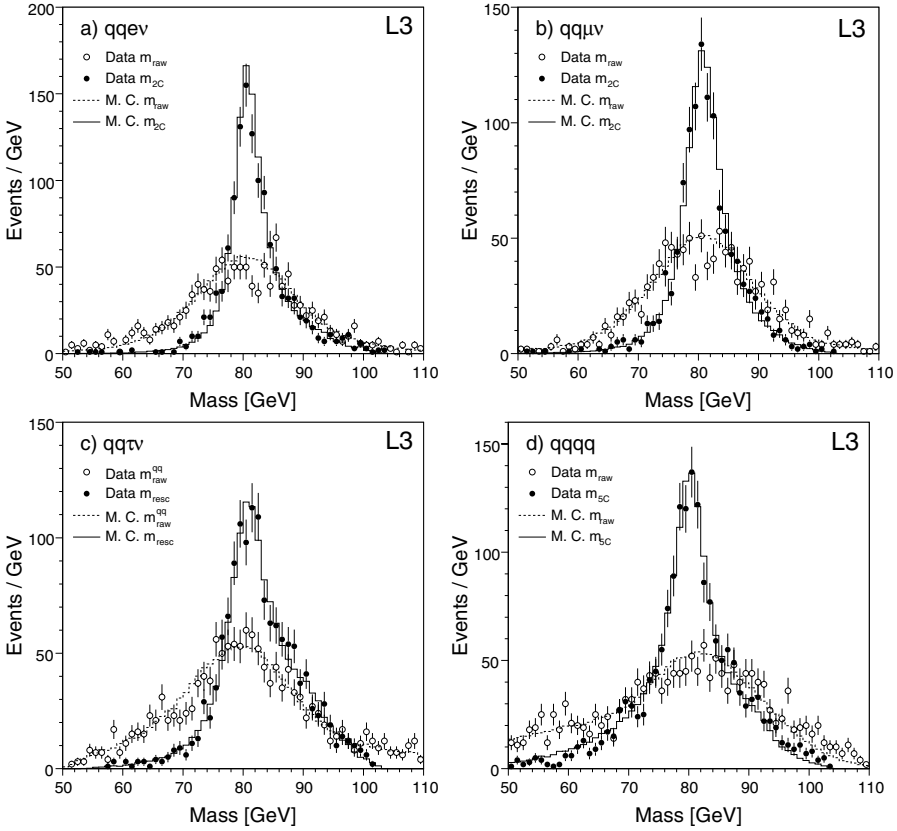

Fig. 6.4. Improvement of the mass resolution due to kinematic constraints for the four final states: (**a**) $qqe\nu$, (**b**) $qq\mu\nu$, (**c**) $qq\tau\nu$, (**d**) $qqqq$. The open circles depict the raw mass resolution showing the reconstructed mass as calculated from the four-momenta of the measured fermions. The full data points represent the mass spectrum after applying the kinematic fit or jet energy rescaling

6.3.3 Jet Pairing in Fully-Hadronic Events

In the fully-hadronic final state of W-pair production no momentum is carried away by undetected neutrinos. None of the constraints has to be used for the calculation of missing momentum and therefore all five constraints are active in the kinematic fit. As a consequence the fully-hadronic channel provides the best mass resolution of all final states.

One complication, however, is the association of the jets to the two W bosons. The four jets can be arranged to two jet-pairs in three different ways. In the case of five jets, ten different associations of the jets to the W bosons are possible. In the case of the L3 analysis [6] the final χ^2 value of the kinematic fit is used to choose the jet association most likely to be the correct one. In

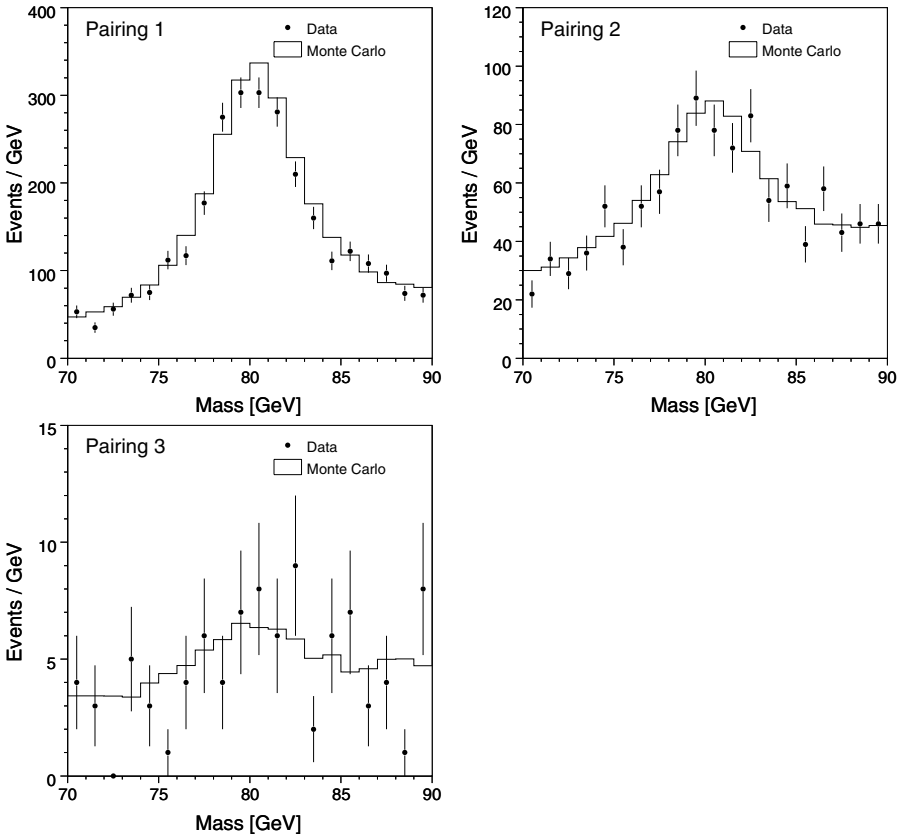

Fig. 6.5. The mass resolution of the *qqqq* event sample of the L3 analysis. Shown are the mass spectra for the (**a**) first, (**b**) second, (**c**) third probable jet pairing

Fig. 6.5 the reconstructed mass spectra for the most, the second most and the third most probable jet pairings in four-jet events are shown. One observes that even the third jet pairing, which is the one with the lowest probability to be the correct one, still contains some information on the W mass.

Therefore, in the L3 analysis, all three pairings of the four-jet final state and the three most probable pairings of the five-jet events are used for the determination of the W mass. ALEPH [4] chooses only one of the three possible jet pairings in four-jet events by selecting the combination with the largest value of the matrix element, $\mathcal{M}(\mathrm{e}^+\mathrm{e}^- \to ffff)$, for the given configuration. In the case of OPAL [7] the two most probable pairings of the four-jet events are considered and the five-jet events are subject to a likelihood algorithm to select the the preferred jet pairing. One input to this likelihood is, for example, the difference of the two W masses in the 4C fit. The calculated jet pairing likelihood is correlated with the mass resolution. Figure 6.6 shows

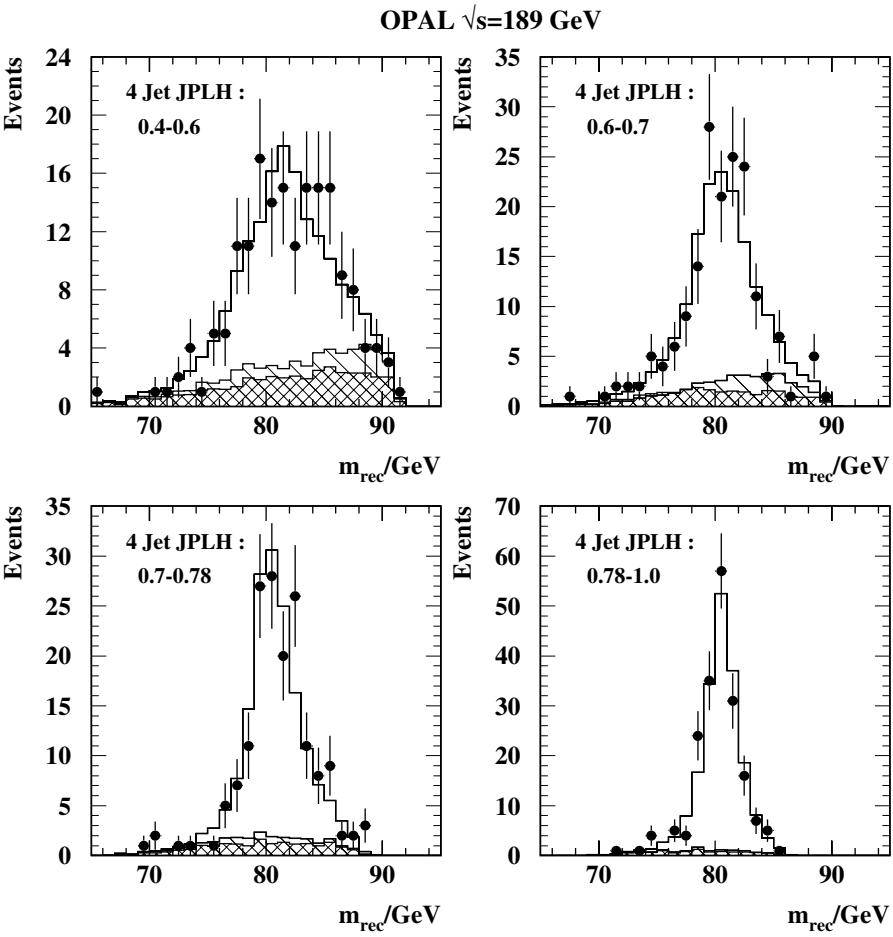

Fig. 6.6. The mass spectrum for $qqqq$ events in bins of the jet-pairing likelihood

that both the mass resolution is improved and the background contamination is reduced with increasing jet-pairing likelihood. This correlation can be exploited in the final mass extraction to improve the statistical sensitivity of the W mass measurement.

6.3.4 Photon and Gluon Radiation

In the kinematic fit energy and momentum conservation are assumed and the four-momenta of the final-state fermions must add to zero. This assumption is wrong in the case of high energy initial-state radiation. Initial-state photons are radiated predominantly along the beam and escape detection. However, in about 5% of the semi-leptonic events, high-energy photons of more than

5 GeV, radiated by the initial-state electrons and positrons, are measured in the detector. Since this initial-state radiation reduces the effective centre-of-mass energy the detected photons are taken into account in the kinematic reconstruction and fitting of the event. This results in a better resolution of the reconstructed invariant masses for those events. However, if photons escape undetected, the analysis relies on the Monte Carlo simulation of this effect. It is therefore essential that initial-state radiation is precisely modelled by the Monte-Carlo simulation to account for this effect. Even low-energy photons in the MeV range, which do not change the event kinematics within the detector resolution, have to be simulated correctly. Since the centre-of-mass energy of the LEP collider is measured with a precision of about 20 MeV, this accuracy has to be matched by the photon simulation. To safely neglect the influence of energy loss due to photon radiation, the energy spectrum of this radiation has to be simulated correctly down to energies below the 10 MeV level (see Sect. 6.5.1).

The invariant-mass resolution in the fully-hadronic final state is improved by taking into account gluon radiation from quarks. If events with hard gluon radiation are clustered into four jets, hadrons originating from the gluon can easily be associated to the wrong W boson. Monte Carlo studies show that clustering the same events into five jets reduces the problem of wrong associated hadrons and the mass resolution in these events improves. On the other hand, this gain has to be weighted against the increased difficulty to find the correct jet combination out of ten possibilities instead of three in the case of four jets.

The Durham clustering parameter, y_{45}, at which the jet reconstruction changes from a four-jet to a five-jet configuration is used to separate events with and without gluon radiation. In the case of the L3 analysis, the events with a $\log y_{45}$ parameter value smaller than -6.0 are treated as four-jet events and the remaining sample as five-jet events. The two samples of about equal size are treated separately since their mass resolutions are different. This yields a reduction of 10% on the uncertainty of the W mass determined in the fully-hadronic channel. The OPAL analysis uses the same separation method, but with a cut at $\log y_{45} = -6.8$. Both analyses are equivalent to the DELPHI approach, where the jets are clustered with a fixed y_{cut} of 0.002, the parameter which defines how far the jet clustering advances. Events remaining with more than five jets are reclustered into five jets. This is identical to a separation of four-jet and five-jet final states at $\log y_{45} = -6.2$.

6.4 Extraction of the W Mass

In Fig. 6.7 the invariant-mass spectra as measured by the DELPHI experiment are presented. Similar spectra are obtained by the other three LEP experiments. The W mass is extracted from these spectra by comparing them with the theoretical expectation based on a Breit-Wigner resonance of the

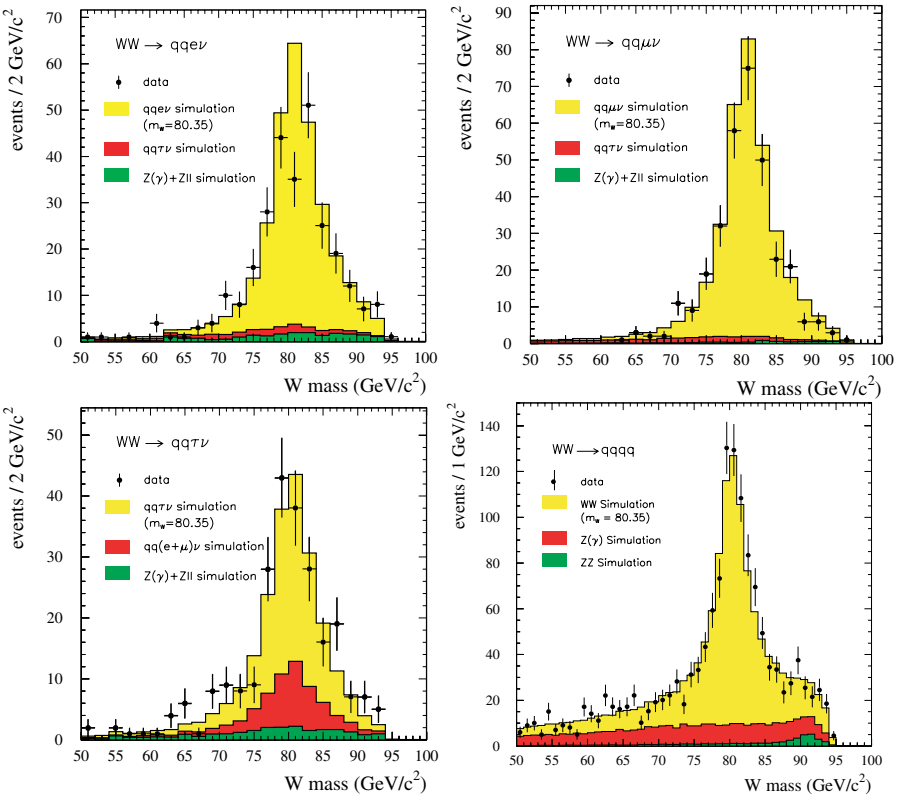

Fig. 6.7. The spectrum of the invariant masses measured by DELPHI for the $qqqq$, $qqe\nu$, $qq\mu\nu$ and $qq\tau\nu$ channels

W boson. The Breit-Wigner function can not be fitted directly to the measured mass spectrum, because effects such as detector resolution or photon and gluon radiation have to be taken into account.

A detailed and precise Monte-Carlo simulation of these effects is mandatory. In principle, the mass of the W boson could be determined by comparing various samples of Monte-Carlo events generated with different W masses to the data and selecting the W mass which yields the best agreement between the mass spectra of data and simulation. Because the production of fully simulated Monte-Carlo events for each possible W-mass value would require too much computing power a re-weighting procedure is applied to construct Monte Carlo samples corresponding to different mass values. Using this method, effects of event selection and resolution are automatically taken into account.

Alternatively, an analytic function can be constructed, which gives a likelihood for each event as a function of m_{W}. A fit of the total likelihood then yields the best estimation of m_{W} for the given set of events. The same fit is done for data and Monte-Carlo and the observed m_{W} shift in the Monte-Carlo

fit is then applied to the data result. By this method several effects, such as detector resolution, hadronisation and photon radiation which can not be described by this analytic function, are taken into account. In the W-mass fits, one imposes the Standard Model relation $\Gamma_{\mathrm{W}} = 3G_{\mathrm{F}} m_{\mathrm{W}}^3 (1+2\alpha_{\mathrm{s}}/3\pi)/(2\sqrt{2}\pi)$. In fits, where also Γ_{W} is extracted, m_{W} and Γ_{W} are treated as independent quantities.

6.4.1 Monte-Carlo Re-Weighting and Binned Likelihood Fit

In the ALEPH analysis [4] m_{W} and Γ_{W} are extracted by fitting invariant mass spectra from fully simulated Monte-Carlo samples to the spectra observed in data. Here, the Monte-Carlo samples are re-weighted using the CC03 matrix elements corresponding to various values of m_{W} and Γ_{W}. The signal Monte Carlo, which is originally generated using a particular value of the W-boson mass, $m_{\mathrm{W}}^{\mathrm{gen}}$, and width, $\Gamma_{\mathrm{W}}^{\mathrm{gen}}$, is modified in a re-weighting procedure to represent a different W mass, $m_{\mathrm{W}}^{\mathrm{rew}}$, and width, $\Gamma_{\mathrm{W}}^{\mathrm{rew}}$. To each Monte-Carlo event, j, a weight, R_j, is assigned defined by the ratio

$$R_j(m_{\mathrm{W}}^{\mathrm{rew}}, \Gamma_{\mathrm{W}}^{\mathrm{rew}}, m_{\mathrm{W}}^{\mathrm{gen}}, \Gamma_{\mathrm{W}}^{\mathrm{gen}}) = \frac{\left|\mathcal{M}(p_j^1, p_j^2, p_j^3, p_j^4, k_j^\gamma, m_{\mathrm{W}}^{\mathrm{rew}}, \Gamma_{\mathrm{W}}^{\mathrm{rew}})\right|^2}{\left|\mathcal{M}(p_j^1, p_j^2, p_j^3, p_j^4, k_j^\gamma, m_{\mathrm{W}}^{\mathrm{gen}}, \Gamma_{\mathrm{W}}^{\mathrm{gen}})\right|^2}\,, \qquad (6.9)$$

where $\mathcal{M}$ is the matrix element of the four-fermion final state under consideration. In contrary to the box method used by L3 and explained in the next section, here the re-weighted Monte Carlo is compared to a binned multi-dimensional data distribution of variables sensitive to m_{W}.

In the $qqqq$ channel a binned two-dimensional likelihood fit is performed to the data distribution of the two masses obtained in the 4C fit. The order of the two masses is randomised before fitting, in order to be consistent with the probability density function, which is symmetric with respect to the two masses. In the case of $qq\ell\nu$ events the mass extraction fit is performed using the mass of the 2C-fit mass and its uncertainty, as estimated by the kinematic fit. As additional information, the 1C mass of the hadronic system is used. This results in a three-dimensional binned likelihood fit which yields a 14% improvement in statistical precision compared to the one-dimensional fit.

The bin sizes are chosen such that the number of events per bin is approximately constant. The number of Monte Carlo events in any bin is required to be larger than 400 to obtain a stable and reliable fit result.

6.4.2 Monte-Carlo Re-Weighting and Box Fit

The L3 experiment measures m_{W} and Γ_{W} [6] using an unbinned maximum likelihood fit, where the likelihood for each selected data event is calculated using the box method [9]. In this method one counts the number of events from a large Monte-Carlo sample, which are located in the kinematic phase

space within a well defined domain (the box) around the data event under consideration. The number of Monte-Carlo events inside the box is used as a measure for the differential cross section, and the likelihood of the given event is calculated from it. The box-fit method using Monte-Carlo re-weighting determines m_{W} and Γ_{W} without any bias as long as the Monte Carlo describes effects such as photon and gluon radiation, hadronisation and detector resolutions correctly.

Separate likelihood functions are calculated for the four final states, $qqqq$, $qqe\nu$, $qq\mu\nu$ and $qq\tau\nu$ as well as for the various different centre-of-mass energies. For each of the combinations a likelihood function, $L(m_{\mathrm{W}}, \Gamma_{\mathrm{W}})$ is calculated from the product of the individual likelihoods, evaluated for each mass reconstruction, i, performed for a given semi-leptonic event or a given pairing of the four- and five-jet samples of the fully-hadronic final state. The likelihoods are calculated from the normalised differential cross sections in terms of the reconstructed masses, m_{inv}:

$$L(m_{\mathrm{W}}, \Gamma_{\mathrm{W}}) = \prod_i \frac{f(m_{\mathrm{W}}, \Gamma_{\mathrm{W}}) \left(\dfrac{\mathrm{d}\sigma(m_{\mathrm{W}}, \Gamma_{\mathrm{W}})}{\mathrm{d}m_{\mathrm{inv}}}\right)_i + \left(\dfrac{\mathrm{d}\sigma_{\mathrm{back}}}{\mathrm{d}m_{\mathrm{inv}}}\right)_i}{f(m_{\mathrm{W}}, \Gamma_{\mathrm{W}})\, \sigma(m_{\mathrm{W}}, \Gamma_{\mathrm{W}}) + \sigma_{\mathrm{back}}} \,, \quad (6.10)$$

where σ and σ_{back} are the accepted signal and background cross sections of the corresponding final state. The normalisation factor $f_i(m_{\mathrm{W}}^{\mathrm{fit}}, \Gamma_{\mathrm{W}}^{\mathrm{fit}})$ is calculated such that the sum of accepted background and signal cross section coincides with the measured cross section. In this way the mass and width are determined from the shape of the invariant mass distributions only.

For the re-weighting procedure, which adapts the generated Monte Carlo sample to the variable W mass in the fit, matrix elements calculated with the EXCALIBUR [10] program are used. This calculation is only based on a pure four-fermion final state. To correct for the effect of initial-state radiation the four-vectors of the fermions within the rest frame of the four-fermion system are used.

After summing the weights, R_j, of all Monte Carlo events, j, in the bin Ω_i around the data event, i, the differential cross section of the signal is given by

$$\left(\frac{\mathrm{d}^2\sigma(m_{\mathrm{W}}, \Gamma_{\mathrm{W}})}{\mathrm{d}m_1\, \mathrm{d}m_2}\right)_i = \frac{\sigma^{\mathrm{gen}}}{N^{\mathrm{gen}}} \frac{1}{\Omega_i} \sum_j R_j(m_{\mathrm{W}}, \Gamma_{\mathrm{W}}, m_{\mathrm{W}}^{\mathrm{gen}}, \Gamma_{\mathrm{W}}^{\mathrm{gen}}) \,. \quad (6.11)$$

In case of background Monte Carlo the same bin size is chosen and the differential distribution of the background is determined by dividing the number of selected background Monte Carlo events, $(N_{\mathrm{back}}^{\mathrm{sel}})_i$, in the bin around a given data event, i, by the bin size, Ω_i:

$$\left(\frac{\mathrm{d}^2\sigma_{\mathrm{back}}}{\mathrm{d}m_1\, \mathrm{d}m_2}\right)_i = \sigma_{\mathrm{back}} \frac{(N_{\mathrm{back}}^{\mathrm{sel}})_i}{\Omega_i} \,. \quad (6.12)$$

One-dimensional boxes in the m_{inv} space are constructed for the determination of Γ_{W}, whereas for the measurement of m_{W} the box-fit procedure is generalised to a two-dimensional differential cross section as function of the 4C and 5C invariant masses.

6.4.3 Event Likelihood from a Convolution Function

In the DELPHI analysis [5] the W mass is determined from an overall minimisation of a product of individual event likelihoods. For each of the selected events a likelihood is calculated by:

$$L(m_{\mathrm{W}}, \Gamma_{\mathrm{W}}) = P_e\, S(m_{\mathrm{fit}}, \sigma_{\mathrm{fit}}, m_{\mathrm{W}}, \Gamma_{\mathrm{W}}) + (1 - P_e)\, B(m_{\mathrm{fit}})\,, \quad (6.13)$$

where P_e is the event purity, S is the function which predicts the invariant-mass spectrum for given m_{W} and Γ_{W} and the function B describes the spectrum of the background events. The reconstructed event mass, m_{fit}, is the result of the kinematic fit.

The signal function S is defined as a convolution of three components, a Breit-Wigner function F_{BW} describing the W lineshape, a radiator function R modelling the ISR spectrum and a Gaussian function G which takes the detector resolution into account:

$$S(m_{\mathrm{fit}}, \sigma_{\mathrm{fit}}, m_{\mathrm{W}}, \Gamma_{\mathrm{W}}) = \int_0^{E_{\mathrm{beam}}} \mathrm{d}m\; G(m - m_{\mathrm{fit}}, \sigma_{\mathrm{fit}}) \cdot \int_0^1 \mathrm{d}x\; R(x)\; F_{\mathrm{BW}}((1-x)m, m_{\mathrm{W}}, \Gamma_{\mathrm{W}})\,. \quad (6.14)$$

The ISR spectrum is parameterised using the well known radiator function

$$R(x) = \beta\, x^{\beta-1} \qquad \text{with} \qquad \beta = \frac{2\pi}{\alpha}\left(\log\frac{s}{m_{\mathrm{e}}^2} - 1)\right)\,. \quad (6.15)$$

A similar event likelihood is constructed for the $qqqq$ event, but here a two-dimensional convolution over the mass range of both W bosons is performed. Then a combined likelihood of the selected data events is calculated from the product of all individual event likelihoods. Maximum likelihood fits are used to extract m_{W} and Γ_{W}.

As the convolution functions described above do not describe all of the physics and detector effects, which influence the invariant-mass spectrum, the result of the maximum likelihood fit is calibrated against Monte Carlo simulation. The simulated events are treated the same way as the data and the difference between the fitted mass and the generated mass is taken as mass bias of the analysis for which the data result is corrected. Alternatively, the mass bias of the analysis can be determined by re-weighting a Monte-Carlo sample such that it agrees with the fit result of the data sample. The mass bias and therefore the corrections to the fitted mass in data are of the order of 50 MeV.

6.4.4 Fit of an Analytic Breit-Wigner Function

The OPAL experiment compares three different methods [7] to extract the W mass from the invariant-mass spectrum: Monte-Carlo re-weighting with a binned likelihood fit to the measured invariant-mass spectrum, the convolution method constructing likelihood curves for each event, and the straight-forward approach of fitting the mass spectrum with an analytic Breit-Wigner function.

OPAL observes that for the $qq\ell\nu$ channel a relativistic Breit-Wigner function with a different width above and below the peak, gives a satisfactory description of the reconstructed mass spectrum:

$$S(m_{\mathrm{inv}}) = A \, \frac{m_{\mathrm{inv}}^2 \Gamma_{+(-)}^2}{(m_{\mathrm{inv}}^2 - m_{\mathrm{W}}^2)^2 + m_{\mathrm{inv}}^2 \Gamma_{+(-)}^2} \, , \tag{6.16}$$

where Γ_+ (Γ_-) is the width assumed for all m_{inv} values above (below) the resonance peak at m_{W}. The widths, $\Gamma_{+(-)}$, are determined from the spectra obtained with Monte-Carlo simulations. The differences in Γ_+ and Γ_- are caused by initial-state radiation, which shifts the reconstructed masses towards higher values. An unbinned maximum likelihood fit of this analytic Breit-Wigner function to the measured mass spectrum is performed, where the shape of the expected background is taken from Monte Carlo and kept fixed during the fit. The fit is restricted to the mass range of 70 GeV $< m_{\mathrm{inv}} <$ 88 GeV, the region where it has been proven in Monte Carlo simulations that the Breit-Wigner function gives a good description of the reconstructed lineshape for at least ten times the integrated luminosity of the data.

The extracted W mass has to be corrected for additional effects not accounted for in the Breit-Wigner fit. The correction is determined by applying the same fit to Monte-Carlo samples. Obviously, with the presented Breit-Wigner fit, where $\Gamma_{+(-)}$ has to be taken from simulation, an extraction of Γ_{W} is not possible.

OPAL has compared the statistical significance of the three different mass extraction methods. The expected statistical uncertainty on m_{W} for the data sample collected at $\sqrt{s} = 189$ GeV is calculated, where one obtains 78 MeV for the Breit-Wigner fit, 76 MeV in case of Monte-Carlo re-weighting and 72 MeV using the event likelihoods. As expected, the calculation of individual event likelihoods yields the highest precision, because it attempts to exploit all available information of the kinematics of each event. Therefore the convolution method is used for the final OPAL result.

6.5 Systematic Uncertainties

The systematic uncertainties of the W-mass measurement after combining the results of the four LEP experiments are summarised in Table 6.1. The following sections describe in detail how the uncertainties due to the various error sources have been estimated.

Table 6.1. Uncertainties on the determination of m_{W} for the LEP combination

Uncertainties on m_{W} [MeV]			
Error Source	$qq\ell\nu$	$qqqq$	Combined
Calibration of $\sqrt{s}$	9	9	9
Detector effects	10	8	9
$4f(\gamma)$ generation	8	5	7
Hadronisation	13	18	14
Colour reconnection	–	35	8
Bose-Einstein correlations	–	9	2
Other	3	10	3
Total Systematic	21	44	22
Total Statistical	30	40	25
Total	36	59	34

6.5.1 Four-Fermion Generation and Photon Radiation

The correct simulation of the four-fermion final state of W-pair production is an important pre-requisite of the W mass analysis. It includes the proper description of the Breit-Wigner lineshape of the W boson including its radiative corrections, the modelling of multiple-photon radiation and the inclusion of interferences with other four-fermion processes.

Especially radiation of photons in the initial state has a large impact on the mass reconstruction and must be modelled with sufficient accuracy. Initial-state radiation removes energy from the event before the formation of the W resonances. Therefore, the W bosons will have less momentum and their decay angle increases. In the reconstruction procedure the kinematic fit constrains the event energy back to the nominal centre-of-mass energy whereas the fermion angles will be unchanged due to the high precision of the angular measurement. This leads to a positive shift of the reconstructed mass. If ISR is switched off completely in Monte Carlo a change of the W mass of about 500 MeV is observed. Due to this large mass shift and the fact that most of the ISR escapes undetected, one relies on the proper and accurate calculation of initial-state radiation.

In addition to initial-state radiation also final-state radiation from the fermions and photon radiation from the W bosons themselves have to be considered. This is done by full $\mathcal{O}(\alpha)$ calculations, in the approximation that these corrections are only relevant for the resonant diagrams. The KandY [11] and the RacoonWW [12] programs are such state-of-the-art Monte-Carlo generators. They are described in detail in Sect. 5.1. RacoonWW is using the constant-width ansatz whereas KandY implements an energy dependent W width. Both definitions of the W propagator differ by 27 MeV in the W mass. Therefore the input value of m_{W} for the RacoonWW program has to be chosen 27 MeV lower than for the KandY program to make the output of both

programs directly comparable. The authors of RacoonWW and KandY have compared the outcome of their programs and estimated the resulting uncertainty on the determination of the W mass to be below 10 MeV [13]. However, their tests are based on generator level studies and neglect explicitly the influence of the kinematic fit.

A dedicated study [14] was performed by Fabio Cosutti comparing the two generators in the case of the DELPHI W-mass analysis. Differences could be tracked down to un-physical cut-offs in the photon radiation of the RacoonWW approach. They can be avoided using an inclusive W-mass reconstruction, combining hard photons to the nearest fermion. Additionally, cross-checks between different input flags of the YFSWW generator were performed. The results were used to estimate the systematic uncertainties due to the modelling of ISR and FSR and due to the missing terms beyond the given $\mathcal{O}(\alpha)$ calculation. Each of these error sources was found to be of the order of only 1 MeV.

In the L3 analysis a total of 300 000 Monte Carlo events of the $qqe\nu$, $qq\mu\nu$ and $qqqq$ final states are generated with the RacoonWW program at $\sqrt{s} = 207$ GeV, including full detector simulation. Events with hard-photon radiation are selected on generator level using the CALO5 algorithm [13], which recombines soft and collinear photons with the nearest fermion. These are then used instead of data in the mass fit which relies on KandY as the reference Monte Carlo. The shift of the W mass derived from the comparison of the programs is scaled by the fraction of events with hard-photon radiation, which is of the order of 10%. In an additional test, the KandY events are reweighted such that they represent the $\mathcal{O}(\alpha^2)$ ISR corrections instead of the $\mathcal{O}(\alpha^3)$ calculation. Based on these tests an uncertainty of 8 MeV is quoted.

In their analyses of data taken at $\sqrt{s} = 189$ GeV, the ALEPH and the OPAL collaboration tried to estimate the systematic uncertainty due to the modelling of ISR by re-weighting simulated KoralW events such that they represent $\mathcal{O}(\alpha)$ instead of the available $\mathcal{O}(\alpha^3)$ corrections. The observed effect is marginal and always below 2 MeV, which is taken as systematic uncertainty.

DELPHI also uses a re-weighting method where they compare the ISR treatments of the KoralW program and the algorithm used in the DELPHI QEDPS program, which is based on a parton shower approach. The largest of the observed mass shifts is conservatively taken as the systematic uncertainty which amounts to 16 MeV.

6.5.2 Hadronisation

After the generation of the four-fermion state the quark pairs are subject to a Monte-Carlo program modelling the hadronisation process. Three different schemes, implemented in the programs Pythia, Herwig and Ariadne, are widely used for this purpose. QCD studies of the LEP 1 data were not able to decide between the predictions of the three programs. Therefore, systematic effects due to modelling of the hadronisation process are determined by

comparing the result of three different mass fits using Monte-Carlo events simulated with the programs Pythia, Herwig and Ariadne, respectively.

The influence of the hadronisation model on the reconstruction of the W mass can be understood in the following way. To calculate the invariant mass of two hadronic jets their energies, the angle between the jets, and the individual jet masses are needed. The effects on the jet energies should be cancelled by the kinematic fit constraining the energy of the jet system to the beam energy. Effects on the inter-jet angle are small, whereas the jet masses depend very much on the hadronisation parameters.

The four-momenta of calorimetric clusters which are used to form hadronic jets are calculated using their energy and angle measurements and assuming their masses to be the pion mass. Frequently produced hadrons with larger masses than pions are kaons and protons. In the jet reconstruction their mass is not properly taken into account, which leads to a shift of the jet masses. This mass shift is corrected during the fit of the data to the Monte Carlo simulation, which also contains these heavier hadrons. On the other hand, if the hadronisation model predicts different multiplicities for these heavier hadrons than present in data, a systematic effect on the measurement of the W mass is expected. The mean number of charged kaons and protons produced in the W decays has been measured in a DELPHI analysis [15]. This measurement is compared to the Monte-Carlo simulation and agreement is found within the statistical precision.

To assess the systematic uncertainty due to hadronisation the ALEPH, DELPHI and OPAL collaborations have compared the W mass results when using the programs Pythia and Herwig, respectively. Here, identical events at the level of the four-fermion state were subject to both hadronisation programs. In addition, DELPHI and OPAL compared Pythia Monte Carlo samples generated with various QCD parameters, for example the hadronisation scale Λ_{QCD} and the shower parameter σ_q, varied with respect to the standard tuning of the Pythia generator.

ALEPH also adjusted the hadronisation models to the data in terms of observables, which are closely related to the hadronisation process, such as the jet masses. The Monte-Carlo events are re-weighted in order to reproduce exactly the corresponding distribution in data. The resulting mass shift evaluated with the re-weighted Monte-Carlo events is never larger than 30 MeV.

In the L3 analysis the Pythia Monte Carlo is compared to Herwig and Ariadne simulations based on identical events at the four-fermion level. In Fig. 6.8 the jet-mass distribution for the three models is compared to data. The comparison shows a slight preference for the Pythia Monte Carlo. To assess the systematic uncertainty due to the hadronisation the data events in the box fit are replaced by high-statistics samples of Herwig and Ariadne events. The differences to the Pythia base-line Monte Carlo are used to estimate the uncertainty due to hadronisation.

Additionally, the Pythia Monte Carlo events are re-weighted such that the mean number of charged kaons and the mean number of protons agree

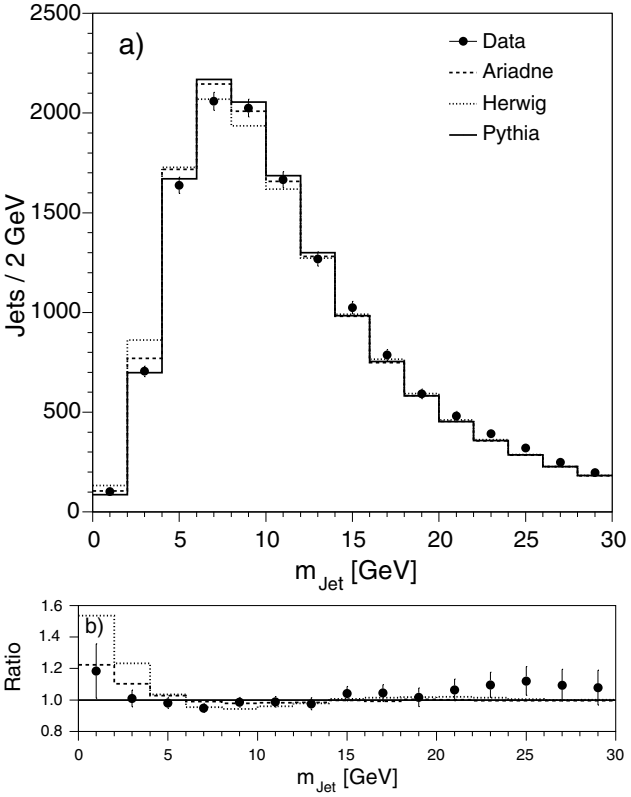

Fig. 6.8. Comparison of the jet-mass spectrum (**a**) of L3 data to three jet-mass spectra predicted by the hadronisation models Pythia, Ariadne and Herwig; Figure (**b**) shows the spectra normalised to the Pythia expectation

with the measurement [15]. It is checked that the invariant-mass spectrum on generator level is not distorted by this re-weighting procedure and that the W mass extracted on generator level does not change. The resulting shift of the W mass is shown in Fig. 6.9. The extracted W mass depends linearly on the number of kaons and protons, and the uncertainty of the measured kaon and proton multiplicities is translated into an uncertainty on the W mass.

6.5.3 Colour Reconnection

The limit on the colour reconnection parameter k_{I} of the SK-I model (see Sect. 5.3) can be translated into a systematic uncertainty of the W-mass determination. Four-fermion final states are simulated with the KandY Monte-Carlo program and the hadronisation of these final states is once simulated with the standard Pythia Monte Carlo and once using the colour-reconnection algorithm. The usual mass extraction method is used with the standard

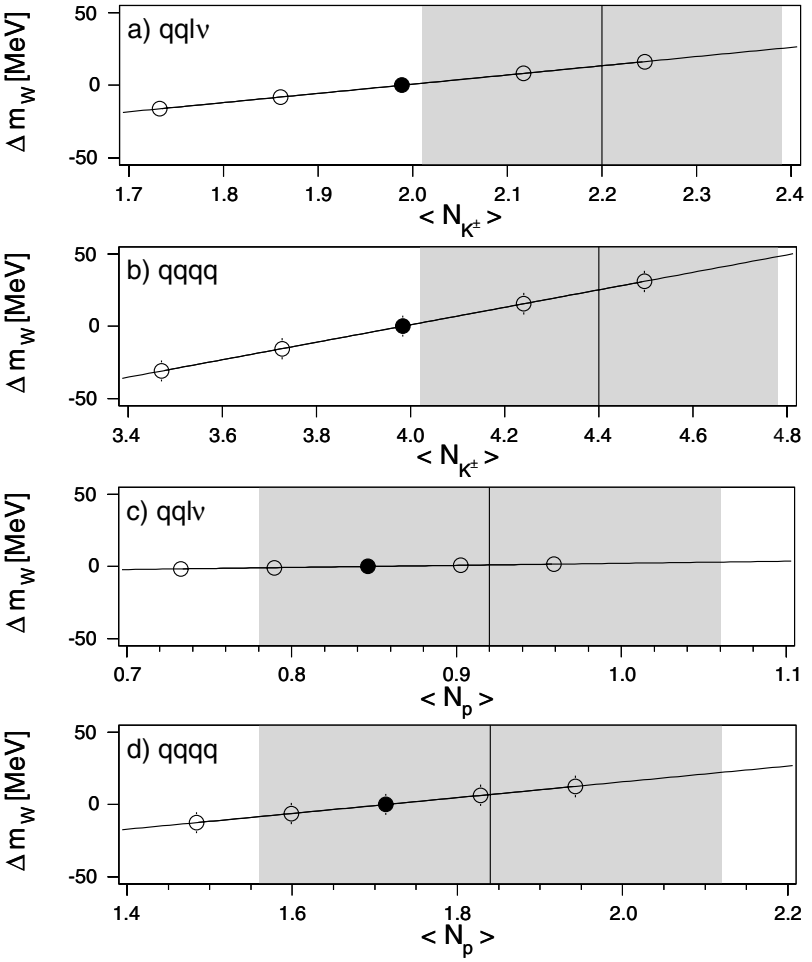

Fig. 6.9. Change of m_{W} in the L3 analysis when re-weighting Monte Carlo events with respect to particle multiplicities: the number of charged kaons for (**a**) $qq\ell\nu$ and (**b**) $qqqq$; the number of protons for (**c**) $qq\ell\nu$ and (**d**) $qqqq$. The *full circle* shows the default Pythia value whereas the *vertical line* shows the multiplicity measured [15]

Monte-Carlo as data and the colour-reconnection Monte Carlo as reference sample. The difference between the input mass of the Monte Carlo and the fit result is the mass bias introduced by colour reconnection. To study the influence of k_{I} the standard simulation without colour reconnection and the SK-I model with 100% reconnection probability are mixed. Both Monte Carlo samples are based on the same events at the four-fermion level. For each event the hadronic final state produced with the standard Pythia setting is replaced by the colour-reconnected final state, if a random number exceeds the specific

event reconnection probability, P_{reco}. This reconnection probability is given by

$$P_{\mathrm{reco}} = 1 - \exp(-f k_{\mathrm{I}}) \,, \tag{6.17}$$

where f is a function of the overlap volume of the two strings.

However, the particle flow analysis is insensitive to colour reconnection effects implemented in other models like Ariadne II and Herwig CR. Although the Ariadne II model has no effect on the particle flow it leads to a significant shift of the W mass which is about -20 MeV for the L3 analysis. Herwig CR introduces a mass bias of -50 MeV. But for all energies and all models the shift of m_{W} is comparable or smaller than the shift predicted by the SK-I model for k_{I} values larger than 1. Hence, the SK-I model is usually used to estimate the systematic uncertainty due to colour reconnection.

Using a cone algorithm for jet clustering lowers the sensitivity to colour reconnection effects, as the analysis will be unaffected by the inter-jet regions where the influence of the CR is largest. Alternatively, removing clusters below a certain momentum cut rejects particles predominantly produced during the non-perturbative phase of the hadronisation process where the colour reconnection effects take place. The shift of the W mass observed between the standard Monte Carlo and various colour reconnection models is shown in Fig. 6.10 for the ALEPH analysis. This mass shift is evaluated for variations of the jet reconstruction where either a cut on the minimum particle momentum, p_{cut}, was applied or the jets were constraint to a cone of radius R. For stronger cuts on p_{cut} or R the W mass shifts due to colour reconnection are significantly reduced.

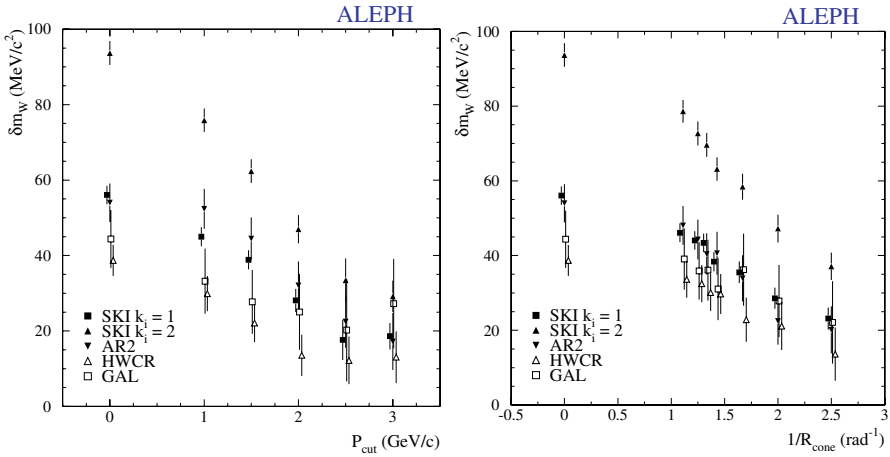

Fig. 6.10. Shift of the W mass between the standard Monte Carlo and various colour reconnection models as function of the cut on the minimum particle momentum, p_{cut}, and on the inverse cone radius, R_{cone}, for the $qqqq$ channel

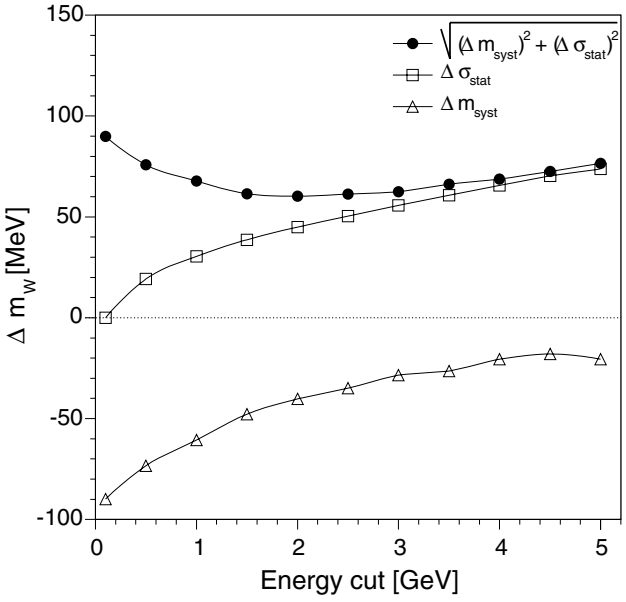

Fig. 6.11. CR effects simulated with the Monte Carlo model SK-I calculated after removing clusters with an energy below a given threshold energy. Shown are the change of m_{W} in Monte Carlo, Δm_{syst}, between the default simulation without CR and the SK-I model using $k_{\mathrm{I}} = 1.1$ and the additional component of the statistical uncertainty on m_{W}, $\Delta\sigma_{\mathrm{stat}}$, after applying the given cluster cut. The quadratic sum of both effects is also shown

The dependency of the W-mass shift on the energy cut is shown in Fig. 6.11 for the case of the L3 analysis. The mass bias is reduced when going to larger values of the energy cut. The statistical uncertainty, however, increases due to the slight degradation of the mass resolution caused by the applied cut. This increase in statistical uncertainty is added in quadrature to the shift of m_{W}. In the case of the L3 analysis a cut at minimum cluster energies of 2 GeV is found to be the optimal choice and is therefore used in the extraction of the W mass in the fully-hadronic final state.

The ALEPH collaboration used the presented cut studies also to extract a limit on the amount of colour reconnection. In the SK-I model the difference of the reconstructed W mass for a given cut relative to the standard analysis without cut increases with increasing reconnection probability. For the data samples also the mass difference between the standard analysis and the cut analysis is studied. The results are consistent with no colour reconnection effect in data and the mass shifts can be used to constrain the SK-I model. This in turn sets limits on the maximum effect on the W mass due to colour reconnection.

6.5.4 Bose-Einstein Effects

Another systematic uncertainty of the W-mass measurement is caused by Bose-Einstein correlations in fully-hadronic events. In particular, the presence of correlations between hadrons coming from different W decays would affect the mass reconstruction.

For the L3 W-mass analysis several Monte Carlo samples with various strengths of inter-W Bose-Einstein correlations, but equal strength of intra-W correlations were subject to the mass extraction procedure. The Bose-Einstein observable J is determined for each of these samples. A linear dependence of the W-mass shift with respect to J is obtained, as presented in Fig. 6.12.

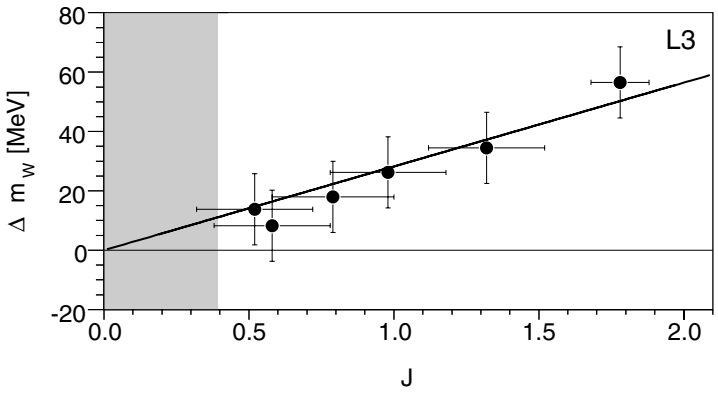

Fig. 6.12. Linearity of W mass shift with respect to the Bose-Einstein correlation observable J

The measurement of the W mass is based on a Monte-Carlo simulation using the LUBOEI BE32 model without inter-W correlations. To estimate the systematic uncertainty due to Bose-Einstein effects the fit is also performed using a simulation with inter-W correlations and according to the Bose-Einstein measurement, presented in Sect. 5.4, 30% of the difference between both results are taken as systematic uncertainty.

6.5.5 Detector Effects

The precision and reliability of the W-mass analysis strongly depends on the quality of the jet measurement. In both, the $qq\ell\nu$ and $qqqq$ channels, the W mass is mainly measured in the hadronic system. The kinematic fit changes mostly the measured jet energies, whereas the angular measurements are much less modified. In a simplified analysis one could measure the invariant mass of a jet pair, and hence the mass of the hadronically decaying W boson, from the rescaled energies and the opening angle of the two jets applying a small

correction due to the finite jet masses. Therefore, especially the directions of the jets have to be measured without any systematic bias, as the opening angle of the jets is directly related to the reconstructed invariant mass.

An angular distortion can be caused by imperfections in the detector alignment and by uncertainties on the length-to-width ratio of the detectors, also known as aspect ratio. These are usually estimated to be negligible. As the decay angles of the W bosons are broadly distributed over all directions, potential angular distortions of any kind should be to first order symmetric in their mass shifts. Therefore they do not affect the W mass, but they lead to an increased W width. Angle dependent effects in the energy scale of the calorimeters could not only cause an offset in the energy measurement of the jets. They could also lead to a bias in the angular measurements of the jets. For example, if clusters in the forward region would be biased to a smaller energy than clusters in the central part of the detector, the direction of the jet would be distorted towards the central detector region. In the ALEPH calibration of jet energies, di-jet events from Z calibration runs have been used to check the jet-energy. In Fig. 6.13 the ratio between the jet energies in data and Monte Carlo is studied as a function of the jet polar angle. Large differences are seen for $|\cos\theta_{\text{jet}}| > 0.95$ and the Monte-Carlo energies are corrected for this effect before the Monte Carlo is used for W-mass extraction.

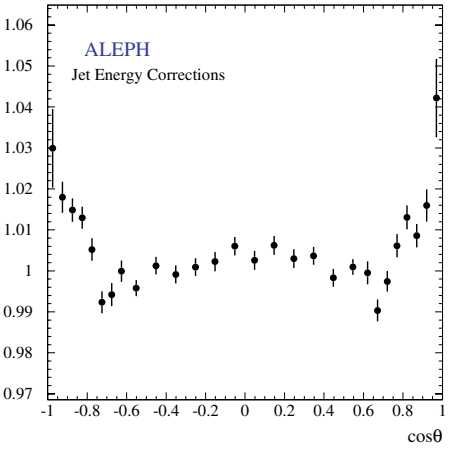

Fig. 6.13. Ratio between the jet energy in data and in Monte Carlo as function of the polar angle derived from Z peak data taken during the calibration runs

L3 uses W-pair events of the *qqqq* channel, where the event is strongly constrained by the kinematic fit. The jet energy has been compared to the jet energy after the kinematic fit. The energy scales differ by $(0.19 \pm 0.23)\%$ in total, which is compatible with zero. Also the angular dependence of the energy scale is studied. Correcting the Monte-Carlo simulation separately for

each polar angle region to agree with the energy scale in data does not change the extracted W mass.

Another approach to get a handle on the systematics of the angular measurement is to compare the angles measured in independent parts of the detector. ALEPH compares the track polar angles as measured by the tracking chamber and the electromagnetic calorimeter. The observed differences between both measurements are simulated by the Monte Carlo to better than 2 mrad. Within the L3 analysis the measurement of the W mass has been repeated using only clusters associated with tracks. For each event, the invariant mass is reconstructed first using the angular information of the calorimetric clusters and then the angles measured in the tracking chamber. The resulting mass shift distribution is shown in Fig. 6.14. Combining all final states leads to a difference on m_{W} between both methods of -2 ± 9 MeV, consistent with zero.

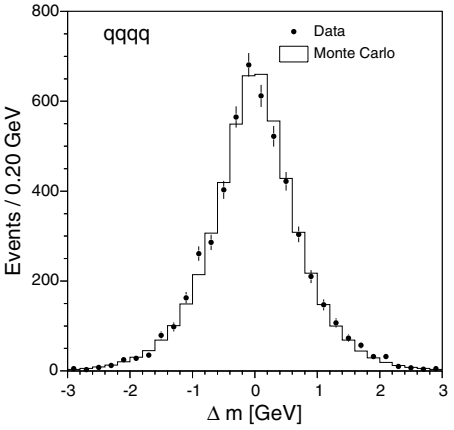

Fig. 6.14. Distribution of the W mass shift between the standard analysis and the jet reconstruction using tracking chamber information only

The systematic uncertainties due to the calibration of the jet energy scales are derived by varying the calorimeter energy scales and the tracking chamber momentum scales over reasonable ranges. The sizes of these variations correspond to the uncertainties estimated from hadronic events collected at the Z resonance. The scale uncertainties differ between the experiments and the specific detector type. They are between 0.2% and 1%, depending on the polar angle. Differences in the description of energy and angular resolution between data and Monte Carlo also affect the W-mass measurement. To check the influence of small changes in the resolutions a typical smearing of the jet energies by 1% and of the jet directions by 0.5° is performed.

The calorimetric energy flow with respect to the jet axis (see Fig. 6.15(a)) has been studied by the L3 collaboration. The distribution shows excellent agreement between data and Monte-Carlo over several orders of magnitude. The impact on the W-mass measurement is studied when clusters outside a given cone around the jet axis are removed from the analysis. No significant shift of the W mass is observed for cones of half-opening angles from 30° to 180° as shown in Fig. 6.15(b) and (c).

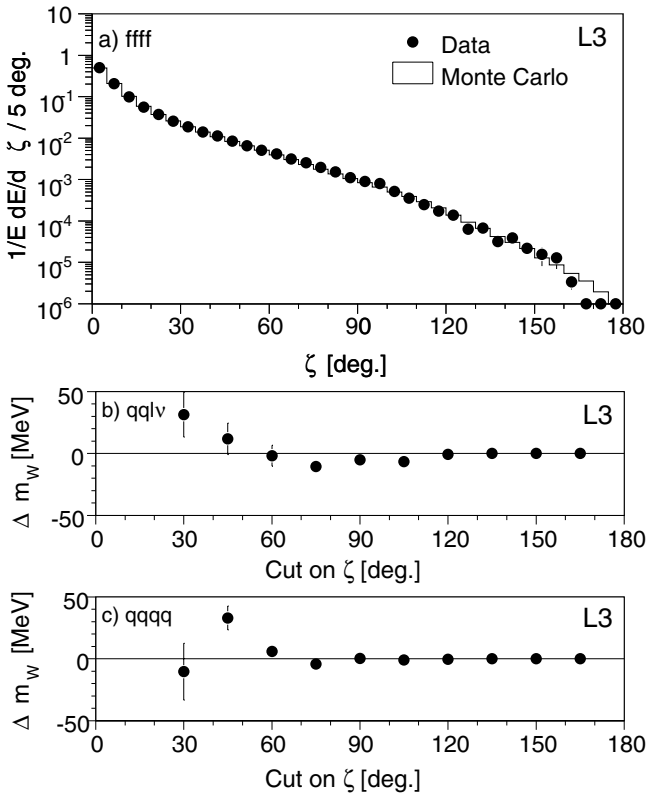

Fig. 6.15. Energy flow with respect to the jet axis for W pair events (**a**) and change of the W mass after removing clusters outside a cone around the jet for semi-leptonic (**b**) and fully-hadronic events (**c**)

For $qqe\nu$ and $qq\mu\nu$ events, possible biases in the reconstruction of the lepton energy also affect the invariant-mass reconstruction. In analogy to hadronic jets, control samples of events selected at the Z pole are used to cross check the reconstruction of leptons. The energy scale of electrons and muons are varied within their accuracy and are used to estimate the systematic

uncertainty due to the lepton energy scale. Effects due to the measurement of the lepton angles are negligible.

In the standard analysis of semi-leptonic W pair events additional calorimetric clusters caused by the charged leptons are associated to one of the jets. This results in a bias on the W mass, if these clusters are not correctly described by the Monte Carlo simulation. Measuring the rate of neutral objects near the high energy electron in $qqe\nu$ events ALEPH observed an excess in data with respect to the Monte Carlo simulation as shown in Fig. 6.16. After removing these energy depositions around the isolated lepton in semi-leptonic events the measurement of the W mass in the semi-leptonic final state changes by -85 MeV. Meanwhile the ALEPH simulation has been corrected and now reproduces the cluster distribution in data. ALEPH and L3 performed a systematic study, where the four-momenta of all clusters within cones of certain opening angles around the lepton are added to the four-momentum of the lepton. The extracted W mass appears to be stable with respect to a variation of the cone angle.

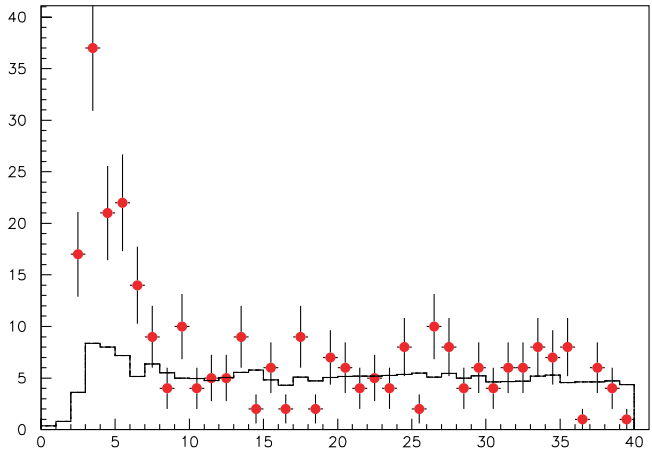

Fig. 6.16. Particle rates with respect to the charged-lepton direction for $qqe\nu$ events as measured by the ALEPH collaboration before applying an cleaning algorithm which removes the satellite clusters in the data events

6.5.6 LEP Beam Energy

As the value of $\sqrt{s}$ is used as a constraint in the kinematic fit, any change of $\sqrt{s}$ causes a shift of the reconstructed mass. In the kinematic fit the exact LEP beam energy is used as determined for the recording time of a given W-pair event.

The beam energy of LEP is known with an accuracy of 10 to 20 MeV depending on $\sqrt{s}$ [16]. The relative error on m_{W} is the same as the relative uncertainty of the beam energy, while the W width is less affected. This has been verified by comparing simulated data samples in which the beam energy used in the kinematic fit is changed accordingly. The complete error matrix of the $\sqrt{s}$ determination, given in Reference [16], is used in the combination of the mass and width measurements performed at different centre-of-mass energies. The error on the beam energy contributes an uncertainty of 10 MeV to the final W mass.

In addition to the uncertainty on the energy scale, an intrinsic width of the beam energy distribution exists. This so called beam spread amounts to about 120 MeV for each beam. Any energy width of the beam would not change the position of the W-boson resonance, but could increase its width. However, the given beam energy width of the order of 0.1% has only little impact on the measurement of the W width and its influence is estimated to be below 5 MeV.

As a cross check of the LEP beam energy, events selected from the $\mathrm{e^+e^-} \to \mathrm{Z}\gamma$ process with hard initial-state radiation were used to measure the mass of the Z boson as presented in Sect. 4.3. Using the precise value Z mass determined at LEP 1 allows to extract the mean $\sqrt{s}$ value from the data. Averaging over all four LEP experiments gives a results consistent with the centre-of-mass energy given by the LEP energy calibration.

6.5.7 Correlations

Correlations between the individual sources of systematic uncertainties have to be considered, when W-mass measurements from different centre-of-mass energies, different final states or different experiments are combined.

In the case of the systematic uncertainty due to the calibration of $\sqrt{s}$ one uses the correlations of the LEP energy determination [16] to combine results from different centre-of-mass energies. Within each final state the uncertainties due to detector effects, the background determination, and the final-state interactions, namely colour reconnection and Bose-Einstein effects, are taken as fully correlated between measurements at different $\sqrt{s}$. Full correlation is also assumed for the uncertainties due to four-fermion generation and hadronisation, which in addition are correlated between all final states.

Due to the different detector setups and selection methods the systematic uncertainties due to detector effects and background determination are taken uncorrelated between the results of the four LEP experiments while full correlation between the experiments is assumed for the effects of initial-state radiation, hadronisation and final state interactions.

6.6 Results for W Mass and Width

The first W-mass measurement at LEP was based on the cross-section behaviour at the threshold of W-pair production (see Sect. 6.1). The individual results of the four experiments are summarised in Table 6.2. Combining these results yields

$$m_{\mathrm{W}} = 80.40 \pm 0.22 \text{ GeV} , \tag{6.18}$$

where the given error is dominated by the statistical uncertainty of the measurement.

Table 6.2. W-mass measurements from the threshold cross section of $\mathrm{e^+e^-} \rightarrow \mathrm{W^+W^-}$ at $\sqrt{s} = 161$ GeV. L3 and OPAL are giving asymmetric errors

Experiment	m_{W} [GeV]
ALEPH	80.14 ± 0.35
DELPHI	80.40 ± 0.45
L3	$80.80^{+0.48}_{-0.42}$
OPAL	$80.40^{+0.46}_{-0.43}$

The results on the W mass from the direct reconstruction are given in Table 6.3. The comparison of the results on m_{W} of the four LEP experiments is illustrated in Fig. 6.17.

Table 6.3. Measurements of the mass of the W boson from direct reconstruction of W decays in $qq\ell\nu$ and $qqqq$ final states, respectively

	m_{W} [GeV]	
Experiment	$qq\ell\nu$	$qqqq$
ALEPH	80.429 ± 0.059	80.475 ± 0.081
DELPHI	80.339 ± 0.075	80.311 ± 0.137
L3	80.212 ± 0.071	80.325 ± 0.080
OPAL	80.449 ± 0.063	80.353 ± 0.083

The combination of all experiments and all energies yields [17]:

$$m_{\mathrm{W}}(qq\ell\nu) = 80.372 \pm 0.030 \pm 0.021 \text{ GeV} \tag{6.19}$$

$$m_{\mathrm{W}}(qqqq) = 80.387 \pm 0.040 \pm 0.044 \text{ GeV} , \tag{6.20}$$

where the first error is statistical and the second is systematic. The weight of the fully-hadronic final state in the combination is found to be 22%. Although better kinematically constrained, the $qqqq$ final state exhibits a worse mass resolution than the $qq\ell\nu$ channel due to the cut on the minimum particle

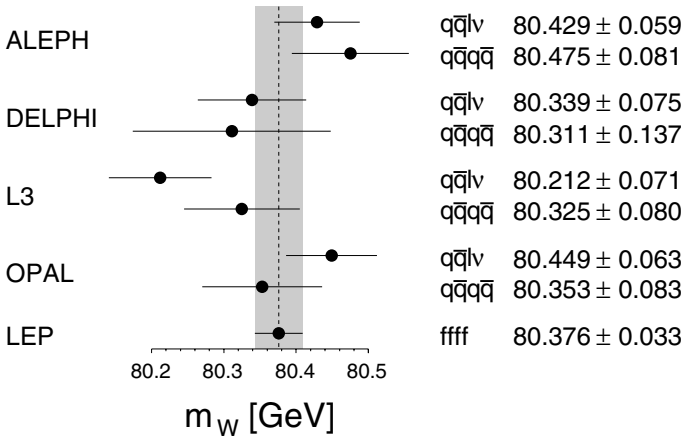

Fig. 6.17. Comparison of W-mass measurements of the four LEP experiments from direct reconstruction of W decays

momentum. The weight of the $qqqq$ channel in the combination is further reduced by the systematic uncertainties from final state interactions which are absent in the $qq\ell\nu$ channel. It is planned to combine the colour reconnection and Bose-Einstein analyses of all four LEP experiments and to consider the combined limits on these effects during the determination of the systematic uncertainty due to final state interactions in each experiment. This would reduce the systematic uncertainty in the $qqqq$ channel and will increase its weight in the final combination.

The difference between the W masses from the semi-leptonic and the fully-hadronic channels is determined to be

$$\Delta m_{\mathrm{W}}(qqqq - qq\ell\nu) = -12 \pm 45 \text{ MeV} . \tag{6.21}$$

This mass difference is compatible with zero, and therefore no indication of a systematic mass bias in the fully-hadronic channel from colour reconnection or Bose-Einstein effects is observed. Systematic uncertainties caused by these effects are excluded in the determination of $\Delta m_{\mathrm{W}}(qqqq - qq\ell\nu)$. Averaging the results of the $qq\ell\nu$ and $qqqq$ channel results in

$$m_{\mathrm{W}}(\text{direct}) = 80.375 \pm 0.025 \pm 0.022 \text{ GeV} . \tag{6.22}$$

The individual results for the direct measurement of the W width at LEP are given in Table 6.4. The four measurements are combined under consideration of the correlations in the systematic uncertainties. The combined value of the W width from LEP is found to be

$$\Gamma_{\mathrm{W}}(\text{direct}) = 2.196 \pm 0.063 \pm 0.055 \text{ GeV} . \tag{6.23}$$

Table 6.4. Measurements of the total decay with of the W boson. Results from direct reconstruction of W decays at 172 GeV $< \sqrt{s} <$ 209 GeV are given

Experiment	Γ_{W} [GeV]
ALEPH	2.14 ± 0.11
DELPHI	2.40 ± 0.17
L3	2.18 ± 0.14
OPAL	2.00 ± 0.14

Combining the results from threshold measurement and direct reconstruction yields

$$m_{\mathrm{W}} = 80.376 \pm 0.033 \text{ GeV} , \tag{6.24}$$

$$\Gamma_{\mathrm{W}} = \ 2.196 \pm 0.084 \text{ GeV} , \tag{6.25}$$

representing the overall result of the complete LEP 2 data sample.

References

1. ALEPH Collaboration, R. Barate et al., Phys. Lett. **B 415**, 435 (1997); DELPHI Collaboration, P. Abreu et al., Eur. Phys. J. **C 2**, 581 (1998); L3 Collaboration, M. Acciarri et al., Phys. Lett. **B 407**, 419 (1997); OPAL Collaboration, K. Ackerstaff et al., Eur. Phys. J. **C 1**, 395 (1998)
2. M.W. Grünewald, Phys. Rep. **322**, 125 (1999)
3. OPAL Collaboration, G. Abbiendi et al., Eur. Phys. J. **C 26**, 321 (2003)
4. ALEPH Collaboration, R. Barate et al., Preprint CERN-PH-EP/2006-004
5. DELPHI Collaboration, J. Abdallah et al., Conf. note DELPHI 2006-011
6. L3 Collaboration, P. Achard et al., Eur. Phys. J. **C 45**, 569 (2006)
7. OPAL Collaboration, G. Abbiendi et al., Eur. Phys. J. **C 45**, 307 (2006)
8. JADE Collaboration, S. Bethke et al., Phys. Lett. **B 213**, 235 (1988); S. Catani et al., Phys. Lett. **B 269**, 432 (1991)
9. D.M. Schmidt, R.J. Morrison and M.S. Witherell, Nucl. Instr. and Meth. **A 328**, 547 (1993)
10. R. Kleiss and R. Pittau, Comp. Phys. Comm. **83**, 141 (1994)
11. S. Jadach et al., Comp. Phys. Comm. **140**, 475 (2001)
12. A. Denner et al., Comp. Phys. Comm. **153**, 462 (2003)
13. S. Jadach et al., Phys. Lett. **B 523**, 117 (2001)
14. F. Cosutti, Eprint hep-ph/0505232 (2005)
15. DELPHI Collaboration, P. Abreu et al., Eur. Phys. J. **C 18** (2000) 203
16. LEP Energy Working Group, R. Assmann et al., Eur. Phys. J. **C 39**, 253 (2005)
17. LEP Electroweak Working Group, Eprint hep-ex/0511027 and `http://lepewwg.web.cern.ch/LEPEWWG/`

7

Fit of Electroweak Parameters to Precision Data

Within the Standard Model the Z mass, m_{Z}, the W mass, m_{W}, and the weak mixing angle, θ_{w}, are related by

$$\cos\theta_{\mathrm{w}} = \frac{m_{\mathrm{W}}}{m_{\mathrm{Z}}} \,, \tag{7.1}$$

which is a prediction of the Higgs mechanism. As presented in Sect. 3.2 the mass of the Z boson, m_{Z}, is known to a very high accuracy of $2.3 \cdot 10^{-5}$. The measurement of the weak mixing angle from electroweak precision observables, as explained in Sect. 3.6, allows to predict the mass of the W boson using equation (7.1). After applying the proper radiative corrections this prediction of the W mass can be compared to the result of the direct measurement. This tests not only the validity of Equation (7.1) on Born level, but also the corresponding electroweak radiative corrections.

7.1 Direct W-Mass Measurement Facing Precision Data

The W mass is measured at LEP 2 studying the W-pair production $\mathrm{e^+e^-} \to \mathrm{W^+W^-} \to f\bar{f}f\bar{f}$, as presented in detail in the previous Chap. 6. At hadron colliders the leptonic decays of singly produced W bosons with electrons or muons in the final state are selected. From the momentum measurement of the leptons the transverse mass is calculated. The transverse mass, i.e. the invariant mass of the transverse momentum of the charged lepton and the missing momentum vector in the plane transverse to the beam, is not affected by the unknown missing momentum along the beam axis. The experiments CDF and D0 have performed a precise measurement [1] of the W mass using the Run I data set of the Tevatron collider. The precision of the Tevatron W mass measurement is currently limited by data statistics. The uncertainty in the lepton energy scale gives the largest contribution to the systematic error. To improve the accuracy of the energy measurement of the leptons, leptonic

Stefan Roth: *Precision Electroweak Physics at Electron-Positron Colliders*
STMP **220**, 133–144 (2006)
DOI 10.1007/3-540-35165-5_7

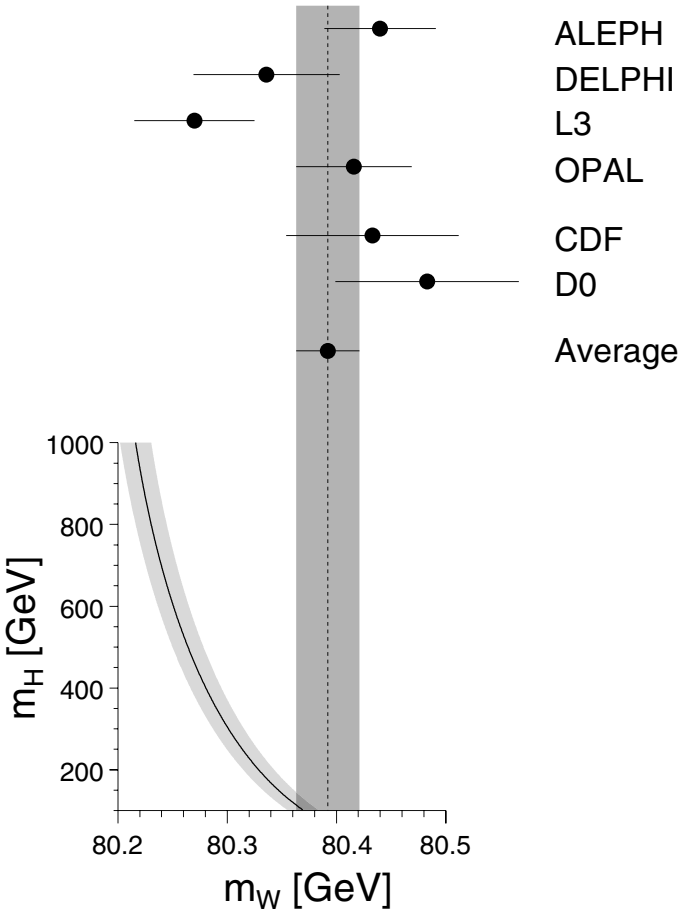

Fig. 7.1. Measurement of the W mass at LEP and Tevatron and comparison with the Standard Model prediction as function of the Higgs mass. The theory uncertainty is dominated by the uncertainties in m_{t} and $\Delta\alpha$ and shown as a band whose width represents the quadratic sum of both effects

Z decays are selected and calibrated using the precise Z mass from the Z resonance scan at LEP.

The results of the Tevatron and LEP experiments on the W mass are in good agreement as shown in Fig. 7.1. All direct W-mass measurements, of which some are still preliminary, result in a world average of:

$$m_{\mathrm{W}} = 80.392 \pm 0.029 \text{ GeV} . \tag{7.2}$$

Additionally the W mass calculated within the Standard Model from the Fermi constant G_{F} is shown as a function of the Higgs mass. The measured W-mass values prefer a light Higgs boson.

As stated above, the measurement of $\sin^2\theta_{\text{eff}}$ at LEP 1 and SLD can be translated into an indirect determination of the W mass. Due to radiative corrections the experimental uncertainty of the top mass and our ignorance about the Higgs mass enter into this calculation. From a fit to all Z-peak data including the direct m_{t} result from Tevatron the best indirect determination of the W mass is obtained:

$$m_{\text{W}}^{\text{indirect}} = 80.361 \pm 0.020 \text{ GeV} . \tag{7.3}$$

This result is in good agreement with the direct measurements from LEP 2 and Tevatron presented above.

Another less precise, indirect measurement of m_{W} is coming from the measurement of neutrino nucleon scattering. Measurements of the NuTeV collaboration [2] show a deviation from the world average on m_{W} of about three standard deviations. Theoretical studies [3] suspect that the uncertainties due to QCD corrections and due to electroweak radiative corrections might be underestimated in this analysis. Another explanation could be a reduced coupling of the neutral current to the neutrinos with respect to the Standard Model prediction. The measurement of the invisible width of the Z boson, Γ_{inv}, which is found to be smaller than the Standard Model prediction, would point into the same direction.

The comparison between the direct and the indirect determination of the W mass assumes that the radiative corrections of the Standard Model, which are used when translating $\sin^2\theta_{\text{eff}}$ into $m_{\text{W}}^{\text{indirect}}$, are correct. To allow the comparison with the direct mass measurement, the effective weak mixing angle is converted into the on-shell mixing angle. The latter one can therefore be expressed as $\cos\theta_{\text{w}} = m_{\text{W}}^{\text{indirect}}/m_{\text{Z}}$ and the ρ-parameter on tree level is given as

$$\rho^{\text{tree}} = \frac{m_{\text{W}}^2}{m_{\text{Z}}^2 \cos^2\theta_{\text{w}}} = \left(\frac{m_{\text{W}}^{\text{direct}}}{m_{\text{W}}^{\text{indirect}}}\right)^2 = 1.0008 \pm 0.0009 . \tag{7.4}$$

The result is compatible with unity which represents of successful test of Equation (7.1) to a very high precision.

7.2 Global Fit to Electroweak Data

Electroweak radiative corrections have been calculated up to the two-loop level, but their accuracy is limited by the experimental uncertainty on the mass of the top quark and by the ignorance on the mass of the Higgs boson. A test of the quantum structure of the Standard Model therefore requires a precise knowledge of the top quark mass, since the radiative corrections depend quadratically on this parameter.

In the year 1995 the experiments at the Tevatron collider discovered the top quark analysing events of the reaction $\text{p}\bar{\text{p}} \rightarrow \text{t}\bar{\text{t}}X \rightarrow \text{b}\bar{\text{b}}\text{W}^+\text{W}^-X$. The mass of the top quark was found to be within the mass range predicted by the

electroweak precision data. If the W boson decays into two quarks, the mass of the top quark can be reconstructed from the invariant mass of the b jet and the two jets coming from the W decay. The published Run-I measurements have been combined with the most recent Run-II measurements representing a data set of 750 pb^{-1} in total [4]:

$$m_{\mathrm{t}} = 171.4 \pm 2.1 \text{ GeV} . \tag{7.5}$$

The calculation of the electromagnetic coupling constant $\alpha(m_{\mathrm{Z}})$ at the energy scale of the Z mass needs the precise knowledge of the vacuum polarisation. The contribution of the five light quark species, $\Delta\alpha^{(5)}_{\mathrm{had}}$, can not be calculated in perturbation theory, but has to be extracted from the total hadronic cross section measured in $\mathrm{e}^+\mathrm{e}^-$ collisions. A very large contribution to $\Delta\alpha^{(5)}_{\mathrm{had}}$ comes from the region of the ρ resonance. The first precise informations in this energy region were obtained by the CMD-2 collaboration using data taken at centre-of-mass energies between 0.61 GeV and 0.96 GeV at the VEPP collider. The measurements of CMD-2 have recently been confirmed by new results from the KLOE collaboration [5]. A recent compilation by Burkhardt and Pietrzyk [6] gives

$$\Delta\alpha^{(5)}_{\mathrm{had}}(m_{\mathrm{Z}}) = 0.02758 \pm 0.00035 . \tag{7.6}$$

Another parameter of the Standard Model to be considered is the strong coupling constant, α_{s}. It enters the electroweak calculations mainly through radiative corrections due to the gluon emission in hadronic final states. This correction changes Γ_{Z} and Γ_{had} in a similar way. Therefore, the hadronic cross section on the Z peak, σ^0_{had}, is only moderately affected. On the other hand, the leptonic peak cross section, σ^0_{lep}, is very sensitive to α_{s} and a fit to the LEP 1 results on σ^0_{lep} yields $\alpha_{\mathrm{s}} = 0.1179 \pm 0.0030$. This value is in good agreement with the result from QCD event shape studies. In the following fits the parameter α_{s} is taken as free parameter and varied during the fits applying no external constraint.

In a global fit to precision data the electroweak observables including their radiative corrections have to be calculated. These corrections are obtained from numerical calculations using computer codes as implemented in the electroweak program libraries ZFITTER [7], TOPAZ0 [8] or GAPP [9].

The fit results presented here are performed within the context of the LEP and SLD electroweak working group. The details of the combination of the electroweak data and the fit of the Standard Model parameters are described in Reference [10]. The semi-analytical program ZFITTER is used to calculate the Standard Model predictions including its higher order corrections. The complete fermionic and bosonic two-loop corrections to m_{W} and the complete fermionic corrections to $\sin^2\theta_{\mathrm{eff}}$ have been calculated recently [11]. The analytical formulas were parametrised as functions of the parameters m_{H}, m_{t}, m_{Z}, $\Delta\alpha$ and α_{s} and implemented in ZFITTER.

The most general electroweak fit includes all Z peak data from LEP 1 and SLD, the W mass, m_{W}, from LEP 2 and Tevatron, the top mass, m_{t}, measured at the Tevatron and $\Delta\alpha^{(5)}_{\mathrm{had}}$. This fit yields a reasonable χ^2 value of

$$\chi^2/\mathrm{d.o.f.} = 17.8/13\ . \tag{7.7}$$

This corresponds to a fit probability of 17% and shows that the electroweak measurements are internally consistent and agree with the Standard Model prediction. Figure 7.2 shows the distribution of the pulls of observables, i.e. the differences between the measured values and the values obtained from the fit in units of standard deviations. The measurements of all electroweak observables are well contained within two standard deviations around the fit results, with the exception of $A^{\mathrm{b}}_{\mathrm{FB}}$.

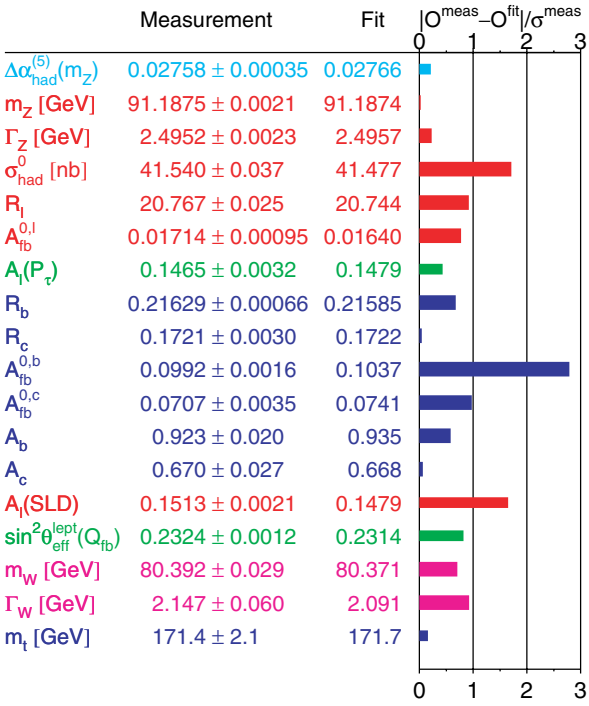

Fig. 7.2. Difference between the measured values of electroweak observables and the values obtained from the final fit result in units of standard deviations

7.3 Higgs Mass Prediction

The electroweak measurements performed at LEP 1 and SLD are combined into a precision value of $\sin^2\theta_{\mathrm{eff}}$ (Fig. 3.6). Using Equation (7.1) and the precisely known Z mass the measurement of the weak mixing angle represents an indirect determination of the W mass. This value of the W mass depends on radiative corrections and hence on the value of the top mass. In Fig. 7.3 the constraint on m_{W} set by the measurement of $\sin^2\theta_{\mathrm{eff}}$ using the electroweak precision data is shown as a function of m_{t}. Also shown is the allowed region of all LEP 1 and SLD electroweak data as a contour in the m_{W} vs. m_{t} plane representing a probability of 68%. The direct measurements of the W-boson mass and the top-quark mass are also indicated. Additionally to the measurements the Standard Model prediction using G_{F} from the muon decay is plotted for various Higgs masses within 114 GeV $< m_{\mathrm{H}} <$ 1000 GeV. Both the indirect and the direct measurements prefer a low Higgs mass.

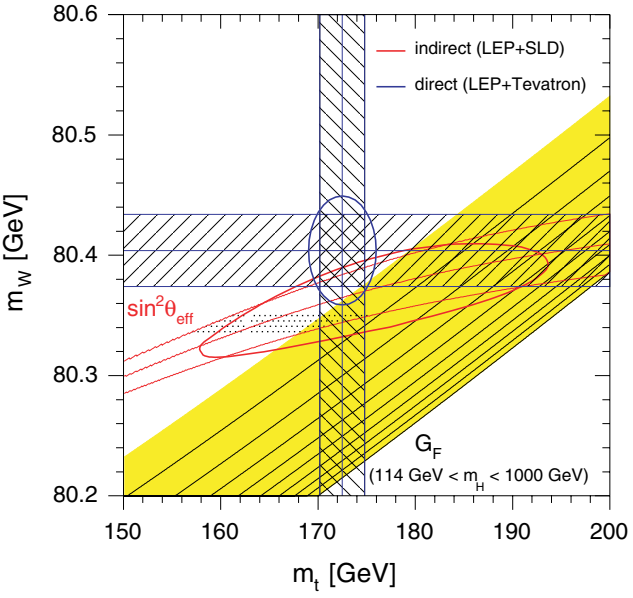

Fig. 7.3. Comparison of direct mass measurements and indirect measurements using electroweak precision data. Also shown is the theory prediction calculated from G_{F} for various Higgs masses, where the presented lines correspond to m_{H} values differing by 100 GeV

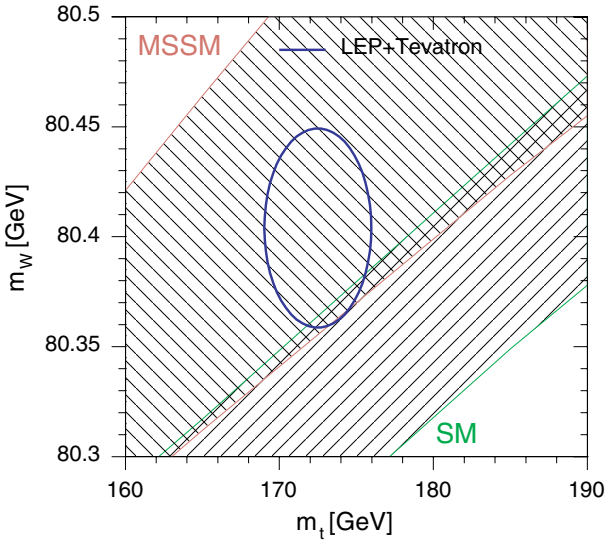

Fig. 7.4. Direct measurements of m_{W} and m_{t} and the mass regions as predicted by the Standard Model (SM) and the Minimal Supersymmetric Standard Model (MSSM), respectively

The radiative corrections to m_{W} have also been calculated in the Minimal Supersymmetric Standard Model (MSSM) [12]. In Fig. 7.4 the direct mass measurements of m_{W} and m_{t} are compared to the theory predictions of the Standard Model (SM) and the MSSM, respectively. The extension of the Standard Model region is determined by the allowed Higgs mass values. In the case of the MSSM, the free parameters of the model are varied. The direct measurements of m_{W} and m_{t} are compatible with the Standard Model for a low Higgs boson mass. However, they tend to prefer the mass region as predicted by the MSSM.

As stated before, the electroweak radiative corrections include a term proportional to the logarithm of the Higgs mass, the only unknown parameter of the Standard Model. Assuming the validity of the Standard Model one can try to extract this term from a global fit to all electroweak observables. Then this allows to set constraints on the mass of the Higgs boson.

The fit of the Standard Model prediction to all electroweak data [10] with the Higgs mass as the only free parameter results in a χ^2 curve as shown in Fig. 7.5. It predicts the mass of the Higgs boson to be 85^{+39}_{-28} GeV which is consistent with the direct searches for the Higgs boson excluding masses below 114.4 GeV (see Sect. 7.4).

Following Gaussian statistics one can calculate the probability density with respect to m_{H}. After integrating this probability density and setting the total probability of the Higgs mass above 114.4 GeV to unity, a curve representing

the confidence level on an upper limit on m_{H} is obtained. Hence, for each mass value in ig. 7.5 the probability that the Higgs boson has a larger mass is given by the 1-C.L. graph. For these calculations those input flags in ZFITTER are used which yield the most conservative upper bound on m_{H} in order to consider the theoretical uncertainties. At 95% C.L. an upper bound on the Higgs mass of 199 GeV is set.

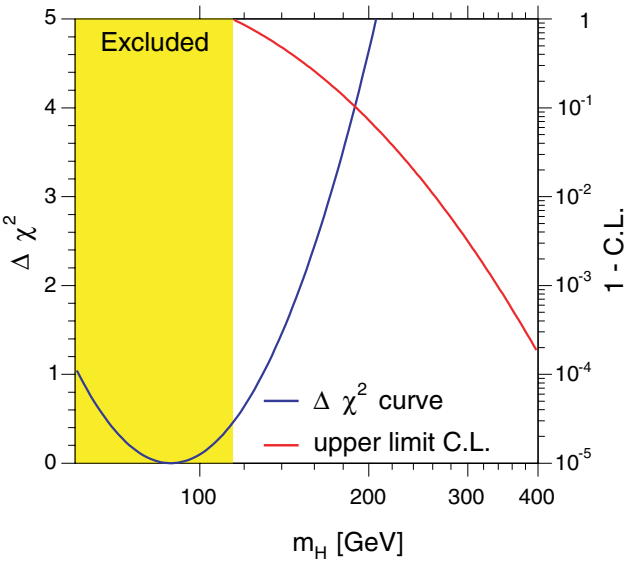

Fig. 7.5. The $\Delta\chi^2$ curve of the global fit of the Standard Model parameters to the electroweak precision data [10]. In addition the confidence level (C.L.) as a function of the upper limit on m_{H} is shown

7.4 Search for the Standard Model Higgs at LEP

Since the start up of LEP the search for the Higgs particle played a key role in the program of the collider. At e^+e^- colliders the large coupling of the Higgs to the Z boson is used to produce Higgs bosons via the Higgs-strahlung process depicted in Fig. 7.6. In the first five years of the LEP program a signal of Higgs production was searched for in the 14 million Z decays recorded on the Z resonance.

In the case of a very light Higgs boson its lifetime becomes rather long and one even has to consider the possibility that the Higgs decays outside the detector. Such light Higgs bosons would manifest themselves by causing missing momentum transverse to the beam direction. Small Higgs masses

could also lead to the decay of the Higgs into a collinear fermion anti-fermion pair. Possible results are for example the so called mono-jets caused by two nearby quarks. In such events the particle pair from the Z decay shows a deviation in its collinearity angle. No such events were found and the Higgs mass range between 0 GeV and 20 GeV was excluded already after one year of data taking at LEP [13].

In the following years until 1995 LEP delivered an integrated luminosity of about 200 pb^{-1} per experiment on the Z resonance. Here the Higgs search concentrated on the typical signature of the Higgs-strahlung process assuming the Higgs to decay mainly into b-quarks. A reliable flavour tagging using the information from the reconstruction of secondary vertices with silicon detectors was essential for this task. The LEP 1 data allowed to exclude the entire mass range of $0 \leq m_{\mathrm{H}} \leq 63.9$ GeV for the Standard Model Higgs boson [14].

The mass range which can be explored at a given centre-of-mass energy is limited by the fact that the Higgs boson has to be produced in conjunction with a real Z boson. For Higgs masses larger than this kinematical threshold the cross section of the process $\mathrm{e^+e^-} \rightarrow \mathrm{HZ}$ rises quickly. This yields a much better signal to background ratio for data taken at centre-of-mass energies above the Z resonance than for Z peak data. During the LEP 2 phase with the increasing energy of the LEP collider the Higgs search was extended to masses as high as 115 GeV [16]. In this mass range the Higgs decays predominantly into b quarks (85%), but also the decay into tau leptons is considered in the analyses. This results in four different final states which have to be studied:

$\mathrm{HZ} \rightarrow \mathrm{b\bar{b}\ q\bar{q}}$	four hadronic jets with two b tags	
$\mathrm{HZ} \rightarrow \mathrm{b\bar{b}}\ \nu\bar{\nu}$	two acoplanar b jets and missing energy	(7.8)
$\mathrm{HZ} \rightarrow \mathrm{b\bar{b}}\ \ell^+\ell^-$	two b jets and two leptons ($\mathrm{e^+e^-}$ or $\mu^+\mu^-$)	
$\mathrm{HZ} \rightarrow \tau^+\tau^-\ \mathrm{q\bar{q}}$	two taus and two jets	

The main background sources are fermion-pair production, in particular the process $\mathrm{e^+e^-} \rightarrow \mathrm{b\bar{b}}$ with gluon radiation in the final state yielding four-jet events with two b tags. Further background comes from four-fermion

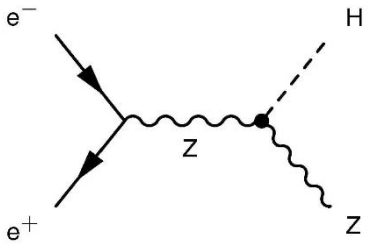

Fig. 7.6. Feynman diagram of Higgs-boson production in $\mathrm{e^+e^-}$ collision through process of Higgs-strahlung

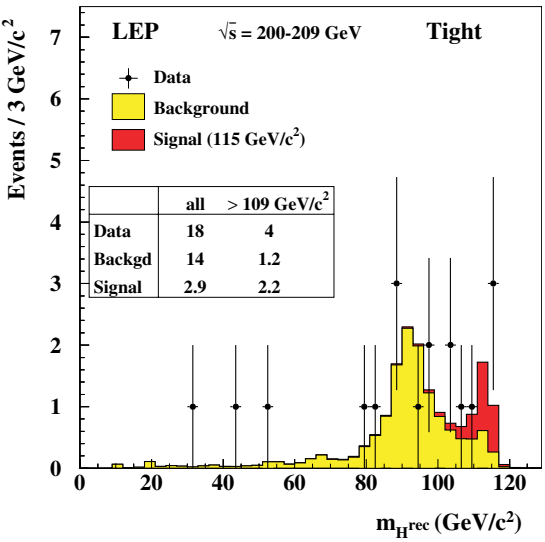

Fig. 7.7. Spectrum of reconstructed Higgs boson mass from the best candidate events recorded by the four LEP experiments. The selected events in data are compared to Monte Carlo expectations, lightly shaded for the background processes and heavily shaded for a Standard Model Higgs boson of 115 GeV mass

production via the $e^+e^- \to W^+W^-$, the $e^+e^- \to ZZ$ processes and the production of single W bosons, $e^+e^- \to We\nu$.

Due to the large hadronic branching fraction of the Z the four-jet topology is the most sensitive channel for the Higgs search. On the other hand this final state suffers from the high potential background of $b\bar{b}$ production and excellent b-tagging performance of the detectors is essential to suppress the background to an acceptable level. Kinematic fits are applied to all of the final states to improve the mass resolution of the hypothetical Higgs boson in candidate events. Here, one exploits the fact that the two objects, jets or leptons, which are not associated to the Higgs boson should stem from a Z boson. Therefore their invariant mass is constrained to the Z mass during the kinematic fit. Figure 7.7 shows the reconstructed mass distribution of the best candidate events from all four experiments compared to the expectation from background processes and the production of a Standard Model Higgs boson of 115 GeV mass.

In the data collected at centre-of-mass energies of up to 202 GeV no indication for a Higgs signal was found by the LEP collaborations. During the year 2000, the last year of LEP operation, substantial data samples were collected at centre-of-mass energies of up to 208 GeV. In their initial data analysis the ALEPH collaboration observed an excess of events consistent with the production of a Standard Model Higgs boson with a mass of 115 GeV [15]. In the final analyses of the four LEP collaborations [16] this result was not

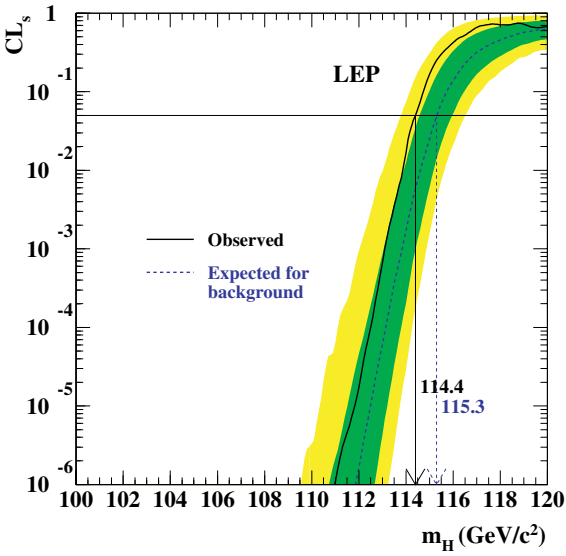

Fig. 7.8. The confidence level, CL_s, as a function of the Higgs mass, m_H, for the signal-plus-background hypothesis. The solid line shows the value observed in data, whereas the dashed line represents the expectation from a pure background hypothesis. The lower bound on the Higgs mass is obtained at a m_H value, where the observed curve gives a probability of $CL_s = 0.05$

confirmed. However, combining the data of the four experiments allowed to set a lower limit on the Higgs mass, m_H.

The hypothesis of Higgs boson production under the presence of the expected background processes is tested as a function of m_H for the given candidate events taking into account their significance at a given m_H value. In Fig. 7.8 the resulting confidence level, CL_s, is shown as a function of the tested mass value, m_H, after combination of the four experiments. The function $CL_s(m_H)$ gives the probability that the observed data are compatible with a Standard Model Higgs of mass m_H. The expected CL_s function from a background-only hypothesis is shown in addition. The latter is derived from a large number of Monte Carlo experiments taking into account the data analyses, event selections and detector performances.

From the intersection of the observed CL_s function with the 5% line the lower limit on the mass of the Higgs boson is derived to be [17]

$$m_H > 114.4 \text{ GeV at } 95\% \text{ C.L .} \tag{7.9}$$

which is the final result of more than 10 years of Higgs search at LEP.

References

1. CDF and D0 Collaborations, V.M. Abazov et al., Phys. Rev. **D 70**, 092008 (2004);
   D0 Collaboration, B. Abazov at al., Phys. Rev. **D 66**, 012001 (2002);
   CDF Collaboration, T. Affolder et al., Phys. Rev. **D 64**, 052001 (2001)
2. G.P. Zeller, Phys. Rev. Lett. **88**, 091802 (2002)
3. K.P.O. Diener, S. Dittmaier and W. Hollik, Phys. Rev. **D 69**, 073005 (2004);
   G.A. Miller and A.W. Thomas, Eprint hep-ex/0204007 (2002)
4. Tevatron Electroweak Working Group, Eprint hep-ex/0603039 (2006);
   D0 Collaboration, B. Abbott at al., Nature **429**, 638 (2004);
   CDF Collaboration, F. Abe et al., Phys. Rev. **D 63**, 032003 (2001)
5. KLOE Collaboration, A. Aloisio et al., Phys. Lett. **B 606**, 12 (2005);
   CMD-2 Collaboration, R.R. Akhmetshin et al., Phys. Lett. **B 578**, 285 (2004);
6. H. Burkhardt and B. Pietrzyk, Phys. Rev. **D 72**, 057501 (2005);
   H. Burkhardt and B. Pietrzyk, Phys. Lett. **B 513**, 46 (2001)
7. A.B. Arbuzov et al., Eprint hep-ph/0507146;
   D. Bardin et al., Comp. Phys. Commun. **133**, 229 (2001)
8. G. Montagna at al., Comp. Phys. Commun. **117**, 278 (1999)
9. J. Erler, Eprint hep-ph/0005084
10. LEP Electroweak Working Group, Eprint hep-ex/0511027 and
    `http://lepewwg.web.cern.ch/LEPEWWG/`
11. M. Faisst et al., Nucl. Phys. **B 665**, 649 (2003);
    M. Awramik et al., Phys. Rev. **D 69**, 053006 (2004);
    M. Awramik et al., Phys. Rev. Lett. **93**, 201805 (2004)
12. S. Heinemeyer et al., Eprint hep-ph/0604147;
    S. Heinemeyer, W. Hollik and G. Weiglein, Phys. Rept. **425**, 265 (2006)
13. ALEPH Collaboration, D. Decamp et al., Phys. Lett. **B 245**, 289 (1990);
    L3 Collaboration, B. Adeva et al., Phys. Lett. **B 252**, 518 (1990)
14. ALEPH Collaboration, D. Buskulic et al., Phys. Lett. **B 384**, 427 (1996);
    DELPHI Collaboration, P. Abreu et al., Nucl. Phys. **B 421**, 3 (1994);
    L3 Collaboration, M. Acciarri et al., Phys. Lett. **B 385**, 454 (1996);
    OPAL Collaboration, G. Alexander et al., Z. Phys. **C 73**, 189 (1997)
15. ALEPH Collaboration, R. Barate et al., Phys. Lett. **B 495**, 1 (2000)
16. ALEPH Collaboration, R. Barate et al., Phys. Lett. **B 526**, 191 (2002);
    DELPHI Collaboration, J. Abdallah et al., Eur. Phys. J. **C 32**, 145 (2004);
    L3 Collaboration, M. Acciarri et al., Phys. Lett. **B 517**, 319 (2001);
    OPAL Collaboration, G. Abbiendi et al., Eur. Phys. J. **C 26**, 479 (2003)
17. LEP Collaborations, Phys. Lett. **B 565**, 61 (2003)

8

Electroweak Physics at an e^+e^- Linear Collider

The measurements at LEP and SLC have tested the electroweak interactions of the Standard Model at the quantum-loop level. Especially, they have proven that the gauge-boson masses are fixed by the electroweak couplings. This is naturally explained by the Higgs mechanism, where the masses are generated by the electroweak coupling of the gauge bosons to a mass generating field, the Higgs field. The proof of the actual existence of the Higgs mechanism is still missing, namely the discovery of the Higgs boson, which is predicted by theory. To a large extent the next two major projects in accelerator based particle physics, the LHC and the ILC, are dedicated to the discovery of the Higgs boson and to precision physics in the Higgs sector.

At the Large Hadron Collider (LHC), currently under construction at CERN, proton-proton collisions at 14 TeV centre-of-mass energies will be studied. The LHC will offer an unprecedented mass reach for the discovery of new elementary particles. The price to pay will be very complicated event signatures which will make it difficult to extract the underlying physics. The reason is that the colliding protons are not fundamental particles, but are built up of quarks and gluons. These are subject to the strong interaction and therefore produce a large amount of QCD background, about 20 events per bunch crossing.

The International Linear Collider (ILC), now under study in a worldwide effort, will offer e^+e^- collisions up to 1 TeV centre-of-mass energy. It will allow high precision measurements of the accessible final states [1]. The advantages are the simple initial state consisting of the point-like electron and positron and the moderate background situation. Both features lead to clean event signatures, where in addition momentum conservation can be assumed allowing the reconstruction of undetected particles. Additional possibilities are the operation with polarised beams or the study of electron-photon and two-photon collisions by using photons from a high intense laser beam back-scattered from the incoming electron beam.

Stefan Roth: *Precision Electroweak Physics at Electron-Positron Colliders*
STMP **220**, 145–167 (2006)
DOI 10.1007/3-540-35165-5_8

8.1 The Physics Potential of an e^+e^- Linear Collider

The cross sections of s-channel processes are typically inversely proportional to the square of the centre-of-mass energy. See for example Fig. 8.1 for an overview of cross sections of typical processes expected at a linear collider. Going from LEP energies of 200 GeV to energies in the 1 TeV range will reduce these cross sections by at least one order of magnitude. This is more than compensated by the projected luminosity of the order of $3 \cdot 10^{34}$ $\mathrm{cm}^{-2}\mathrm{s}^{-1}$. For example, with the anticipated collected luminosity of 100 fb^{-1} per year in the order of 10^4 Higgs events could be observed in a one-year running.

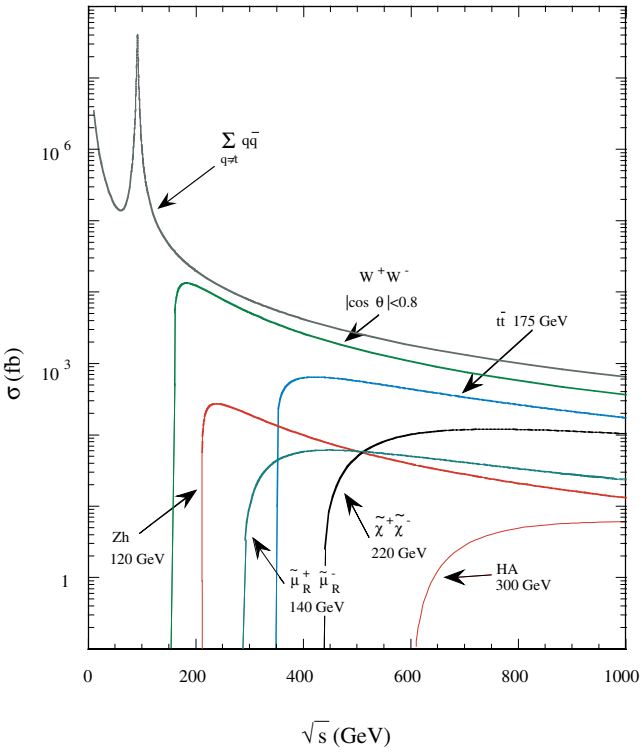

Fig. 8.1. Cross sections for some interesting processes at e^+e^- colliders

If the Standard model Higgs boson exists it will be discovered at the LHC. Then a linear collider will be able to measure all of its properties like mass, spin and coupling strengths to bosons and fermions with very high precision. This will answer the question whether the Higgs boson has the properties as predicted by the Standard Model or a more complicated Higgs mechanism, based on an extended Higgs sector, is at work. It will be possible to measure the Higgs mass with a precision of 50 MeV and to determine the branching

ratios of the Higgs decays to a few percent. By studying the ZHH final state even the Higgs self-coupling can be measured to 20% accuracy.

An e^+e^- linear collider will open a next chapter in precision tests of the Standard Model. An important ingredient will be the precise measurement of the top-quark mass. The top quark is by far the heaviest fermion with a mass of about 173 GeV. The measurement of the total cross section of top-pair production from a scan around the production threshold will determine the top mass with an accuracy of better than 100 MeV. This is more than an order of magnitude more precise than envisaged at the LHC. In addition measurements of the mass of the W boson and of the weak mixing angle can be performed with the proposed Giga-Z option of a linear collider which will deliver unprecedented luminosity in the energy region between 90 GeV and 200 GeV.

8.2 Electroweak Gauge Bosons

The mass of the Z boson is known from LEP with a precision of 2 MeV. This precision was obtained in an energy scan of the Z resonance with very precise calibration of the centre-of-mass energy. An accuracy of 10^{-5} was reached because the electron storage ring LEP allowed to exploit the method of resonant beam depolarisation. The determination of the beam energy will be much more difficult at a linear collider and the final uncertainty on the mean centre-of-mass energy will be of the order of 10^{-4}.

Hence at a linear collider an improvement of the Z mass measurement will not be possible. On the other hand an improved measurement of the W mass can be obtained from a scan around the W-pair production threshold. The envisaged high luminosity and polarisation at a linear collider will allow a measurement of the W mass with a precision of 6 MeV [2] using an integrated luminosity of 100 fb^{-1}, which corresponds to one year of data taking.

To exploit the threshold scan for a W-mass measurement the dependence of the total W-pair production cross section on the centre-of-mass energy must be known to high precision. Near threshold the s-channel contribution is suppressed with respect to the t-channel by a factor β^2, where β is the velocity of the W boson. The t-channel contribution depends only on the well known Weν coupling, so that the total cross section is independent of potential new physics changing the triple gauge couplings. However, the double pole approximation which was very successful for calculations of the continuum is no longer valid near the threshold. For example, the Coulomb correction changes the cross section by about 6%. New calculations of the four-fermion production including radiative corrections are needed to reach a 0.06% precision which is necessary to keep the theoretical error on m_{W} below 1 MeV.

Additionally the beam-strahlung which is caused by the extremely small beam sizes in the final focus of a linear collider (see Sect. 8.6) will change the effective centre-of-mass energy of the individual events. Hence, the available

luminosity will not be delivered at the nominal centre-of-mass energy, but will be distributed to lower values. This will lead to a reduction of the W-pair threshold cross section by about 7%. To achieve the envisaged accuracy in the W-mass measurement the beam-strahlung spectrum has to be known with sufficient accuracy. In contrary to initial-state radiation, which is known from QED with very high precision, the beam-strahlung depends heavily on beam parameters, especially at the final focus. It can be calculated only with limited precision. Therefore, it has to be measured during physics operation using for example the acollinearity distribution of Bhabha scattering at small angles [3]. It should be possible to measure the average energy loss with an accuracy better than 0.1%, which matches the needs of the W-mass measurement.

As stated above, the beam energy has to be known as precisely as possible, because it influences the measurement of the W mass directly. Alternatively to beam instrumentation diagnostics measuring the beam energy directly, recorded events of $Z\gamma$ production can be used. In the case of a linear collider, the luminosity will be high enough to concentrate on the di-muon decay of the Z boson which should have the lowest systematic uncertainties. Not only the mean energy will be accessible, but the angular resolution of the detector will suffice to also extract information on the luminosity spectrum. Another option would be to repeat the threshold scan for Z-pair production $e^+e^- \rightarrow ZZ$ and calibrate the W threshold using the precise knowledge of the Z mass from LEP 1.

Near threshold the t-channel neutrino exchange dominates W pair production. This pure charged-current interaction only couples to the ${e_R}^+{e_L}^-$ helicity combination, which is one out of four possibilities. Colliding beams of 100% polarised electrons and positrons would give the possibility to either quadrupling the cross section (${e_R}^+{e_L}^-$) or switching off W-pair production (${e_L}^+{e_R}^-$). This would allow to measure the background at each energy point without relying on Monte-Carlo predictions. In reality maximum achievable polarisations are expected to be 80% for electrons and 60% for positrons. Using polarised beams introduces an additional systematic uncertainty caused by the limited knowledge on the degree of polarisation. A strategy has been proposed [2] to achieve the best precision on the W mass by dividing a given luminosity onto the different beam polarisations and energies. In Fig. 8.2 the resulting sensitivity of the W-pair threshold scan on the W mass is demonstrated. The ratio of the actual cross section for a W mass of 80.36 GeV is shown together with the prediction for slightly different W masses. Simulated data points of the suggested threshold scan including the expected statistical uncertainty are also included. From this analysis a final error on the W mass of 6 MeV is predicted.

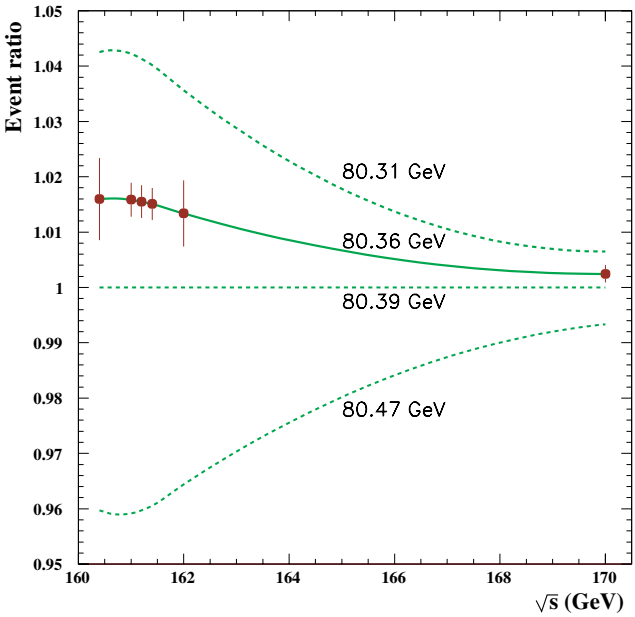

Fig. 8.2. Energy scan of the W-pair production threshold. Shown are fictive measurements of the cross section of W-pair production as they can be obtained by a few months of data taking at the design luminosity of a linear collider. These measurements are compared to the expectation usgreing various values of the W mass

8.3 Precision Measurement of the Top Mass

Its large mass makes the top quark an interesting object of investigation. According to the Standard Model it has by far the largest Yukawa coupling to the Higgs boson and should therefore be closely linked to the mechanism of mass generation and electroweak symmetry breaking. A consequence of the large top mass is the large mass splitting in the top-bottom weak isospin dublett. It prevents the heavy top quark from decoupling from radiative corrections. Therefore electroweak corrections typically depend on m_{t}^2. To perform precision tests of the electroweak theory on the quantum-loop level, the top-quark mass has to be determined very precisely.

The fermion masses and mixing angles are purely free parameters in the Standard Model. Just as the electroweak theory relates the masses of W and Z bosons to the weak mixing angle a future theory of flavour dynamics should be able to predict relations between lepton and quark masses. If the top mass could be measured at the permill level the top mass would be the best-known quark mass value, matching the precision of the τ mass in the lepton sector.

Due to its large mass the top quark is the only quark which is not subject to hadronisation. Instead it decays into a b-quark and an on-shell W boson

before hadronisation takes place. The short lifetime of the top also prevents quarkonium production, the typical structure of bound states and resonances that normally appears near the production threshold of new quark flavours. Instead, the decay time of the top quark is shorter than the quarkonium revolution time and toponium can not form. However, remnants of the toponium S-wave resonances induce a fast rise of the cross section near the threshold. This steep rise actually is the basis for a high-precision measurement of the top mass. Due to the short top decay time the interaction region of the two top quarks is restricted to small distances well below $\Lambda_{\mathrm{QCD}}^{-1}$ and the process can be calculated in perturbative QCD. Additionally, a small attractive Yukawa force due to Higgs exchange has to be taken into account. QCD corrections of next-to-next-to-leading order (NNLO) to the cross section have been calculated [4]. The NNLO correction was found to be as large as the next-to-leading order (NLO) correction and even the shift of threshold position was in the order of 1 GeV. This is unexpected as, according to the considerations above, perturbation theory should be applicable for this problem.

The systematic uncertainties of these calculations arise from the following sources: the dependence of the cross section on α_{s}, on the definition of the top-mass parameter and on the renormalisation scale. The last item also includes uncertainties due to uncalculated higher orders. A special top-mass definition was proposed by Beneke [5] to stabilise the location of the cross-section threshold with respect to the NNLO corrections. It replaces the usually used "pole mass" by the "potential-subtracted" mass, $m_{\mathrm{PS}}(\mu)$, which can be related to the conventional mass definition by a well-behaved perturbative expansion. At the same time the ordinary colour Coulomb potential is replaced by the subtracted potential $V(r, \mu)$. After $m_{\mathrm{PS}}(\mu)$ has been measured it can be related to the pole mass which is the mass definition used in electroweak theory. The dependence on the factorisation scale cancels out during this process. A similar suggestion introducing the "1S mass" was given by Hoang and Teubner [6]. In total, a theoretical error on the top mass of 100 MeV is estimated.

The steep rise of the cross section of top-pair production is smeared out by the effect of beam-strahlung. This effect has to be known and simulated with sufficient precision. In Fig. 8.3 the excitation curve of top-pair production is shown including the effects of beam-strahlung and initial-state radiation. The dashed and dotted curves indicate the cross section for top masses varied by ± 100 MeV. The result of a two-parameter fit of the NNLO cross-section formula to the simulated data is also included in Fig. 8.3.

If one is using the threshold mass definitions (PS or 1S mass) the correlation between m_{t} and α_{s} is sufficiently low and one can derive the top mass with a statistical precision of about 50 MeV. The remaining dependence on α_{s} is still under investigation and further reductions on the theoretical uncertainty are expected. The exchange of a potential Higgs boson of mass 115 GeV would increase the cross section by about 5% . Measuring the maximum of the total cross section immediately after the threshold would give direct access to the Yukawa coupling of Higgs and top. Recent work from Martinez and

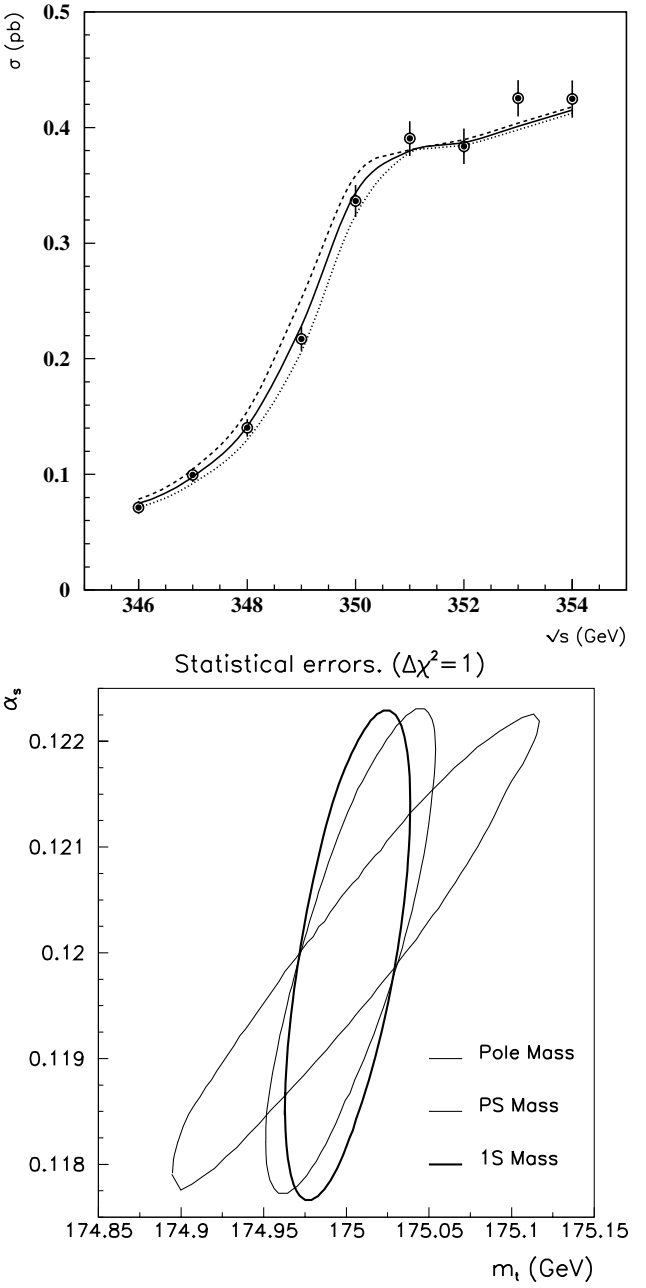

Fig. 8.3. Total cross section of top-pair production near the threshold including simulated data points from an integrated luminosity of 100 fb^{-1} (*upper plot*) and error ellipse of the statistical uncertainty in α_s and m_t from a 2-parameter fit to the simulated data (*lower plot*)

Miquel [7] studies the feasibility of extracting the top mass, the top width, α_s and the top Yukawa coupling in a multi-dimensional fit to the measurements performed in a threshold scan. In addition to the total cross section the fit uses two observables, namely the top momentum distribution and the top forward-backward asymmetry, to reduce the correlations of the fit parameters.

As explained above, top physics will be a very important issue of a linear-collider project [8]. To perform all the suggested measurements a detector at a linear collider has to identify and reconstruct top-pair events reliably. Hence, it has to cope with a final state of up to six jets, which are highly boosted. A large detector with high granularity is required to be able to differentiate all particles inside these narrow jets. Two of the jets are b-jets and therefore good b-tagging capabilities are required for the vertex detector.

8.4 Higgs Mass and Couplings

The mass of the Higgs boson is a free parameter of the Standard Model. Its value enters the prediction of electroweak observables accessible at LEP only through radiative corrections. Here the dependence on the Higgs mass is logarithmic and therefore the predictive power of the electroweak precision measurements is limited. Today the electroweak fits set an upper limit on the Higgs mass of 199 GeV at 95% confidence level. From the direct search at LEP Higgs masses below 114 GeV are excluded.

If the Standard Model Higgs exists it will be discovered at the LHC. In addition the mass of the Higgs boson can be measured with an accuracy of about one permill over the whole mass range. At a linear collider an improvement of a factor of three can be expected in the precision of the Higgs mass [9]. Here, Higgs bosons will be produced via Higgs-strahlung or WW-fusion. Both processes are depicted in Fig. 8.4. The fusion of two Z bosons is suppressed due to the weaker coupling of the Z to the electrons. The cross section of Higgs production as function of the centre-of-mass energy and the branching ratios of the different Higgs decay channels as function of the Higgs mass are shown in Fig. 8.5.

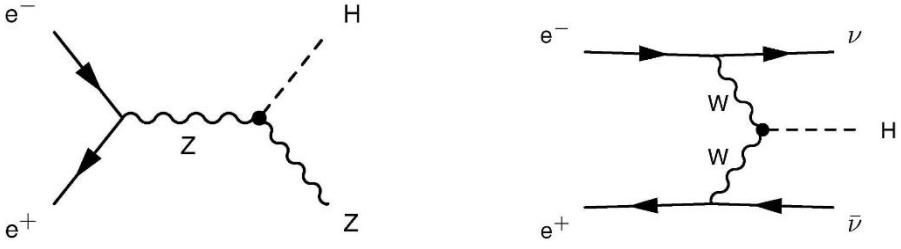

Fig. 8.4. Feynman diagram of Higgs boson production through the Higgs-strahlung and WW-fusion processes

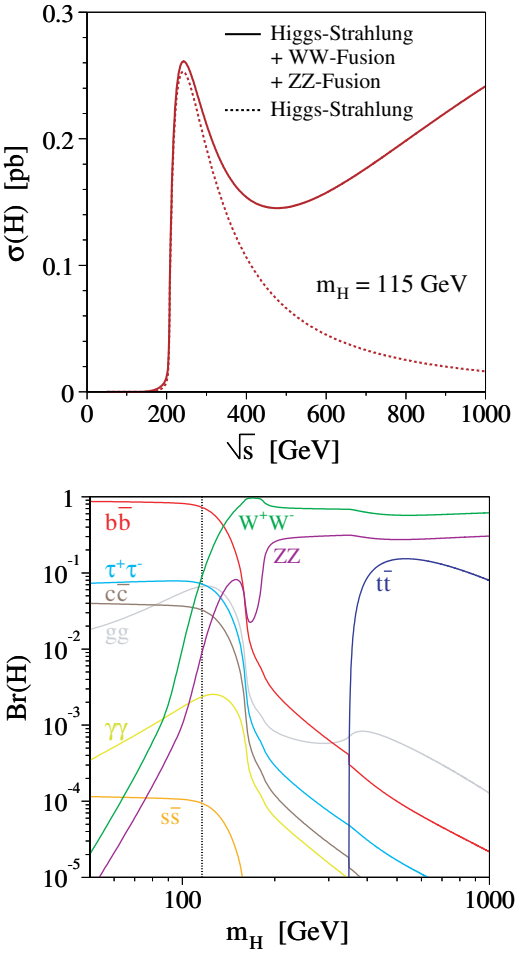

Fig. 8.5. Cross section of Higgs production as function of $\sqrt{s}$ (*upper plot*) and branching ratios into different decay channels as function of m_{H} (*lower plot*)

The Higgs-strahlung process offers the possibility to detect the Higgs boson without any assumptions on its decay and hence on its coupling to fermions or bosons. The existence of the Higgs boson in the final state is deduced from the recoil mass of a real Z boson which in turn can be identified by the invariant mass of its decay products. The most precise reconstruction is expected from Z decays into electron or muon pairs. In Fig. 8.6 the recoil-mass spectrum which will be obtained from the muon momenta is shown.

In the Standard Model the Higgs boson decays predominantly into the most heavy particles accessible. For Higgs masses below 130 GeV the dominant decay channel will be b-quark pair production, giving two jets with a

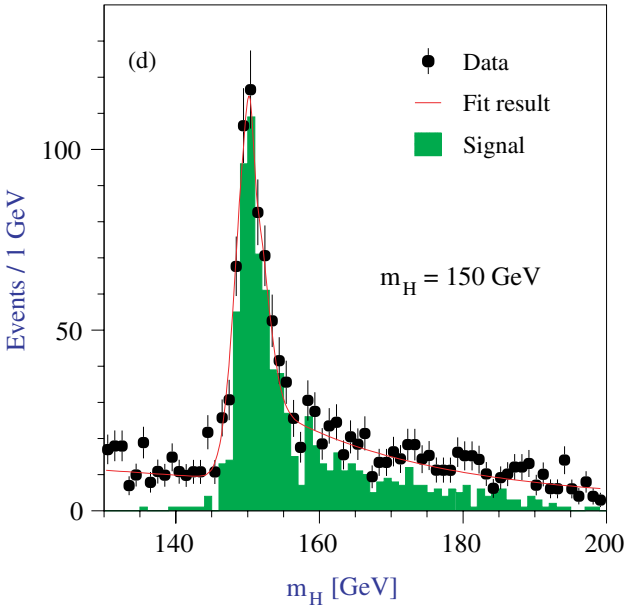

Fig. 8.6. Recoil-mass spectrum of $e^+e^- \to HZ \to W^+W^- \mu^+\mu^-$ events as expected for a linear collider with $m_H = 150$ GeV and $\sqrt{s} = 350$ GeV

secondary vertex due to the long lifetime of the B mesons. To measure the Higgs mass most precisely a kinematic fit of the whole event will be performed and a mass resolution of 50 MeV is expected. For Higgs masses above 150 GeV the Higgs boson will predominantly decay into a W pair. Here, a Higgs mass reconstruction is only possible when both W bosons decay hadronically. Alternatively, the recoil-mass spectrum calculated from the decay products of the recoiling Z can be used to measure the Higgs mass. From the $q\bar{q}\,W^+W^-$ final state a precision of 130 MeV is obtained for 500 pb^{-1} luminosity at 350 GeV centre-of-mass energy. The $l^+l^-\,W^+W^-$ final state with the Z boson decaying either into an electron or a muon pair delivers an event sample smaller by a factor of 10. Nevertheless, from the recoil-mass spectrum of the lepton pair a comparable uncertainty on the Higgs mass of 100 MeV is expected, the smaller statistics being compensated by the better mass resolution.

The recoil-mass spectrum provides the possibility to find the Higgs boson even in the case it decays invisibly, as expected from some SUSY models. To exploit the recoil-mass spectrum of the Z-decay leptons, a precise determination of the lepton momenta is mandatory. Ideally, the recoil-mass spectrum of the lepton pair should be limited only by the natural width of the Z boson and not by detector resolution. This requires an extraordinary momentum resolution for charged tracks. The uncertainty on the transverse momentum

should be better than $\Delta(1/p_{\mathrm{T}}) = 5 \cdot 10^{-5}$ GeV^{-1}. This has large implications on the detector design and especially for the tracking system (see Sect. 8.7).

The possibility to identify the production of a Higgs boson using the recoil mass of the Z decay products provides a largely unbiased measurement of the Higgs branching ratios and hence its couplings to the other particles [10]. According to the Standard Model the Higgs couplings to fermions $g_{\mathrm{H}ff} = m_f/v$ are completely fixed by the fermion masses m_f. Their precise measurement will then represent a test of the Yukawa sector of the Higgs mechanism. With the anticipated luminosities of a linear collider the measurement of Higgs decays into $\mathrm{b\bar{b}}$, $\mathrm{c\bar{c}}$ and $\tau^+\tau^-$ pairs seems feasible. The couplings to the lighter quarks and leptons are too small for the observation of these decays. The selection of the b- and c-quark final states is based on jet flavour capabilities of the detector. Precise vertexing and specific calorimetric signatures will allow to select the $\mathrm{H} \to \tau^+\tau^-$ decays. For Higgs masses below 140 GeV these decay modes have branching ratios large enough to be measured with an accuracy comparable to their theoretical error. For higher Higgs masses, when the Higgs decay into W pairs becomes dominant, at least the $\mathrm{H} \to \mathrm{b\bar{b}}$ decay can still be measured to better then 10%. The Higgs Yukawa coupling of the top quark is the largest coupling in the Standard Model: $g_{\mathrm{Htt}} = 0.72$ (compared to $g_{\mathrm{Hbb}} = 2 \cdot 10^{-2}$). For a light Higgs boson the Higgs decay into top pairs does not take place. Nevertheless, the Htt coupling is indirectly accessible in the loop process $\mathrm{H} \to \mathrm{gg}$ and directly in the Yukawa process $\mathrm{e^+e^-} \to \mathrm{t\bar{t}H}$. The latter process has a cross section of only 0.5 fb for $m_{\mathrm{H}} = 120$ GeV. The Feynman diagrams of both processes are depicted in Fig. 8.7. With an integrated luminosity of 1000 fb^{-1} at $\sqrt{s} = 800$ GeV the Higgs-top Yukawa coupling can be extracted with an accuracy of about 5% [10].

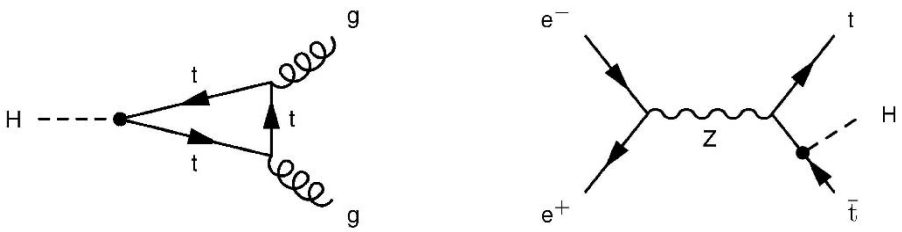

Fig. 8.7. Feynman diagrams of the Higgs decay into two gluons, $\mathrm{H} \to \mathrm{gg}$, and the Yukawa process, $\mathrm{e^+e^-} \to \mathrm{t\bar{t}H}$

The Higgs field constitutes a doublet of the weak isospin. Hence the Higgs boson itself couples through electroweak gauge coupling to the W and Z boson and the coupling strength is given by $g_{\mathrm{H}VV} = 2m_V^2/v$ for $V = \mathrm{W}, \mathrm{Z}$. At a linear collider both couplings can be measured independently with high precision. The Higgs coupling to the Z boson is probed with the Higgs-strahlung process where the coupling g_{HZZ} enters at tree level. The recoil-mass method provides

a cross-section measurement independent of the Higgs boson decays. A 5% measurement of this cross section should be feasible. Only for Higgs masses above 160 GeV the accuracy worsens because of the decreasing production cross section. The process of WW-fusion can be used to measure the Higgs coupling to the W boson. Figure 8.8 shows for the $b\bar{b}\nu\bar{\nu}$ final state how the WW-fusion process can be separated from the Higgs-strahlung process using the missing mass in the event. In case of the Higgs-strahlung the missing mass, which is actually the invariant mass of the neutrino system, should coincide with the Z mass. The WW-fusion process shows a distribution at higher missing mass values. From a simultaneous fit of the two contributions to the measured missing-mass spectrum one will be able to extract the WW-fusion cross section with accuracies between 3% and 13% for Higgs masses between 120 GeV and 160 GeV [11].

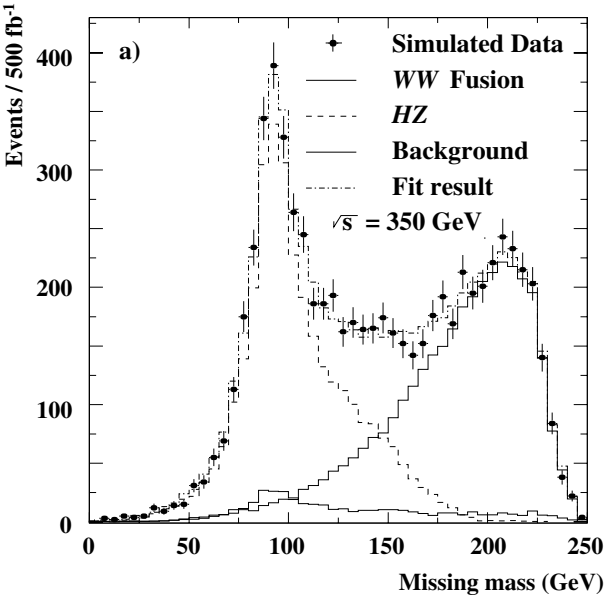

Fig. 8.8. Missing-mass spectrum of the WW-fusion process $e^+e^- \to H\nu\bar{\nu} \to b\bar{b}\nu\bar{\nu}$ for $m_H = 120$ GeV and $\sqrt{s} = 350$ GeV

Another goal in Higgs physics, the determination of spin and parity of the Higgs, can easily be accomplished with an energy scan at production threshold. Figure 8.9 demonstrates that the Standard Model value of the spin, $J = 0$, can be unambiguously verified through the measurement of the cross section of Higgs production using a total luminosity of 20 fb^{-1} distributed in three energy points.

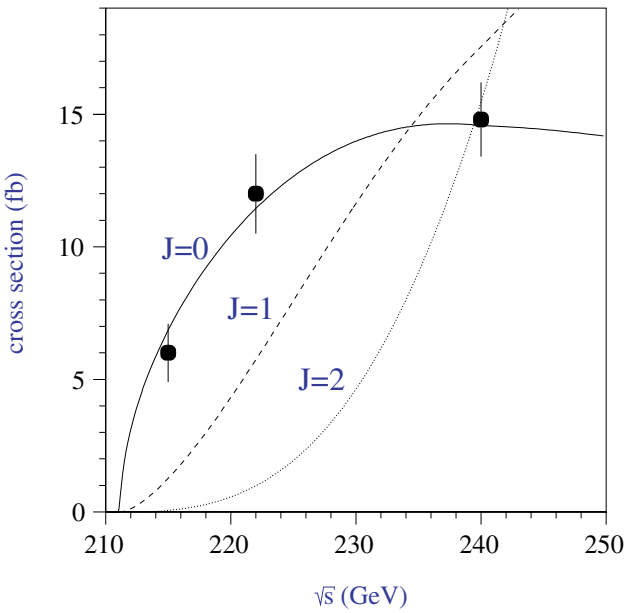

Fig. 8.9. Determination of the spin J of the Higgs boson from an energy scan at the production threshold. Shown are cross section curves for the three spin hypotheses together with simulated data for a total luminosity of 20 fb^{-1}

Another key measurement in the Higgs sector would be the measurement of the Higgs potential which would be the most direct proof for the concept of electroweak symmetry breaking. An expansion of the Higgs potential $V(H)$ around its vacuum expectation value v can be written as

$$V(H) = \lambda v^2 H^2 + \lambda v H^3 + \frac{1}{4}\lambda H^4 \,. \tag{8.1}$$

Whereas the first term represents the Higgs mass, $m_{\mathrm{H}} = \sqrt{2\lambda}v$, the second and the third imply the existence of triple and quartic Higgs boson vertices. Knowing the mass of the Higgs boson defines the parameter λ and the trilinear and quadrilinear couplings can be predicted unambiguously.

The trilinear coupling $g_{\mathrm{HHH}} = 3\lambda = \frac{3m_{\mathrm{H}}^2}{2v}$ can be accessed through the analysis of pair-production of Higgs bosons. In Reference [12] light Higgs bosons with masses below the $\mathrm{W^+W^-}$ threshold were considered, produced via the double Higgs-strahlung process and decaying in the dominant decay channel $\mathrm{H} \to \mathrm{b\bar{b}}$. The three Feynman diagrams of double Higgs-strahlung are depicted in Fig. 8.10. Large irreducible backgrounds are caused by electroweak and QCD processes which lead to the same final state $b\bar{b}b\bar{b}Z$. Kinematic cuts on the invariant masses of the b-quark pairs and on the polar angles of the jets should allow to reduce this background to a manageable level. Nevertheless, as

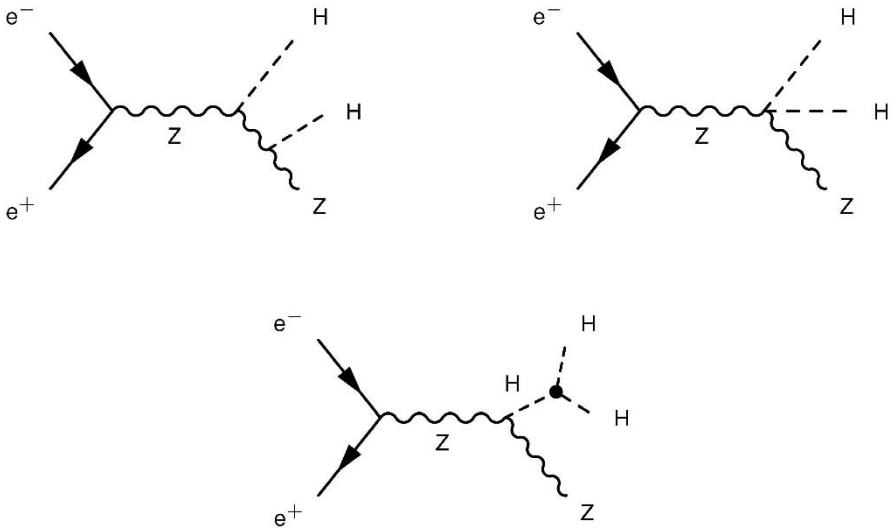

Fig. 8.10. Feynman diagrams of double Higgs production; the last diagram is sensitive to the triple Higgs boson vertex

the number of signal events is rather low, the trilinear couplings will only become measurable with very high luminosity, excellent b-tagging performance and a good jet resolution of the detector.

8.5 Complementarity of a Linear Collider and the LHC

In the past high-energy physics has profited a lot from the synergy between proton-(anti)proton colliders providing the highest possible particle energies, and e^+e^- colliders allowing measurements of very high precision.

For instance, after the measurement of electroweak interference effects at the e^+e^- collider PETRA the electroweak gauge bosons W and Z were discovered at the proton-antiproton collider SppS. Then the experiments at the e^+e^- colliders LEP and SLC performed high-precision analyses of the Z resonance sensitive to quantum-loop effects which allowed to deduce the mass range of the heavy top quark. Shortly later the top quark was discovered in the predicted mass interval at the proton-antiproton collider Tevatron. Since then the measurement of the top mass at the Tevatron together with the precision electroweak measurements from LEP and SLD have constrained better and better the allowed mass range of the the Higgs boson. The near future will show whether the proton-proton collider LHC will discover the Higgs boson in the predicted mass range.

The experimental programs of the LHC and an e^+e^- linear collider should clarify how the elementary particles obtain mass and reveal the mystery of

electroweak symmetry breaking. This will be accomplished either by the discovery of the Higgs particle or the measurement of new effects not predicted in the Standard Model. Due to its high collision energy the LHC has the higher mass reach for the discovery of heavy particles. On the other hand, at a linear collider, the clean experimental environment will allow precision measurements. Once the Higgs particle is detected at the LHC, precision measurements at a linear collider, especially of its branching fractions, will clarify whether it has the properties as expected by the Standard Model. To fully explore the mechanism of mass generation the high-energy measurements at the LHC have to be combined with the very precise measurements at a linear collider. Especially the question whether the concept of unification of forces can be extended and the coupling constants of the electroweak and the strong interaction unify at very high energy scales, not directly accessible to accelerator experiments, will require precision measurements that can only be accomplished at a linear collider.

The impact of the LHC results on the operation of a linear collider and the complementarity of both accelerators is worked out in detail in Reference [13]. If the LHC would discover a light Higgs boson, a linear collider will perform a precise measurement of its properties: mass, branching ratios and self-coupling. If a weakly interacting stable particle would be discovered at the LHC, an analysis at a linear collider will figure out whether this particle can account for the amount of dark matter observed in the universe. In the case supersymmetric particles are observed at the LHC, a linear collider will allow to perform a precise measurement of the accessible mass spectrum. Due to its high precision a linear collider might even be sensitive to quantum-loop effects of this new physics. This could allow to infer the existence and the mass of additional heavy particles missed by the LHC and too massive to be directly produced at a linear collider.

8.6 The International Linear Collider ILC

The project of the International Linear Collider (ILC) aims for e^+e^- collisions in the energy range from the Z mass, 91 GeV, up to about 1 TeV. It should provide these interactions with a luminosity of at least $3 \cdot 10^{34}$ $cm^{-2}s^{-1}$, which is more than three orders of magnitudes larger than what was achieved at LEP.

As the energy loss due to synchrotron radiation grows proportional to E_b^4, where E_b is the energy of the beam, a circular machine is not feasible for beam energies above 250 GeV. Therefore, both the electrons and the positrons will be brought to their final energy in two linear accelerators heading each other. The layout of the current ILC design consisting of two 15 km long linear accelerators heading on each other is shown in Fig. 8.11. The collision energy has to be supplied to the beam particles in one pass, therefore high accelerating gradients of at least 25 MV/m are mandatory to keep the accelerator at a reasonable length. As the beams are brought into collisions only once before

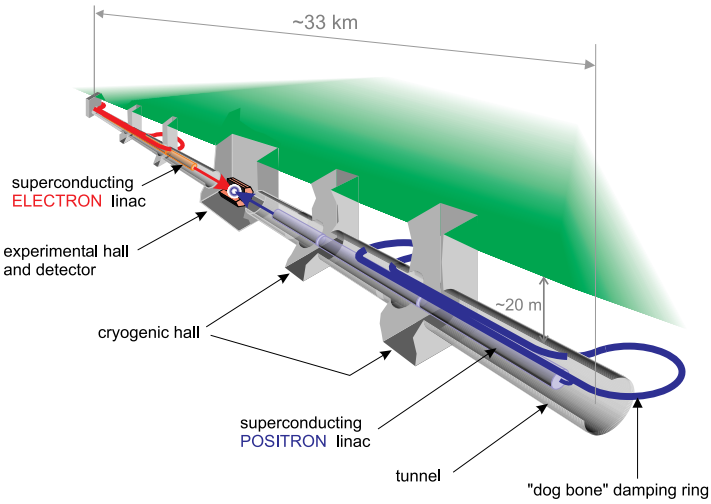

Fig. 8.11. The layout of the ILC in the current design stage. Two linear accelerators, one for the electrons and one for the positrons are heading each other

they are wasted in a beam dump the beams are squeezed to a very small cross section by the final focus system in order to achieve the required luminosity.

Colliding these very tiny beams leads to an immense charge density at the interaction point which in turn produces magnetic fields of the order of 10^3 T acting on the beam particles. These high magnetic fields are the source of intense synchrotron radiation, in this case called beam-strahlung. Although the beam-strahlung is focused along the beam line interactions with downstream accelerator components or the conversion into e^+e^- pairs could lead to severe background inside the detector.

While the luminosity is inversely proportional to the area of the beam cross-section, $\sigma_x\sigma_y$, the intensity of the beam-strahlung is inversely proportional to the two-dimensional variance of the charge distribution, $\sigma_x^2 + \sigma_y^2$. Therefore, preparing very flat beams with $\sigma_x \gg \sigma_y$ will minimise the beam-strahlung for a given beam cross-section. To reach the required luminosity, beams of 5 nm height and 500 nm width have to be delivered by the final-focus system. Scaling the results of the final-focus test beam [14] at SLAC to the ILC energies indicates that the required beam sizes can be achieved. Nevertheless, these extremely small beams have to be brought into collision. Removing ground motions from the final-focus quadrupoles and an additional sophisticated feed-back of the online luminosity monitoring to the beam steering will be required. Additionally, new methods have to be developed to measure the size of such tiny beams [15]

To keep the electrical power needed for the ILC at an acceptable level the RF will be switched on only for a small part of the total operation time. In the current design trains of about 3000 bunches are accelerated in 1 ms long

pulses. These pulses are repeated with a frequency of 5 Hz. The luminosity increases linearly with the number of bunches, but quadratically with bunch charge. Therefore, the total charge of the pulses should be squeezed into the smallest number of bunches possible. In the current design bunch charges of up to 8 nC will be accelerated to achieve the design luminosity.

High acceleration gradients lead to RF losses in the cavities. Therefore, superconducting technology has been chosen as baseline for the ILC design in order to minimise these losses. Within the linear collider R&D project TESLA (TEV Superconducting Linear Accelerator) [16] superconducting cavities with high accelerating gradients were developed, constructed and tested [17]. In contrary to the LEP cavities, which consisted of a niobium coated copper structure, those cavities are produced from ultra-pure niobium sheets, which are deep-drawn into half cells and then welded to 9-cell cavities. The TESLA cavities are manufactured industrially and are then subject to special treatments at the laboratories KEK and DESY. It was shown that especially the electro-polishing of the inner surfaces of the cavities helps to improve their performance.

Although the cavities are cooled with superfluid helium at temperatures of about 2 K where niobium is in its superconducting phase, a small surface resistance for the radio-frequency currents remains which is caused by residual impurities in the niobium bulk. The surface resistance increases quadratically with the cavity frequency. The RF frequency of 1.3 GHz of the TESLA design is a balance between the surface resistance and the cavity size which would become too large for very small frequencies. The size of accelerating structures of the TESLA design is significantly larger than compared to alternative proposals which were based on normal conducting cavities. This entails less strict requirements on the alignment of the accelerating structures and on the steering of the beam through the cavities.

The remaining resistance of a given cavity can be quantified in terms of Q_0, the quality factor for an unloaded cavity. The quality factor is the number of oscillations after which the amplitude of a freely-oscillating system is diminished to $1/e$. With the RF power intended the cavities must achieve a Q_0 of more than 10^{10}.

In Fig. 8.12 the quality factor measured as a function of the accelerating gradient is shown for industrially produced nine-cell cavities. Most of them were supplied by the company ACCEL in Bergisch-Gladbach (Germany), then sent to KEK in Japan for the electro-polishing of the inner surfaces and finally tested at DESY. For all devices a gradient of 35 MV/m is reached before the quality factor drops below the critical value. It has been verified that they preserve their excellent performance after installation into an accelerating module consisting of the helium cryostat and the RF power couplers. One of the cavities has been operated more than 1000 hours at an accelerating gradient of 35 MV/m without loss of performance including tests with electron beam.

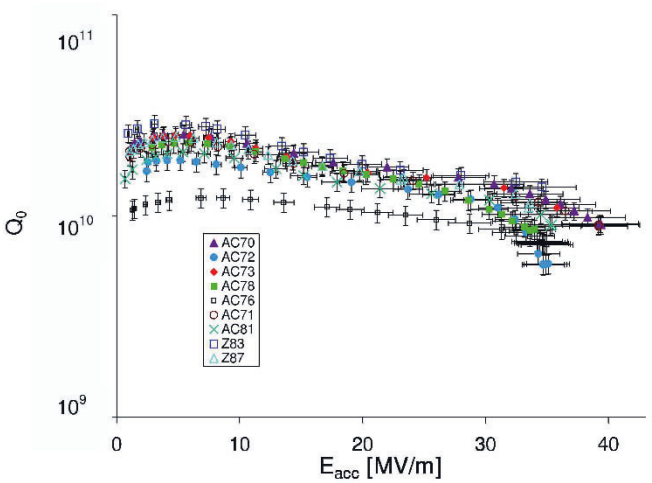

Fig. 8.12. Performance of electro-polished nine-cell cavities of TESLA type. The quality factor is measured as function of the accelerating gradient. All cavities reach gradients of 35 MV/m or more

8.7 Detector Development for the ILC

The physics goals and the accelerator design have large implications on the concept for a detector a the ILC. With respect to LEP a wider range of particle energies – from GeV to TeV – must be measured. In addition more complex final states are expected like, for example, the double Higgs-strahlung, $e^+e^- \rightarrow ZHH$, already discussed in Sect. 8.4. Moreover, the higher energy causes a larger Lorentz boost of the produced jets and therefore leads locally to very high particle densities. As compared to LEP and SLC a higher background level is expected at the ILC which is mainly caused by the intense beam-strahlung produced during the interpenetration of the strongly focused electron and positron beams. Important components of the background originating from the beam-strahlung are the low-energy e^+e^- pairs from the conversion of the photons within the heading bunch and neutrons produced through photonuclear reaction by photons hitting down-stream components of the accelerator.

Another important difference between linear and circular e^+e^- colliders is the largely different time structure of the bunch interactions. This implies consequences for the trigger and read-out scheme of the detector. For instance, in the TESLA design about 1 ms long trains containing 2820 bunches separated by 337 ns are planned. Per second five of these trains are produced and brought into collision. It is planned to store all detector information recorded during one bunch train into front-end buffers and to exploit the long time intervals between consecutive trains to read out the detector and to decide which events have to be written into persistent storage. This scheme would

render any hardware based trigger unnecessary and avoid any dead time of the data acquisition.

A concept for particle detection at the ILC and a first detector design have been presented within the technical design report of the TESLA project [18]. To address the challenges mentioned above additional detector R&D and design studies are necessary. These R&D efforts aim for a detector with the best possible energy, momentum and vertex resolutions. The identification of b- and c-quarks originating from the Higgs decay requires a reliable reconstruction of secondary vertices using a high-performance silicon pixel detector. The energy and momentum resolution are directly linked to the ability of the detector to reconstruct the massive resonances expected in the processes containing Higgs and SUSY particles. Excellent momentum resolution for individual tracks is provided by a large-volume drift chamber constructed as a Time Projection Chamber (TPC). Beside the momentum resolution for individual particles also jet energies have to be measured with high precision. This will be accomplished using the particle-flow algorithm where each particle measured in the tracker is associated to the corresponding cluster in the calorimeter. Calorimeters of very high granularity are needed for this task. Another important issue is the detector hermeticity, especially for the detection of missing energy signatures as expected in many SUSY scenarios.

The detector configuration as proposed in the TESLA technical design report [18] is presented in Fig. 8.13. It shows the layout of the detector whose main parts are a silicon vertex detector, a time projection chamber, electromagnetic calorimeters and muon chambers. All detector components except the muon chambers reside within a homogeneous magnetic field of 4 T provided by the superconducting solenoid coil. In the following, the design considerations and the ongoing R&D studies on the vertex detector, the main tracker and the calorimeter system are presented. For other important components of this detector like, for example, the instrumented mask the reader is referred to the TESLA TDR [18].

The main task of the vertex detector is the precise reconstruction of secondary vertices in order to identify jets originating from the hadronisation of b- or c-quarks. This is particularly important for the measurement of the branching ratios of the Higgs boson. Unfortunately the high centre-of-mass energies at the ILC do not help to reconstruct the decay vertices of long-lived particles as the larger decay lengths are compensated by smaller decay angles. Therefore an optimised detector design is mandatory for obtaining an improved vertexing performance. One aims at an impact parameter resolution of

$$\Delta(d_0) < 5\mu\mathrm{m} + 10\mu\mathrm{m}/(p\sin^{3/2}\theta)\ , \tag{8.2}$$

where the first term originates from the intrinsic detector resolution and the second term is caused by multiple scattering which depends on the momentum and polar angle of the particle. The intrinsic detector resolution has to be optimised, but even more important, the uncertainty caused by multiple

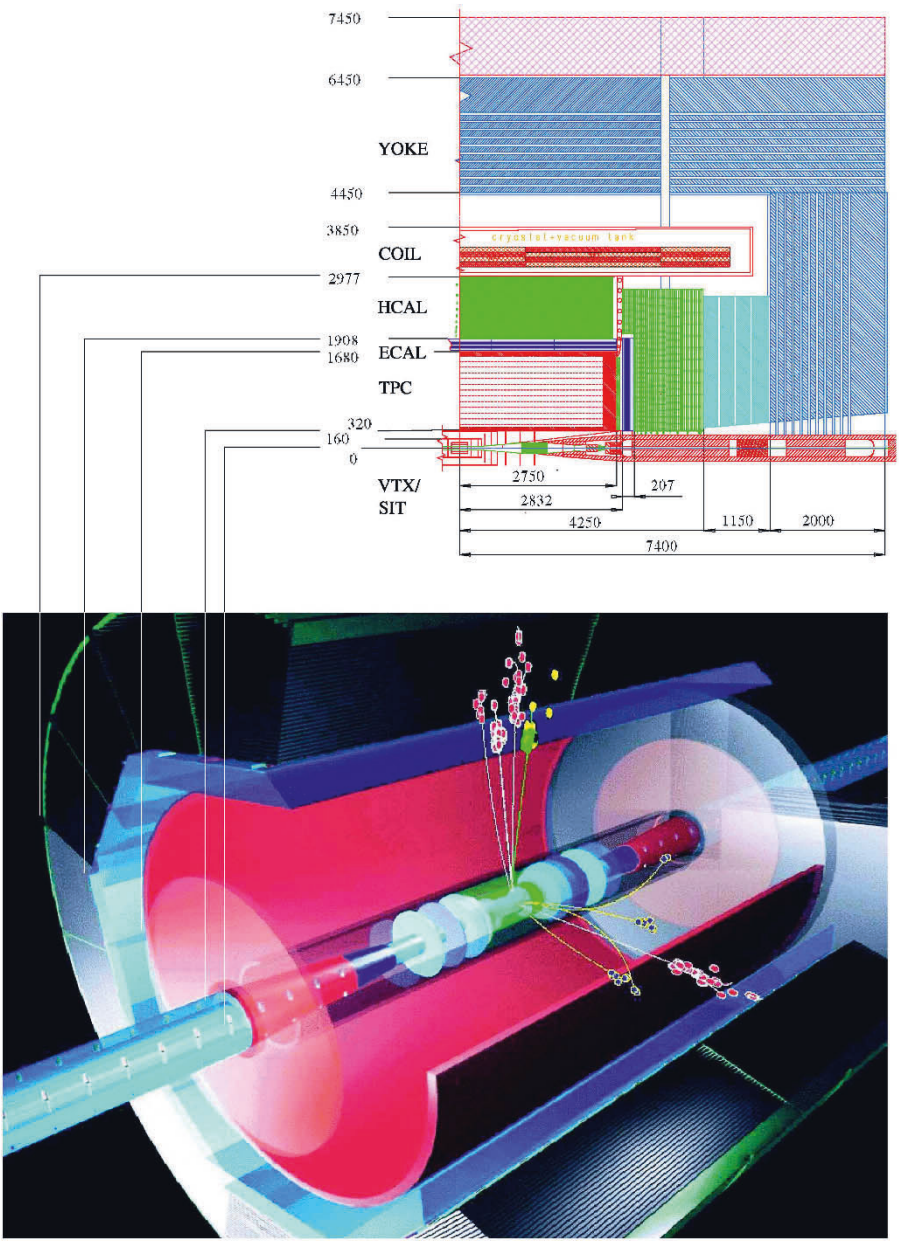

Fig. 8.13. The detector layout as proposed in the TESLA technical design report. Starting from the interaction region the main components are the vertex detector (VTX), the time projection chamber (TPC), the electromagnetic and hadronic calorimeters (ECAL, HCAL), the superconducting solenoidal magnet coil (COIL) and the magnet yoke (YOKE) which is instrumented with muon chambers

scattering in the device has to be minimised. In the current design the vertex detector consists of five layers of thin silicon pixel sensors allowing stand-alone tracking and internal calibration of the device. To keep the multiple scattering at the smallest possible level one aims at a material budget of only 0.06% of a radiation length per layer which corresponds to 60 μm of silicon. Such silicon sensors have been obtained by thinning fully processed and functional devices via the partial etching of the silicon bulk. Developing a structure to support such thin and fragile sensors is another important design issue for the vertex detector. For the architecture of the sensors three different technologies are currently investigated [19]: the charge coupled device (CCD), which has successfully been used at the SLD detector, the depleted field effect transistor (DEPFET), a fully-depleted low-noise sensor which measures the amount of charge collected directly at the location of the individual pixel, and the CMOS monolithic active pixel sensor (MAPS) which integrates the sensitive sensor and the pre-amplifying electronics on one CMOS chip.

A large-volume Time Projection Chamber (TPC) will be operated as the main tracker and will perform precise measurements of the momenta of charged particles. It combines the advantages of having a large sensitive volume and many reconstructed space points together with a very small material budget. This will avoid too much material in the tracker which would compromise the performance of the precision electromagnetic calorimeter. The ionisation tracks produced in the drift volume of a TPC are projected onto the endplates where a readout structure reconstructs the 2D image of the track. The z coordinate is measured using the drift time information. Traditionally wire grids stretched across the endplates are used for gas amplification where pad structures pick up the signals produced by the motion of the positive ion clouds. Unfortunately, the momentum resolution of these devices is limited due to the large wire distances of the order of 1 cm, $\boldsymbol{E} \times \boldsymbol{B}$ effects near the wires and the slow ion signal.

To set the goal for the momentum resolution consider again the unbiased reconstruction of the Higgs boson from the recoil mass spectrum of the lepton pair coming from the recoiling Z in the Higgs bremsstrahlung process (Fig. 8.6). In the ideal case the recoil mass resolution would be limited only by the natural width of the Z boson. Following this and other considerations the momentum resolution of the tracking system is required to be

$$\Delta(1/p_{\mathrm{T}}) < 5 \cdot 10^{-5}\,\mathrm{GeV}^{-1}\,. \tag{8.3}$$

To achieve this figure for each track 200 true space points have to be reconstructed with a single point resolution of 100 μm in the bending plane. This constitutes an improvement of about a factor of ten compared to the TPCs operated at LEP. To achieve this improvement the classical method of gas amplification using proportional wires has to be given up. Instead, the use of micro pattern gas detectors [20] like Gas Electron Multipliers (GEM) or Micromegas has been proposed. These devices are structured in the sub-mm range and show no preferred direction, thus any $\boldsymbol{E} \times \boldsymbol{B}$ effects are much

smaller and isotropic. In the case of GEMs, the sensitive pads directly detect the amplified electron signal and moreover, the slow ion tail is cut off since the ion cloud does not reach the induction region just above the pad plane. This results in a fast and narrow charge signal. Finally, the feed-back of ions into the drift volume of the TPC is intrinsically suppressed for these devices due to the highly asymmetric electric fields between the drift and the amplification region.

Since the transverse dimension of the electron cloud produced by GEMs or Micromegas is much smaller than the induced signal from proportional wires the signal is sometimes concentrated on only one pad. This would prevent the improvement of the spatial resolution by calculating centre-of-gravity of the signals on adjacent pads. This drawback can be avoided by reducing the pad size to the expense of an increase of the number of read-out channels. One solution currently under discussion would be the replacement of the pad plane by a highly integrated silicon read-out chip, where the pads of the input channels are equally distributed over one of the chip surfaces.

The main goals of the calorimeter system are an excellent energy resolution for electrons and photons and a high angular resolution for the particles forming a jet. The momentum of the charged particles, contributing on average about 60% to the jet energy, can be determined precisely in the tracking system. Another 30% of the energy is carried by photons which can be measured with high accuracy in the electromagnetic calorimeter. Only the energy measurement of the remaining 10%, consisting of neutral hadrons, suffers from the large fluctuations in hadronic interactions. Detailed studies have shown that the optimum jet energy resolution can be achieved if the energy deposition of each particle is measured separately and each particle track reconstructed in the tracking system is associated to the corresponding energy cluster. Then, depending on the particle type, either the track momentum, the electromagnetic energy or the hadronic energy is used to determine the contribution of the given particle to the jet energy.

This strategy requires a highly granular calorimeter in order to separate the energy depositions of nearby particles. The required transverse segmentation of the electromagnetic calorimeter is given by the Molière radius which should be as small as possible. An ideal candidate would be a silicon-tungsten calorimeter which has a Moliere radius of 9 mm. The current design consists of 40 layers of tungsten plates interleaved with silicon sensors which are segmented into individual diodes of 1 cm^2 size. A total area of about 2000 m^2 of silicon would be necessary which makes the electromagnetic calorimeter the most expensive part of the detector. The energy resolution is expected to be

$$\Delta E/E < 0.1/\sqrt{E/\mathrm{GeV}}\,. \tag{8.4}$$

The performance of such a calorimeter must still be demonstrated using a large scale prototype.

For the design of a hadron calorimeter with high granularity the feasibility of a digital read-out has been investigated. It would consist of very small sen-

sitive cells of about 1 cm^3 size. A candidate for these cells are small scintillator pads connected to optical fibres which extract the light to photo-sensitive devices. The option envisaged for the read-out would be to detect for each cell only a "hit" or "no hit" signal which would simplify the front-end electronics and reduce the amount of data to be read out. This concept is called digital hadron calorimeter and would make the large number of channels feasible.

References

1. A. Accomando et al., Phys. Rep. **299**, 1 (1998);
   J.A. Aguilar-Saavedra et al., DESY 2001-011C and hep-ph/0106315;
   T. Abe et al., SLAC-R-570 and hep-ex/0106057
2. G.W. Wilson, LC note LC-PHSM-2001-009
3. S.T. Boogert and D.J. Miller, Eprint hep-ex/0211021 (2002)
4. A.H. Hoang and T. Teubner, Phys. Rev. **D 60**, 114027 (1999);
   K. Melnikov and A. Yelkhovsky, Nucl. Phys. **B 528**, 59 (1998);
   O. Yakovlev, Phys. Lett. **B 457**, 170 (1999);
   M. Beneke, A. Signer and V.A. Smirnov, Phys. Lett. **B 454**, 137 (1999);
   T. Nagano, A. Ota and Y. Sumino, Phys. Rev. **D 60**, 114014 (1999)
5. M. Beneke, Phys. Lett. **B 434**, 115 (1998)
6. A.H. Hoang and T. Teubner, Phys. Rev. **D 60**, 114027 (1999)
7. M. Martinez and R. Miquel, Eur. Phys. J. **C 27**, 49 (2003)
8. A. Juste et al., Eprint hep-ph/0601122
9. P. Garcia-Abia, W. Lohmann and A. Raspereza, LC note LC-PHSM-2000-062;
   P. Garcia-Abia and W. Lohmann, EPJdirect **C 2**, 1 (2000)
10. M. Battaglia, Eprint hep-ph/9910271 (1999)
11. K. Desch and N. Meyer, LC note LC-PHSM-2001-025
12. F. Boudjema and E. Chopin, Z. Phys. **C 73**, 85 (1996);
    D.J. Miller and S. Moretti, Eur. Phys. J. **C 13**, 459 (2000);
    M. Battaglia, E. Boos, W.-M. Yao, Eprint hep-ph/0111276 (2001);
    A. Djouadi et al., Eur. Phys. J. **C 10**, 27 (1999)
13. G. Weiglein et al., Eprint hep-ph/0410364 (2004)
14. V. Balakin, Phys. Rev. Lett. **74**, 2479 (1995)
15. T. Shintake, Nucl. Inst. Meth. **A 311**, 453 (1992)
16. J.A. Aguilar-Saavedra et al., DESY 2001-011B
17. L. Lilje et al., Nucl. Inst. Meth. **A 524**, 1 (2004);
    L. Lilje et al., Nucl. Inst. Meth. **A 516**, 213 (2004);
    B. Aune et al., DESY 2000-031, PRST-AB 3, 092001 (2000)
18. J.A. Aguilar-Saavedra et al., DESY 2001-011D
19. C. Damerell, LC note LC-DET-2001-023;
    P. Fischer at al., LC note LC-DET-2002-004;
    M. Winter et al., LC note LC-DET-2001-017
20. F. Sauli, Nucl. Inst. Meth. **A 386**, 531 (1997);
    Y. Giomataris, Nucl. Inst. Meth. **A 376**, 29 (1996);

9

Summary and Conclusions

The successful operation of the e^+e^- colliders SLD and LEP during the last decade of the 20th century constituted the advent of precision electroweak physics testing the electroweak Standard Model to unprecedented accuracy. Especially the properties of the heavy electroweak gauge bosons, $W^{\pm}$ and Z have been determined to very high precision.

The value of the Z mass was measured with an accuracy of 23 ppm by the scan of the Z lineshape at LEP 1:

$$m_{\mathrm{Z}} = 91.1875 \pm 0.0021 \text{ GeV}$$

This makes it to one of the better known physical constants, an order of magnitude more precisely measured than the gravitational constant, for example. Additionally the couplings of the Z to the various fermions were derived from the cross section and asymmetry measurements. They are found to be in excellent agreement with the Standard Model expectations and revealed the existence of weak quantum corrections. The results of SLD and LEP 1 are combined into a precise determination of $\sin^2\theta_{\mathrm{eff}}$ which in turn can be converted into a prediction of the W mass.

At LEP 2 the centre-of-mass energy was increased above the threshold of W-pair production. In total 40,000 W-pair events were recorded which allowed to study production and decay of the W bosons in great detail. It was shown that the triple gauge couplings exist as predicted by the theory. Additional theoretical work was necessary to describe the process of W-pair production with the accuracy needed to match the experimental precision. Examples are the radiative corrections to four-fermion production and the modelling of interactions in the final state of fully hadronic events. This theoretical work together with comprehensive studies of experimental systematic effects allowed the measurement of the W mass with an accuracy of better than half a permill. Together with the measurements at the Tevatron one obtains as current world average:

$$m_{\mathrm{W}} = 80.392 \pm 0.029 \text{ GeV}$$

Stefan Roth: *Precision Electroweak Physics at Electron-Positron Colliders*
STMP **220**, 169–170 (2006)
DOI 10.1007/3-540-35165-5_9

These results are complemented by the Tevatron $p\bar{p}$ experiments which contributed to electroweak physics, most importantly, by the discovery of the top quark and the measurement of its mass. The fit of the Standard Model parameters to all electroweak measurements verifies the self-consistency of the theory. Additionally it shows that radiative corrections are needed to describe the data and that the Standard Model is correct at the one-loop level. Especially the additional information on the top mass from the Tevatron improves the accuracy of the indirect determination of the W mass using the precision observables from SLD and LEP 1. This value and the direct W-mass measurement agree within the experimental uncertainty. Assuming the Standard Model to be correct, this comparison yields information on its last unknown parameter, the mass of the still undiscovered Higgs boson, m_{H}. One derives an upper limit on the Higgs mass of:

$$m_{\mathrm{H}} < 199 \text{ GeV (at 95\% C.L.)}$$

If the Standard Model is correct and the Higgs boson exists it will be discovered soon after the startup of the LHC. If the Higgs exists an interesting question is wether the Higgs mass is indeed found in the range predicted by the precision electroweak data. This would constitute another example of the synergy between precision measurements at e^+e^- colliders and the discovery potential of hadron colliders. If the Higgs boson will be discovered the origin of the electroweak symmetry breaking still remains a mystery. Theories beyond the Standard Model which would explain the symmetry breaking could either be identified by the discovery of new particles and phenomena or by the detailed study of the Higgs sector. Especially for the latter case the advent of an e^+e^- linear collider with centre-of-mass energies up to the TeV range is required. It would allow to fix the properties of the Higgs boson and measure the Higgs potential through the study of Higgs self couplings. Together with an improved accuracy on other electroweak observables like, for example, the top mass and the W mass it would show wether the observed Higgs sector is described by the Standard Model or a more general theory has to be considered.

Index

Springer Tracts in Modern Physics

178 **Capillary Surfaces**
Shape – Stability – Dynamics, in Particular Under Weightlessness
By Dieter Langbein 2002. 182 figs. XVIII, 364 pages

179 **Anomalous X-ray Scattering for Materials Characterization**
Atomic-Scale Structure Determination
By Yoshio Waseda 2002. 132 figs. XIV, 214 pages

180 **Coverings of Discrete Quasiperiodic Sets**
Theory and Applications to Quasicrystals
Edited by P. Kramer and Z. Papadopolos 2002. 128 figs., XIV, 274 pages

181 **Emulsion Science**
Basic Principles. An Overview
By J. Bibette, F. Leal-Calderon, V. Schmitt, and P. Poulin 2002. 50 figs., IX, 140 pages

182 **Transmission Electron Microscopy of Semiconductor Nanostructures**
An Analysis of Composition and Strain State
By A. Rosenauer 2003. 136 figs., XII, 238 pages

183 **Transverse Patterns in Nonlinear Optical Resonators**
By K. Staliūnas, V. J. Sánchez-Morcillo 2003. 132 figs., XII, 226 pages

184 **Statistical Physics and Economics**
Concepts, Tools and Applications
By M. Schulz 2003. 54 figs., XII, 244 pages

185 **Electronic Defect States in Alkali Halides**
Effects of Interaction with Molecular Ions
By V. Dierolf 2003. 80 figs., XII, 196 pages

186 **Electron-Beam Interactions with Solids**
Application of the Monte Carlo Method to Electron Scattering Problems
By M. Dapor 2003. 27 figs., X, 110 pages

187 **High-Field Transport in Semiconductor Superlattices**
By K. Leo 2003. 164 figs.,XIV, 240 pages

188 **Transverse Pattern Formation in Photorefractive Optics**
By C. Denz, M. Schwab, and C. Weilnau 2003. 143 figs., XVIII, 331 pages

189 **Spatio-Temporal Dynamics and Quantum Fluctuations in Semiconductor Lasers**
By O. Hess, E. Gehrig 2003. 91 figs., XIV, 232 pages

190 **Neutrino Mass**
Edited by G. Altarelli, K. Winter 2003. 118 figs., XII, 248 pages

191 **Spin-orbit Coupling Effects in Two-dimensional Electron and Hole Systems**
By R. Winkler 2003. 66 figs., XII, 224 pages

192 **Electronic Quantum Transport in Mesoscopic Semiconductor Structures**
By T. Ihn 2003. 90 figs., XII, 280 pages

193 **Spinning Particles – Semiclassics and Spectral Statistics**
By S. Keppeler 2003. 15 figs., X, 190 pages

194 **Light Emitting Silicon for Microphotonics**
By S. Ossicini, L. Pavesi, and F. Priolo 2003. 206 figs., XII, 284 pages

195 **Uncovering *CP* Violation**
Experimental Clarification in the Neutral K Meson and B Meson Systems
By K. Kleinknecht 2003. 67 figs., XII, 144 pages

196 **Ising-type Antiferromagnets**
Model Systems in Statistical Physics and in the Magnetism of Exchange Bias
By C. Binek 2003. 52 figs., X, 120 pages

197 **Electroweak Processes in External Electromagnetic Fields**
By A. Kuznetsov and N. Mikheev 2003. 24 figs., XII, 136 pages

Springer Tracts in Modern Physics

198 **Electroweak Symmetry Breaking**
The Bottom-Up Approach
By W. Kilian 2003. 25 figs., X, 128 pages

199 **X-Ray Diffuse Scattering from Self-Organized Mesoscopic Semiconductor Structures**
By M. Schmidbauer 2003. 102 figs., X, 204 pages

200 **Compton Scattering**
Investigating the Structure of the Nucleon with Real Photons
By F. Wissmann 2003. 68 figs., VIII, 142 pages

201 **Heavy Quark Effective Theory**
By A. Grozin 2004. 72 figs., X, 213 pages

202 **Theory of Unconventional Superconductors**
By D. Manske 2004. 84 figs., XII, 228 pages

203 **Effective Field Theories in Flavour Physics**
By T. Mannel 2004. 29 figs., VIII, 175 pages

204 **Stopping of Heavy Ions**
By P. Sigmund 2004. 43 figs., XIV, 157 pages

205 **Three-Dimensional X-Ray Diffraction Microscopy**
Mapping Polycrystals and Their Dynamics
By H. Poulsen 2004. 49 figs., XI, 154 pages

206 **Ultrathin Metal Films**
Magnetic and Structural Properties
By M. Wuttig and X. Liu 2004. 234 figs., XII, 375 pages

207 **Dynamics of Spatio-Temporal Cellular Structures**
Henri Benard Centenary Review
Edited by I. Mutabazi, J.E. Wesfreid, and E. Guyon 2005. approx. 50 figs., 150 pages

208 **Nuclear Condensed Matter Physics with Synchrotron Radiation**
Basic Principles, Methodology and Applications
By R. Röhlsberger 2004. 152 figs., XVI, 318 pages

209 **Infrared Ellipsometry on Semiconductor Layer Structures**
Phonons, Plasmons, and Polaritons
By M. Schubert 2004. 77 figs., XI, 193 pages

210 **Cosmology**
By D.-E. Liebscher 2005. Approx. 100 figs., 300 pages

211 **Evaluating Feynman Integrals**
By V.A. Smirnov 2004. 48 figs., IX, 247 pages

213 **Parametric X-ray Radiation in Crystals**
By V.G. Baryshevsky, I.D. Feranchuk, and A.P. Ulyanenkov 2006. 63 figs., IX, 172 pages

214 **Unconventional Superconductors**
Experimental Investigation of the Order-Parameter Symmetry
By G. Goll 2006. 67 figs., XII, 172 pages

215 **Control Theory in Physics and other Fields of Science**
Concepts, Tools, and Applications
By M. Schulz 2006. 46 figs., X, 294 pages

216 **Theory of the Muon Anomalous Magnetic Moment**
By K. Melnikov, A. Vainshtein 2006. 33 figs., XII, 176 pages

217 **The Flow Equation Approach to Many-Particle Systems**
By S. Kehrein 2006. 24 figs., XII, 170 pages

219 **Inelastic Light Scattering of Semiconductor Nanostructures**
By Christian Schüller 2007. 105 figs., XII, 178 pages

220 **Precision Electroweak Physics at Electron-Positron Colliders**
By Stefan Roth 2007. 107 figs., X, 174 pages